2015

Applications of clumped-isotope palaeothermometry

Florian W. Dux
University of Wollongong, fdux@uow.edu.au

Applications of clumped-isotope palaeothermometry

This thesis is submitted in partial fulfilment of the requirements of the degree of

DOCTOR OF PHILOSOPHY

from

UNIVERSITY OF WOLLONGONG

by

FLORIAN W. DUX

BSc (Hons) Adv.

SCHOOL OF EARTH AND ENVIRONMENTAL SCIENCES

2015

CERTIFICATION

I declare that this thesis, submitted in partial fulfilment of the requirements for the award of Doctor of Philosophy, in the School of Earth and Environmental Sciences, University of Wollongong, is wholly my own work unless otherwise referenced or acknowledged. The document has not been submitted for qualifications at any other academic institution.

Florian W. Dux

31 March 2015

"I have not failed. I've just found 10,000 ways that won't work."
Thomas A. Edison

Acknowledgements

Thank you to the University of Wollongong and the School of Earth and Environmental Sciences for providing me with the opportunity to undertake my university studies from undergraduate to PhD.

To my supervisors, Allan Chivas and Adriana Garcìa. I would like to thank you for the opportunity to undertake this study and send me on a path of becoming geochemist. I thank Allan for the suggestion and providing the facilities to study clumped isotopes, this has allowed me to pursue an analytical technique that has the potential to revolutionise the way we calculate palaeotemperatures. Thank you Adriana for the support and encouragement and revisions of many versions of chapters and papers.

Thank you to all the administrative staff at the University of Wollongong, Denise and Wendy for your logistical help to cut through the university system. Thank you to our head of school Zenobia Jacobs and Laurie Chisolm and previously Colin Murray-Wallace, for providing a wonderful working environment. Thank you to all the technical staff in the department, Jose, Heidi, Terry for their help with samples, maps and supplies. A big thanks goes to Lili Yu and Helen Price for their assistance with ICP-MS analyses and laboratory work, I could not have done it alone.

I would like to thank Paul Carr, Brian Jones and Bruce Selleck for providing the glendonite samples as well as invaluable field notes and insight. The Riversleigh fieldwork was funded by ARC grant LP0989969. In addition, I would like to thank Michael Archer, Suzanne Hand, Karen Black, Jon Woodhead, Ian Graham, Henk Godthelp, Elena Platonova and others for their help and guidance in the field at Riversleigh. I would like to acknowledge the Australian Museum for providing the Sydney Harbour shell samples and for allowing me access to their extensive collection. I would also like to acknowledge David Fink and ANSTO in their assistance in the dating of the Sydney Harbour shells (ANSTO grant 04/029).

David Wheeler, my partner in geochemical crime, from your knowledge of mass spectrometers to fixing whatever Murphies Law decides to break on a given day this would not have been possible without your wisdom, thank you.

To my fellow PhD companions, thank you for your help, support, jokes, and lending an ear when I just wanted someone to complain to. I wish you all well and hope you reach your goal and Ilaroy.

I would like to thank my family, mum Sabine, dad Rüdiger, brother Henrik and my grandmother Johanna (Momo), for all your support and encouragement over the years from my undergraduate studies to the toils of my honours and the journey of my PhD. Without your washing of clothes, countless dinners and wise words this would not have been possible. Thank you to my close friends, whether you are far away or close, you have helped me through all of this. Thank you to Ken and Margaret Kermode for accepting me into your family and home.

Finally thank you to my rock, light and angel, Stephanie. Words cannot describe how much I appreciate your presence in these last years. You have kept me sane and have made me a better person. Thank you from the bottom of my heart.

Abstract

Standard palaeotemperature equations, used to interpret the formation conditions of carbonate materials, are generally problematic. This is due to the need to know both the $\delta^{18}O$ value of the water and the precipitated carbonate to complete the equation. The clumped-isotope method overcomes these uncertainties by examining the affinity of heavy isotopes bonding ($^{13}C^{18}O^{16}O$ = $^{47}CO_2$) in favour of bonding to lighter isotopes ($^{12}C^{16}O^{16}O$ = $^{44}CO_2$) in evolved CO_2 from carbonates. This process of "clumping" is sensitive to ambient temperature, so can be used to determine palaeotemperature, but is independent of bulk isotopic composition of the original water. Measured values (Δ_{47}) are expressed as per mil variation of the relative abundance of an isotopologue compared to the theoretical predicted relative abundance based on a stochastic random distribution.

Clumped-isotope analysis utilises an ultra-high sensitive gas-source dual inlet mass spectrometer and measures all six masses of CO_2 simultaneously (i.e. 44, 45, 46, 47, 48 and 49) to an accuracy of ± 0.01 per mil (‰) (i.e. CO_2 mass 47/44 ratio). These high levels of accuracy and precision were achieved by using an updated form of the original clumped isotope method with a Thermo Finnigan™ MAT 253. Long analysis times (approximately 4 hours) and long integration times (26 seconds) were used to determine carbonate formation temperatures with errors of ± 2 °C. This required manual CO_2 gas collection by vacuum line extraction with cryogenic purification. Temperature stability was maintained by a temperature-controlled water bath (± 0.1 °C) during the carbonate reaction. Ambient room air-temperature for the mass-spectrometer was also controlled (± 0.1 °C). An improved gas chromatographic (GC) purification step, using an Agilent™ 7890A gas chromatograph with customised sample inlet system and trapping system, was used to remove hydrocarbon and chloride contamination. Analysis of inter-laboratory standards and comparisons to calibrated standard gases, heated gas samples and standard water equilibration samples were used for standardisation of all unknown samples.

Three different types of carbonate precipitates were analysed for their applicability to the "clumped-isotope" palaeothermometer. Results demonstrate that Permian cold-water carbonates, also termed glendonites, provide clumped isotope temperatures of 1.9 ± 2.0 to 9.8 ± 4.9 °C. These temperatures represent cold-water climatic conditions in the Permian within the Sydney Basin, Australia. Late Neogene glendonites from the Taymyr Peninsula, Russia, also provide cold-water temperature conditions of 6.5 ± 4.1 °C. Calculated formation temperatures correlate well to

published modern glendonite formation conditions. This shows that the clumped isotope method is able to determine some glendonite formation temperatures. This allows us to directly infer the environmental conditions at the time of formation. However, it is also apparent that post-depositional alteration by heating through burial and fluid-rock interaction has a profound effect on the palaeotemperature results.

Carbonates from cave deposits from the Riversleigh fossil area, Australia, include speleothem deposits (flow stone, cave pearls, calcite rafts and travertine rim pools). Speleothem precipitates were used to calculate an ambient formation temperature of 19.6 ± 4.8 °C. This indicates the ambient temperature in the Riversleigh area in the Middle Miocene. Additionally, a stalagmite speleothem was analysed providing a calculated formation temperature ~10 °C higher than carbonate in the immediate surrounding area. This confirms previous work showing that non-equilibrium precipitated speleothem material registers low Δ_{47} values and thus calculated formation temperatures that are too high. Calcite rafts and flowstones from Riversleigh also exhibit temperature discrepancies of ~7 to 9 °C.

Molluscs were one of the first materials to be analysed by the clumped isotope method. This study investigates a mollusc assemblage dredged from Sydney Harbour, Australia with dates between 570 ± 80 and 7980 ± 80 years BP (AMS ^{14}C) (i.e. much of the Holocene). These molluscs were analysed to provide insight into the temperature variation of Sydney Harbour during the Holocene. Upon analysis of the carbonate powders excessive organic hydrocarbon contamination was found that was not able to be removed from the extracted carbon dioxide gas. Altering the purification procedure, used for all other carbonate extractions, had little effect on the calculated Δ_{47} values and their subsequent temperature. None of the analyses of the molluscs in this study yielded plausible palaeotemperature results due to the inability to fully remove the contamination.

This study reports the first set of clumped-isotope results from the University of Wollongong laboratory. Improvements were made to previously developed analytical systems to more accurately and precisely determine carbonate formation temperatures. This study has indicated that the cold-water carbonate glendonite and equilibrium precipitated cave deposits have the potential to be utilised as reliable clumped isotope palaeotemperature proxies. Further improvements in the clumped isotope method are needed to more accurately investigate both of these types of material as well to resolve the origin of discrepancies in the mollusc clumped-isotope results.

Table of Contents

Certification II

Acknowledgements V

Abstract VII

Table of Contents XI

List of Equations XV

List of Figures XVIII

List of Tables XXVII

List of Abbreviations XXXIII

Chapter 1 - Introduction 1

1.1 Palaeotemperature reconstruction 3

1.2 Clumped Isotopes 5

1.3 Previous applications 7

1.4 Glendonites 8

1.5 Cave formations 9

1.6 Shells 10

1.7 Summary 11

Chapter 2 - Clumped isotopes: a review 13

2.1 Introduction 14

2.2 Multiply substituted isotopologues 15

2.3 Principles of clumped isotope carbonate palaeothermometry 17

2.4 Applications of clumped isotopes 20

2.4.1 Sea-surface temperatures 20

2.4.2 Corals 21

2.4.3 Terrestrial fossil material 21

2.4.4 Speleothems 22

2.4.5 Soil carbonates 22

2.4.6 Metamorphism and diagenesis 23

2.4.7 Atmospheric carbon dioxide 23

2.4.8 Methane 24

2.5 CO_2 preparation 25

2.5.1 Phosphoric acid digestion of carbonates 25

2.5.2 Reaction limitations and considerations 28

2.5.3 Gas extraction 29

2.5.4 Cryogenic separation 29

2.6 Sample CO_2 purification 31

2.7 Δ_{47} mass spectrometry 35

2.7.1 Quantification of the mass-47 anomaly 37

2.7.2 Reference frame and calibration 40

2.7.3 Pressure baseline (PBL) correction 46

2.7.4 Acid fractionation factor 47

2.7.5 Δ_{47}-*T* palaeotemperature equation 48

Chapter 3 - Methods 51

3.1 Introduction 52

3.2 Sample pre-treatment 52

3.3 Elemental composition analysis 53

3.3.1 X-ray powder diffraction (XRD) 53

3.3.2 Inductively coupled plasma mass spectrometry (ICP-MS) 54

3.4 Micromorphology and thin sections 56

3.5 Accelerator mass spectrometry ^{14}C dating 58

3.6 Clumped-isotope sample gas preparation 59

3.6.1 Phosphoric acid preparation 59

3.6.2 Sample digestion 60

3.6.3 Vacuum system 63

3.6.4 Cryogenic trapping 65

3.6.5 Gas extraction apparatus 65

3.6.6 Gas yields 66

3.6.7 Working gas 67

3.6.8 Heated gas standards 67

3.6.9 Temperature-controlled water equilibrations 68

3.7 Clumped-isotopes: sample gas purification 70

3.8 Clumped-isotopes: mass spectrometry 73

3.8.1 Clumped-isotope measurements 75

3.8.2 Empirical transfer function 75

3.8.3 Palaeotemperature determination 81

3.8.4 Internal carbonate reference standards 83

Chapter 4: Cold-water carbonates 85

4.1 Introduction 86

4.2 Background 87

4.2.1 Natural ikaite formation 88

4.2.2 Geographic occurrence of ikaite and glendonite 90

4.2.3 Synthetic ikaite precipitation 93

4.2.4 Morphology of ikaite and its pseudomorphs 94

4.2.5 Stable isotopes of glendonites 96

4.3 Methods 97

4.3.1 Glendonite sample powder preparation 97

4.3.2 Polished block 98

4.4 Results 99

4.4.1 Sample material and site descriptions 99
4.4.2 Glendonite morphology and mineralogy 105
4.4.3 Growth zoning in glendonite 106
4.4.4 Glendonite trace-element composition 108
4.4.5 Glendonite mineralogy 109
4.4.6 Stable isotope results 110
4.5 Discussion 116
4.5.1 Sydney Basin 116
4.5.1 Tasman Basin 118
4.5.2 Kola Peninsula 119
4.5.3 Taymyr Peninsula 120
4.5.4 North American thinolite (Type A) pseudomorphs 120
4.5.5 Relationship of calcite to water of hydration and ambient pore water 121
4.6 Conclusions 123

Chapter 5: Cave Systems of Riversleigh, Queensland 127
5.1 Introduction 128
5.2 Background 129
5.2.1 Carbonate karst chemistry 130
5.2.2 Speleothem morphology 132
5.2.3 The geology of the Riversleigh area 133
5.2.4 Dating of the Riversleigh deposits 135
5.3 Methods 137
5.3.1 Sample collection and preparation 137
5.3.2 Thin sections 138
5.3.3 Isotopic analysis 138
5.4 Results and discussion 139
5.4.1 Carbonate facies descriptions 139

5.4.1.1 Neville's Garden site (NG) 139

5.4.1.2 Godthelp Hill area 147

5.4.1.3 Bitesantennary site (BC) 159

5.4.1.4 Cleft of Ages site (CA), White Hall site (WH), Oncoid site (OS) and Ringtail site (RT) 169

5.4.2 Clumped-isotope Δ_{47} palaeotemperature determinations 176

5.4.2.1 Neville's Garden site 177

5.4.2.2 Inabayence and Camels Sputum sites 177

5.4.2.3 Stalagmite site 178

5.4.2.4 Bitesantennary site 178

5.4.2.5 Cleft of Ages, Oncoid and White Hall sites 179

5.4.2.6 Ringtail site 180

5.4.3 Enriched Δ_{47} values and associated highly negative temperatures 181

5.4.4 Calculated $\delta^{18}O$ of host waters 183

5.5 Conclusions 186

Chapter 6: Sydney Harbour: tropical or temperate waters? 189

6.1 Introduction 190

6.2 Background 192

6.2.1 Calcification physiology 193

6.2.2 Dissolved inorganic carbonate (DIC) source 194

6.2.3 Shell sampling strategies 194

6.2.4 Clumped isotopes and biogenic carbonates 195

6.3 Methods 199

6.3.1 Specimen classification and nomenclature 199

6.3.2 Shell carbonate sampling and preparation 201

6.3.3 ^{14}C dating by AMS 202

6.3.4 Isotopic analysis 202

6.4 Results and discussion 203

6.4.1 Shell taxonomy and descriptions 203

6.4.2 Significance of species diversity 211

6.4.3 Shell ages and ^{14}C dating 215

6.4.4 Conventional $\delta^{13}C$ and $\delta^{18}O$ results 216

6.4.5 Clumped-isotope analysis 218

6.4.6 Isotopic shell zone partitioning 219

6.4.7 $\delta^{18}O$ of precipitating host water 220

6.5 Conclusions 223

Chapter: Synopsis 225

References 229

Appendix 1: ICP-MS tuning parameters 249

Appendix 2: MAT253 tuning parameters 251

Appendix 3: Clumped-isotope calculations 253

Appendix 4: Clumped-isotope analysis sample log 269

Appendix 5: Dux, F.W., Chivas, A.R., Garcia, A. (2015). Trace-element and stable-isotope chemistry of gyrogonites of the euryhaline charophyte *Lamprothamnium*. *Aquatic Botany* **120**: 51-59. 275

Appendix 6: Chivas A.R. and Dux, F.W. (2015). Clumped Isotope Geochemistry. In: *Principles and Practice of Analytical Techniques in Geosciences*, Grice, K. (edit). 1st edition, Chapter: 2, Royal Society of Chemistry, pp.35-48. 285

List of Equations

Chapter 1: Introduction

Equation 1.1: $T\,(°C) = 16.9 - 4.2(\delta^{18}O_c - \delta^{18}O_w) + 0.13(\delta^{18}O_c - \delta^{18}O_w)^2$ 4

Equation 1.2: $\Delta_{47} = \left[\left(\frac{R_{47}}{R_{47}^*}-1\right) - \left(\frac{R_{46}}{R_{46}^*}-1\right) - \left(\frac{R_{45}}{R_{45}^*}-1\right)\right] \times 1000$ 5

Equation 1.3:

$\Delta_{47} = (0.0539 \pm 0.0013)10^6/T^2 + (0.0388 \pm 0.0155)$ (1SE) $r^2 = 0.92$ 5

Chapter 2: Clumped isotopes: a review

Equation 2.1: $CaC^{16}O_3 + H_2{}^{18}O = CaC^{18}O^{16}O_2 + H_2{}^{16}O$ 17

Equation 2.2: $T\,℃ = a + b\,(\delta_c - \delta_w) + c\,(\delta_c - \delta_w)^2$ 18

Equation 2.3: $Ca^{13}C^{16}O_3 + Ca^{12}C^{18}O^{16}O_2 = Ca^{13}C^{18}O^{16}O_2 + Ca^{12}C^{16}O_3$ 19

Equation 2.4: $Ca^{12}C^{17}O^{16}O_2 + Ca^{12}C^{18}O^{16}O_2 = Ca^{12}C^{18}O^{17}O^{16}O + Ca^{12}C^{16}O_3$ 19

Equation 2.5: $3[M^{+2}]CO_3 + 2H_3PO_4 \rightarrow [M^{+2}]_3(PO_4)_2 + 3CO_2 + 3H_2O$ 25

Equation 2.6: $\alpha = (^{18}O/^{16}O)_{carbonate} / (^{18}O/^{16}O)_{CO_2}$ 26

Equation 2.7: $\Delta_i = \left(\frac{R_i}{R_i^*}-1\right)\cdot 1000$ 38

Equation 2.8 a: $\Delta_{47} = \left[\left(\frac{R_{47}}{R_{47}^*}-1\right) - \left(\frac{R_{46}}{R_{46}^*}-1\right) - \left(\frac{R_{45}}{R_{45}^*}-1\right)\right] \times 1000$ 38

Equation 2.8 b: $\therefore\ \Delta_{47} = \left[\frac{\left(\frac{R_{47}}{2\cdot R_{13}\cdot R_{18}+2\cdot R_{17}\cdot R_{18}+R_{13}\cdot (R_{17})^2}\right)}{-\left(\frac{R_{46}}{2\cdot R_{18}+2\cdot R_{13}\cdot R_{17}+(R_{17})^2}\right) - \left(\frac{R_{45}}{R_{13}+2\cdot R_{17}}\right)+1}\right] \times 1000$ 38

Equation 2.9: $\delta_i = \left[\left(\frac{R_{i(SG)}}{R_{i(WG)}}\right)-1\right]\cdot 1000$ 38

Equation 2.10 a: $[^{12}C] = \frac{1}{(1+[R_{13}])}$ 39

Equation 2.10 b: $[^{13}C] = \frac{R_{13}}{(1+[R_{13}])}$ 39

Equation 2.10 c: $[^{16}O] = \frac{1}{(1+[R_{17}]+[R_{18}])}$ 39

Equation 2.10 d: $[^{17}O] = \frac{R_{17}}{(1+[R_{17}]+[R_{18}])}$ 39

Equation 2.10 e: $[^{18}O] = \frac{R_{18}}{(1+[R_{17}]+[R_{18}])}$ 39

Equation 2.11 a: $^{18}\alpha = \frac{(\delta^{18}O_{(carbonate)} + 1000)}{(\delta^{18}O_{(water\text{-}measured)} + 1000)}$ 41

Equation 2.11 b: $1000\ \ln\alpha_{(calcite\text{-}water)} = 2.78\left(10^6 T^{-2}\right) - 2.89$ 41

Equation 2.11 c: $1000\ \ln\alpha_{(calcite\text{-}water)} = 18.03\left(10^3 T^{-1}\right) - 32.17$ 41

Equation 2.11 d: $1000\ \ln\alpha_{(aragonite\text{-}water)} = 17.88\left(10^3 T^{-1}\right) - 31.14$ 41

Equation 2.12:

$\Delta_{47} = (0.0526\pm0.0025)10^6/T^2 + (0.0520\pm0.0284)(1SE)\ r^2 = 0.93$ 42

Equation 2.13:

$\Delta_{47} = (0.0539\pm0.0013)10^6/T^2 + (0.0388\pm0.0155)(1SE)\ r^2 = 0.92$ 42

Equation 2.14:

$\Delta_{47\text{-}RF} = 0.003\left(\frac{1000}{T}\right)^4 - 0.0438\left(\frac{1000}{T}\right)^3 + 0.2553\left(\frac{1000}{T}\right)^2 - 0.2195\left(\frac{1000}{T}\right) + 0.0616$ 43

Equation 2.15: $\Delta_{47\text{-}(EG\ vs\ WG)}$ versus $\delta^{47}{}_{\text{-}(EG\ vs\ WG)}$ to give $\Delta_{47\text{-}(EG\ vs\ WG)0}$ 45

Equation 2.16: $\Delta_{47\text{-}RF} = slope_{ETF} * \Delta_{47\text{-}(EG\ vs\ WG)0} + intercept_{ETF}$ 45

Equation 2.17: $\Delta_{47\text{-}(SG\ vs\ WG)0} = \Delta_{47\text{-}(SG\ vs\ WG)} - \delta_{47\text{-}(SG\ vs\ WG)} * slope_{EGL}$ 45

Equation 2.18: $\Delta_{47\text{-}RF} = \Delta_{47\text{-}(SG\ vs\ WG)0} * Slope_{ETF} + intercept_{ETF}$ 45

Equation 2.19:

$1000\ \ln\propto_{CO_2(acid)\text{-}\Delta_{47}} = \frac{(0.022434 \pm 0.001490) * 10^6}{T^2} - (0.2524 \pm 0.0168)$ 48

Equation 2.20: $\Delta_{47} = 0.0592 * 10^6 * T^{-2} - 0.02$ 49

Equation 2.21: $\Delta_{47} = (0.0605 \pm 0.0014) * 10^6 * T^{-2} - (0.031 \pm 0.016)$ 49

Equation 2.22: $\Delta_{47} = (0.0636 \pm 0.0049) * 10^6 * T^{-2} - (0.0047 \pm 0.0520)$ 49

Equation 2.23: $\Delta_{47} = (0.0526 \pm 0.0025) * 10^6 * T^{-2} - (0.0520 \pm 0.0284)$ 49

Equation 2.24: $\Delta_{47} = (0.0555 \pm 0.0027) * 10^6 * T^{-2} - (0.0780 \pm 0.0298)$ 49

Chapter 3: Methods

Equation 3.1: $CaCO_3(mg) = \frac{[\text{Manometer shift (mm Hg)} - 5.1915]}{21.123}$ 66

Equation 3.2: $\Delta_{47\text{-RF}} = 1.0006\ \Delta_{47[\text{EG vs WG}]0} + 0.8396$ 77

Equation 3.3:
$\Delta_{47(abs)} = (0.98 \pm 0.01) * \left(\frac{-3.407*10^9}{T^4} + \frac{2.365*10^7}{T^3} - \frac{2.067*10^3}{T^2} - \frac{5.880*10^9}{T^4}\right) + (0.293 \pm 0.004)$ 82

Equation 3.4: $\Delta_{47\text{-RF}} = 1.0005\ \Delta_{47[\text{EG vs WG}]0} + 0.8396$ 82

Chapter 4: Cold-water carbonates

Equation 4.1: ikaite ⇔ aragonite or calcite + water
$CaCO_3 \cdot 6H_2O \Rightarrow CaCO_3 + 6\ H_2O$
100 volumes ⇒ 32.3 volumes + 94.5 volumes 88

Chapter 5: Cave Systems of Riversleigh, Queensland

Equation 5.1: $HCO_3^- + H^+ \rightarrow CO_2 + H_2O$ 130

Equation 5.2: $R = k^4(HCO_3^-)_S\ (Ca^{2+})_S - k_1(H^+)_S - k_2(H_2CO_3^*)_S - k_3$

$R = \alpha\ (c - c_{eq})$ 130

Equation 5.3: $R_{AV} = (c - c_{eq})\left[1 - \exp\left(-\frac{T\alpha}{\delta}\right)\right] \delta / T$ 131

Chapter 6: Sydney Harbour: temperate or tropical waters?

Equation 6.1: $T°C = 16.9 - 4.69 \cdot [\delta^{18}O_{(calcite)}VPDB - \delta^{18}O_{(water)}VSMOW] + 0.17$
$\cdot [\delta^{18}O_{(calcite)}VPDB - \delta^{18}O_{(water)}VSMOW]$ 220

List of Figures

Chapter 2: Clumped –isotopes: a review

Figure 2.1: Calcite atomic lattice structure showing homogeneous isotope exchange between carbonate ions. Substitution of the heavy isotopes (i.e. ^{18}O) in favour of a lighter isotope (^{16}O) occurs due to the preferential clumping of multiple substituted isotopologues in carbonate molecules such as calcite, vaterite and aragonite, modified from diagram in Eiler (2013). 16

Chapter 3: Methods

Figure 3.1: Carbonate rock classification, redrafted from Folk (1959, 1962), Dunham (1962) and Scholle & Ulmer-Scholle (2003). 57

Figure 3.2: Phosphoric acid preparation equipment. Setup includes a hot-plate with pyrex beaker and glass stirring rod as well as magnetic stirring spin bar. Temperature is monitored through mercury thermometer and K-type thermocouple with digital readout. 60

Figure 3.3: Carbonate reaction apparatus including glass stopcock valve assembly (left), lubricated with vacuum grease and glass side-arm reaction vessel (right); with acid reservoir and sample chamber (total length of 150mm), connected to the valve assembly with vacuum grease. The scale bar has a grid spacing of 1cm. 61

Figure 3.4: Schematic diagram of temperature controller (Julabo®) and water circulator in equilibration/reaction water bath, with reaction side-arm vessel holder and insulating lid and base, temperature control precision of ± 0.1 °C. 62

Figure 3.5: Glass gas-extraction vacuum line; schematic diagram. TR1, TR2 and TR3 are removable dewar flasks, the manometer uses a dual edged 100 cm ruler. 63

Figure 3.6: Glass gas-extraction vacuum line; photograph. A, B, side-arm vessel connection ports; C, D, break-seal tube connection ports; DP, mercury diffusion pump; T_1, T_2 and T_3 are removable dewar flasks, the manometer uses a dual edged 100 cm ruler. 64

Figure 3.7: Sample gas pipette, showing O-ring valves and ¼ inch connecting tubes. 68

Figure 3.8: View of the modified Agilent® 7890A GC. (A) indicates the sample introduction loop and 4-way change-over valve, (B) indicates the thermal conductivity detector (TCD) with modified sample collection tubing carrying purified gas to a stainless-steel U-trap. 70

Figure 3.9: Schematic diagram of the gas chromatograph (GC) purification system, showing gas flow geometry from the sample introduction (S), through the sample valve (SV) diverting flow of the gas through the sample loop or directly into the GC, thermal conductivity detector (TCD) and flame ionisation detector (FID), changeover valve (CV) and U-trap and associated trap valves (TV1, TV2). 72

Figure 3.10: Schematic diagram of MAT 253 customised sample and reference gas introduction system. S; sample gas vessel/break-seal, R; reference gas vessel, S1; Sample valve 1, S2; Sample valve 2, R1; Reference valve 1, R2; Reference valve 2, VV; Vacuum Valve and TP; Turbo Pump (MAT 253). 74

Figure 3.11: Water-equilibrated and heated gas regressions for each temperature condition. This plot represents the non-linearity correction for the University of Wollongong clumped isotope laboratory. 76

Figure 3.12: Intercepts of the $\Delta_{47[EG\ vs\ WG]0}$ values against the 'true' or theoretical value (Wang et al., 2004) an equilibrated CO_2 gas at a given temperature. This plot represents the empirical transfer function for the University of Wollongong clumped isotope laboratory. 77

Chapter 4: Cold-water carbonates

Figure 4.1: Pressure-temperature phase relations in the freshwater-saturated calcium carbonate system. Naturally observed ikaite occurs between -1.9 and 7 °C (shaded). In order for ikaite precipitation to occur, both high alkalinity conditions to achieve super saturation and elevated phosphate levels must be present to reduce calcite/aragonite precipitation. Modified from Marland (1975) by Bischoff et al. (1993a) and De Lurio and Frakes (1999). 87

Figure 4.2: Global glendonite and ikaite occurrences, showing the dominant high latitude polar, sub-polar to temperate geographic distribution of glendonites. Ikaite occurrence is denoted by *. 92

Figure 4.3: Ikaite crystal showing pyramidal crystal habbit, forming a square bi-pyramidal sigmoidal crystal. The crystal usually carries imperfections such as chipped corners and gouges. Stylised diagram from Buchardt et al. (2001). 95

Figure 4.4: Glendonite – GL-1, Glendon, Hunter Valley, N.S.W, Australia. 5cm scale bar, 1cm subdivisions. 100

Figure 4.5: Glendonite – GL-1 (cut surface), Glendon, Hunter Valley, N.S.W, Australia. 5cm scale bar, 1cm subdivisions. 100

Figure 4.6: Glendonite - OR-1A/B, Olenitsa River, Kola Peninsula, Russia. 5cm scale bar, 1cm subdivisions. 101

Figure 4.7: Glendonite - OR-2A/B, Olenitsa River, Kola Peninsula, Russia. 5cm scale bar, 1cm subdivisions. 101

Figure 4.8: Glendonite - OR-3, Olenitsa River within concretion, Kola Peninsula, Russia. 5cm scale bar, 1cm subdivisions. 101

Figure 4.9: Glendonite - BR-1, Bol'shayaBalakhnya River, Taymyr Peninsula, Siberia, Russia. 5cm scale bar, 1cm subdivisions. 102

Figure 4.10: Glendonite - BR-1, Bol'shayaBalakhnya River, Taymyr Peninsula, Siberia, Russia. 5cm scale bar, 1cm subdivisions. 102

Figure 4.11: Thinolite – AL-1A/B/C, Alkali Lake, Lake Country, East Oregon, USA. 5cm scale bar, 1cm subdivisions. 103

Figure 4.12: Thinolite – ML, Mono Lake, California, USA. 10cm scale bar, 1cm subdivisions 104

Figure 4.13: Glendonite, GL-1 from Glendon, NSW, Australia. Polished cross section, a) off white to pale yellow region of secondary calcareous mud, b) dark highly crystalline zone with large crystals up to 1 cm in length, c) internal zone with smaller crystals with some lighter coloration. The sample was previously broken (horizontal crack at label 'c') but reattached with resin, and polished. 107

Figure 4.14: Conventional $\delta^{13}C_{carbonate}$ ‰ (VPDB) values plotted against $\delta^{18}O_{carbonate}$ ‰ (VPDB) values to show differences in relationships between glendonites from various geographic locations in relation to the generally accepted range of values for freshwater limestone (f.w. LS), deep marine and shallow marine limestone (d.m. and s.m. LS) and

evaporative limestone (evap. LS) as postulated by Whiticar and Suess (1998). 108

Figure 4.15: Glendonite $\delta^{18}O_{water}$ (±1σ) (VSMOW) values of the precipitating host water calculated from Δ_{47} values plotted in relation to the calculated temperatures formation temperatures (°C) calculated from Δ_{47} values of glendonites from the Sydney Basin, Tasman Basin and Taymyr Peninsula. 115

Chapter 5: Cave Systems of Riversleigh, Queensland

Figure 5.1: Classification of bulk carbonate rock composition, showing the dolomite content (in %) of total carbonate and the proportions of impurities (the composition name should be stated if the impurities are known). Modified from Leighton and Pendexter (1962). 129

Figure 5.2: (I) Values of α in relation to temperature for various flow thicknesses δ, (A) δ=0.005cm, (B) δ=0.0075cm and (C) δ=0.01cm, for laminar flow. (II) Precipitation rates for various flow thicknesses δ, (A) δ=0.005cm, (B) δ=0.0075cm, (C) δ=0.01cm, (D) δ=0.02cm, (E) δ=0.04cm, as a function of calcium concentration (c) for laminar flow. (III) Deposition rates for various boundary-layer thicknesses in turbulent flow in a depth of 2 cm (Baker et al., 1998). 131

Figure 5.3: Locality map of the Riversleigh fossil sites showing the extent of the Karumba Sedimentary Basin, northwest Queensland. 133

Figure 5.4: Summary stratigraphic diagram of the Riversleigh deposits. The most fossil-rich deposits are represented by System A, B, C and D limestone as well as younger cave deposits and other fill deposits. Modified from initial findings by Archer et al. (1994) and updated with information by Woodhead et al. (2014). 134

Figure 5.5: Stratigraphic age relationships of the Riversleigh Oligocene, Miocene and Plio-Pleistocene deposits. Deposits are dated on the basis of marine bio-correlation (shell symbol) and vertebrate stage-of-evolution bio-correlation. The radiometric-dates derive from U/Pb dates of carbonate material (radiation symbol) from Woodhead et al. (2014). 136

Figure 5.6: Riversleigh area map showing the major geological outcrop units (see legend), System B (AL-90, CA - Cleft of Ages, WH - White Hall, OS – Oncoid Site, and RT - Ringtail) and

System C (NG – Neville's Garden, BC – Bitesantennary, CS – Camels Sputum, IN – Innabayence and SG – Stalagmite) as well as the basal Cambrian limestone (CL). 137

Figure 5.7: Photograph and sketch of the Neville's Garden site showing the cave base material NG-1A with the overlying flowstone NG-1B and overlying cave fill material NG-1C and NG-3. Overlying these layers is the red/brown terra rossa layer. Superimposed on this are modern soil and rock detritus. The photograph is taken facing south into the plateau. 140

Figure 5.8: NG-1 flowstone; flowstone layering overlying a cave base limestone with later cave-fill deposit above. From the lower part of the Neville's Garden site. 5cm scale bar, 1 cm subdivisions. 143

Figure 5.9: NG-1B (A) Flowstone showing lamination and growth lines from bottom to top (plane-polarised light); (B) Flowstone in polarised light showing crystal size changes along the growth lines of the lamination structures from right to left (cross-polarised light); (C) Growth lines in a flowstone speleothem, red/brown lines may indicate iron oxide staining or possible bacterial lamination of flowstone formation surface. Calcite crystals grow across some of these features (cross-polarised light); (D) NG-3 Intrasparite, near to equal amounts of spar and micrite matrix with some lithic fragments, shows layering of micritic and spar calcite (cross-polarised light). All sections are oriented with the original vertical component towards the top of the page. 144

Figure 5.10: NG-3 limestone cave fill. The upper portion contains chert nodules with red/brown terra rossa fine-grained mudstone. 10cm scale bar, 1cm subdivisions. 145

Figure 5.11: Terra rossa, overlying NG-3. Vertical view onto an exposed bedding plane showing thr morphology of small mud-cracks. 146

Figure 5.12: Photograph and sketch of the Camels Sputum site showing the cave roof, primary and secondary cave fill and cave floor structures. The surface and basal debris is not related to the lithology of the site. The photograph is taken facing southeast into the plateau 148

Figure 5.13: CS-1 intramicrite, showing micrite matrix with clasts and vein fill of spar crystals. There are some detrital quartz grains and bone and shell fragments (cross-polarised light). The section is oriented with the original vertical component towards the top of the page. 150

Figure 5.14: CS-3 unsorted lithic biosparite, (A) showing two gastropod shells and bivalve shell fragments with micrite matrix and spar cement infill (plane-polarised light). (B) Showing spar cement fill incorporating quartz fragments and pelletal material (cross-polarised light). Sections are oriented with the original vertical component towards the top of the page. 151

Figure 5.15: CS-5 Fossiliferous pelmicrite, showing large fossiliferous micrite fragment on left, incorporating a gastropod as well as fragmented bivalve shell. Some spar infilling is also present. Pellets are common as well as smaller lithic micrite fragments. The cement is a essentially spar calcite with some fine-grained mud surrounding some pellets (plane-polarised light). The section is oriented with the original vertical component towards the top of the page. 152

Figure 5.16: CS-7 Crystalline calcite, showing large calcite spar grains (cross-polarised light). The section is oriented with the original vertical component towards the top of the page. 152

Figure 5.17: CS-9 Crystalline calcite; stalagmite structure; (A) interlocking calcite crystal structure showing stained growth lines (plane-polarised light); (B) crystal structure shown growing through stained growth lines (cross-polarised light). Sections are oriented with the original vertical component towards the left of the page. 153

Figure 5.18: Photograph of the Inabayence site, showing the sample locations in the two stage excavation pit. The sketch is drawn facing southeast into the plateau. 154

Figure 5.19: IN-2; Crystalline spar calcite with mud lamination around disjointed crystals with some fine crystalline calcite vein precipitation (plane-polarised light); (B) IN-3; Finely crystalline spar calcite with no apparent matrix cement; the framework contains many pores (cross-polarised light). Sections are oriented with the original vertical component towards the top of the page. 156

Figure 5.20: IN-4B (A) Uppermost layer of the Inabayence site; showing fine laminations of detrital silt and mud, some quartz grains are present (A: cross-polarised light). (B) Shows thicker veins of crystalline calcite interbedded with finer mud sediments (B: cross-polarised light). Sections are oriented with the original vertical component towards the top of the page. 157

Figure 5.21: Stalagmite site (SG), showing sampling sites of the stalagmite from the oldest to youngest precipitating layer

(SG-1 to 3). The photograph is orientated facing south into the plateau; the surface of the outcrop is nearly horizontal. 158

Figure 5.22: Diagrammatic profile of the Bitesantennary site, showing stratigraphic layers, incorporating the early Cambrian sandstone and conglomerate layers, the overlying Carl Creek Limestone and the Oligo-Miocene System A unit in conjunction with the System B cave deposits of the Bitesantennary Site (BC). Modified from Archer et al. (1994). 159

Figure 5.23: View of the Bitesantennary area, showing the approximate stratigraphic boundaries as depicted in Figure 5.22. The approximate sample locations are marked showing their spatial relationship to the appropriate stratigraphic layer. The photograph is taken from the base of the Bitesantennary area, and the view is to the southeast and uphill. The person at the top of the hill is approx. 1.8 m tall. The scale is distorted at the bottom of hill due to the gradient. 160

Figure 5.24: Bitesantennary thin section photographs. (A, B) BC-1 Immature quartz sandstone (A; plane-polarised light), showing the bedding of the sandstone as well as lamination of quartz grains in iron oxide mud and micrite matrix (B; cross-polarised light); (C, D) BC-3 Limestone conglomerate (C; plane-polarised light) showing micrite clasts and quartz grains in micritic and oxidised clay matrix and calcite spar fracture fill (D; cross-polarised light). Sections are oriented with the original vertical component towards the top of the page. 163

Figure 5.25: BC-5 Fossiliferous micrite, showing calcite pore fill. The matrix is mainly micritic with some quartz and shell fragments (plane-polarised light). The section is oriented with the original vertical component towards the top of the page. 164

Figure 5.26: BC-9 spar calcite on clay base. The spar calcite crystals are coarser towards the centre of the flow channel or pipe (A: plane-polarised light, B: cross-polarised light). Sections are oriented with the original vertical component towards the top of the page. 164

Figure 5.27: BC-12 Micrite matrix and spar calcite cement supported micrite fragments. Spar calcite veins transverse micrite fragments with oxidised micrite fragment boundaries (cross-polarised light). The section is oriented with the original vertical component towards the top of the page. 165

Figure 5.28: BC-14 Oosparite - cave pearl deposit in thin section. (A, B, C, D) Oolite cave pearls showing muddy micrite in thin concentric layers; (E) Spar calcite that has infilled a dissolution hollow; (F) Bone fragment with calcite infill. (A, B, E: cross-polarised light; C, D, F: plane-polarised light). Sections are oriented with the original vertical component towards the top of the page. 167

Figure 5.29: BC-14 cave pearl layer deposit, showing well defined cave pearls in two distinct layers (Layer 1 and 2), cave pearls are smaller nearer the base, forming two distinct zones of coarse and fine cave pearls in each layer (Zone A and B). Cave pearl layers grade into a massive fine-grained micritic limestone. White circles show Δ47 sampling sites, white boxes and letters correspond to areas coverd by thin section in Figure 5.28. 5cm scale bar, 1 cm subdivisions. 168

Figure 5.30: Cleft of Ages site sample outcrop, showing the exposed fossiliferous limestone and sample locations. Photograph is orientated facing northeast. 169

Figure 5.31: CA-2; (A) Sub-rounded bone fragment in micrite matrix in association with spar calcite (cross-polarised light); (B) Rounded quartz grains in micrite matrix in association with bone fragments and a calcite vein (cross-polarised light). Sections are oriented with the original vertical component towards the top of the page. 170

Figure 5.32: WH-1; crystalline spar calcite and microspar cement. Calcite raft grading is apparent from tightly bound microspar on top into larger crystals of calcite on the bottom. Nearer the bottom of the illustration, more calcite microspar has infilled around the larger crystals (plane-polarised light). Section is oriented with the original vertical component towards the top of the page. 172

Figure 5.33: WH-5showing A: Crystalline spar calcite with, B: microspar cement and dark micrite infill (A, B: cross-polarised light). Sections are oriented with the original vertical component towards the top of the page. 173

Figure 5.34: Oncoid site sample outcrop, showing the exposed cave pearl bearing limestone with smaller pearls on top and larger cave pears below. Photograph is orientated facing northeast. 173

Figure 5.35: OS-1 and 3; Cave pearls encased in calcite spar cement. A and B: show a cave pearl containing a calcite spar core surrounded by finer-grained calcite growth layers stained with darker organic matter (A: plane-polarized light; B: cross-polarised light). OS-3; C and D: shows a cave pearl

containing a lithic core surrounded by finer-grained calcite growth layers stained with darker organic matter (C and D: plane-polarised light). Sections are oriented with the original vertical component towards the top of the page. 175

Figure 5.36: RT-1; A: shows a gastropod shell with spar calcite infill. B: shows a bivalved shell in micrite matrix (A and B: cross-polarised light). Sections are oriented with the original vertical component towards the top of the page. 175

Figure 5.37: Riversleigh $\delta^{18}O$ (±1σ) (VSMOW) values of the precipitating host water calculated from Δ_{47} values plotted in relation to the calculated temperatures formation temperatures (°C) calculated from Δ_{47} values of Riversleigh carbonate samples from Faunal Systems C and B. Ellipses, in solid black and dashed black, show the approximate grouping for faunal systems C and B. 183

Figure 5.38: Conventional $\delta^{13}C_{carbonate}$ ‰ (VPDB) values plotted against $\delta^{18}O_{carbonate}$ ‰ (VPDB) values showing the differences between the various Riversleigh fossil sites. 185

Chapter 6: Sydney harbour: tropical or temperate waters?

Figure 6.1: Δ_{47} measurements by Came et al. (2007), Keating-Bitonti et al. (2011) and Csank et al. (2011) on mollusc shells and their respective growth temperatures. Δ_{47} values are plotted using the empirical calibration by Ghosh et al. (2006). The plotted lines represent the empirical calibration (Ghosh et al., 2006) and the revised synthetic calibration (Zaarur et al., 2013). 192

Figure 6.2: Δ_{47} measurements by Henkes et al. (2013) on bivalve, gastropod, cephalopod and brachiopod shells and their respective growth temperatures. The Δ_{47} values are plotted into the absolute reference frame scale (RF) (Dennis et al., 2011). The lines represent the Ghosh et al. (2006) empirical calibration, the Zaarur et al. (2013) revised synthetic calibration and the Henkes et al. (2013) calibration for shell data at various temperatures. 193

Figure 6.3: Schematic diagram of a typical mollusc gastropod (fusiform welk shell; left) and a typical mollusc bivalve (Venus clam shell; right). 196

Figure 6.4: Schematic diagram of a bivalve (left) and gastropod (right) showing shell partitioning zones for isotopic analysis. Shells have been sub-sectioned into two zones (a) and (b). 197

Figure 6.5 Photographs of Sydney Harbour shells; A, B: *Tawera lagopus*, C, D: *Erosaria eburnea* E, F: *Callista kingii*, G, H: *Pinaxia coronate*, I, J: *Mammilla simiae*, K, L: *Euprotomus iredalei*, M, N: *Dolomena dilatata*, (all have 5cm scale bars with 1cm subdivisions). 209

Figure 6.6*:* Photographs of Sydney Harbour shells; O, P, Q, R: *Monilea lentiginosa*, S, T: *Contradusta walkeri*, U, V: *Terebra cingulifera*, W, X: *Ranularia dunkeri*, (O, P, Q, R, S, T, U, V, W, X have 5cm scale bars with 1cm subdivisions).Y, Z: *Tonna tessellata* (Z and Y have 10cm scale bars with 1cm subdivisions). 210

Figure 6.7: Mollusc $\delta^{18}O$ ‰ (±1σ) (VSMOW) for MAT253 and $\delta^{18}O$ ‰ (±0.1) (VSMOW) PRISM values in relation to the equivalent conventional ^{14}C age (ka BP) for the '*Triton*' site. Superimposed Holocene time intervals are provided; (a) Sub-Atlantic (2.5 ka – present), (b) Subboreal (5 ka – 2.5 ka), (c) Atlantic (8 ka – 5 ka), (d) Boreal (9 ka – 8 ka) and (e) Preboreal (10 ka – 9 ka) (Mangerud et al. 1974) using the NGRIP ice core record data of Vinther et al. (2009). 212

Figure 6.7: Calculated mollusc precipitation temperatures (°C ± 1σ) and calculated $\delta^{18}O_{water}$ ‰ (±1σ) (VSMOW) values from conventional $\delta^{13}C_{carbonate}$ and $\delta^{18}O_{carbonate}$ values in relation to the equivalent conventional ^{14}C age (ka BP) for the '*Triton*' site. Diamonds and solid line represent the calculated precipitation temperatures and circles and dashed line represent the $\delta^{18}O$ values. 222

List of Tables

Chapter 2: Clumped –isotopes: a review

Table 2.1: Palaeotemperature equation values, used in conjunction with Equation 2.2. 18

Table 2.2: Gas Chromatography fused silica column comparisons. 34

Table 2.3: Abundances of CO_2 assuming stochastic (random) distribution, assuming bulk $^{13}C/^{12}C$ ratios equal to PDB and $^{18}O/^{17}O/^{16}O$ ratios equal to SMOW, adapted from Eiler (2007). 37

Table 2.4: Theoretical equilibrium values based on interpolation of a fourth order polynomial regression equation (from Wang et al., 2004; Dennis et al., 2011). 43

Chapter 3: Methods

Table 3.1: Multi-elemental stock solution element concentration and composition (Merck, 2014). 55

Table 3.2: Oztech Reference gas values, reported in PDB and VSMOW for carbon dioxide. 67

Table 3.3: MAT253 Faraday Cup resistor values and associated mass number. 73

Table 3.4: Theoretical calculated values of equilibrium CO_2 clumping based on a fourth-order polynomial calculated from zero-point energies and normal mode wave numbers, modified from Wang et al. (2004). 76

Table 3.5: Water equilibrated (10, 25 and 50 °C) and heated gas (1000 °C) standard gases regression slopes and intercepts ($\Delta_{47[EG\ vs\ WG]0}$) used in generating the empirical transfer function in Table 3.6. 79

Table 3.6: Equilibrated and heated gas calibration standards as used to generate the empirical transfer function of five different MAT 253 instruments at the University of Wollongong, California Institute of Technology, Harvard University, John Hopkins University and Yale University, modified from Dennis et al. (2011). 80

Table 3.7: Δ_{47}-T calibration equations based on the original Ghosh et al., (2006) synthetic calcite calibration. 82

Table 3.8: Δ_{47}-T calibration equations based on the updated combined synthetic calcite and biogenic carbonate calibration. 82

Table 3.9: Carrara Marble standards in the absolute reference frame. With temperature calculated using the synthetic calibration of Ghosh et al. (2006) projected into the absolute reference frame by Dennis et al. (2011). 83

Chapter 4: Cold-water carbonates

Table 4.1: Minor-element composition of the carbonate fraction of glendonite samples. The compositions are shown as a molar fraction as well as their chemical formula in the form of (cation)CO_3. 108

Table 4.2: Mineralogical composition of glendonite samples. Based on XRD results of powdered samples. Compositions are shown as percentages of total sample composition of each mineral phase. 19

Table 4.3: Clumped-isotope ($\Delta_{47\text{-RF}}$), calculated temperature (T) and $\delta^{13}C$ and $\delta^{18}O$ values for glendonites and associated calcite mineral samples. 110

Chapter 5: Cave Systems of Riversleigh, Queensland

Table 5.1: Neville's Garden site. (A) XRD mineral phase contents (wt %) of the homogenised sample powder; (B) ICP-MS carbonate cation substitution in molar percent, based on total molar concentration; (C) Carbonate classification through point count analysis from thin sections using the Folk (1959) system. 142

Table 5.2: Camels Sputum site. (A) XRD mineral phase content (wt%) of the homogenised sample powder; (B) ICP-MS carbonate cation substitution in molar percent, based on total molar concentration; (C) Carbonate classification through point count analysis from thin sections using the Folk (1959) system. 149

Table 5.3: Inabayence site, (A) XRD mineral phase content (wt%) of the homogenised sample powder; (B) ICP-MS carbonate cation substitution in molar percent, based on total molar concentration; (C) Carbonate classification through point count analysis from thin sections using the Folk (1959) system. 155

Table 5.4: Bitesantennary site (A) XRD mineral phase contents (wt%) of the homogenised sample powder; (B) ICP-MS carbonate cation substitution in molar percent, based on total molar concentration; (C) Carbonate classification through point count analysis from thin sections using the Folk (1959) system. 161

Table 5.5: Cleft of Ages, White Hall, Oncoid and Ringtail sites. (A) XRD mineral phase contents (wt%) of the homogenised sample powder; (B) ICP-MS carbonate cation substitution in molar percent, based on

total molar concentration; (C) Carbonate classification through point count analysis from thin sections using the Folk (1959) system. 171

Table 5.6: Clumped isotope results for the Riversleigh area fossil sites, tabulated in stratigraphic order. The Δ_{47} values are presented in the absolute reference frame of Dennis et al. (2011), Temperatures are calculated using the clumped isotope palaeotemperature equation of Zaarur et al. (2014). All Δ_{47} and conventional $\delta^{13}C_{(VPDB)}$ and $\delta^{18}O_{(VSMOW)}$ values are standardised against high purity Oztech gases, Carrara marble (CM-1) and laboratory standard analytical grade calcium carbonate with known isotopic compositions. Measurements were replicated 2 to 4 times per sample. 182

Chapter 6: Sydney Harbour: temperate or tropical waters

Table 6.1: Shells from *Triton* site, Sydney Harbour. Collected between 1928 and 1929 by dredging the sediment of the bottom of the water channel in Sydney Harbour and Port Jackson, Sydney, NSW, Australia. Shells were identified between 1970 and 1999 using available taxonomic dichotomous keys. Taxonomic names have been re-written to the current accepted status given by the World Register of Marine Species (2015). 212

Table 6.2: Radiocarbon ages of shells from Sydney Harbour arranged in order of increasing age. 215

Table 6.3: Conventional stable-isotope results using both the PRISM IRMS (UOW) and the MAT253 (UOW) for all bivalves and gastropods from the *Triton* site'. 217

Table 6.4: Conventional stable-isotope results using both the PRISM IRMS (UOW) and the MAT253 (UOW) for all bivalves and gastropods from the '*Triton*' site for different growth zones. 220

Table of abbreviations

Δ_{47}	$\left[\left(\frac{R_{47}}{R_{47^*}}\text{-}1\right)\text{-}\left(\frac{R_{46}}{R_{46^*}}\text{-}1\right)\text{-}\left(\frac{R_{45}}{R_{45^*}}\text{-}1\right)\right]\times 1000$
δ^{47}	$\delta^{47}=\left(\frac{Rsa_{47}}{\frac{Rrg_{47}+Rrg_{47}}{2}}\right)\text{ - }1 * 1000$
A	ampere
AAS	atomic absorption spectrophotometry
AMS	accelerator mass spectrometry
ANU	Australian National University
BP	before present
$CaCO_3$	calcium carbonate as calcite or aragonite
$CaCO_3.6H_2O$	calcium carbonate hexahydrate
$(CaMg)CO_3$	dolomite
$CaSO_4 \cdot 2H_2O$	gypsum
CO_2	carbon dioxide
$^{47}CO_2$	carbon dioxide with $^{13}C^{18}O^{16}O$, $^{12}C^{18}O^{17}O$, etc.
$CO_{2(s)}$	dry-ice
$\delta^{13}C$, $\delta^{18}O$, $\delta^{17}O$	normalised $^{13}C/^{12}C$ ratio, $^{18}O/^{16}O$ ratio, $^{17}O/^{16}O$ ratios
^{13}C, ^{12}C	carbon with mass-13 and mass-12
$^{13}CH_3$, $^{12}CD_3$	methane with $^{13}C^1H_3$ and $^{13}C^1H_3$
CrO_3	chromium trioxide (chromium(VI) oxide)
°C	degrees Celsius

δD	normalised $^{2}D/^{1}H$ ratio
EG	equilibrated gas
EGL	equilibrated gas line
FID	flame ionisation detector
GC	gas chromatograph
H_2O	water
H_2O_2	hydrogen peroxide
H_3PO_4	phosphoric acid
HCl	hydrochloric acid
HCO_3^-	bicarbonate
HG	heated gas
$Hg_{(l)}$	liquid mercury
HgDP	mercury diffusion pump
HMC	high-magnesium calcite
HNO_3	nitric acid
HV	high voltage
ICP-MS	inductively coupled plasma - mass spectrometry
ICP-OES	inductively coupled plasma - optical emission spectroscopy
ID	internal diameter
IRMS	isotope ratio mass spectrometer
kW	kilowatt
LN_2	liquid nitrogen
$MgCO_3$	magnesite
µV, mV, V, kV	microvolt, millivolt, volt, kilovolt

µg, µL, µmol	microgram, microlitre micromole
µg, mg, g, kg	microgram, milligram, gram, kilogram
µm, mm, m, km	micrometre, millimetre, metre, kilometre
NaOH	sodium hydroxide
$NaSO_4 \cdot CaSO_4$	glauberite
OD	outside diameter
^{18}O, ^{17}O, ^{16}O	oxygen with mass-18, mass-17 and mass-16
P_2O_5	phosphorus pentoxide
PBL	pressure base line
PCM	pressure control module
PDB	Pee Dee Belemnite
ppm, ppb	parts per million (10^{-6}), parts per billion (10^{-9})
Psi	pounds per square inch
pMC	percent modern carbon
%, ‰	per cent, per mill
RF	Reference Frame
SMOW	Standard Mean Ocean Water
TCD	Thermal Conductivity Detector
UHP	Ultra High Purity
UOW	University of Wollongong
VPDB	Vienna Pee Dee Belemnite
VSMOW	Vienna Standard Mean Ocean Water
XRD	X-ray diffraction
XRF	X-ray fluorescence

Chapter 1: Introduction

Isotope geochemistry is a key part of the Earth sciences and provides the foundation of the numerical geological timescale and enables the reconstruction of past climates, ambient environmental conditions and geochemical histories. Stable isotope mass spectrometry, a sub-discipline of isotope geochemistry, is concerned with mass-dependent and mass-independent isotopic fractionation rather than natural radiogenic decay. Advances in stable-isotope analytical techniques have progressively broadened the discipline by adding to the range of elements that can be analysed and their applications. Among these advances is the understanding and recognition of isotopic ordering or 'clumping' in molecules and the principal mechanisms that control this. Of particular interest to this study is the occurrence of multiply substituted isotopologues; i.e. those molecules with more than one rare isotopic species. It is now understood that this 'clumping' (of rare isotopes) is temperature-sensitive and accordingly has the potential to be widely utilised as a new means of determining palaeotemperatures (Ghosh et al., 2006a; Eiler, 2007; Affek et al., 2008; Guo et al., 2008).

Isotopic geochemical proxies have advanced significantly since their initial development in the 1940s and 1950s when they were first used to provide palaeoceanographic temperature reconstructions of marine molluscs from their oxygen isotopic compositions (Urey, 1947; McCrea, 1950; Epstein et al., 1951, 1953). The development of this technique set the foundations for the light-element gas-source isotope-ratio mass spectrometry of carbonates. Further improvements in accuracy and precision, as well as automation of measurements and the introduction of globally available isotopic calibration standards, established the modern practice and understanding of the stable-isotope systematics of carbonate minerals.

Clumped isotope geochemistry builds upon conventional light-element gas-source stable-isotope mass spectrometry that measures cardinal masses 44, 45 and 46 of extracted CO_2 to deduce $^{13}C/^{12}C$ and $^{18}O/^{16}O$ ratios. More recently, clumped-isotope methods, which measure mass 47 (largely $^{13}C^{18}O^{16}O$) have been developed to overcome some of the shortcomings of conventional carbonate isotopic analyses. Clumping is the affinity of heavy or rare isotopes to bond together in favour of bonding with lighter or common isotopes. The measurement of this 'clumping' of ^{13}C-^{18}O-^{16}O or its deviation (Δ_{47}) in abundance from a stochastic random distribution (attained at high temperature) is temperature dependent. This temperature dependence displays a sensitivity of about 0.004 ‰ in Δ_{47} per degree Celsius, at low temperatures (>50 °C).

Therefore, measurement of the Δ_{47} value can be used as a palaeothermometer for the formation temperature of carbonates. Δ_{47} can be commonly measured to a precision of ± 0.01 ‰; this equates to a sensitivity of about ± 2 °C. Importantly the Δ_{47} value is independent of the bulk $\delta^{18}O$ value (a measure of the $^{18}O/^{16}O$ ratio) of the water from which inorganic or biogenic carbonate minerals precipitate. Therefore, palaeotemperatures can be recovered without knowledge of the $\delta^{18}O$ value of the original host water, and which has long limited the application of conventional $\delta^{18}O$ values to palaeothermometry.

A detailed summary of the literature and background knowledge key to the clumped isotope method and its development is provided in Chapter 2. An improved clumped-isotope analysis method is presented in Chapter 3. It represents modification of current methods (e.g. those used at California Institute of Technology; Harvard University; Yale University; Johns Hopkins University; Geological Institute ETZ, Zurich; Tulane University and the Geological Institute, Tokyo). Improvements on sample gas extraction and purification are demonstrated as well as optimisation of instrumental parameters. This study predominantly aims to advance the range of terrestrial carbonate materials that may be appropriate for use as palaeotemperature indicators using the clumped isotope palaeothermometer. This is achieved by investigating three distinct sample types presented in Chapters 4, 5 and 6. The cold-water carbonate glendonite is explored in Chapter 4 as a potential palaeotemperature indicator of polar aquatic conditions (2 to 7 °C) at the time of the pseudomorph's deposition. Speleothem carbonate deposits of the Riversleigh cave systems and associated megafauna fossil assemblages are explored in Chapter 5. The chapter will report if the equilibrium precipitated speleothem cave deposits are suitable for clumped isotope palaeotemperature investigations. Finally in Chapter 6, the results of an assemblage of Holocene molluscs from the Sydney Harbour basin are reported.

1.1 Palaeotemperature reconstruction

The investigation of past climate relies on constraining both the palaeotemperature and the past hydrological regime of the environment. Previous isotope-based palaeoenvironmental reconstructions have focussed on sedimentary records from ocean basins and ice cores allowing detailed characterisation of global changes in the marine and atmospheric environment. However, difficulties remain in the characterisation of terrestrial palaeoclimates. Records from lake sediment cores, soil profiles, speleothem and various fossil assemblages have been used to provide evidence of palaeoclimatic change. Unfortunately, terrestrial archives offer temporally limited and commonly ambiguous evidence. Such records must be verified using multiple proxies. However, there are no direct terrestrially based systems recording air temperatures that do not contain some level of uncertainty. It is therefore imperative to develop analytical techniques applicable to palaeoenvironmental reconstructions of global temperature and hydrological change over long-term timescales and with minimal ambiguity.

The oldest and most commonly utilised isotopic analysis technique for palaeoenvironmental temperature investigations is the oxygen-isotope carbonate-water thermometer (Urey, 1947; McCrea, 1950; Epstein et al., 1951, 1953). This has been applied to carbonate- and carbonate-containing minerals formed in a wide range of environments by various biological and abiotic processes (e.g. O'Neil et al., 1969; Horibe and Oba, 1972; Erez and Luz, 1983 and Chivas et al., 2002). The $\delta^{18}O$ value of carbonates is governed by the $\delta^{18}O$ value of the host fluid from which the carbonate was precipitated. This $\delta^{18}O$ value is also controlled by the ambient temperature at which carbonate formation occurred. Thus, if the oxygen isotope ratio ($^{18}O/^{16}O$; represented as $\delta^{18}O$) of a carbonate phase is measured, it is possible to infer the formation temperature. However, this phenomenon is hindered by the premise of knowing the $\delta^{18}O$ value of the precipitating host water to make unambiguous temperature estimates. This can be independently measured (by oxygen isotope records of ice-cores); however, it is commonly estimated, adding to the uncertainty of the palaeotemperature calculation.

The $\delta^{18}O$ value of marine water can be determined for some Quaternary sedimentary deposits (~<1 million years old, Shackleton, 1967; Schrag et al., 1993, 1995, 2002). However, for older marine deposits and terrestrial depositional settings, this approximation includes large sources of uncertainty. This is typically due to unknown evaporation dynamics and recharge which cannot be accounted for by empirical models.

Initial palaeotemperature equations produced by Epstein et al. (1951, 1953) and Craig (1965) from calcitic marine molluscs, provided the first documented account of oxygen isotope values

and their relationship to the temperature of calcite precipitation. Their research has allowed the documentation of carbonate-water fractionation mechanisms that is present in carbonate-secreting organisms. Organisms such as molluscs, gastropods, foraminifers, charophytes and ostracods secrete carbonate in isotopic equilibrium with their surrounding host water, albeit with various 'vital effect' offsets. Accordingly, a suite of virtually parallel organism-specific curves can be produced, relating $\delta^{18}O_{carbonate}$ to the formation temperature of the biogenic carbonate. Among these are; calcitic molluscs (Epstein et al., 1953; McCrea, 1950; Craig, 1965; Horibe and Oba, 1972) and updated data on the calcitic portion of the blue mussel *Mytilus edulis* (Wanamaker et al., 2007), foraminifers (Erez and Luz, 1983), ostracods (Xia et al., 1997; Chivas et al., 2002) and charophytes (Dux et al., 2015).

These temperature equations take the generalised form:

$$T\,(°C) = 16.9 - 4.2(\delta^{18}O_c - \delta^{18}O_w) + 0.13(\delta^{18}O_c - \delta^{18}O_w)^2$$

$\delta^{18}O_c$ –measured $^{18}O/^{16}O$ ratio of precipitated carbonate compared to the VPDB standard.

$\delta^{18}O_w$ - measured $^{18}O/^{16}O$ ratio of host water compared to the VSMOW standard.

Equation 1.1 – Epstein et al. (1951, 1953) modified by Craig (1965)

The $\delta^{18}O$ value of the carbonate ($\delta^{18}O_c$) can be measured by acid digestion (with H_3PO_4) of the carbonate material and the subsequent analysis of the evolved carbon dioxide gas. The $\delta^{18}O$ value of the water ($\delta^{18}O_w$) is required and must be estimated if isotopic values are not available by monitoring the relevant modern aquatic environment (for contemporary carbonate-secreting systems). The quadratic terms (i.e. 16.9, 4.2 and 0.13, see Equation 1.1) will change depending on the carbonate material utilised to create the temperature equation. For older carbonate materials, where samples of the original host water are not available, there can be difficulties. This dilemma highlights the need to develop a technique that avoids the prerequisite of knowing the isotopic composition of the host fluid in order to determine the palaeotemperature of carbonate material.

1.2 Clumped Isotopes

The clumped isotope method measures the abundance of multiply substituted isotopologues in carbonates. Analysis is performed on extracted carbon dioxide gas from the original carbonate using phosphoric acid digestion. The degree of 'clumping' among rare heavy isotopes of ^{13}C and ^{18}O into compounds containing at least two of these rare species (i.e. $^{13}C^{16}O^{18}O$, $^{12}C^{18}O^{18}O$ etc.) is controlled by a homogeneous equilibrium reaction. This is ultimately expressed as a ratio of the $^{47}CO_2$ value in a sample in relation to the stochastic or random isotopologue distribution. This is termed Δ_{47} and is expressed as per mil (‰) variation in CO_2 (i.e. mass 45, 46, 47 etc., see Equation 1.2).

$$\Delta_{47}= \left[\left(\frac{R_{47}}{R_{47}^*}-1\right)-\left(\frac{R_{46}}{R_{46}^*}-1\right)-\left(\frac{R_{45}}{R_{45}^*}-1\right)\right]\times 1000$$

R - measured sample ratios for CO_2, calibrated to the reference gas.

R^* - calculated stochastic ratios for CO_2 with hypothetical values for $\delta^{13}C$ = 0 ‰, $\delta^{18}O$ = 0‰, Δ_{47} = 0‰, calibrated against the working reference gas.

Equation 1.2 - Eiler et al., 2007, 2013

Equilibrium reactions of this kind are directly temperature dependent but are independent of bulk isotopic composition of the precipitating fluid (Equation 1.3). Thus, by measuring the isotopic value of carbon dioxide gas evolved from the solid carbonate mineral, a formation temperature can be determined. Significantly, this information can be utilised to calculate $\delta^{18}O$ values of the precipitating host water, in conjunction with carbonate-water palaeotemperature equations (of the form of Equation 1.1).

$$\Delta_{47} = (0.0539 \pm 0.0013)10^6/T^2 + (0.0388 \pm 0.0155) \quad (1SE) \qquad r^2 = 0.92$$

Equation 1.3 - Zaarur et al., 2013

Several variations of the clumped isotope method have been applied. Most institutions use the Finnigan MAT253 mass spectrometer although different sample reaction mechanisms are used. The California Institute of Technology (Ghosh et al., 2006a; Ghosh et al., 2006b; Ghosh et al., 2007; Guo et al., 2009; Tripati et al., 2010; Passey et al., 2010; Daëron et al., 2011; Thiagarajan et al., 2011) and Yale University (Affek et al., 2008; Huntington et al., 2009; Brand et al., 2012; Zaarur et al., 2011, 2013; Kluge et al., 2014) are utilising the McCrea-type glass-sidearm reaction vessel system. Harvard University hase adopted the common-acid-bath (CAB) reaction method (Dennis and Schrag, 2010; Dennis et al., 2011; Dennis et al., 2013; Fernandez et al., 2014). Johns Hopkins University uses similar equipment for their system (Passey and Henkes, 2012; Henkes et al., 2011, 2013; VanDeVelde et al., 2013). The Geological Institute, ETH, Zurich uses the Keil IV reaction device (Schmid and Bernasconi, 2010; Bernasconi et al., 2011, 2012; Grauel et al., 2013). The University of California also uses a MAT253 (He et al., 2012). Other instruments such as the Isoprime are used at Tulane University (Rosenheim et al., 2013, Fernandez et al., 2013) in conjunction with the McCrea-type reaction vessel, whereas the Tokyo Institute of Technology, Japan, has developed a method using the Finnigan Delta XP mass spectrometer (Yoshida et al., 2012) also using McCrea-type reaction vessels.

This study uses a modification of the McCrea-type reaction procedure (Ghosh et al., 2006a) by adapting aspects from a range of these laboratory setups to facilitate more accurate and precise analytical measurements. This is used in conjunction with an all glass vacuum extraction line to digest sample carbonates. This allows a 2 to 20 mg carbonate sample size range. Additionally, samples containing as little as 7% w/w carbonate can be analysed in oversized side-arm reaction vessels. Carbon dioxide gas is extract via side-arm acid reaction vessels using highly purified ~103 % orthophosphoric (H_3PO_4) acid (1.93 g/cm^3) in association with cryogenic separation (liquid nitrogen and dry-ice/ethanol slurries). The reaction temperature is precisely controlled by a water bath with ± 0.1 °C temperature tolerance.

Gas purification is vital for clumped-isotope analyses. Therefore, a refined gas purification system was developed. A gas chromatography separation technique, similar to Ghosh et al. (2006a), was developed using a modified helium carrier gas chromatograph. Oven temperatures were regulated to -20 °C to retain contaminants in association with a divinyl-benzene polymer capillary to achieve required hydrocarbon and halocarbon removal from the extracted carbon dioxide.

A high-resolution MAT253 dual-inlet mass spectrometer was used to achieve suitable analytical precision. This allows precision of ± 0.01 ‰ to be achieved as well as allowing for large samples and long counting times of the sample gas. This equates to 100 x the charge collection of a clumped isotope measurement over a conventional dual inlet measurement. Standard stainless steel sample gas inlet capillaries were changed to electro-polished nickel capillaries to reduce

isotopic fractionation by facilitating better flow (Passey et al., 2010). All measurements were standardised to the new absolute reference frame (Dennis et al., 2011) for reporting Δ_{47} values and their equivalent temperatures, encompassing the heated-gas-line (HGL) and empirical-transfer-function (ETF) corrections (Dennis et al., 2011; Zaarur et al., 2013). In addition to internal laboratory standards (AR-$CaCO_3$) and standardised reference gases (OzTech), various inter-laboratory standards such as ETH-1, ETH-2, ETH-3 and ETH-4 (provided by S. Bernasconi) and FH (Fast Haga) and CM-1 (Carrara Marble 1; provided by Caltech) were analysed for inter-laboratory comparison.

1.3 Previous applications

The clumped isotope method has been applied to a variety of environmental settings encompassing various carbonate-containing materials. This is an effort to constrain the palaeotemperature regime of these environments and to solve and reconstruct their respective palaeoclimatic histories.

Initial work using the clumped-isotope method in palaeotemperature reconstruction focused on inferring uplift rates from palaeosols (Ghosh et al., 2006b; Huntington et al., 2010). These soil carbonates appear to have good Δ_{47} reproducibility. Multiple studies spanning the Cenozoic have been undertaken in attempts to constrain the erosion and weathering systematics of these environments (Quade et al., 2007, 2013; Passey et al., 2010; Snell et al., 2012; Peters et al., 2013; VanDeVelde et al., 2013).

Palaeoceanographic studies have been used to successfully determine key changes in Earth climatic history in the older parts of the geological record by utilising corals and brachiopods. In the tropical oceans of the Late Ordovician (~445 million years ago) a short cooling period from 37 to 32 °C is demonstrated; indicative of glaciation (Finnegan et al., 2011). Warm ocean temperatures are reported in the Early Silurian (~430 million years ago; Came et al., 2007) as well as high tropical sea-surface temperatures (~39 °C) in the Late Permian (Brand et al., 2012). Additional applications in the Cretaceous interior seaway (Dennis et al., 2013) and warm ocean conditions in the Eocene (Keating-Bitonti et al., 2011) have been investigated successfully.

Palaeotemperature records utilising speleothems exhibit a disequilibrium isotopic effect. This limits their application in isolation; however, these records may be aided by other geochemical

proxies to clarify these uncertainties (Daëron et al., 2011; Affek et al., 2008; Affek, 2013; Wainer et al., 2011; Kluge and Affek, 2012; Kluge et al., 2013).

The carbonate constituent of bioapatite in terrestrial vertebrates has been investigated with some success; increasing the applicability of the clumped-isotope method to the field of palaeontology. Studies by Eagle et al. (2010, 2011), indicated that the core body temperatures of dinosaurs may be higher than initially anticipated. Other investigations of vertebrate physiology are thus possible. Additional terrestrial applications have also been conducted in calcitic molluscs (Csank et al., 2011) and aragonitic land snails (Zaarur et al., 2011).

Finally, clumped isotopes have been applied to carbonates from shallow hydrothermal vein formation, fault plane mineralisation, diagenetic processes, low-temperature metamorphism and ore deposition dynamics (Ferry et al., 2011; Bristow et al., 2011; Huntington et al., 2011; Swanson et al., 2012). Additional investigation of the cooling kinetics of high temperature carbonates show complexity and additional advances of the clumped-isotope method (Passey and Henkes, 2012; Dennis and Schrag, 2010).

This thesis study aims to further the application of clumped-isotope palaeothermometry through the study of glendonites, cave deposits and molluscs from an array of different palaeoenvironmental settings to determine if these sample types are amenable to the clumped isotope method.

1.4 Glendonites

Glendonites are calcium carbonate pseudomorph minerals formed by the dehydration of ikaite (calcium carbonate hexahydrate; $CaCO_3.6H_2O$). Ikaite only occurs in a narrow range of formation conditions (i.e. <7 °C, alkaline and organic-carbon rich depositional environments). The presence of the glendonite pseudomorph of the precursor mineral ikaite in Permian to recent glacial marine deposits as well as their occurrence as thinolite deposits in terrestrial lacustrine environments has been used as an indicator of cold-water polar and glacial water occurrences (Bischoff et al., 1993a, 1993b; Burchard et al., 1998, 2001; Selleck et al., 2007, Lu et al., 2012). Additionally, their presence has been linked to conditions of highly alkaline organic-rich reduced environments in both the marine and terrestrial realm (De Lurio and Frakes, 1999; Hugget et al., 2005). Their presence in sedimentary sequences shows promise to constrain the palaeoenvironmental evolution of glacial environments and with the use of clumped isotopes will

elucidate and constrain the difference in formation temperatures of the pseudomorph structure in these environments. Ikaite has been postulated to form at -2 to 5 °C (Bischoff et al., 1993a, 1993b; De Lurio and Frakes, 1999). At temperatures outside this range the mineral is unstable and will dehydrate to calcite or aragonite. However, if conditions remain stable, substitution of calcite into the ikaite mineral structure will occur preserving the lattice structure and form the glendonite pseudomorph. Thus, the presence of these structures indicates the past presence of cold water conditions within the environment. This has the potential to provide a vital tool in reconstructing marine glacial depositional environments around the world. These materials have yet to be explored using clumped isotope palaeothermometry.

This thesis study aims to utilise the clumped-isotope method to better understand the processes of glendonite formation and preservation and to determine their usefulness in palaeoclimatic research. Glendonites from nine localities around the world, including Siberia in northern Russia, western United States of America and various localities from inland and coastal Australia have been collected. These were provided by Prof. Paul F. Carr (University of Wollongong) and Dr. Bruce Selleck (Colgate University) in relation to their work on glendonite and ikaite occurrences in Australia in (Selleck et al., 2007). The specimens originate from a wide variety of geological settings and various geomorphological regimes and processes. The inherent temperature trend that these specimens represent is expected to elucidate the formation temperature conditions of the glendonite pseudomorph and give an insight into the occurrence and formation history of ikaite occurrences around the globe.

1.5 Cave formations

Cave systems and their associated morphological structures have been investigated in palaeoenvironmental studies for decades. Stalagmite carbonate precipitates can provide detailed high resolution geochronologies and oxygen isotope records as well as being archives of trapped dust and pollen. However, there are many variables that must be considered in conventional and clumped-isotope mass spectrometry analysis and interpretation of these analyses to make a reliable speleothem-based palaeotemperature record (Affek et al., 2013; Kluge et al., 2013; Kluge and Affek, 2012; Wainer et al., 2011). Speleothems typically do not precipitate carbonate minerals at equilibrium conditions. Precipitation may be complicated by dynamic evaporation and degassing of HCO_3^-/CO_2 systems. This complicates the identification of an exact carbonate formation temperature. This is evident by examining cave floor and stalagmite deposits, which commonly report Δ_{47} temperatures up to 8 °C different to the actual cave air temperature (Affek

et al., 2008). Disequilibrium effects of 1.1 to 4.5 ‰ have been reported between measured temperatures and Δ_{47}-derived cave temperatures (Daëron et al., 2011). Other speleothem deposits potentially precipitate calcium carbonate at equilibrium conditions with a host fluid, such as cave pearls, pool stones, calcite rafts and rim pool calcifications. These formation types may be more useful in representing equilibrium formation temperatures. However, they only provide a low resolution and short-term record of cave development. Cryogenic cave carbonates deposited as coarse carbonate crystals exhibit depleted Δ_{47} values, indicating disequilibrium precipitation, reporting temperatures between 3 and 18 °C. Alternatively, fine grained cryogenic cave deposits exhibit isotopic enrichment disequilibrium fractionation leading to highly negative reported formation temperatures (Kluge et al. 2014). This study aims to contribute to the understanding of equilibrium formation temperatures in cave deposits which currently remain relatively unexplored.

The Riversleigh Oligo-Miocene to Quaternary cave systems of north-eastern Queensland, Australia and their associated bone deposits will aid in advancing the understanding of how speleothem deposits record palaeoenvironmental temperature change. In addition to flowstone, cave pearl and calcite rafts, various macro-fossil specimens have also been discovered. These include mollusc shells, reptile, fish and other vertebrate bones and form part of the megafauna assemblage of the Riversleigh fossil area. In recent studies, clumped isotopes have been successfully used to determine body temperatures of terrestrial vertebrates (Eagle et al., 2010, 2011). Fossil bone, teeth and minor shell fragments at Riversleigh from a range of vertebrates show potential to unveil average body temperatures of these organisms and aid in the palaeobiological reconstruction of their physiology and metabolisms.

1.6 Shells

Marine and terrestrial molluscs have been widely used for palaeotemperature proxies in conventional oxygen-isotope as well as in clumped-isotope palaeothermometry. The first data on marine brachiopods and molluscs, three samples each respectively, were reported by Came et al. (2007). The restricted size of the data set did not allow for definite conclusions to be made. However, results indicate that shell carbonate precipitates in equilibrium and that molluscs conform to the inorganic synthetic carbonate temperature calibration line. Later more detailed work by Henkes et al. (2013) confirms that molluscs precipitate calcium carbonate at approximately equilibrium conditions with their host waters. Additionally, it has been shown that brachiopod calcite exhibits nearly identical clumped isotope reordering kinetics as optical calcite

under the same burial conditions (Passey and Henkes, 2012). Recently a high-resolution palaeotemperature record has been produced using modern bivalve molluscs, allowing for seasonal temperature changes to be investigated (Petrizzo et al., 2014). There is therefore, a significant need to expand our understanding of the range of growth temperatures and the diversity of taxa applicable to further develop additional clumped isotope calibrations. This will aid in providing a more comprehensive data set of marine and terrestrial invertebrates, and to determine their usefulness in palaeothermometry.

In this study we aim to characterise the palaeotemperature signature of a suite of Holocene age molluscs (bivalves and gastropods) within Sydney Harbour to gather an understanding of Holocene nearshore ocean temperatures in this area. Dredge samples were collected in the 1930s and catalogued by the Australian Museum. Various specimens of this assemblage are known to primarily inhabit tropical marine climates. Their presence within the subtropical to temperate Sydney Harbour aquatic environment of today poses the question whether the nearshore water temperature has substantially changed over the course of the Holocene.

1.7 Summary

Clumped isotope thermometry is still a relatively new and therefore constantly evolving geochemical analytical technique. Since its inception by Eiler and Schauble (2004) and subsequent theoretical calculations by Wang et al. (2004) on the fundamental thermodynamics of the mass 47 anomaly, there have been many publications investigating the range of applications that this technique can be applied to in the investigation of the clumped isotope method as a tracer of $\Delta_{47}/\delta^{18}O_{CO_2}$ in atmospheric gases (Eiler and Schauble, 2004; Affek and Eiler, 2006; Eiler, 2013). Additionally, Yeung et al. (2012) postulate uses in global gas budgets from trapped gases in ice cores. More recently additional systematics in isotopologues of CH_4 have been investigated to establish a methane formation thermometer (Stolper et al., 2014).

The initial development has subsequently led to the clumped isotope technique being applied into the realm of carbonate formation palaeothermometry. From early work on surface corals (Ghosh et al., 2006) and fish otoliths (Ghosh et al., 2007), research has expanded and now includes molluscs and brachiopods (Came et al., 2007; Eagle et al., 2013; Henkes et al., 2013), foraminifers and coccoliths (Tripati et al., 2010; Grauel et al., 2013), inorganic siderite ($FeCO_3$; Fernandez et al., 2014), speleothems (Daëron et al., 2011; Affek et al., 2008; Affek, 2013; Wainer et al., 2011; Kluge and Affek, 2012; Kluge et al., 2013), soil carbonates (Quade et al., 2007, 2013;

Passey et al., 2010; Snell et al., 2012; Peters et al., 2013; VanDeVelde et al., 2013), palaeosols (Ghosh et al. 2006b; Huntington et al., 2010), diagenesis, low-temperature metamorphism and ore deposition (Ferry et al., 2011; Bristow et al., 2011; Huntington et al., 2011; Swanson et al., 2012), higher temperature carbonates and erosion rates (Dennis and Schrag, 2010), cooling and kinetics (Passey and Henkes, 2012).

Many of these applications have increased our understanding of carbonate formation temperatures and their relationship to various environmental settings. This allows us to more accurately constrain the temperature and aqueous-phase chemical processes occurring within these environments than can be achieved by conventional isotopic means.

Chapter 2: Clumped isotopes: a review

2.1 Introduction 14
2.2 Multiply substituted isotopologues 15
2.3 Principles of clumped isotope carbonate palaeothermometry 17
2.4 Applications of clumped isotopes 20
2.4.1 Sea-surface temperatures 20
2.4.2 Corals 21
2.4.3 Terrestrial fossil material 21
2.4.4 Speleothems 22
2.4.5 Soil carbonates 22
2.4.6 Metamorphism and diagenesis 23
2.4.7 Atmospheric carbon dioxide 23
2.4.8 Methane 24
2.5 CO_2 preparation 25
2.5.1 Phosphoric acid digestion of carbonates 25
2.5.2 Reaction limitations and considerations 28
2.5.3 Gas extraction 29
2.5.4 Cryogenic separation 29
2.6 Sample CO_2 purification 31
2.7 Δ_{47} mass spectrometry 35
2.7.1 Quantification of the mass-47 anomaly 37
2.7.2 Reference frame and calibration 40
2.7.3 Pressure baseline (PBL) correction 46
2.7.4 Acid fractionation factor 47
2.7.5 Δ_{47}-T palaeotemperature equation 48

2.1 Introduction

This chapter outlines the clumped isotope geothermometry method, the background and fundamentals of multiply substituted isotopologues and their relationship to singly substituted isotopologues associated with conventional stable isotope measurements of oxygen and carbon are explored. Emphasis will be given to the specific uncertainties of conventional stable isotope measurements as palaeotemperature indicators. This will be contrasted to the advantage that the use of multiply substituted "clumped" isotopologues in stable isotope chemistry provides. The range of applications of the clumped isotope method has progressively expanded together with the advancements of the analytical technique. This chapter summarises the major uses of the technique and emphasises the relevance of these to carbonate palaeothermometry and palaeoclimate research. The fundamentals of the 'clumped-isotope' method will then be reviewed in detail. Key analytical concepts are presented and their influence and importance to the clumped isotope method are demonstrated. Finally, the currently accepted analytical reference frame and measurement calibration will be reviewed. The calibration and presentation of results has rapidly changed with the introduction of the absolute reference frame (abs) for clumped isotope measurements by Dennis et al. (2011), as well as the emergence of the pressure base line (PBL) reference frame. These, in turn, have affected the currently accepted palaeotemperature equations for carbonates.

2.2 Multiply substituted isotopologues

Since the first fundamental understanding of isotopes in the 1940s, through pioneering work of the Chicago group (McCrea, 1950; Epstein et al., 1953) following the work of Harold Urey (1947), the theory and application of stable isotope fractionation to geochemistry was established. Conventional oxygen and carbon isotope analyses of carbonates have been fundamental in investigating a wide range of materials forming in numerous environments constrained by various biological and abiotic processes and factors. From the principles of oxygen isotope thermodynamic dependence, the carbonate-water thermometer was created and has been widely used as an environmental proxy for palaeotemperature investigation.

As a result of their natural abundance, common or 'light' isotopes of carbon and oxygen (^{12}C and ^{18}O) more readily bond together due to their increased concentrations (i.e. $^{12}C^{16}O_2$). Rare or 'heavy' isotopes of carbon and oxygen (^{13}C, ^{18}O and ^{17}O) are less abundant and have a lower concentration in nature. Therefore, they are less common in molecular structures.

To understand the relevance of the heavy isotopes of oxygen and carbon (^{18}O, ^{17}O and ^{13}C) in the molecular bonding in carbonates, the thermodynamic control of the abundance of singly and multiply substituted isotopes must be considered (Eiler, 2007, 2013). The phenomenon of a molecule exhibiting multiple isotopic identities is referred to as an isotopologue (i.e. variations in atomic mass). This implies that a molecule contains elements which exhibit two or more isotopes. Most molecules commonly exhibit single heavy isotope substitution (For example, carbon dioxide single substitution may include $^{12}C^{16}O^{18}O$, $^{13}C^{16}O^{16}O_2$ or $^{12}C^{17}O^{16}O$. Multiply substituted isotopologues contain two or more of these rare isotope substitutions (i.e. carbon dioxide multiple substitution may include $^{12}C^{18}O_2$, $^{13}C^{18}O^{16}O$, or $^{12}C^{17}O^{18}O$).

Isotopologues form through thermodynamically controlled processes. These are driven by bond formation energy and energy dispersion of bonds within a molecular structure. In the case of the carbonate mineral, heavy isotope exchange can occur at three sites around a carbon atom at the centre of the carbonate molecular structure (Eiler, 2007). The surrounding oxygen atoms are free to exchange within the molecular lattice of the carbonate mineral (Figure 2.1). This substitution occurs due to energy rebalancing within the lattice at different rates and is thermodynamically controlled by the ambient temperature of the mineral structure.

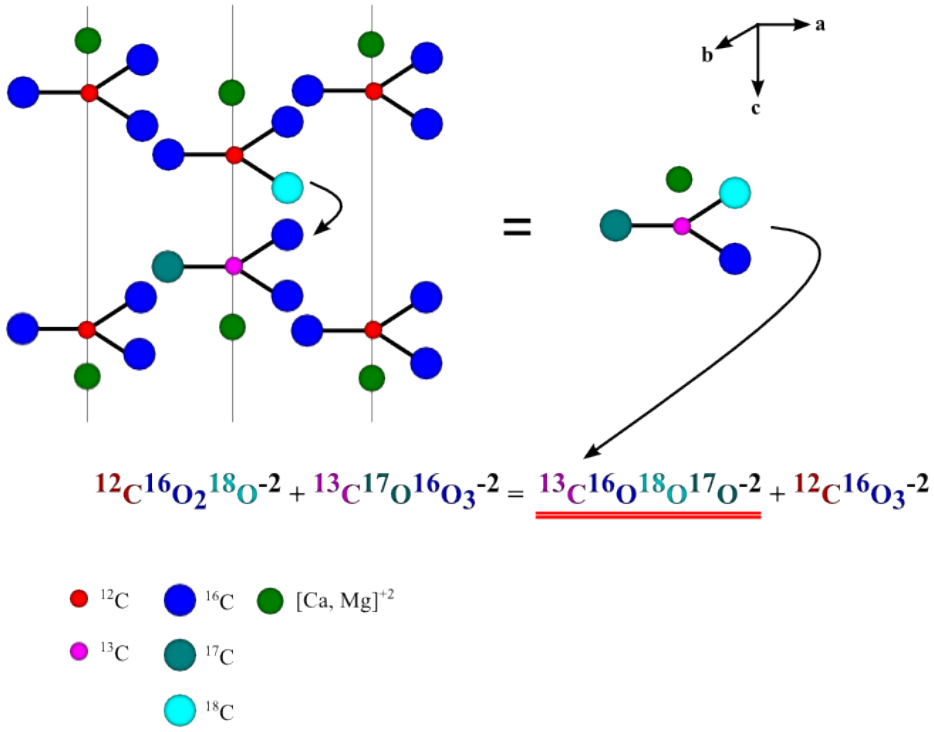

Figure 2.1: Calcite atomic lattice structure showing homogeneous isotope exchange between carbonate ions. Substitution of the heavy isotopes (i.e. ^{18}O) in favour of a lighter isotope (^{16}O) occurs due to the preferential clumping of multiple substituted isotopologues in carbonate molecules such as calcite, vaterite and aragonite (modified from diagram in Eiler, 2013).

Heavy or rare isotope substitution reduces the atomic vibration frequencies of a molecule and therefore lowers its vibrational energies of the molecule. This process is commonly referred to as 'zero-point energy'. This factor is the key contributor controlling equilibrium stable isotope fractionation in molecules (Wang et al., 2004; Eiler, 2007). This is illustrated in Figure 2.1 where substitution of a singly substituted isotopologue changes its vibrational frequency to form a multiply substituted isotopologue (Eiler, 2013) with reduced vibrational energy.

This energy change is generally greater than twice the lowering of a single species substitution. This effect of the affinity for heavy or rare isotopes to be multiply substituted into molecules is stronger at lower temperatures. The effect reduces at higher temperatures (>200 °C, Eiler et al., 2007), where the isotopes favour the random stochastic distribution. That is, a state in which all the stable isotopes in a certain population of molecules are randomly distributed among all possible isotopologues. This temperature dependence of multiple substitutions of heavy elements of carbon and oxygen into a molecule, specifically carbonate, is the fundamental concept of the clumped isotope measurement technique (Eiler and Schauble, 2004; Eiler, 2006, 2007, 2013).

2.3 Principles of clumped isotope carbonate palaeothermometry

The carbonate clumped isotope thermometer is a complex and specialised tool to constrain the formation temperature of carbonates within the environment in which they formed. To understand the principles of the technique, reference must be drawn to conventional carbonate isotope palaeothermometry, specifically the widely used Urey carbonate-water oxygen isotope exchange thermometer (Urey, 1947). This pioneering work focused on oxygen isotope fractionation between marine carbonate and seawater, whereby carbonate and water form a thermodynamic equilibrium at the Earth's surface, forming a heterogeneous isotope exchange reaction where the isotopes of oxygen exchange in an equilibrium reaction at a specific temperature yielding a characteristic isotopic signature of the resulting carbonate (Equation 2.1).

This heterogeneous reaction (in calcite) takes the form of:

$$CaC^{16}O_3 + H_2{}^{18}O = CaC^{18}O^{16}O_2 + H_2{}^{16}O \qquad \textbf{Equation 2.1}$$

This principle has been the basis of many other studies that have evolved from this theory (e.g. McCrea, 1950 and Epstein et al., 1951). However, the conventional oxygen isotope thermometer is not without its limitations. It relies on three fundamental factors to successfully determine the formation temperatures of carbonate minerals.

Firstly, in order to understand the composition of the precipitated carbonate material and its formation temperature, the isotopic composition of the precipitating host water must be known. Unfortunately, there are few direct constraints of the oxygen isotope composition of water in association with carbonates through the geological record that have been preserved. Due to this, conventional oxygen isotope measurements and palaeotemperature calculations using this heterogeneous system contain a compromise in the assumption of the isotopic composition of the precipitation host water. Such palaeotemperature equations by Kim and O'Neil (1997b) contain three unknown variables (a, b and c) in order to solve the palaeotemperature equation (Equation 2.2).

$$T\,℃ = \mathbf{a} + \mathbf{b}\,(\delta_c - \delta_w) + \mathbf{c}\,(\delta_c - \delta_w)^2 \qquad \textbf{Equation 2.2}$$

Table 2.1: Palaeotemperature equation values, used in conjunction with Equation 2.2.

Reference	Type	*a*	*b*	*c*
McCrea (1950)	Inorganic	16.0	-5.17	0.09
Epstein et al. (1951)	Mollusc	16.5	-4.30	0.14
Craig (1965)	Mollusc	16.9	-4.20	0.13
O'Neil et al. (1969)*	Inorganic	16.9	-4.38	0.10
Kim and O'Neil (1997)*	Inorganic	16.1	-4.64	0.09
Wanamaker et al. (2007) *	Mollusc	16.19	-4.69	0.17

*Conversion from a '$10^3 \ln\alpha$' notation to a quadratic equation as in Equation 2.2.

Secondly, biogenically precipitated carbonates exhibit species-specific variations from inorganic equivalent carbonate material formed in the same host water. These are termed 'vital effects', and occur for marine animal carbonate in sea water. In some instances these vital effects in particular species exhibit such large variation from their inorganic counterparts that quantitative palaeotemperature reconstruction is not possible. However, for most biogenic carbonate precipitations these vital effects can be accounted for using empirical calibration through culturing growth studies. These culturing experiments must be undertaken with great care under highly controlled conditions of temperature, chemical composition and pH values of the precipitation host water. Through this an accurate species-specific calibration can be constructed for a wide range of biogenic materials from marine to brackish and freshwater aquatic systems (e.g. Chivas et al., 2002; Wanamaker et al., 2007).

Thirdly, diagenesis is likely to occur in a variety of different environments. Carbonate minerals are commonly affected by diagenesis, changing the composition and structure of the carbonate lattice. These changes in carbonate character have been known to lead to significant changes in the $\delta^{18}O$ ($^{18}O/^{16}O$ mass ratio) of carbonate sediments and diagenetically altered biogenic fossil material (O'Neil et al., 1969; O'Neil, 1986; Kim and O'Neil, 1997)

These shortcomings are significant limiting factors for the application of the conventional oxygen isotope thermometer to carbonates. Thus, it is necessary to construct a palaeothermometer that overcomes these barriers and allows more accurate measurements to be taken of both biogenic and inorganic carbonate material. In contrast, the carbonate clumped isotope thermometer is concerned with examining the homogeneous equilibrium among a single phase form in carbonate.

This homogeneous reaction (in calcite) takes the form of:

$$Ca^{13}C^{16}O_3 + Ca^{12}C^{18}O^{16}O_2 = Ca^{13}C^{18}O^{16}O_2 + Ca^{12}C^{16}O_3 \quad \textbf{Equation 2.3}$$

$$Ca^{12}C^{17}O^{16}O_2 + Ca^{12}C^{18}O^{16}O_2 = Ca^{12}C^{18}O^{17}O^{16}O + Ca^{12}C^{16}O_3 \quad \textbf{Equation 2.4}$$

The reaction is concerned with the ordering or 'clumping' of the rare heavy ^{13}C and ^{18}O isotopes into bonds with each other forming the $^{13}C^{18}O^{16}O_2{}^{2-}$ ion. This equilibrium reaction is principally different from the conventional oxygen isotope method, in that it is a homogeneous exchange reaction (Equation 2.3 and 2.4). There is no phase change between the two compounds as there is in conventional methods, where the ^{18}O isotope changes between the mineral and the water phase. Thus, the equilibrium constant for the reaction is an internal product of the reaction and not influenced by the isotopic composition of either phase. Additionally, the equilibrium constants should not be affected by any co-existing host water or the bulk isotopic ($^{18}O/^{16}O$, $^{17}O/^{16}O$ and $^{13}C/^{12}C$ ratio) composition of the mineral (Schauble et al., 2004).

Therefore, at equilibrium, change in the mass-47 ($\Delta_{^{13}C^{18}O^{16}O_2}$) value of the carbonate is predicted to vary as a function of temperature (equal to the equilibrium constant) through the homogeneous isotope exchange reaction (Equation 2.3 and 2.4). This forms the principle of clumped isotope thermometry (Eiler, 2007, 2011, 2013).

2.4 Applications of clumped isotopes

The clumped isotope palaeothermometer exhibits a relatively simple pattern. In temperatures ranging from 0 to 40 °C there is a single trend of increasing Δ_{47} of CO_2 extracted by acid digestion with decreasing temperature. This trend holds despite the combination of a wide range of biological and synthetic carbonate sources (Eiler, 2013; Zaarur et al., 2013). The clumped isotope method is only marginally influenced by non-equilibrium effects and other sample-specific vital effects (Eiler, 2013). As previously discussed, these effects complicate and even limit the use of the conventional oxygen isotope ($\delta^{18}O$) palaeothermometer. It is therefore necessary to discuss different applications of the clumped isotope palaeothermometer individually due to these sample-specific effects. The method has been applied to a variety of geological environments over much of the geological timescale.

2.4.1 Sea-surface temperatures

Numerous studies have explored sea-surface temperatures and their relationship to Earth climate change in various parts of the geological record. Palaeoceanography has utilised many marine organisms, such as brachiopods and molluscs, to successfully demonstrate the applicability of the carbonate clumped isotope palaeothermometer to this domain. Warmer-than-present ocean temperatures are demonstrated in the Early Silurian (~430 Ma) using mollusc and brachiopods (Came et al., 2007), and exceedingly warm tropical sea-surface temperatures (to 39 °C) are proposed for the end-Permian extinction from brachiopod shells and associated whole-rock and cement material (Brand et al., 2012). Other studies have investigated the North American Cretaceous interior seaway and associated cooling conditions using cephalopod macrofossils (Dennis et al., 2013). A short interval of cooling is also established for Late Ordovician glaciation tropical oceans (Finnegan et al., 2011). Warm conditions of the Eocene (~50 Ma) at higher latitudes from subtropical bivalves has also been reported (Keating-Bitonti et al., 2011). This shows that clumped isotopes are readily applicable to determine sea-surface temperatures.

2.4.2 Corals

The first attempts to apply the clumped isotope method to geological material provided evidence for the presence of vital effects (Ghosh et al., 2006a). Deep sea corals and equatorial summer growth bands from the Red Sea conform to the standard inorganic calcite calibration. However, winter growth bands of equatorial corals do not appear to conform. This indicates that such material may be exempt from bulk isotopic effects of their environment (Ghosh et al., 2006a). Other near-surface corals also exhibit enrichment of ^{13}C-^{18}O heavy isotope clumping (Saenger et al., 2012). A large study on deep sea coral found no systematic significant vital effects in Δ_{47} composition. Included materials displayed a large range in the bulk isotopic composition of both $\delta^{13}C$ and $\delta^{18}O$ values (Thiagarajan et al., 2011). This suggests that shallow growing corals exhibit a significant vital effect, whereas deep sea corals do not.

2.4.3 Terrestrial fossil material

Meteoric water, in terrestrial environments exhibits large isotopic variations in $\delta^{18}O$. This precludes the use of conventional oxygen isotope palaeothermometry due to its reliance on knowing the bulk isotopic composition of the precipitating host water. Many studies have therefore focused on understanding clumped isotope records of lake carbonates and their associated fossil material. Work on aragonitic molluscs by Eagle et al. (2012) suggests that these organisms preserve average seasonal growth temperatures. Other work on aragonitic land snails suggests that the Δ_{47} temperature relationships exhibit non-equilibrium vital effects associated with the organisms' body temperature (Zaarur et al., 2013). Similar work on freshwater molluscs from the Canadian Arctic show palaeotemperatures up to 15 °C warmer during the Pliocene than today, indicating amplified Arctic warming during the Pliocene above the global 2-3 °C temperature increase (Csank et al., 2011). Additionally, bone material has also been analysed to further elucidate the palaeotemperature regimes of terrestrial environments and provide insight into the physiologies of extinct organisms. Bioapatite samples of modern and extant taxa were analysed yielding Δ_{47} temperature relationships indistinguishable from inorganically precipitated calcite (Eagle et al., 2010). More recent work on fossilised sauropod teeth from the Jurassic suggests that dinosaurs may have had body temperatures closer to that of mammals. This does not follow the previously assumed trend of body temperature scaling with increased mass. This may indicate that sauropods had mechanisms to self-regulate temperature to prevent excessively high body temperatures (Eagle et al., 2011).

2.4.4 Speleothems

Speleothem carbonates such as stalactites, stalagmites and flowstones commonly display Δ_{47} disequilibrium and are not readily usable individually in palaeotemperature reconstruction analogues (Affek et al., 2008; Daëron et al., 2011; Wainer et al., 2011; Kluge and Affek, 2012; Affek, 2013; Kluge et al., 2013). These studies have shown speleothem material exhibiting systematically lower growth temperatures than their expected formation temperatures. This reflects kinetic isotope effects as shown by Guo et al. (2009) and Daëron et al. (2011), such as bicarbonate dehydrogenation and carbonic acid dehydration chemistry. Speleothem cave deposit isotopic dynamics are highly complex and are controlled by various external processes, such as cave air composition, evaporation rates, water sources and biological activity. These additional factors add to the difficulty of utilising Δ_{47} values as a palaeotemperature signature in cave systems. Some kinetic isotopic fractionation can be accounted for as suggested by Affek et al. (2014). However, these corrections may be spatially specific to a specific cave system and not able to be used as a general correction procedure in all situations. Supplementation by an additional independent analytical technique and multiple proxies may be necessary to realise their full potential in palaeoclimatic reconstructions.

2.4.5 Soil carbonates

Soil carbonate Δ_{47} values appear to reflect their formation temperatures, in comparison to the standard inorganic-carbonate clumped isotope calibration. (Quade et al., 2007, 2013). Investigations have revealed that tropical environments exhibit soil nodule carbonate clumped isotope temperature variability close to that of mean annual temperatures (Snell et al., 2012). Soil temperature records from higher latitude environments display warmer than mean annual temperature, this indicates soil carbonate forms preferentially in the warm season (Peters et al., 2013). This typically coincides with summer seasons, exhibiting dry conditions, appropriate for carbonate precipitation. However, seasonal trends and latent radiant ground heat appear to influence the ground temperature record as well (Passey et al., 2010). Records spanning the Cenozoic rock record have been scrutinised, possibly providing a useful means of understanding seasonality in terrestrial environments when combined with additional temperature proxies (VanDeVelde et al., 2013). Several investigations have used carbonate from palaeosols to infer uplift histories for the Andes, Colorado and Tibetan Plateaux (Ghosh et al., 2006b; Huntington et

al., 2010, Quade et al., 2011; Carrapa, et al., 2014; Hoke et al., 2014; Fan et al., 2014), with varying degrees of success.

2.4.6 Metamorphism and diagenesis

Higher temperature carbonate deposition (100 to 200 °C) associated with deep geological settings is amenable to investigation using clumped isotopes. The dynamics of fluid migration and hydrothermal carbonate deposition in deeper geological processes will elucidate processes of cooling kinetics and vein deposition. In work by Passey and Henkes (2012), these processes show a high degree of complexity and will require further categorisation. Depth erosion profiles and associated temperature responses have been examined by Dennis and Schrag (2010) and allow the investigation of high temperature carbonates and the change in Δ_{47} at increased pressure regimes. Shallow hydrothermal vein formation, mineralised fault planes, diagenesis, low-temperature metamorphism and ore deposition systematics have also been subjected to the clumped isotope method with varying degrees of success (Bristow et al., 2011; Huntington et al., 2011; Swanson et al., 2012). Recently high temperature non-calcite carbonates have been investigated, results suggested that the clumped isotope palaeothermometer holds for calcite, dolomite and magnesite at temperatures above 50 °C (Ferry et al., 2011; John et al., 2014; Sena et al., 2014; Vandeginste et al., 2014).

2.4.7 Atmospheric carbon dioxide

The clumped isotope method was originally utilised to distinguish modern CO_2 sources from car-exhaust pollution, respiration and tropospheric influences (Eiler and Schauble, 2004; Affek and Eiler, 2006; Eiler, 2013). Additionally minor isotopologues of O_2 namely $^{18}O^{18}O$ and $^{17}O^{18}O$ can be analysed to establish global atmospheric budgets of oxygen. This may be expanded and utilised in ice core samples to establish global distribution trends and enriched oxygen trapping in the polar ice caps (Yeung et al., 2012).

2.4.8 Methane

The development of high-resolution gas-source mass spectrometry and its application to clumped isotopes, has facilitated the broadening of the discipline into investigating the composition of methane and its isotopologues ($^{13}CH_3$, $^{12}CD_3$ etc.). From the initial investigation of δD and $\delta^{13}C$ of methane as tracers of sources and sinks there has been development of a methane palaeothermometer (Stolper et al., 2014). The application of this thermometer allows distinction between biogenic and thermogenically derived methane in natural samples. This has the potential to allow for the identification of methane formation sites and source materials and to understand the geochemistry of methane formation (Eiler et al., 2013).

2.5 CO_2 preparation

From the pioneering works of Urey (1947), Epstein et al. (1953) and McCrea (1950), the basic principles of carbon dioxide extraction from carbonate samples for the use in stable isotope gas mass spectrometry have not changed significantly. The process involves liberating carbon dioxide (CO_2) from a carbonate-containing (CO_3^{-2}) compound by reaction of the solid sample material with an excess of hydrogen (H^+) ions to allow the production of a gaseous phase which can then be analysed. However, this procedure still relies on various factors to be readily controlled in order to produce accurate and precise analysis over multiple samples and over time produce replicable results.

There are many factors to consider in the initial sample cleaning and preparation, carbon dioxide extraction, purification procedures as well as the analysis procedure to ascertain the relevant isotopic ratios. These problems do not solely restrict themselves to carbonate clumped isotopic analysis, but equally effect standard oxygen-18 and carbon-13 isotopes, nitrogen-15, sulfur-based isotopic work, as well as compound-specific stable isotope analysis.

2.5.1 Phosphoric acid digestion of carbonates

The method of extracting CO_2 from carbonates has evolved into a standard technique for almost all carbonate analyses for the use in stable isotope mass spectrometry. This involves the reaction of orthophosphoric acid in a closed reaction vessel with the carbonate material at a set temperature; see Equation 2.5 (McCrea, 1950; Swart et al., 1991).

This follows the reaction:

$$3[M^{+2}]CO_3 + 2H_3PO_4 \rightarrow [M^{+2}]_3(PO_4)_2 + 3CO_2 + 3H_2O \qquad \textbf{Equation 2.5}$$

The principal technique remains the same; however, the experimental parameters vary significantly depending on the analysis. Commonly varied characteristics of the method include the sample size, reaction time and reaction temperature. Each of these having a different effect on

the isotopic fractionation that occurs during the reaction process altering the isotopic composition of the CO_2 produced.

There are three principal types of methods commonly used; the "sealed vessel", "common acid bath" and the "acid-on-sample" method, each has advantages and disadvantages in their application. Both the "sealed vessel" (Ghosh et al., 2006; Huntington et al., 2009; Fernandez and Rosenheim, 2013; Rosenheim et al., 2013) and the "common acid bath" (Dennis and Schrag, 2010; Passey et al., 2010; Henkes et al., 2012; Ferry et al., 2011; Dennis, et al., 2013) methods have been used for preparing carbon dioxide gas samples for clumped isotope analyses. Recently there have also been attempts to use the Kiel IV carbonate device (Schmid and Bernasconi, 2010; Grauel et al., 2013; Bernasconi et al., 2013) to react and process clumped isotope samples.

From, Equation 2.5, it can be seen that all products of the reaction contain oxygen. As the carbonate reacts, carbon dioxide is produced resulting in the loss of an oxygen atom (i.e. removal of one oxygen atom from CO_3^{-2} to CO_2), thus isotopic fractionation occurs. The carbon in both the carbonate and carbon dioxide is equal so all carbon appears to be converted. This phenomenon of imbalance in the oxygen is referred to as the oxygen isotopic fractionation factor, see Equation 2.6 (for a particular acid at a given temperature, Swart et al., 1991).

This is defined by:

$$\alpha = (^{18}O/^{16}O)_{carbonate} / (^{18}O/^{16}O)_{CO_2} \qquad \textbf{Equation 2.6}$$

(for phosphoric acid at 25 °C)

This value varies for different compounds and at various temperatures and is also highly dependent on the reaction method used. This has been reported by McCrea (1950), Sharma and Clayton (1965), Friedman and O'Neil (1977), Land (1980) and reviewed by Swart et al. (1991) showing that while significantly different oxygen isotopic compositions can be produced from carbonate material depending on the reaction method used. This has recently been updated further by Kim and O'Neil (1997) and Kim et al. (2007). However, carbon isotope fractionation seems to be insensitive to both applied temperature and technique. Therefore, it is important to utilise a single method and reaction temperature combination for clumped isotope measurements to constrain the amount of fractionation variability that may be produced.

There are three principal areas in any method used that must be considered in accounting and contributing to the acid fractionation factor as shown by Swart et al. (1991):

i. Gas exchange between the CO_2 produced in the reaction; the water produced by the reaction and the water already present in the acid before the reaction began must be considered. McCrea (1950) originally suggested that the fractionation is insignificant. However, later investigation suggests that there may be increased fractionation for higher reaction temperatures and reaction times where the reacted CO_2 is still in contact with the acid, (Epstein et al., 1953; Kim and O'Neil, 1997).
ii. The dissolution of CO_2 into the reaction acid. This dissolution effect reaches an equilibrium partial pressure in the reaction vessel while the reaction is taking place. This has two main implications; that the CO_2 may not exolve in a constant manner from the acid creating an isotopic effect and that not all of the CO_2 will be recovered. The latter is governed by the temperature of the acid and the specific gravity of the acid being used in the reaction. Isotopic effects may be pronounced in situations where the sample carbonate size is quite small compared to the acid volume, thus trapping or retaining more of the produced CO_2 in the acid (Swart et al., 1991).
iii. Differences in gas extraction temperature in relation to acid reaction temperature may also have an isotopic effect on the CO_2 gas. The gas may take much longer to exsolve from solution where the temperature differences between reaction temperature and ambient temperature in the laboratory are high (Swart et al., 1991).

Reaction acid viscosity and therefore its purity, has a profound effect on CO_2 degassing from that acid. Depending on the original concentration of the phosphoric acid when it is acquired from the manufacturer, the acid may require additional purification. This is typically 85 to 95 % (in commercially available material). It is common practice to increase this concentration by adding P_2O_5 to react with any H_2O present or by heating the acid by using a vacuum oven or boiling to drive off any excess water (de Groot, 2008). This will create orthophosphoric acid (H_2+nP_nO(3n+1)) at >100 % concentration with higher viscosities. However, creating an acid with a higher density and thus, lower equilibrium vapour pressures also has disadvantages. These include low rates of reaction, particularly at low temperatures; trapping of CO_2 bubbles and an increased number of O-bearing polymers with unknown isotopic fractionation factors.

2.5.2 Reaction limitations and considerations

The reaction temperature and the length of reaction time used for the evolution of the carbon dioxide gas is dependent upon two main factors. Firstly, the mineralogy in carbonates has a profound effect on the reaction rate of phosphoric acid and carbonate powder. Mg-, Mn- and Fe-containing carbonates such as magnesite, dolomite and siderite may take several hours to weeks for the reaction to reach completion. In contrast, Ca-containing compounds typically react in minutes to hours depending on the reaction temperature. Secondly, it is evident that the proportion of carbonate in the whole sample also plays a role in the final carbon dioxide yield of the extraction. In addition to gas exchange, dissolution and acid viscosity effects are also crucial in determining reaction times as well as temperature (Sharma and Clayton, 1965; O'Neil et al., 1969; Swart et al., 1991).

Different forms of calcium carbonate, such as calcite, aragonite and vaterite also appear to affect the reaction process. Reaction times of carbonates in the clumped isotope method vary depending on the reaction procedure used. Isolated side-arm reaction vessel gas extraction using vacuum extraction lines commonly requires a reaction time of 12 to 24 hours due to the low temperature (25 °C). This may need to be lengthened, depending on the mineralogy of the material (de Groot, 2008).

In contrast, common-acid-bath (CAB) systems require shorter reaction times of ~10 minutes (Passey et al., 2010). This is due to their higher reaction temperatures (commonly 90 °C), which accelerates the carbonate-acid reaction. However, the CAB method also has its disadvantages. As previously stated, phosphoric acid is highly viscous and has a high specific gravity, this causes it to retain dissolved carbon dioxide gas in the acid bath. This may lead to a memory effect of carbon dioxide gas dissolved in the acid to exolve during the sample reaction of another carbonate sample. This has the potential to change the isotopic composition of the collected gas sample; by being a mixture of two or more sample gas extractions.

Various reaction temperatures have been employed in carbon dioxide extraction by acid digestion of carbonates (McCrea, 1950; Epstein et al., 1953; O'Neil et al., 1969). Kim and O'Neil (1997) found that there are differences in the acid fractionation factors for different temperatures and mineralogies. Acid digestion reaction use temperatures depending on the apparatus employed to undertake the analysis. Side-arm vessel, acid-on-sample, common-acid-bath or the more recent Kiel-carbonate device have all been utilised successfully for the clumped isotope technique (Eiler, 2013). Typical reaction temperatures for clumped-isotope acid reactions range from 25 °C in side-arm vessel extractions (Ghosh et al., 2006, 1010; Dennis and Schrag, 2010; Huntington et al.,

2010) to 90 °C in the common-acid-bath method (Passey et al., 2010; Henkes et al., 2012; Ferry et al., 2011). A new approach using ~200 µg of carbonate sample in a modified Keil IV carbonate reaction device at 70 °C reaction temperature has had varying degrees of success (Schmid and Bernasconi, 2010; Grauel et al., 2013; Bernasconi et al., 2013).

Due to the high viscosity and high density of phosphoric acids (approx. 1.93 g/cm^3 for ~103 % H_3PO_4) carbon dioxide formed in the reaction with carbonate will be dissolved into the liquid phase. This has the potential to cause fractionation of the evolved CO_2 gas. This effect is intensified if a large volume of excess acid is used in the carbonate-acid reaction due to the increase in volume of possible dissolution. Thus, only a moderate excess should be used to minimise this effect. It is speculated that up to 0.4 mg of reacted carbonate evolved CO_2 gas remains in 1 ml of acid (de Groot, 2008).

2.5.3 Gas extraction

Recapture of produced gases by acid digestion can be achieved by several processes. It is typically done by using a glass or stainless steel vacuum line to transfer evolved gases from the site of sample reaction (side-arm vessels, CAB or Kiel-carbonate device) through a purification process and finally to the mass spectrometer for analysis (McCrea, 1950; Epstein et al., 1951, 1953). This method has subsequently been modified in many other publications with the basic principles remaining. Transferring of CO_2 gas using cryogenic separation (liquid nitrogen and dry-ice ethanol slushes) to separate gaseous contaminants from the acid reaction to aid in purification of the sample gas (Eiler and Schauble, 2004; Affek et al., 2006; Ghosh et al., 2006). This may be combined with inert gas carriers to move gases through other purification media (Passey et al., 2010; Huntington et al., 2010). However, a vacuum system must be present to ensure unwanted contaminant material is able to be evacuated from the system prior to analysis.

2.5.4 Cryogenic separation

The main method used to manipulate gases is in a vacuum line and to transfer them is by cryogenic separation. Liquid nitrogen is typically used to do this; it will readily separate most condensable compounds from the gas phase into a solid at -198 °C (Table 2.2). In the case of the extraction of CO_2 gas from carbonate material the main compound that needs to be removed is

water vapour evolved during the hydrolysis reaction of carbonate with phosphoric acid (Equation 2.5). Other potential by-products such as hydrocarbon, halocarbon and phosphorus compounds are possible as well. Incondensable atmospheric gases such as nitrogen, oxygen and argon can be separated through liquid nitrogen cryogenic trapping condensable gases (CO_2 and H_2O) and pumping away the non-condensable fraction (O_2 and N_2). Some contaminant gases will be retained by liquid nitrogen; however CO_2 gas will also be frozen. Therefore, a secondary cryogenic substance ($CO_{2(s)}$ 'dry ice') is needed to separate water vapour and carbon dioxide gas by virtue of different freezing points (Rondeau, 1966).

The temperature of the gas can be controlled by boiling (e.g. liquid nitrogen, LN_2), sublimation (e.g. CO_2) or melting temperatures (e.g. ice). By combining various organic compounds with either liquid nitrogen (LN_2) or dry-ice ($CO_{2(s)}$) in crushed form to create "slurries" or "slushes" that optimise the cooling potential at various temperatures and allow for a high surface area contact between the mixture and the cold trap glass extraction line components (Phillips and Hume, 1968). This allows the initial reaction products to be frozen by liquid nitrogen, by subsequent changeover to a higher temperature cold slush (-76 °C), water vapour and other contaminants are retained in the trap. This allows the evolved carbon dioxide to move through the extraction line to be measured and collected for analysis.

2.6 Sample CO_2 purification

The clumped isotope method has always been subject to concerns of contamination throughout the carbon dioxide extraction process (Eiler and Schauble, 2004; Shauble et al., 2004; Ghosh et al., 2006). The nature of the sample material can predispose some samples to contain more unwanted contaminant compounds than others, such as bioapatite tooth enamel or carbonate minerals which formed in areas rich in organic matter.

Isotopes of similar weights have the potential to mask the isotopic signal of the analysed masses 44, 45, 46 and 47 for carbon dioxide. This is termed isobaric mass interferences (Eiler and Schauble, 2004; Affek and Eiler, 2006; Guo et al. 2009; Huntington et al., 2009, Dennis et al., 2010). If present, this would lead to an enriched signal to be detected by the mass spectrometer causing a higher mass count of the carbon dioxide sample measured. Compounds of foremost concern are those containing or having derivatives of hydrocarbons and halocarbons. Fractionation and fragmentation products of these substances have atomic masses similar to that of the isotopologues of carbon dioxide (e.g. $^{12}C^{35}Cl$). Fractionation products of these groups may undergo recombination reactions within the mass spectrometers high voltage electron ionisation (EI) source to produce isobaric interferences. Therefore, their presence interferes with the abundance of the carbon dioxide molecules to be analysed. These compounds are very difficult to impossible to eliminate with a conventional vacuum extraction and associated cryogenic separation methods, as described in Chapter 2.5.4. This is a significant problem for the analysis of more complex organic-rich samples such as soils, bone and chondrites (Eagle et al., 2013; Hough et al., 2014; Peters et al., 2012; Quade et al., 2013) due to their inclusions of complex hydrocarbons and sulfur compounds (Eiler, 2011). Consequently, there is need to find an effective method to eliminate these contaminants. Certain points, however, must be considered in the pursuit of purifying a gas sample deemed for isotopic analysis. The purification process must not fractionate the isotopic composition of the CO_2. It is imperative that no other additional contaminants are introduced or come into contact with the sample gas during the purification process. Additionally, the sample gas must not be significantly heated above room temperature to prevent a secondary temperature equilibration at an uncontrolled and unknown intermediate temperature.

To overcome these complications, Eiler and Schauble (2004) explored the use of fused silica columns, with a carrier gas stream at a controlled temperature. Purification was carried out by entraining extracted CO_2 samples in a helium (He) carrier stream and passing it over a packed gas chromatography (GC) column. The column used was a 17.2 m PoraPLOT Q packed column

(bonded polystyrene-divinylbenzene) held at 25 °C during hydrocarbon separation and later baked to higher temperatures to clean the column of residuals (Eiler and Schauble, 2004). This method has also been utilised by Yoshida et al. (2012).

Gas chromatography methods subsequently explored include:

- Chrompack Poraplot-Q GC column (25 m, 0.32 mm ID) used at room temperature with a 3 mL/min helium carrier gas flow. This was modified to a Supelco Q-Plot (30 m, 0.53 mm ID) column held at -10 °C with a 2 mL/min gas flow rate (Affek and Eiler, 2006).
- Supelco Q-Plot GC column (30 m, 0.53 mm ID) held at -20 °C using a constant helium gas stream of 2 mL/min with addition post run column baking at 150 °C (Ghosh et al., 2006, 2007; Guo et al., 2009; Thiagarajan et al., 2011).
- Supelco Q-Plot GC column (30 m, 0.53 mm ID) held at -20 °C with a helium carrier gas flow rate of 3 mL/min (Affek et al., 2008; Huntington et al., 2009, 2010; Quade et al., 2013; Zaarur et al., 2011, 2013).

Packed-column chromatography methods include:

- Stainless steel U-trap packed with PoraPak Q (divinyl benzene polymer) glass packing material held at -20 °C (Passey et al., 2010; Dennis and Schrag, 2010)
- PoraPak-Q, packed into stainless steel U-trap, held at -15 °C using an ethylene glycol and LN_2 mixture (Rosenheim et al., 2013).

The use of packed columns has prevailed as the favoured purification technique, after cryogenic separation, in all subsequent clumped-isotope research projects. This is primarily due to the ease of including the gas chromatography purification step into the gas extraction line equipment with relatively minor modification. However, both systems have proven to be equally effective in removing hydrocarbon and halocarbon contaminants from carbon dioxide gas samples for clumped isotope measurements (Eiler, 2013; Affek, 2014)

In both of these systems, some form of a divinylbenzene polymer packing type is utilised to separate polar and non-polar gases. Carbon dioxide samples are allowed to passively flow through the column under the sample's own vapour pressure using cryogenic sample transfer techniques. Alternatively sample gases are entrained into an inert carrier gas stream and cryogenically separated upon passing through the column, helium is typically used. The helium must be of high grade with minimal contamination, it is also advantageous to pass helium carrier gas through molecular sieves to remove any residual moisture and or hydrocarbons.

Columns can be subjected to various temperature regimes to achieve adequate sample separation of the major (CO_2, H_2O, O_2, Ar) and minor (hydrocarbons, halocarbons and fragmentation

products) sample gas constituents. Both packed and capillary columns require cooling from -10 to -20 °C to achieve adequate separation.

Various column diameters and lengths have been utilised in various laboratory setups for the purification of CO_2 gas for clumped isotope analysis. For fused silica capillaries, the predominant trend is for the use of 0.53 mm internal diameter (ID) capillaries (Ghosh et al., 2006a; Huntington et al., 2009). However, 0.32 mm ID capillaries have also been used (Eiler and Schauble, 2004; Affek et al., 2006).

Several column lengths have been interchangeably used throughout the progression and modification of the CO_2 purification protocol from the initial methods to maximise contaminant separation. Initial studies by Eiler and Schauble (2004) used 17.4 m columns with later applications of the fused silica gas chromatography columns adopting 25 m and 30 m lengths to improve sample separation by allowing for lower carrier gas flow rates and larger sample sizes due to prolonged elution times (Ghosh et al., 2006a; Huntington et al., 2009).

Various manufacturers have developed fused silica and packed columns for gas separation. Table 2.2 summarises three capillaries offered by Agilent, Sigma-Aldrich and RESTEK respectively. All of these capillaries display equally acceptable characteristics for their use in carbon dioxide purification and the separation of hydrocarbon contaminants. The listed manufacturers also produce styrene/divinylbenzene polymer packing material as well as pre-packed columns for the same application.

Table 2.2: Gas Chromatography fused silica column comparisons

Name	Column Type	Packing Type	Description
HP-PLOT-Q Agilent ®	fused silica	bonded polystyrene-divinylbenzene	targeted separation of apolar and polar compounds including: Hydrocarbons (natural gas, refinery gas, ethylene, propylene, all C1-C3 isomers); CO_2, methane, air/CO, and water; Polar solvents (methanol, acetone, methylene chloride, alcohols, ketones, aldehydes, esters); and sulfur compounds (H_2S, mercaptans, COS). (Agilent, 2014)
Supelco-Q PLOT Sigma-Aldrich®	fused silica	divinylbenzene polymer	effectively resolves carbon dioxide (CO_2) and C1-C4 hydrocarbons at above ambient temperatures. It is also suitable for analyses of sulfur gases, alcohols, ketones, aldehydes, and many polar compounds. Gasoline and other petroleum fractions can be analysed as well. (Sigma-Aldrich, 2014)
Rt-QS-Bond RESTEK®	fused silica	divinylbenzene polymer	excellent for analysis of C1 to C3 isomers and alkanes up to C12. High retention for CO_2 simplifies gas analysis; CO_2 and methane separated from $O_2/N_2/CO$ (Note: $O_2/N_2/CO$ not separated at room temperature) (Restek, 2014)

The implementation of a gas purification technique utilising gas chromatography has been proven to greatly improve the purity extracted gases of the clumped isotope method (Eiler and Schauble, 2004). Contaminants may be in the form of hydrocarbons, $^{12,13}C_3{}^{1}H_8$ (mass 44, 45, 46 or 47), $^{12,13}C_2{}^{1}H_5{}^{16,17,18}O^{1}H$ (mass 46, 47, 48 or 49), halocarbons, $^{12,13}C^{35.36}Cl$ (mass 47, 48 or 49), $^{35,36}Cl^{12,13}C^{1}H$ (mass 48 or 49), and their respective fragmentation products as well as recombinant fractionation molecules formed in the ionisation source (Eiler and Schauble, 2004; Affek and Eiler, 2006; Ghosh et al., 2006). Whichever technique is utilised it is imperative that some form of hydrocarbon and halocarbon purification is undertaken to minimise isobaric interferences. Measurements made without the use of such purification techniques are almost certain to contain contamination, which may be evident in the higher analysed masses of the isotopologues of carbon dioxide (mass 48 and 49).

2.7 Δ_{47} mass spectrometry

The nature of the clumped isotope method requires the use of a very stable and precise mass spectrometer (MS) with dual inlet capabilities. This is primarily due to the need for extremely long counting times and thus very long sample analysis runs. Therefore, thermodynamic stability of the mass spectrometer is primal to obtaining accurate results and improving the overall precision of a measurement cycle.

Mass spectrometry has evolved dramatically over the past 50 years with instruments becoming more reliable, easier to control and to use. This has allowed for a wider application range of the technology. The key elements required for analysing clumped isotopes using mass spectrometry are similar to those for conventional stable isotope ratio measurements. Many of the mass sector single-focusing instruments can be utilised in clumped isotopes. Additionally, various other components are required to complement a magnetic sector MS to allow highly accurate sample scans over long counting times thus achieving the necessary high precision. Other high efficiency components required include; a stable electron ionisation (EI) source, to provide a continuous ion stream to the instrument and an array of simultaneous ion current detectors in the form of Faraday cups with adequate current amplification (Eiler, 2007). A sophisticated gas inlet system must be present to handle the pure reference gases as well as sample gas material to supply the mass spectrometer with gases that are contaminant free, are not subject to possible isotopic fractionation, or memory lag effects (Ghosh and Brand, 2003).

Four basic prerequisites are required of mass spectrometers used for clumped isotopes:

- high abundance sensitivity, due to the small abundance fraction of the requisite isotopologues (44.4 ppm for $^{13}C^{18}O^{16}O$, assuming stochastic distribution, see Table 2.4).
- high precision measurement of the isotope ratios is required (10^{-5}), due to the relatively small signal intensities of the rare isotopes in the sea of common isotopes in carbon dioxide (commonly less than 10^{-3}).
- high sample purity with minimal contamination of isobaric interferences, this can be reduced by a high degree of mass resolving power of the mass spectrometer.
- original bond integrity between the isotopes of the analyte must be maintained; and redistribution of isotopes among the original isotopologue during preparation or analysis must be avoided or the measurement is rendered meaningless (Eiler, 2007).

In contrast, inlet systems for clumped isotope measurements differ from those of conventional stable mass-spectrometry analysis. This is primarily due to the increased volume of gas that needs

to be generated to ensure adequate gas supply for the long counting times of the mass spectrometer while measuring a particular gas sample. These long counting times are required due to the nature of the clumped-isotope species only comprising a small fraction of most natural gases. However, high precisions of the isotopic ratio, up to 10^{-5}, are needed to accurately establish palaeothermometry relationships and thus very long counting times and large sample sizes are required. This is due to the fact that isotope measurements need to be made with internal precisions of up to a few hundredths of a per mil requiring up to 10x the charge collected than for conventional oxygen isotope measurements. Exceptional precision up to 0.01 ‰ requires an even greater charge of up to 100x than is needed for conventional gas-source dual-inlet mass spectrometry (Eiler, 2007).

Inlet systems typically comprise various pipes, capillaries, manual and automated valves, connection fittings, gauges and vacuum pump arrangements (Ghosh and Brand, 2003). This inlet arrangement will vary considerably depending on the carbonate preparation procedure in place. It will also depend on the type of vessel or container the reacted and or purified gas is presented to the mass spectrometer. This may be in the form of a “tube-cracker” if using borosilicate glass or quartz break seals. Gas may also be contained in glass or stainless steel sample vessels or U-trap arrangements. More recently, gas extraction and purification instrumentation is connected to the mass spectrometer directly through silica or stainless-steel capillaries. Additionally Peterson and Shrag (2014) have successfully developed a high efficiency dual-reservoir technique allowing the analysis of micro-carbonates without the need for a Keil IV carbonate device.

Instruments that fulfil these demands have been developed by various manufacturers such as Thermo Scientific producing the MAT 253 IRMS used in the initial applications and method development of the clumped isotope technique and the Delta V Plus IRMS only recently being applied with some success. IsoPrime has also developed an instrument, the Isoprime100 IRMS recently being applied to clumped isotopes as well as a Nu Instruments Perspective IRMS.

2.7.1 Quantification of the mass-47 anomaly

All previous clumped-isotope analyses on carbonate minerals have been performed by acid-digestion of the carbonate mineral to carbon dioxide gas. Analyses are made which measure the differences in carbon dioxide isotopologue ratios, with specific reference to the $^{13}C^{18}O^{16}O$ and $^{12}C^{18}O^{17}O$ multiply substituted isotopologues (Table 2.3, Eiler 2007). These form ~96% and 3% of the mass-47 signal in carbon dioxide generated in the acid-digestion reaction. The ratio of this mass anomaly is then compared to the other mass ratios (Eiler, 2007, 2013).

Table 2.3: Abundances of CO_2 assuming stochastic (random) distribution, assuming bulk $^{13}C/^{12}C$ ratios equal to PDB and $^{18}O/^{17}O/^{16}O$ ratios equal to SMOW, adapted from Eiler (2007).

Mass	Isotopologue	Abundance
44	$^{12}C^{16}O_2$	98.40%
45	$^{13}C^{16}O_2$	1.11%
	$^{12}C^{17}O^{16}O$	748 ppm
46	$^{12}C^{18}O^{16}O$	0.40%
	$^{13}C^{17}O^{16}O$	8.4 ppm
	$^{12}C^{17}O_2$	0.142 ppm
47	$^{13}C^{18}O^{16}O$	44.4 ppm
	$^{12}C^{17}O^{18}O$	1.5 ppm
	$^{13}C^{17}O_2$	1.6 ppb
48	$^{12}C^{18}O_2$	3.96 ppm
	$^{13}C^{17}O^{18}O$	16.8 ppb
49	$^{13}C^{18}O_2$	44.5 ppb

The clumped isotope method describes values of Δ_i for various gases to represent either an enrichment or depletion of a specific isotopologue, where the change (Δ) represents the variation in the ratio of mass *i* relative to the expected amount of that specific mass ratio R^* in a material analysed which conforms to the random stochastic distribution of an isotopologue R_i^*.

The mass 47 anomaly is represented by a change (Δ) in mass ratio. The Δ_i denotes the differences in abundances from the stochastic distribution, this is given by a per mil (‰) deviation (Equation 2.7). R_i represents the isotopologue ratio of interest and R_i^* represents the pool of isotopes in the stochastic distribution of isotopologues.

$$\Delta_i = \left(\frac{R_i}{R_i^*} - 1\right) \cdot 1000 \qquad \textbf{Equation 2.7}$$

In the case of CO_2 the Δ_i is given as Δ_{47}. Therefore the deviation in relative abundance of $^{13}C^{18}O^{16}O$ (mass 47 anomaly) is used as it most closely reflects the natural occurrence of $^{13}C^{18}O^{16}O$ and it is the most abundant form of mass 47 in carbonates. This variation in mass 47 is expressed in Equation 2.8a. Equation 2.8b is a substituted form of Equation 2.8a including the R_{13} and R_{18} ratios for carbon and oxygen for masses 45, 46 and 47.

$$\Delta_{47} = \left[\left(\frac{R_{47}}{R_{47^*}} - 1\right) - \left(\frac{R_{46}}{R_{46^*}} - 1\right) - \left(\frac{R_{45}}{R_{45^*}} - 1\right)\right] \times 1000 \qquad \textbf{Equation 2.8a}$$

$$R^{45*} = R_{13} + 2 \cdot R_{17}$$

$$R^{46*} = 2 \cdot R_{18} + 2 \cdot R_{13} \cdot R_{17} + (R_{17})^2$$

$$R^{47*} = 2 \cdot R_{13} \cdot R_{18} + 2 \cdot R_{17} \cdot R_{18} + R_{13} \cdot (R_{17})^2$$

$$\therefore \Delta_{47} = \left[\begin{array}{c} \left(\frac{R_{47}}{2 \cdot R_{13} \cdot R_{18} + 2 \cdot R_{17} \cdot R_{18} + R_{13} \cdot (R_{17})^2}\right) \\ - \left(\frac{R_{46}}{2 \cdot R_{18} + 2 \cdot R_{13} \cdot R_{17} + (R_{17})^2}\right) - \left(\frac{R_{45}}{R_{13} + 2 \cdot R_{17}}\right) + 1 \end{array}\right] \times 1000 \qquad \textbf{Equation 2.8b}$$

These R ratios for mass 47, 46 and 45 are measured abundance ratios relative to the mass 44 anomaly. They are derived from measured raw δ values for mass 47, 48 and 49 for the sample (SG) in reference to a working gas (WG) standard of known isotopic composition.

$$\delta^i = \left[\left(\frac{R_{i(SG)}}{R_{i(WG)}}\right) - 1\right] \cdot 1000 \qquad \textbf{Equation 2.9}$$

The R* ratios are calculated R values based on the measured δ^i values if the sample had stochastic distribution of all the possible isotopologues (Equation 2.9). The R* ratio for mass 47, 46 and 45 can be calculated from the R_{13}, R_{17} and R_{18} abundance ratios $^{13}C/^{12}C$, $^{17}O/^{16}O$ and $^{18}O/^{16}O$ for the sample values, given that the R_{13} and R_{18} values are calculated from the measured R_{45} and R_{46}

ratios of the sample. This allows us to assume the stochastic distribution. R_{17} is calculated from R_{18} based on the specific mass-dependent fractionation (Huntington et al., 2009).

This is based on the assumption of a stochastic distribution of the R^* values where $\Delta_{47} = 0$. This is because R_{13}, R_{17} and R_{18} abundance ratios are calculated from the measured $\delta^{13}C$ and $\delta^{18}O$ values of the samples (Ghosh et al., 2006a; Huntington et al., 2010; Dennis et al., 2011). By using standard ratio assumptions of $R_{13} = 0.0003799$, $R_{17} = 0.0020052$ and $R_{18} = 0.0112372$, the stochastic distribution is calculated for ^{12}C, ^{13}C, ^{16}O, ^{17}O and ^{18}O, as shown in equation 2.10 a, b, c, d, e (Gonfiantini et al., 2005; Brand et al., 2010).

$$[^{12}C] = \frac{1}{(1+[R_{13}])}$$

$$[^{13}C] = \frac{R_{13}}{(1+[R_{13}])}$$

$$[^{16}O] = \frac{1}{(1+[R_{17}]+[R_{18}])}$$

$$[^{17}O] = \frac{R_{17}}{(1+[R_{17}]+[R_{18}])}$$

$$[^{18}O] = \frac{R_{18}}{(1+[R_{17}]+[R_{18}])}$$

Equation 2.10 a, b, c, d, e

A detailed calculation of the Δ_{47} value and standard values used to calculate the stochastic distribution is given in Chapter 3.8.1. The Δ_{47} value for the carbonate sample is termed a raw $\Delta_{47\text{-raw}}$ value. This is expressed as a $\Delta_{47}\text{-}_{(SG\text{-}WG)}$ value, relative to the sample gas (SG) and the working gas (WG) of the mass spectrometer. This raw sample value must be further calibrated and incorporated into the absolute reference frame of clumped isotope measurements to standardise the value to account for mass spectrometer non-linearity effects such as time scaling and ion source scrambling.

2.7.2 Reference frame and calibration

In order to correctly interpret isotopic data and perform further data analysis, results must be presented in a uniform way to allow direct comparison on a common scale in relation to known constants. A reference frame must therefore be constructed to adequately quantify the clumped isotope measurement. Over the past decade the clumped-isotope thermometer has been calibrated using various analogues. Some discrepancies are present among the various approaches with the source of error still to be fully determined. Two distinct alternatives have been explored. Firstly, using synthetically grown inorganic calcite at known controlled temperatures, this is referred to as the Ghosh et al. (2006a) temperature calibration scale. Alternatively the absolute reference frame for temperature calibration is used, using equilibrated H_2O-CO_2 at known temperatures as well as heated gases (Dennis et al., 2011 and Zaarur et al., 2013).

2.7.2.1 Synthetic carbonate calibration

Initial calibration of the clumped isotope palaeothermometer by Ghosh et al. (2006a) was based on Δ_{47} measurements of seven synthetic calcite samples formed by controlled temperature precipitation experiments in the laboratory, between 1 and 50 °C. Precipitation experiment setup was similar to methods used by Kim and O'Neil (1997) and a similar experimental setup was utilised by Zaarur et al. (2013) in a revised and independent clumped isotope calibration using synthetically precipitated calcium carbonate.

Ghosh et al. (2006a) first grew calcite from inorganic solutions of sodium bicarbonate and calcium chloride. This generated low $CaCO_3$ yields, thus the procedure was modified. A calcite-saturated solution was prepared with de-ionied water and high purity calcium carbonate (Ghosh et al., 2006). The solution was acidified by bubbling high purity CO_2 through the solution while stirring, by removal of CO_2 of the solutions causing the precipitation of carbonate. Precipitation is facilitated by bubbling high purity N_2 gas through the respective solutions (10-50 mL/min flow rate). Each precipitation experiment was conducted at various temperatures (1 ± 0.2, 23 ± 1, 33 ± 2, and 50 ± 2 °C) using ice-baths, room temperature and heated water baths. Solutions were allowed to thermally equilibrate for one hour prior to the start of the relevant reaction (Ghosh et al., 2006). Zaarur et al. (2013) conducted similar experiments, although precipitation temperatures covered a wider range than previously (5, 8, 15, 25, 35, 50 and 65 °C), and reactions were allowed to continue for up to 4 days.

Precipitated calcium carbonate was collected by filtration and dried using vacuum desiccation at room temperature in both instances. Mineralogy was then determined by x-ray diffraction (XRD) to confirm the precipitated materials' composition. Synthetic carbonate precipitation by both Ghosh et al. (2006a) and Zaarur et al. (2013) showed that the produced carbonates were polymorph mixtures. Precipitated carbonates were primarily composed of calcite with traces of vaterite and aragonite. The presence of other polymorphs in various ratios is temperature dependent. Higher temperatures (> 50 °C) are more likely to produce aragonite. Vaterite appears to be more commonly formed at lower temperatures (8 °C; Zaarur et al., 2013).

Δ_{47} values for these temperature calibrations range from 0.73 ‰ to 0.513 ‰ (± 0.019) for temperatures of 5 to 65 °C (Zaarur et al., 2013). Values from Ghosh et al. (2006) range from 0.77 ± 0.022 ‰ to 0.55 ± 0.023 ‰ at temperatures of 1 to 50 °C. In addition, the isotopic composition of the precipitating host water, $\delta^{18}O_{(water)}$, was measured. This was compared to calculated $\delta^{18}O_{(water)}$ values. These were computed by using the measured $\delta^{18}O_{(carbonate)}$ and $^{18}\alpha$ (Equation 2.11a) values derived from the acid fractionation equations (Equation 2.11, b, c and d) and precipitation experiment temperatures (Friedman and O'Neil, 1977; Kim and O'Neil, 1997 and Kim et al. 2007b).

$$^{18}\alpha = \frac{(\delta^{18}O_{(carbonate)} + 1000)}{(\delta^{18}O_{(water\text{-}measured)} + 1000)}$$

$$1000 \ln\alpha_{(calcite\text{-}water)} = 2.78\left(10^{6}T^{-2}\right) - 2.89$$

$$1000 \ln\alpha_{(calcite\text{-}water)} = 18.03\left(10^{3}T^{-1}\right) - 32.17$$

$$1000 \ln\alpha_{(aragonite\text{-}water)} = 17.88\left(10^{3}T^{-1}\right) - 31.14 \qquad \textbf{Equation 2.11 a, b, c, d}$$

The $\delta^{18}O$ carbonate values of the previous precipitation studies appear to generally agree with the previous studies on synthetically grown carbonates (Ghosh et al., 2006a). However, some slight differences are apparent in the fractionation patterns (Dennis and Schrag, 2010). Results indicate that discrepancies between different synthetic $CaCO_3$ calibrations are not a factor of differences in precipitation methods due to the high similarity of experimental setup among the studies. However, some inconsistency may arise from unaccounted water evaporation; this would lower the isotopic values of the precipitated carbonate (Zaarur et al. 2013). Further inconsistencies may

arise from differences in precipitation rates, in relation to supersaturation rates in the precipitating solution. A lower degree of fractionation was observed in faster growing calcite by Dietzel et al. (2009) and Gabitov et al. (2012), possibly indicating the preferential uptake of ^{16}O into fast precipitating carbonates. This may explain the slight differences in isotopic values between studies due to the differences in precipitation rates in various temperature conditions. Despite these discrepancies, the results of all calibrations to date reflect precipitation close to equilibrium conditions (Kim and O'Neil, 1997; Freidman and O'Neil, 1977; Ghosh et al., 2006; Kim et al., 2007a, 2007b; Deitzel et al., 2009; Gabitov et al., 2012; Zaarur et al., 2013). Therefore, the dissolved inorganic bicarbonate from the supersaturated precipitation solution has undergone full isotopic exchange and has reached isotopic equilibrium conditions with the host water at a specified temperature.

This results in a clumped isotope thermometer calibration of synthetic $CaCO_3$, aims to characterise the Δ_{47}-T relationship. The original calibration data set was analysed with relatively low precision, compared to recent typical analysis techniques (Zaarur et al., 2013). This results in a large relative calibration error (Equation 2.12). This can be minimised by additional data points at a wider range of temperatures or analysis of the sample material at higher precision. It should be noted that this calibration only takes into account the synthetically precipitated carbonate materials. If additional data from biologically precipitated carbonates are added, the calibration changes (Equation 2.13). The slope is only marginally affected within error, whereas the intercept exhibits a more profound change. The addition of biogenic carbonate data reduces the error of the slope of the line due to more data points as well as reducing the error of the intercept (Zaarur et al., 2013). However, the overall correlation (r^2) is marginally reduced from 0.93 to 0.92, respectively.

Combined Δ_{47}-T Ghosh et al. (2006) and Zaarur et al. (2013) synthetic carbonate palaeothermometer calibration.

$$\Delta_{47} = (0.0526 \pm 0.0025)10^6/T^2 + (0.0520 \pm 0.0284)\ (1SE) \quad r^2 = 0.93 \quad \textbf{Equation 2.12}$$

Combined Δ_{47}-T synthetic carbonate calibration with all previously analysed biogenic carbonates (Zaarur et al., 2013)

$$\Delta_{47} = (0.0539 \pm 0.0013)10^6/T^2 + (0.0388 \pm 0.0155)\ (1SE) \quad r^2 = 0.92 \quad \textbf{Equation 2.13}$$

2.7.2.2 Absolute reference frame

There remains a need to construct a reference frame for clumped-isotopes that can empirically account for fragmentation and recombination reactions. These may occur in the mass spectrometer ion source and other analytical fractionation artefacts. These can affect the isotopologue ratios in the carbonate clumped isotope thermometer (Dennis et al., 2011).

In light of this, an empirical calculation, known as an empirical transfer function, can be prepared by using calculations of the expected abundances of isotopologues in CO_2 that have reached full thermodynamic equilibrium at various temperatures. This is based on the application of quantum mechanical and statistical thermodynamic principles (Wang et al., 2004). Values are derived from fourth order polynomial regression equations, shown in Table 2.5. It is constructed from thermodynamic zero point energies and normal mode wave numbers (Dennis et al., 2011). It can be expressed as a polynomial equation (Equation 2.14) relating calibrated reference (RF) temperature to the Δ_{47} value; this is used to construct an empirical transfer function (ETF) (Dennis et al., 2011).

$$\Delta_{47\text{-RF}} = 0.003 \left(\frac{1000}{T}\right)^4 - 0.0438 \left(\frac{1000}{T}\right)^3 + 0.2553 \left(\frac{1000}{T}\right)^2 - 0.2195 \left(\frac{1000}{T}\right) + 0.0616$$

Equation 2.14

Table 2.5: Theoretical equilibrium values based on interpolation of a fourth order polynomial regression equation (from Wang et al., 2004; Dennis et al., 2011).

Temperature (°C)	$\Delta_{47\text{-RF}}$
0	1.0705
8	1.0208
10	1.0089
25	0.9252
27	0.9147
50	0.8050
1000	0.0266

The creation of an ETF allows for the correction of analyses for instrument disambiguity. There are subtle differences in mass spectrometer measurements (of 1% or lower) forming a linear discrepancy between measured current intensity ratios and actual isotopic abundance ratios. This can be calibrated for by measuring equilibrated CO_2 gases with Δ_{47} values which are known to be nominally equal at various controlled temperatures (Huntington et al., 2009; Dennis et al., 2011).

This has the additional effect of eliminating chances for method-induced error in the gas preparation stage such as acid fractionation, reaction temperature and other experimental artefacts. Previously postulated "scrambling" effects in the mass spectrometer ion source are also accounted for by this standardised calibration and reporting of Δ_{47} values (Dennis et al., 2011).

In order to constrain the absolute reference frame for the Δ_{47} values and derived temperatures it is necessary to obtain CO_2 gases with equilibrium Δ_{47} values at various low temperature points that are within the possible range of values for the selected sample material (Dennis et al., 2011; Passey et al., 2012). Many protocols exist for producing gases at isotopic equilibrium. This has primarily been done in water samples destined for conventional isotopic analysis (de Groot et al., 2009). Each of these created gases must be different in their bulk isotopic ($\delta^{18}O$, $\delta^{13}C$) composition. These must be equilibrated at a common temperature to yield CO_2 gases that are all understood to be identical in their Δ_{47} value.

This procedure is commonly accomplished by using a combination of heated gas and water-equilibrated carbon dioxide samples, (HG-CO_2 and H_2O-CO_2), at 1000 °C and 1 to 75 °C, respectively, but varies in different laboratories (Zaarur et al., 2013). Heated gas samples are produced by taking a high purity CO_2 cylinder gas and heating it to 1000 °C for 2 hours in a furnace. This has the effect of forcing the CO_2 gas to randomise its isotopic composition, where all isotopologues conform to the natural stochastic random distribution. Water-equilibrated gas samples utilise a common high purity CO_2 cylinder gas in conjunction with water samples of different isotopic signatures in sealed equilibration vessels. These are immersed into temperature controlled baths of varying temperatures, typically 10 ºC, 25 ºC and 50 ºC (Dennis et al., 2011). This technique is typically performed for conventional $\delta^{18}O$ measurements of natural waters whereby the $\delta^{18}O$ of CO_2 is measured after isotopic exchange has occurred and equilibrium has been reached in an enclosed system. The equilibrium exchange reaction process is performed in the same manner in the 'clumped-isotope' method. However, the Δ_{47} value is not dependent on the $\delta^{18}O$ value. The Δ_{47} value is not sensitive to the isotopic composition of the water but is sensitive to temperature equilibration. It is, however, necessary to utilise equilibration waters that have a range of $\delta^{18}O$ values in order to show the non-linearity of the mass spectrometer (Huntington et al., 2009). This will produce gas samples with equilibrated Δ_{47} values at the selected temperatures.

Two measured values are required, Δ_{47} and δ^{47} (both in relation to a common working reference gas). These analyses yield a linear trend which defines the non-linearity of the mass spectrometer (Huntington et al., 2009; Dennis et al., 2011). Non-linearity is plotted as $\Delta_{47(raw)}$ versus δ^{47}. This will yield a measurement of $\Delta_{47\text{-(EG vs WG)0}}$ that is corrected for the non-linearity effect of the mass

spectrometer from the equilibrated gas samples in association with the heated gas samples at various temperatures, the heated gas or equilibrated gas line correction (Equation 2.15).

$\Delta_{47\text{-(EG vs WG)}}$ versus $\delta_{47\text{-(EG vs WG)}}$ to give $\Delta_{47\text{-(EG vs WG)0}}$ **Equation 2.15**

Combining the $\Delta_{47\text{-(EG vs.WG)0}}$ and $\Delta_{47\text{-RF}}$ of the equilibrated gas line and the theoretical values by Wang et al. (2004) yields an empirical transfer function (ETF), with associated r^2 values (Equation 2.16).

$$\Delta_{47\text{-RF}} = \text{slope}_{\text{ETF}} * \Delta_{47\text{-(EG vs WG)0}} + \text{intercept}_{\text{ETF}} \quad \textbf{Equation 2.16}$$

Raw measurement sample values can then be converted to the absolute reference frame. If a constant working-gas (WG) is assumed in the mass spectrometer, and is used for all isotopic analysis, the variation between the intercept of the regression lines is the difference in Δ_{47} of the equilibrated gases and the working gas. Firstly, the sample gas is corrected for non-linearity to give the $\Delta_{47\text{-(SGvsWG)0}}$ using the slope of the equilibrated gas line (EGL) (Equation 2.17). The empirical transfer function is then applied, to project the $\Delta_{47\text{-(EGvsWG)0}}$ value into the reference frame (RF), reporting the 'true' $\Delta_{47\text{-RF}}$ value of the gas sample (Equation 2.18).

$$\Delta_{47\text{-(SG vs WG)0}} = \Delta_{47\text{-(SG vs WG)}} - \delta_{47\text{-(SG vs WG)}} * \text{slope}_{\text{EGL}} \quad \textbf{Equation 2.17}$$

$$\Delta_{47\text{-RF}} = \Delta_{47\text{-(SG vs WG)0}} * \text{slope}_{\text{ETF}} + \text{intercept}_{\text{ETF}} \quad \textbf{Equation 2.18}$$

Where: RF - reference frame absolute
SG - sample gas
ETF - empirical transfer function
WG - working gas
EGL - equilibrated gas line

Previous ETFs from various institutions have yielded slopes of values 1.0105 to 1.1548 and intercepts of 0.9194 to 0.9539 (California Institute of Technology, Harvard University, John Hopkins University, Yale University). A summary of empirical transfer functions from various institutions is provided in Dennis et al. (2011).

2.7.3 Pressure baseline (PBL) correction

The initial approach of reporting Δ_{47} values by using the heated-gas line (HGL) calibration method (Huntington et al., 2009) or the later developed 'absolute reference frame' and equilibrated-gas line (EGL) by Dennis et al. (2011) correcting for scale compression (i.e. fragmentation and recombination of molecules in the ion source) both suffer from long-term slope drift. Subsequently, it has been shown that accurate characterisation of the baseline signals of the Faraday cup collectors possibly provides a better system of correcting for long-term instrument signal drift.

Ion beam quantification involves the measurement of the voltage intensity of an ion beam by a Faraday collector in comparison to the background voltage (if the ion beam is focussed correctly into the detector cup with minimal scatter). Typical background signal intensities are measured on the mass spectrometer (i.e. MAT 253) prior to a measurement being made. This background 'correction' uses identical tuning parameters to a sample acquisition for clumped-isotope analysis of a carbon dioxide gas evolved from carbonate or a reference gas.

Despite this, there appears to be a distinct difference in the off-peak background signal on either side of the m/z HV signal when gas is introduced into the ion source compared to when no-gas is in the ion source and the instrument is under vacuum (He et al., 2012). It has also been observed that whilst gas is being admitted to the source that background signal intensities shift to negative numbers on one or both sides of the signal peak.

These phenomena have been monitored continuously on many of the MAT253 instruments in various laboratories. The baseline off-peak signal change can be monitored prior to a mass spectrometry run commencing, during and post analysis. This has shown that, the baseline signal value shifts can effect Δ_{47} values as well as δ^{47} values on a long-term basis (month to year) and even on a short-term basis of a single mass spectrometry sample analysis run. This effect is exacerbated when using excessively small sample sizes and increasing the bellows pressure to the limits of the dual-inlet bellows (He et al., 2012). If PBL corrections are made in consistent intervals the need to perform lengthy heated gas and equilibrated gas measurements can be reduced. However, there is still the need to calibrate the clumped isotope method to both heated gas and equilibrated gas samples. In addition the PBL calibration is highly instrument specific and may be more or less suitable depending on the types of sample and amounts of sample being processed on a daily basis.

2.7.4 Acid fractionation factor

Since the introduction of the clumped isotope method there have been various improvements to increase the productivity and analytical efficiency of the technique. Two limiting factors can be identified. Firstly, the analysis time of a single replicate sample ranges between 2 to 4 hours to achieve the necessary counting statistics required to accurately make a Δ_{47} measurement and report an accurate formation temperature. This is currently unavoidable, however, improvements in the method such as those presented by Petersen and Schrag (2014) and increased use of the Keil-carbonate device will allow smaller samples to be more commonly analysed with adequate precision and accuracy. Secondly, the rate of liberation of carbon dioxide (CO_2) from sample carbonate (CO_3) through phosphoric acid digestion is a crucial limiting factor. Initial studies of Δ_{47} analysis utilised side-arm vessel reaction at 25 ℃ (Ghosh et al., 2006a,b). At this relatively low temperature sample reaction is slow, requiring up to 18 to 38 hours for calcite and aragonite and days to weeks for siderite ($FeCO_3$) and high magnesium carbonates (HMC – $MgCO_3$) such as dolomite and magnesite (Ghosh et al., 2006a,b; Guo et al., 2009; Wacker et al., 2013; Defliese et al., 2015).

In order to increase the analytical efficiency of the acid reaction step a higher acid digestion temperature must be used. Typically, other acid reactions are performed at 90 °C using the common acid bath (CAB) method. Increasing the reaction temperature creates an offset in Δ_{47} values between samples analysed at 25 °C and 90 °C. Similar effects have been well documented for conventional $\delta^{18}O$ methods (Swart et al. 1991; Kim et al. 1997). If carbonates are reacted at 90 °C, results must be corrected to the 25 °C reaction temperature to bring results into the absolute reference frame to allow for meaningful comparisons of sample material to be made.

To date only two studies have focused on phosphoric acid digestion fractionation relationships in clumped isotopes. Wacker et al. (2013) used both the sealed reaction vessel and common acid bath methods at 25 °C and 90 °C respectively. Better reproducibility was achieved using the common acid bath method at 90 °C. This is likely due to the increased reaction time, associated with the 25 °C method, allowing for more pronounced re-equilibration with evolved H_2O. Additionally, effects of different carbonate mineralogy as well as sample size were examined (i.e. calcite and aragonite). Results showed that the different minerals behave nearly identically, with increased sample size leading to better reproducibility (Wacker et al., 2013; Defliese et al., 2015). In work by Defliese et al. (2015), measuring phosphoric acid fractionation factors across a 25 to 90 °C temperature range showed that calcite, aragonite and dolomite behave in a similar manner. Results do not suggest any isotopic composition effects on the fractionation factor. This suggests

that a single temperature-dependent acid fractionation factor relationship (Equation 2.19) may be able to be applied for most carbonate materials (Defliese et al., 2015)

$$1000 \ln \propto_{CO_2(acid)\text{-}\Delta_{47}} = \frac{(0.022434 \pm 0.001490) * 10^6}{T^2} - (0.2524 \pm 0.0168) \quad \textbf{Equation 2.19}$$

However, when applying the new acid fractionation factor for previously published Δ_{47}-temperature data a significant calibration difference is evident between samples analysed at 25 °C and those at higher temperatures using the common acid bath method. Results indicate that applying a common acid fractionation factor framework for all Δ_{47} data does not solve all calibration discrepancies (Defliese et al., 2015). This further indicates that other method parameters are the potential cause of calibration differences.

2.7.5 Δ_{47}-T palaeotemperature equation

As previously discussed, in Chapter 2.2, the bonding among oxygen and carbon isotopes is not random. If bonding of isotopologues in carbon dioxide were random, the isotopic composition would be that of the stochastic random distribution (Eiler, 2007). However, abundances of natural carbonates deviate from this stochastic distribution, the affinity of the clumping of the heavy isotopes ^{13}C and ^{18}O is favoured as a function with decreasing temperature. Thus, this degree of clumping at thermodynamic equilibrium can be utilised to provide a measure of the temperature conditions in the environment in which the carbonate was formed (Schauble et al., 2006; Ghosh et al., 2006). It is not possible to analyse carbonate directly for isotopic abundance ratios; however, it is possible to measure carbon dioxide gas evolved from the carbonate through acid digestion at controlled temperatures. This yields CO_2 gas exhibiting different but reproducable abundance proportions as in the original carbonate (Guo et al., 2008). Some corrections such as acid fractionation and calibration correction must also be taken into consideration, these are discussed below.

Several temperature relationships have been reported, using synthetic carbonate, biogenic carbonate as well as carbon dioxide equilibration to constrain the Δ_{47}-*T* relationship (Ghosh et al., 2006; Equation 2.20). The calibration was based on inorganic, synthetically precipitated calcite grown at temperatures between 0 and 50 °C.

$$\Delta_{47} = 0.0592 * 10^{6} * T^{-2} - 0.02$$ **Equation 2.20**

This was recalculated using a least squares linear regression (Equation 2.21) to incorporate the uncertainties of the Ghosh et al. (2006) Δ_{47}-*T* measurements (Huntington et al., 2010).

$$\Delta_{47} = (0.0605 \pm 0.0014) * 10^{6} * * T^{-2} - (0.031 \pm 0.016)$$ **Equation 2.21**

These synthetic carbonate calibrations have been re-calculated (Equation 2.22) into the absolute reference frame by Dennis et al. (2011) to give temperature equations based on a two-point secondary transfer function, in a calibration range of 1 to 50 °C.

$$\Delta_{47} = (0.0636 \pm 0.0049) * 10^{6} * T^{-2} - (0.0047 \pm 0.0520)$$ **Equation 2.22**

This temperature calibration has since been improved by a revision of the original method by Zaarur et al. (2013). The calibration is also based on synthetically precipitated calcium carbonate between 5 and 65 °C (Equation 2.23) widening the previous temperature calibration and providing more data to strengthen previously recorded relationships. It is presented in the Ghosh et al., (2006a) reference frame.

$$\Delta_{47} = (0.0526 \pm 0.0025) * 10^{6} * T^{-2} - (0.0520 \pm 0.0284)$$ **Equation 2.23**

This has also been recalibrated in Equation 2.24, into the absolute reference frame (Dennis et al. 2011) by Zaarur et al. (2013).

$$\Delta_{47} = (0.0555 \pm 0.0027) * 10^{6} * T^{-2} - (0.0780 \pm 0.0298)$$ **Equation 2.24**

The revised calibration by Zaarur et al. (2013) agrees within 1 °C to the original temperature calibration by Ghosh et al. (2006) at the 25 to 39 °C temperature range. However, this difference becomes more apparent at lower temperatures (<16 °C). Discrepancies are also present at higher temperatures. These uncertainties are more significant at the higher temperatures that lie outside the calibration range. This is discussed in detail by Zaarur et al. (2013) with specific reference to work on palaeosol carbonates associated with the altiplano uplift (Ghosh et al., 2006b), whereby effects of altitude and uplift rates add to the palaeotemperature problem. Analysis of sea-surface temperatures during glaciation (Finnegan et al. 2011) and Arctic temperatures from freshwater mollusc shells (Csank et al., 2011), pose potential calibration problems at the lower temperature range. Some of the inconsistencies between the two temperature calibration results may be seasonal growth artefacts or resemble species dependent vital-effects, although further investigation is required.

Chapter 3: Methods

3.1 Introduction 52
3.2 Sample pre-treatment 52
3.3 Elemental composition analysis 53
3.3.1 X-ray powder diffraction (XRD) 54
3.3.2 Inductively coupled plasma mass spectrometry (ICP-MS) 54
3.4 Micromorphology and thin sections 56
3.5 Accelerator mass spectrometry ^{14}C dating 58
3.6 Clumped-isotope sample gas preparation 59
3.6.1 Phosphoric acid preparation 59
3.6.2 Sample digestion 60
3.6.3 Vacuum system 63
3.6.4 Cryogenic trapping 65
3.6.5 Gas extraction apparatus 65
3.6.6 Gas yields 66
3.6.7 Working gas 67
3.6.8 Heated gas standards 67
3.6.9 Temperature-controlled water equilibrations 68
3.7 Clumped-isotope: sample gas purification 70
3.8 Clumped-isotopes: mass spectrometry 73
3.8.1 Clumped-isotope measurements 75
3.8.2 Empirical transfer function 75
3.8.3 Palaeotemperature determination 82
3.8.4 Internal carbonate reference standards 82

3.1 Introduction

This chapter presents a detailed account of the methods used in this study. Emphasis is placed on the modifications made to the conventional 'clumped-isotope' method to improve the precision and accuracy of the results. To fully determine the carbonate formation temperature using the 'clumped-isotope' method it is necessary to characterise, describe and classify the environmental conditions of the depositional environment of each sample. ICP-MS and XRD analyses were used to determine sample mineralogy. Thin section analysis and detailed carbonate textural classification was conducted using point counting and morphological descriptions. Radiocarbon (^{14}C) dating as well as biostatigraphic age determination provided a geochronologic context for the samples. The chapter further describes the details of the laboratory method used to determine the clumped-isotope formation temperatures of the carbonate materials examined.

This study also represents the first data set produced by the clumped isotope laboratory at the University of Wollongong, Australia. It utilises a MAT253 IRMS with customised inlet tubing and nickel capillaries. The gas extraction procedure uses side-arm acid reaction vessels in conjunction with a glass gas extraction line. Extracted gas samples are purified using a gas chromatograph with fused-silica tubing with cryo-cooling capabilities in an inert helium carrier gas flow. Thus this thesis serves as a commissioning review and exploration for potential clumped-isotope applications at the University of Wollongong.

3.2 Sample pre-treatment

Due to the variation among the different types of samples in this study, various pre-treatments were employed. The materials include; cold-water carbonates (glendonites), carbonate speleothem deposits (flow stone, cave pearls, vein spar, stalagmites and calcite rafts) and associated bioapatite in the form of bone carbonate and biogenic carbonates of molluscs (gastropods and bivalves). These will be discussed in detail in Chapters 4, 5 and 6, respectively.

In all treatment processes it is imperative that no foreign carbonate material is introduced into the sample. Care must be taken to eliminate contamination by foreign hydrocarbon and or halocarbon compounds, which have the potential to cause mass interference and greatly affect isotopic signature. The carbonate sample must not be subjected to high temperatures for elongated periods

of time, as re-equilibration or recrystallisation could occur, leading to isotopic fractionation. Finally, representative homogeneous subsamples are taken, by bulk grinding of samples from all specimens that do not favour or skew the isotopic results (Ghosh et al., 2006a, Eiler, 2007).

All specimens were rinsed and air dried as an initial pre-treatment process, as well as being sonicatied in distilled water to remove any adhering particulates. Samples were stored in sealed plastic sample bags to reduce contamination. The use of metal tools was limited to minimise the introduction of metal particulates. Additionally, hydrocarbons and halocarbons in the form of oils, greases, solvents and chlorine-containing acid (i.e. HCl) were critically avoided in all cutting and grinding preparatory stages. Samples consisting of bulk whole-rock samples were cut using a diamond bladed bench saw operating with a water cooling solution. Samples were meticulously cleaned post cutting, using plastic tweezers, nylon brushes and distilled water to remove any particulate contaminants introduced or created by the cutting process.

3.3 Elemental composition analysis

Mineralogical determination can be performed by X-ray diffraction (XRD) of powdered sample material. Whereas elemental composition analysis is performed by X-ray fluorescence (XRF), inductively coupled plasma-optical emission spectroscopy (ICP-OES) or atomic absorption spectrophotometry (AAS), for major element analyses. However, trace element analysis requires a higher level of both precision and accuracy to determine the exact elemental composition of the sample material; this can be achieved by inductively coupled plasma-mass spectrometry (ICP-MS). Measuring the elemental composition of the carbonate sample (i.e. calcium, magnesium, iron concentrations) may assist in understanding the fundamental isotopic equilibrium processes of glendonites and cave formations. Understanding the elemental distribution of minor ion substitution in carbonates may give an indication of isotopic fractionation mechanisms within a particular depositional environment which may be difficult to understand using isotopic data alone. Variations in major-element substitution may indicate various stages of diagenesis or differences in precipitation host water and changes in surrounding geological formations.

3.3.1 X-ray powder diffraction (XRD)

Phase identification of crystalline material was performed by X-ray powder diffraction at UOW. Analyses were made with a Spellman DF3 generator attached to a copper X-ray tube and Philips PW 1078/24 Goniometer (1 kW). Quantitative mineral phase identifications were then made using Siroquant ™ in conjunction with Traces™ software packages.

Sample preparation for these analyses consisted of manual wet grinding of all samples in an agate mortar and pestle. To reduce heat, 95% ethanol (denatured) was added while grinding to not alter the temperature signature of the sample material. Samples were then air dried under a laminar fume hood or placed on a hotplate at 50 °C for 2 minutes. This heating allowed evaporation of ethanol and any other residual moisture, without heating the sample significantly. Samples were stored in plastic flip-top vials or in sealed plastic sample bags. All samples were placed into a vacuum desiccator after preparation to eliminate latent water vapour from contaminating the prepared powders.

3.3.2 Inductively coupled plasma mass spectrometry (ICP-MS)

Trace element analysis was carried out using an Agilent® 7500CS(Ce) ICP-MS at UOW in conjunction with Chemstation® software to determine trace-element ratios in this study. Pre-cleaning procedures were adapted and modified from procedures used by Puller (2006) and Dux et al. (2015) for vial, pipette and associated sample and standard containers.

Sample powders were prepared by wet grinding with ethanol to reduce heat from grinding friction as the same sample powder was used in subsequent isotopic analysis. Sample powders were weighed using a microanalytical balance (accuracy of 10^{-7} gram). All sample manipulation tools such as tweezers, weighing boat and containers were pre-cleaned with deionised water and non-metal objects where used wherever possible to reduce the possibility for contamination and additional sources of iron (Fe), aluminium (Al) and other metals which may substitute for calcium (Ca) in a carbonate. Finally, nitrile, powder-free gloves were used in all ICP-MS sample preparation procedures. All sample preparation was carried out under a laminar-flow hood to eliminate airborne contamination.

Standards were prepared using a 14-element 'multi-elemental' (Merck®) stock solution, of varying concentrations specific to each element (Table 3.1). These were prepared at 0, 0.01, 0.05, 1, 5, 10, 25, 50, 100 and 200 ppb concentrations. Sample solutions were diluted to fall within the calibrated ranges required for the elements analysed. Tuning parameters (Appendix 1) were adjusted to give maximum sensitivity for the major elements Ca, Mg, Fe, Mn, Al and Sr.

Table 3.1: Multi-elemental stock solution element concentration and composition (Merck, 2014).

	0 ppb	**0.01 ppb**	**0.05 ppb**	**1 ppb**	**5 ppb**	**10 ppb**	**25 ppb**	**50 ppb**	**100 ppb**	**200 ppb**
7 Li	x	x	x	x	x	x	x			
23 Na	x	x	x	x	x	x	x	x	x	x
25 Mg	x	x	x	x	x	x	x	x	x	x
27 Al	x	x	x	x	x	x	x			
39 K	x	x	x	x	x	x	x	x	x	x
48 Ca	x	x	x	x	x	x	x	x	x	x
55 Mn	x	x	x	x	x	x	x			
56 Fe	x	x	x	x	x	x	x			
63 Cu	x	x	x	x	x	x	x			
66 Zn	x	x	x	x	x	x	x			
88 Sr	x	x	x	x	x	x	x			
208 Pb	x	x	x	x	x	x	x			
238 U	x	x	x	x	x	x	x			

Carbonate samples (typically in the range of 150-300 µg) were transferred to ICP-MS vials and digested with ~2 mL of 2 % HNO_3 (SupraPure®) for a minimum of 12 hours or until the sample was fully dissolved into solution. A ~10 mg aliquot of this solution was diluted to a weight of 4 g, to produce sample dilution factors (DF) of approximately 4,000,000.

Data processing was performed using Microsoft Excel™ software to compute final concentrations and errors. Molar ratios were assigned to each sample based on molar concentration as percent of total concentration. It was assumed that all elements contributed to the substituted species on the carbonate ion (CO_3^{2-}). Thus, the major-element compositions of carbonate were determined based on percentage molar abundance.

3.4 Micromorphology and thin sections

Thin section preparation was required for cave carbonates (speleothems) from Riversleigh (Chapter 5) that were not readily identifiable in the field and in bulk hand specimens. Examples of specific depositional features and fossil material and their relationship to the host rock were selected to be studied in more detail. This was to provide a broad representation of various carbonate structures associated with cave systems, examples of bone fragments and other skeletal material as well as micro-depositional structures within the bulk limestone. A total of 32 cover-slipped, 30 µm thin sections were produced by standard methods at UOW.

Thin sections were analysed using a petrographic microscope with polarised light microscopy capabilities, as well as a point counter to log the abundance of carbonate microstructures. Seven primary characteristics were recorded using the point-count method (Leighton and Pendexter, 1962): matrix; spar; oolites; fossils; bone fragments; pellets and lithic fragments. These were then used in the overall composition determination and classification. Additionally this information was cross referenced with results of the XRD analysis results and trace-element data from ICP-MS analysis. Point counting was conducted at 400 counts per slide with a step interval of 8 µm and 100 steps per row. These counts were used to calculate the composition of the rock samples based on Folk's (1962) classification of carbonate textures (Figure 3.1).

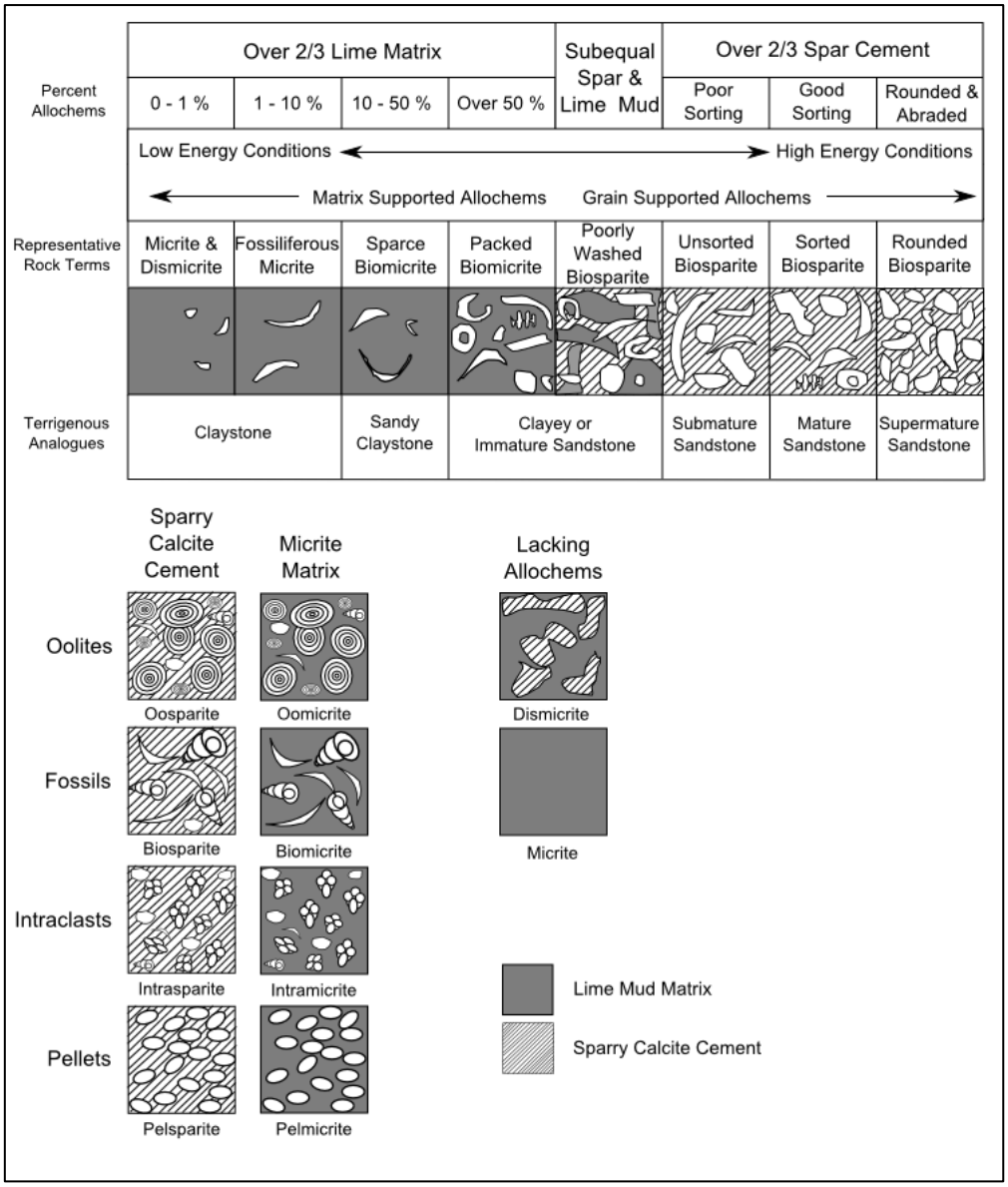

Figure 3.1: Carbonate rock classification, redrafted from Folk (1959, 1962), Dunham (1962) and Scholle & Ulmer-Scholle (2003).

The Folk (1962) carbonate classification system was used to classify the carbonate-containing rocks of the Riversleigh fossil area in Queensland, Australia, because it classifies the textures of the rock based on the control of the water energy in the depositional environment. Within the Folk classification system, the rock type is differentiated by the sparite to micrite grain ratio. In addition, the proportion of allochems within the rock is used to subdivide rocks with sparry calcite and microcrystalline matricies containing either intraclasts (lithic fragments), ooids, fossils or biota (molluscs, brachiopods, bone fragments) or peloid-dominated carbonate rocks.

3.5 Accelerator mass spectrometry ^{14}C dating

The ^{14}C ages for this study were prepared following standard ANSTO AMS radiocarbon methods (Hua et al., 2001, 2004; Fink et al., 2004). This consisted of physical cleaning and mild acid pre-treatment to remove any contaminants that may influence the isotopic signature of the sample. All samples destined for ^{14}C analysis in this study were carbonate samples such as fossil shell or crystalline calcium carbonate. These were hydrolysed to carbon dioxide gas using 10-20 mg of sample reacted with H_3PO_4 (85%, ~2 ml) in tap sealed side-arm vessels, using a modified method from McCrea (1950). These are reacted overnight at 60 °C and the evolved CO_2 gas is extracted using a vacuum extraction line and cryogenically frozen into a standard volume to determine CO_2 yield (Hua et al., 2001).

The extracted CO_2 sample then undergoes graphitisation for analysis by accelerator mass spectrometry (AMS). Graphite is prepared by the reduction of carbon dioxide with an excess of zinc and iron catalysts at 400 and 600 °C, respectively, in the presence of hydrogen. The reaction lasts 6-10 hours. Upon completion, the remaining graphite-iron mixture is pressed into an aluminium cathode for measurement.

Values for the AMS analyses are reported as $\delta^{13}C$ (‰ PDB) standardised to VPDB standard nomenclature, standard error is ± 0.1 ‰ (Fink et al., 2004). Percent modern carbon (pMC) as computed values from the mass spectrometry output data, with a standard error of ± 0.3-0.5 pMC at 100 µA measuring the $^{14}C^{4+}$ isotope. ^{14}C age (years BP), rounding, calculation norms and data reporting are based on Stuiver and Polach (1977), errors are given to 1σ (SD) in years. These measurements were made through AINSE (Australian Institute of Nuclear Science and Engineering) Analysis Grant 04/029.

3.6 Clumped-isotope sample gas preparation

In order to employ the clumped isotope method to determine carbonate formation temperatures, the solid phase carbonate is transformed into gaseous CO_2 for isotopic analysis. Historically this has been done using phosphoric acid (McCrea, 1950; Epstein et al., 1953). The evolved carbon dioxide gas is then purified using various cryogenic separation techniques in order to present the mass spectrometer with high purity carbon dioxide. These steps require attention to detail and meticulous analytical precision. This section outlines the specific gas preparation and analytical steps in this study, with emphasis on the modifications made in reference to previous instrumental equipment usage.

3.6.1 Phosphoric acid preparation

Reagent grade phosphoric acid 85 % (Merck Scientific) was heated for four to six hours on two to three consecutive days to ~100 ºC. The acid heating was conducted on a magnetic stirrer hotplate. The acid heating vessel was attached to a rotary vacuum pump (RV), using non-compressible plastic tubing and glass adapters. Water vapour, boiled out of the acid was captured in a LN_2 glass trap. Boiling of acid was replicated on consecutive days until a sufficient volume corresponding to ~15 % of the initial starting volume was extracted to produce phosphoric acid with a concentration >100 %.

This method was later replaced by preparing phosphoric acid using the method advocated by Coplen et al. (1983). Acid was prepared by dissolving 1000 g of P_2O_5 in 2150 g of 85 % H_3PO_4 in a large borosilicate beaker. After dissolution, 5 mg of chromic oxide (CrO_3) is added, the solution is then covered and heated at 200 °C for 7 hours. Post initial heating, 1.5 mL of hydrogen peroxide (H_2O_2) are added and the solution heated to 220 °C for a further 4.5 hours. The acid is cooled overnight and the density checked. If density was not sufficiently high, acid was reheated and small amounts of phosphorus pentoxide (P_2O_5) added. The prepared acid then requires 1 month of ageing before it can be used.

Concentration of the acid was determined in three ways. Difference in volume of the acid pre/post boiling was measured and the concentration calculated. Alternatively handheld density meter and/or acid-base titration against standardised sodium hydroxide (NaOH) solution, using a methyl

orange indicator was used to find the endpoint. Acid is then kept in a 60 °C oven and when not in use, in sealed borosilicate glass bottles.

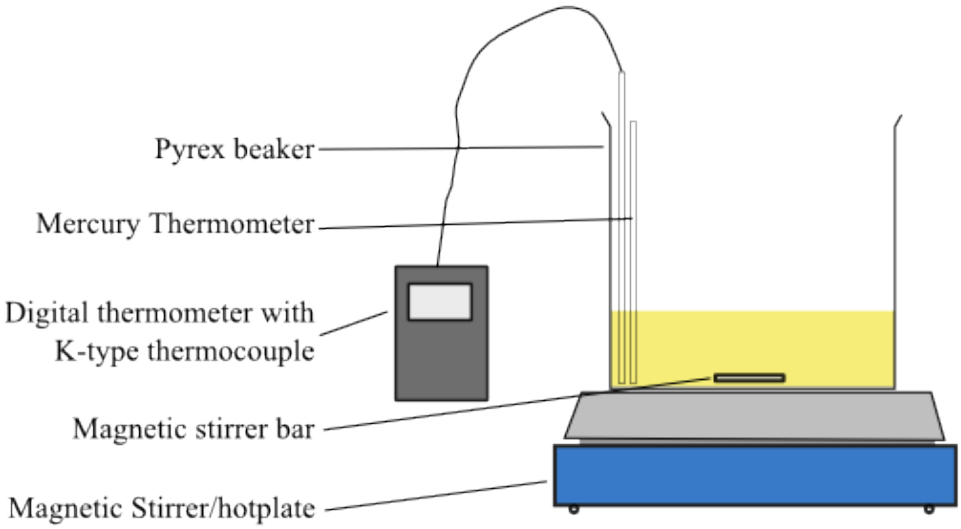

Figure 3.2: Phosphoric acid preparation equipment. Setup includes hot-plate with pyrex beaker, glass stirring rod and magnetic stirring spin bar. Temperature is monitored through mercury thermometer and K-type thermocouple with digital readout.

3.6.2 Sample digestion

In this study, closed reaction vessels were used (Ghosh et al., 2006a, 2010; Dennis and Schrag, 2010; Huntington et al., 2010). Glass side-arm reaction vessels were used with greased connections and keyed vacuum-pocket valve assemblies or 'stopcocks' (Figure 3.3). One of two sizes of reaction vessels were used, depending on the sample size of the carbonate material. Small 20 mm internal diameter (ID) vessels were used for pure (>95 %) carbonates. For samples with a lower carbonate content, a 40 mm ID vessel was used. This equates to an approximate eight fold volume increase of the vessel.

Bioapatite (bone) samples or tooth enamel require the larger gas expansion volume due to the longer reaction times required. The reactive nature of the process causing the movement of unreacted material onto the walls of the reaction vessel, also warrants the larger surface area of the reaction vessel. Additionally, for low carbonate content materials such as bone and teeth (~7% $CaCO_3$), up to 100 mg of sample material is required, compared to 10 mg for pure carbonates.

Figure 3.3: Carbonate reaction apparatus including glass stopcock valve assembly (left), lubricated with vacuum grease and glass side-arm reaction vessel (right); with acid reservoir and sample chamber (total length of 150mm), connected to the valve assembly with vacuum grease. The scale bar has a grid spacing of 1cm.

Weighed powdered sample material is carefully placed into the bottom of the reaction vessel using an aluminium weighing-boat and steel forceps. Phosphoric acid is then introduced into the side arm portion of the vessel using a disposable 5 mL polyethylene syringe and flexible polyethylene tube (10 cm). A volume of 2 mL of ~103% orthophosphoric acid (H_3PO_4) was used in all reactions to maintain constant sample:acid ratios (i.e. 2 mL H_3PO_4 to 10 mg $CaCO_3$).

The side-arm reaction vessel containing both the phosphoric acid and carbonate sample powder are then evacuated on the vacuum extraction line (Section 3.6.3) to $<10^{-3}$ mbar over 30 minutes to 2 hours. Reaction vessels are then closed using the glass stopcocks and removed from the vacuum line. Evacuated side-arm reaction vessels are placed into a water bath at 25 ± 0.1 °C for a minimum of 4 hours to equilibrate both the phosphoric acid and the sample powder to the required reaction temperature of 25 °C. The water bath is temperature controlled by a Julabo immersion heater, controlling water temperature to ± 0.1 °C whilst continuously circulating the water (Figure 3.4).

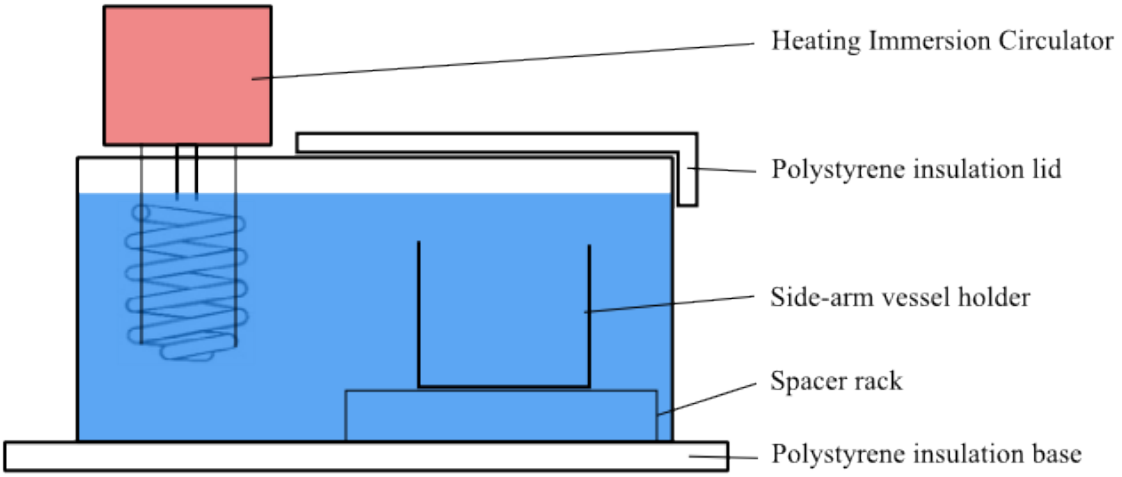

Figure 3.4: Schematic diagram of heating immersion circulator (Julabo®) in equilibration/reaction water bath, with reaction side-arm vessel holder and insulation lid and base, temperature control precision of ± 0.1 °C.

Once temperature equilibration is completed the side-arm reaction vessels are removed briefly from the water bath. Side-arm vessels are then tilted to combine the acid with the sample powder to start the reaction. Acid is poured over the sample slowly to minimise the vigour of the reaction and to ensure all the sample powder comes into contact with the phosphoric acid. The reaction is allowed to continue for a minimum of 12 to 16 hours for the reaction to come to completion. Samples are removed from the temperature bath immediately prior to gas extraction on the following day. Additionally, the laboratory room temperature is controlled to 21 ± 0.2 °C to reduce temperature contrast during sample movement and while the reacted sample is stored between analysis steps.

3.6.3 Vacuum system

A modified extraction method similar to the method described by Epstein (1953) and Ghosh et al. (2006a) was used. Some modifications were in response to laboratory equipment available and physical geometry constraints.

A rotary vane vacuum backing pump (Edwards – RV5 Pump) was used to provide crude evacuation of the extraction line system. This was coupled with an all glass molecular diffusion pump. High purity mercury ($Hg_{(l)}$) was used to drive the pump in favour of mineral oil diffusion pumps to limit potential hydrocarbon contamination. The mercury diffusion pump (HgDP) was heated using a cast aluminium block with cartridge heater at ~250 °C to vaporise the liquid mercury.

Cooling was provided by an aquarium water pump connected to the water jacket of the diffusion pump, to recondense mercury vapour and drive the molecular pumping system. The flow rate of the water pump was approximately 70 L/h allowing for sufficient cooling to provide maximum pumping potential for the vacuum system. Between the RV vacuum pump and the HgDP a dry-ice (carbon dioxide $CO_{2(s)}$) ethanol slurry trap was used to trap any water vapour evolved in the extraction line, preventing ingress of moisture into the vacuum pump. A liquid nitrogen (LN_2) trap in front of the HgDP acts as a secondary water vapour and other condensable gases trap. This trap was baked daily while isolated from the rest of the extraction line to reduce contamination (Figure 3.5).

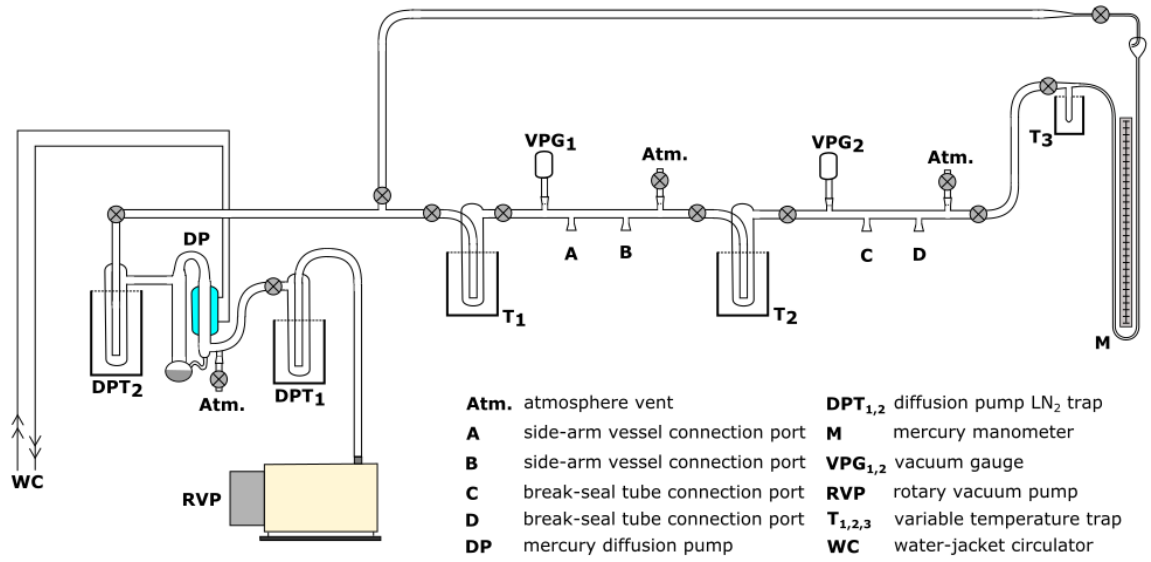

Figure 3.5: Glass gas-extraction vacuum line; schematic diagram. T_1, T_2 and T_3 are removable dewar flasks, the manometer uses a dual edged 100 cm ruler.

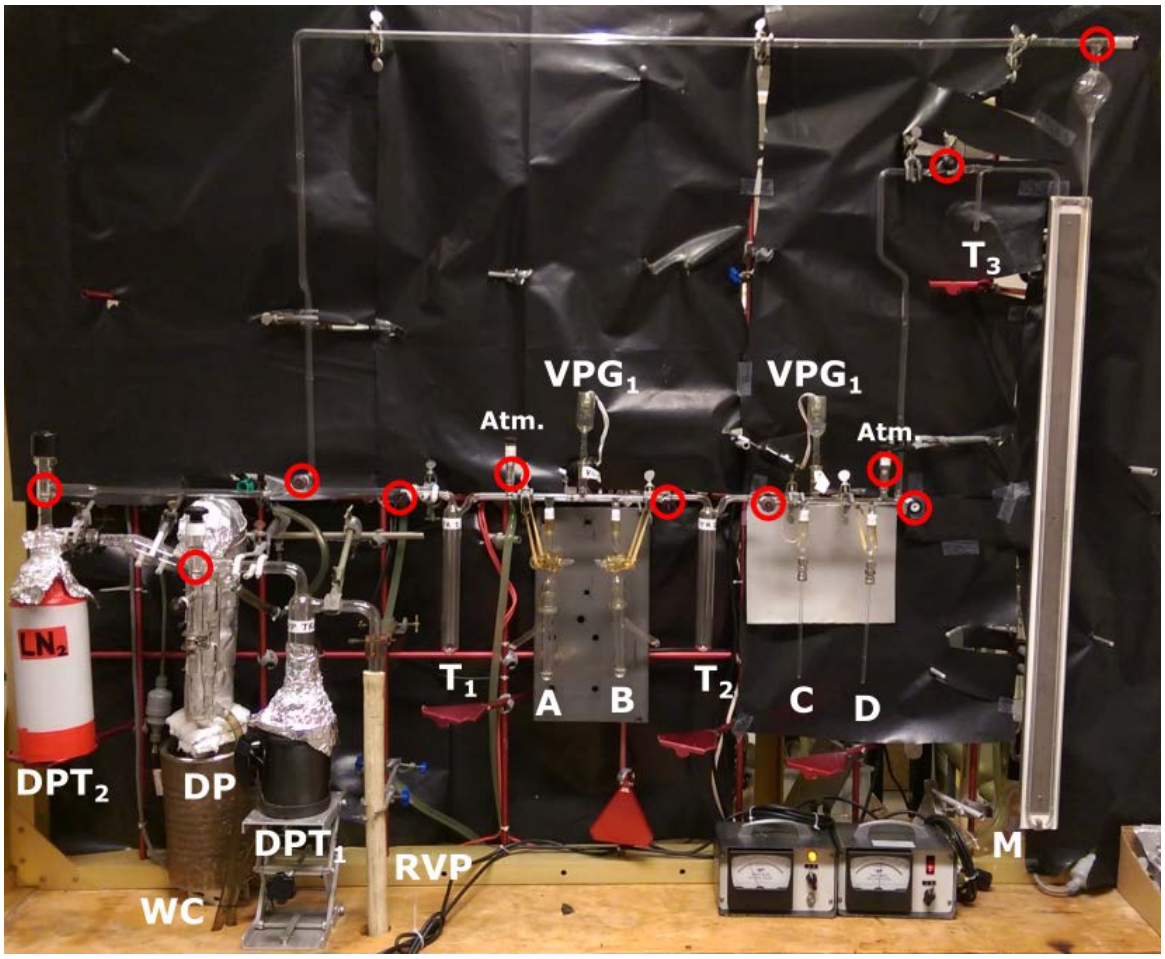

Figure 3.6: Glass gas-extraction vacuum line; photograph. A, B, side-arm vessel connection ports; C, D, break-seal tube connection ports; DP, mercury diffusion pump; T_1, T_2 and T_3 are removable dewar flasks, the manometer uses a dual edged 100 cm ruler.

3.6.4 Cryogenic trapping

Cryogenic mixtures are used to transfer condensable gases in the glass vacuum extraction line. The following mixtures were used in this study. Dry-ice ($CO_{2(s)}$) and ethanol (ethyl alcohol, 95 %) mixture at a 70/30 ratio, giving a temperature of -78 °C (Phillips and Hume, 1968). Dry ice was crushed from a larger block (made in the laboratory using a cylinder of liquid CO_2) and slowly mixed with ethanol in a stainless steel vacuum dewar. Liquid nitrogen (LN_2) and Isopropyl alcohol (2-pentanol, 95 %) mixture giving a temperature of -89 °C (Rondeau, 1965). Liquid nitrogen was slowly poured into the isopropyl alcohol while continuously stirring.

Both mixtures were effective at holding steady temperature. It was found, however, that dry-ice/ethanol mixtures hold their temperature for a longer time than liquid nitrogen/isopropyl alcohol slushes. Dry-ice/ethanol mixtures are also more practical for use as they are quicker to prepare and can be re-used on the extraction line pumping system. Therefore dry-ice/ethanol mixtures were preferentially utilised.

3.6.5 Gas extraction apparatus

Gas extractions were carried out utilising two large glass traps and one small sample cold finger in conjunction with four sample ports (Figure 3.5, A, B, C and D). These sample ports allowed connection of side-arm reaction vessels, gas capture vessels, break seals and gas sample tubes used for H_2O-CO_2 equilibrations and heated-gas sample preparation. Gas movement and vacuum condition was monitored throughout a sample gas extraction using two Hastings Vacuum DV-5 filament-type thermocouple gauges.

A mercury-filled manometer is used to measure the yield of carbon dioxide gas evolved from the acid reaction with the carbonate. Gas displaces the mercury in a thin capillary glass tube and the displacement is recorded to monitor the amount of gas evolved. The sample gas is then transferred into glass break seals (~200 mm length, 5 mm OD, 3 mm ID) prepared with a propane-air gas torch for normal borosilicate glass break seals and H_2O-CO_2 equilibration samples, or a propane-oxygen welding torch for sealing quartz break seals for heated-gas samples.

3.6.6 Gas yields

The gas yield, extracted from the carbonate-bearing sample is calculated at the point of sample extraction before the gas sample is taken to further gas chromatography purification and isotopic analysis. This is done by using a calibrated mercury-filled manometer and cold finger arrangement on the gas extraction line at a constant volume of expansion (McCrea, 1950). The shift in the manometer reading caused by the gas displacement of the sample when compared to the calibration curve can be used to ascertain a yield estimate of the reacted sample material. This can then be used to confirm the relative carbonate composition of the sample (Equation 3.3).

$$CaCO_3(mg) = \frac{[Manometer\ shift\ (mm\ Hg) - 5.1915]}{21.123}$$ **Equation 3.1**

3.6.7 Working gas

In order to make relaible measurements on the MAT 253, a homogeneous ultra-high purity carbon dioxide gas (BOC – Ultra High Purity Carbon Dioxide - UHP-CO_2) was used as a daily working gas to make the dual inlet sample-to-standard comparisons. A smaller reference gas volume of 150 cm^3 was used as an aliquot taker to introduce the working gas to the machine. The cylinder was evacuated and heated to drive off any accumulated moisture. The cylinder was then purged with gas twice and filled to approximately 1 atm (~14.7 psi or 1 bar). A single reference gas cylinder refill was originally postulated to last for many months during the analysis procedure. However, due to gradual depletion of the reference gas, the cylinder had to be refilled and cross referenced using other standard gases to insure the isotopic composition of the gas had not changed significantly. This was accomplished by periodically analysing three Oz-tech carbon dioxide cylinder gases of known isotopic composition to characterise the working gas.

3.6.8 Heated gas standards

This preparation technique was modified to suit the facilities at UOW from the method used at Caltech and Yale (Dennis et al., 2011; Passey et al., 2012). Heated CO_2 sample gases are prepared to have their isotopic composition randomly distributed among all possible CO_2 isotopologues. This implies that they have a Δ_{47} value of zero and have reached a stochastic distribution. These are prepared by using a variety of gas samples with a wide range of known $\delta^{13}C$ and $\delta^{18}O$ values that bracket the unknown samples that will be analysed to construct the absolute reference frame for the analyses conducted. In this study the heated reference gases were prepared from 4 different CO_2 gases. One in-house ultra high purity CO_2 (BOC- UHP-CO_2) and three Oztech CO_2 reference gases (OzT-1, OzT-2, OzT-3, Table 3.2).

Table 3.2: Oztech Reference gas values, reported in PDB and SMOW for carbon dioxide.

Gas Code	$\delta^{13}C$ (PDB)	$\delta^{18}O_{gas}$ (PDB)	$\delta^{18}O$ (SMOW)
UOW-1906C-A	-3.63	-15.78	25.04
UOW-1874C-A	-40.71	-29.65	10.59
UOW-1845C-A	-10.41	-9.84	31.22
WOLL-1996C-B	-3.64	-15.76	25.05
WOLL-1873C-B	-40.61	29.54	10.71
WOLL-1952C-B	-10.41	-9.89	31.17

Aliquots of gas were prepared using a glass gas pipette with O-ring valves (Figure 3.7) to transfer CO_2 equivalent to 200-300 µmol (~2-3x size of a normal sample). Gases were prepared in the same way as a normal carbonate sample, using the vacuum extraction line and cryogenic trapping as all other samples and standard material (Chapter 3.6). Gases were then flame sealed in quartz break-seals (1/4" OD x ~20 cm) and heated in a furnace at 1000 ºC for 2 hours. The break-seals were removed from the furnace while still at the equilibration temperature and allowed to cool to room temperature quickly. This was to prevent slow cooling and possible re-equilibration at an intermediate temperature while cooling. Break-seals were then stored at room temperature prior to analysis and/or further purification, if needed. Heated gas samples were stored for up to 6 months before analysis.

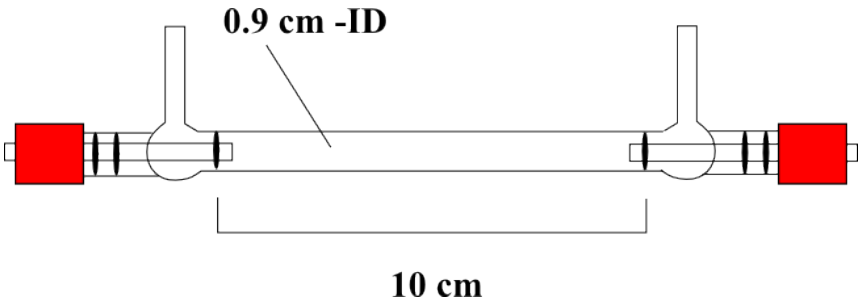

Figure 3.7: Sample gas pipette, showing O-ring valves and ¼ inch connecting tubes.

3.6.9 Temperature-controlled water equilibrations

In order to constrain the absolute reference frame for the Δ_{47} values and derived temperatures it is necessary to obtain CO_2 gases with equilibrium Δ_{47} values at various low temperature points that are within the possible range of values for the selected sample material (Dennis et al., 2011; Passey et al., 2012). These equilibrium gases can be obtained by isotope exchange between CO_2 and H_2O at various desired temperatures. These CO_2-H_2O equilibrations are typically performed at temperatures of 10 ºC, 25 ºC and 50 ºC (Dennis et al., 2010), but vary in different laboratories. This provides the basis of the Δ_{47} scale, in association with the heated gas reference frame as presented (Dennis et al., 2011; Passey et al., 2012).

Water equilibration is typically performed for conventional $\delta^{18}O$ measurements of natural waters whereby the $\delta^{18}O$ value of CO_2 is measured after isotopic exchange has occurred and equilibrium has been reached in a closed system. The equilibrium exchange reaction process is performed in the same manner in the 'clumped-isotope' method. However, the Δ_{47} value is not dependent on the $\delta^{18}O$ value. The Δ_{47} value is not sensitive to the isotopic composition of the water but is

sensitive to temperature fluctuations. However, it is necessary to utilise equilibration waters that have a range of $\delta^{18}O$ values in order to determine the non-linearity of the mass spectrometer. This should also be reflected by the relation of the CO_2-H_2O gases to the heated gas sample.

In this study, 5 different waters were used for the CO_2-H_2O equilibration. Three standard waters ANU A-1 ($\delta^{18}O$ = -31.75 ‰ VSMOW), ANU C-1 ($\delta^{18}O$ = -5.86 ‰ VSMOW), ANU P-1 ($\delta^{18}O$ = -4.53 ‰ VSMOW) were characterised by independent analysis on a PRISM Micromass-IRMS at UOW. In addition, the laboratory de-ionised Milli-Q water (Milli-Q) was used as well as water enriched by evaporating laboratory Milli-Q® water (50 % volume reduction over 4 hours).

CO_2-H_2O equilibration was performed in glass break seals (6.35mm 1/4" OD x ~20 cm) at the required temperature, in an insulated water bath (Glass tank; ~50 L capacity) with a temperature controller (Julabo Heating Circulator - ±0.1 ºC temperature control). Water samples were injected into the break seals using a micro pipette (100 µL). Water was then shaken to the bottom of the break seal. The water sample was then frozen inside the break seal with LN_2. The H_2O filled break seal was then attached to the vacuum extraction line where the air in the H_2O sample tube was pumped away, while the water was still frozen in LN_2. The break seal was then isolated using a stainless steel Ultra-Torr® tube connector with a ball valve while the CO_2 gas is introduced into the extraction line. A conventional ultra high purity CO_2 (BOC) cylinder gas was used as an equilibration gas, aliquots of gas were taken using a glass thimble with O-ring valves to transfer CO_2 equivalent to 200-300 µmol (~2-3 of a normal sample) into a U-trap to remove any non-condensable gases. Gas yield was then calculated using a mercury-filled manometer on the vacuum line. CO_2 gas was then passed over a dry-ice/ethanol slush trap before being transferred to the H_2O filled break seal by freezing it with LN_2.

Break seals were fully immersed into the water bath, to ensure all isotopic exchange occurs at the same temperature for the entire sample. Water bath temperatures of 10 ºC, 25 ºC, and 50 ºC (± 0.1 °C) were utilised for all CO_2-H_2O equilibrations. Break seals remained in the water bath for 1-3 days to allow for complete equilibration to occur.

The CO_2 is extracted in the same manner as a conventional carbonate sample (as described previously). As the samples are taken out of their respective temperature baths they must be quenched with LN_2, freezing the CO_2 and H_2O to ensure that the isotope exchange does not continue at an unwanted temperature. The break seal is scored with a glass knife and inserted into a stainless steel tube-cracker assembly. The CO_2 sample is extracted and processed using the same developed protocol as a carbonate sample, undergoing the same extraction, purification and analysis treatments. After extraction is completed and the CO_2 sample is dry and free of residual H_2O and other hydrocarbon/halocarbon, the sample can be stored at room temperature for several months prior to analysis.

3.7 Clumped-isotopes: sample gas purification

In this study, a combined system of a temperature controlled gas chromatograph (GC, Agilent® 7890A) was used with controlled gas flow to remove hydrocarbon and halocarbon impurities from the sample CO_2 gas. This was coupled with a flow controller (Deans Switch© Agilent). This allowed for the sample gas, once eluted from the column, to be diverted to either; a thermal conductivity detector (TCD) and metal U-trap for collection, or a flame ionisation detector (FID) to be categorised more accurately to indicate possible occurrences and composition of contaminants.

Figure 3.8: View of the modified Agilent® 7890A GC. (A) indicates the sample introduction loop and 4-way change-over valve, (B) indicates the thermal conductivity detector (TCD) with modified sample collection tubing carrying purified gas to a stainless-steel U-trap.

A customised stainless steel sample introduction loop and 4-way valve system was added to the stock Agilent® 7890A GC sample introduction system (Figure 3.8, A). In conjunction with this a customised stainless steel sample collection system was also constructed (Figure 3.8, B).

This setup was chosen to introduce the extracted carbon dioxide gas samples from the carbonate extraction line to the system with minimal chance of external atmospheric contamination. Additionally, the gas collection setup was also designed for maximum gas recovery with no introduction of external atmospheric contamination.

From previous work using packed porous silica columns, a similar process was used with a different column type and a more controllable gas flow and monitoring arrangement. An Agilent® HP-PLOT-Q GC column was used in the gas chromatograph to separate the sample gas as it was deemed to have the most suitable column phase type and properties. HP-PLOT columns are polystyrene-divinylbenzene compound based, which allow for separation of both polar and non-polar compounds from the CO_2 sample. These include various hydrocarbon and halocarbon compounds, as well as water, that may have been introduced into the sample. A column of 30 m length and 530 µm ID was chosen to optimise flow rate and extraction time while still providing adequate gas separation to divide the gas flow and isolation of the CO_2 from the potentially entrained contaminates. Helium carrier gas flow rate was set to 2 mL/min using the GC pressure control module (PCM). The column was mounted into the temperature-controlled GC oven and held at -20 °C for the duration of the carbon dioxide purification. The CO_2 signal was monitored by observing a non-destructive thermal conductivity detector (TCD) signal within the gas stream. Once the CO_2 signal returned to background signal levels the oven temperature was increased to 180 °C to move the contaminants through the column. Temperature ramping was performed manually by adjusting temperature control through the Agilent GC software. Simultaneously, the gas flow was switched to the flame ionisation detector (FID) to plot the elution times and peak strengths of any material left in the column. Typical purification run times were ~40 minutes for a standard calcium carbonate sample (~10 mg) or equivalent. Post-run procedures between samples consisted of a gradual heating over 10 minutes to preserve column life, and then holding at 150 °C for 40 minutes to drive off any remaining contaminants in the column. The gas flow was also increased to 5 mL/min to purge the inlet sample introduction system as well as the column of any residual gas.

Purified CO_2 gas was collected by cryogenic LN_2 trapping in stainless steel U-traps (Figure 3.9) with needle valves (TV1 and TV2) which were then transferred to the mass spectrometer for analysis or reconnected to the vacuum extraction line for resealing in glass break seals. Carbon dioxide samples purified by this method still contained some helium carrier gas from the purification process. This was later removed by utilising the vacuum pumping system on the MAT 253 mass spectrometer while the CO_2 sample was still frozen in liquid nitrogen.

Samples were also resealed in glass break seals on the extraction line if immediate sample gas purification was not possible. However, the residual helium carrier gas must be removed and

separated from the CO_2 gas in the stainless steel U-traps from the GC purification procedure, preferably immediately after purification.

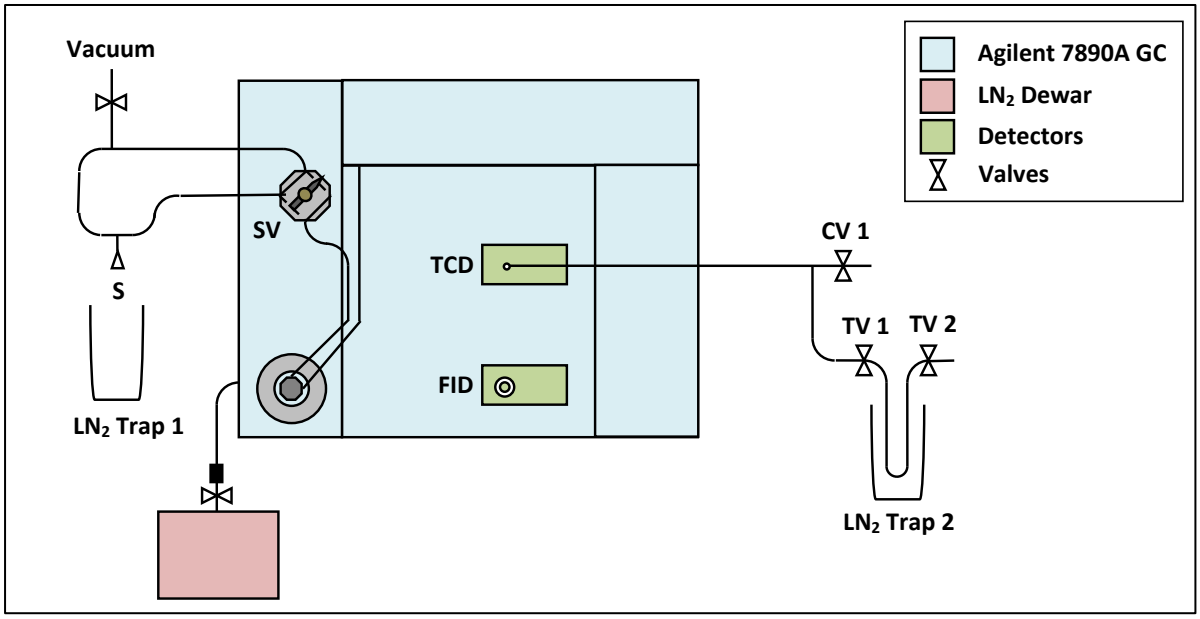

Figure 3.9: Schematic diagram of the gas chromatograph (GC) purification system, showing gas flow geometry from the sample introduction (S), through the sample valve (SV) diverting flow of the gas through the sample loop or directly into the GC, thermal conductivity detector (TCD) and flame ionisation detector (FID), changeover valve (CV) and U-trap and associated trap valves (TV1, TV2).

3.8 Clumped-isotopes: mass spectrometry

A Thermo Finnigan MAT 253 was utilised to make the mass spectrometric analysis of the evolved CO_2 gas. It has been set up using the following resistors on the Faraday cup voltage collectors (Table 3.3).

Table 3.3: MAT253 Faraday Cup resistor values and associated mass number.

Cup Number	Resistor (Ω)	Mass
1	$3x10^8$	
2	$3x10^8$	44
3	$3x10^{11}$	45
4	$1x10^{11}$	46
5	$1x10^{11}$	
6	$1x10^{12}$	47
7	$1x10^{12}$	48
8	$1x10^{12}$	49

The MAT 253 is equipped with a dual-inlet sample introduction system with customised external sample introduction plumbing to receive prepared gas samples both from the carbon dioxide extraction line and the preparative gas chromatograph setup (Figure 3.10). Note that the system is self-contained and is not directly connected to either the gas extraction line or the preparative GC. This is to allow the mass spectrometer to be housed completely separate to the both the gas extraction and the preparative GC. This has been done to minimise the temperature fluctuation within the room of the MAT 253 to reduce signal instability during an analysis run. The room containing the mass spectrometer is both temperature and humidity controlled to ± 0.1 ºC by a dedicated air-conditioning system. Both the air-conditioning system and the mass spectrometer have an uninterrupted power supply (UPS) connected to them with a 6 hour battery supply. Samples can also be analysed by the machine from a remote location to minimise the need to enter/exit the room, further disturbing the temperature equilibrium. The room is kept at a constant 22.0 ± 0.1 ºC and 50 % humidity. Furthermore, the surrounding corridors and rooms (in a basement) are at approximatly the same conditions, to better maintain stability.

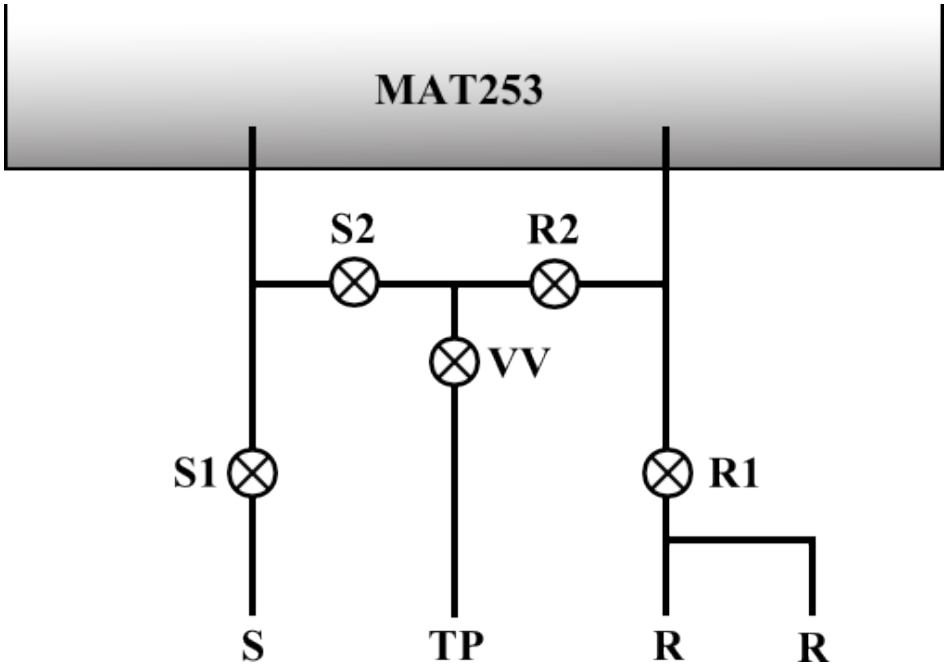

Figure 3.10: Schematic diagram of MAT 253 customised sample and reference gas introduction system. S; sample gas vessel/break-seal, R; reference gas vessel, S1; Sample valve 1, S2; Sample valve 2, R1; Reference valve 1, R2; Reference valve 2, VV; Vacuum Valve and TP; Turbo Pump (MAT 253).

Measurements on the MAT253 were made with an acceleration potential (HV) of approx. 9.5 kV with the "sulfur-window" closed. Each sample measurement consisted of 12 acquisitions of 10 cycles, each cycle comprises one set of 26 s integrations of reference gas and sample gas through the change-over valve. Between each individual acquisition an automatic bellows pressure balance was performed to yield 8 V on mass 44 on both the sample and reference gas bellows. A background measurement was performed before each acquisition set. Peak centring was performed manually on cup 2 at the beginning of a measurement set and was rechecked at the end of a measuring set. If the peak centre had changed substantially or was centring off-peak, the measurement set was discarded. Individual cycles had a duration of approximately 20 to 30 minutes. This equates to an approximate analysis time of 4 hours per sample. The capillary flow rate was adjusted to yield a 2 V signal on mass 44 at a bellows pressure of 20 mbar. Capillary balancing was checked weekly with a maximum capillary misbalance of 0.5% between sample and reference capillary flowrate. For detailed tuning parameters and IRMS specifications see Appendix 2.

3.8.1 Clumped-isotope measurements

The method for calculating the Δ_{47} value and the associated temperature anomaly from analysed CO_2 has evolved substantially since its introduction by Eiler and Schauble (2004). Detailed accounts of calculations are provided in the works of Huntington et al. (2009), Dennis et al (2011) and Zaarur et al. (2013) in the form of MATLab script and code files. Additional definitions of constants are provided by Brand et al. (2010). In this study these comprehensive calculations have been amalgamated into a refined set of calculation steps which was used to process all the clumped isotope data in this study. See Appendix 3 for a detailed account of the calculations, equations and constants used for the determination of the Δ_{47} anomaly.

The Dennis et al. (2011) method is used for transposing the raw Δ_{47} measurements into the absolute reference frame using the empirical transfer function method. This utilises heated gas (HG – 1000 °C) and equilibrated gases (EG) at 15, 25 and 50 °C as well as standard Oztech gases to calibrate the clumped isotope palaeothermometer. In addition, standard Carrara Marble (CM-1) and Sigma carbonate (AR) were used as reference standards during the analyses.

3.8.2 Empirical transfer function

In order to convert raw measurements of Δ_{47} of carbonates into a common, absolute reference frame we must construct an empirical transfer function to transpose raw Δ_{47} values into the Δ_{47abs} reference frame. Firstly, the expected abundances of isotopologues in a thermodynamically equilibrium carbon dioxide sample are calculated based on quantum mechanical statistical principles to spectroscopic data of carbon dioxide (Wang et al., 2004). This defines the reference frame and is a more robust reference frame than isotopic fractionation due to inherent problems with mixing diffusion and gravitational settling (Dennis et al., 2011). Secondly, a set of carbon dioxide gases must be prepared that differ in bulk isotopic composition but have been equilibrated at known temperatures. This is discussed in detail in Sections 3.6.8 and 3.6.9.

In this study, water-equilibrated or equilibrated gas (EG) samples and heated gas (HG) samples were prepared at 10, 25, 50° C and 1000 °C respectively. These are all plotted in reference to the mass spectrometer working gas (WG), common to all measurements. The linear trend produced by these gases by plotting the $\Delta_{47[EG\ vs\ WG]}$ value against the $\delta^{47}{}_{[EG\ vs\ WG]}$ value. This trend is used to define the non-linearity of the mass spectrometer being used, as shown in Figure 3.11. The resulting intercepts of these trend lines yields the difference between the equilibrated gases and the working gas also known as the $\Delta_{47[EG\ vs\ WG]0}$ at their respective temperatures (Table 3.5).

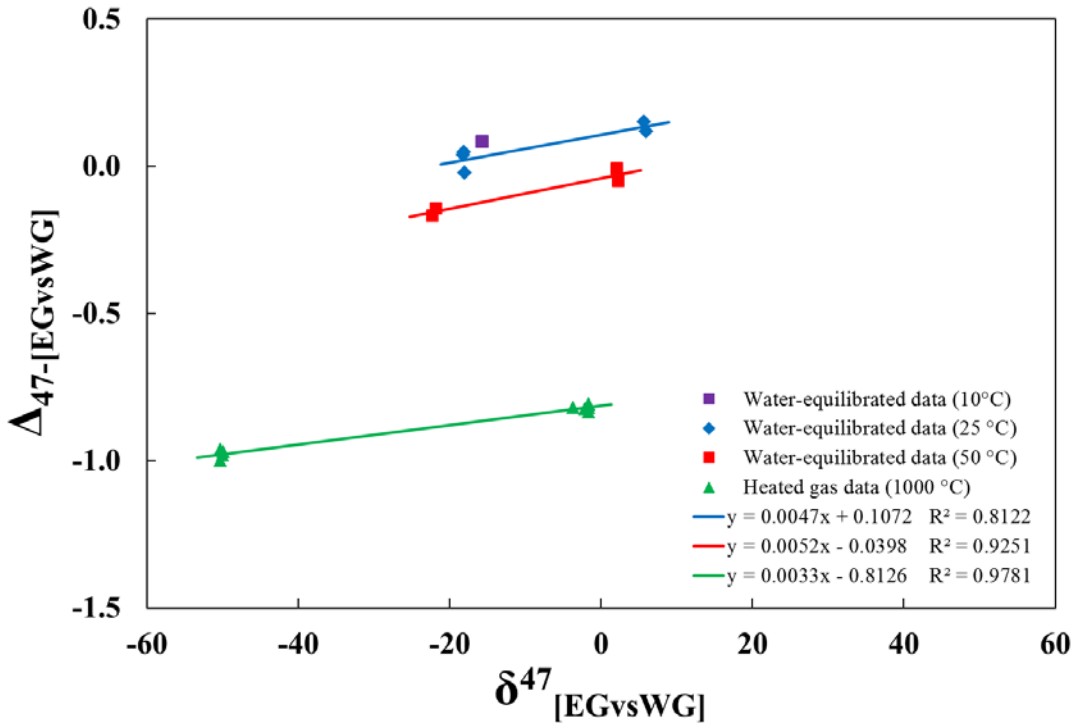

Figure 3.11: Water-equilibrated and heated gas regressions for each temperature condition. This plot represents the non-linearity correction for the University of Wollongong clumped isotope laboratory.

Values for the Δ_{47} from Wang et al. (2004) are characteristic at their respective theoretical equilibration temperatures and represent the absolute Δ_{47} value of a particular equilibration temperature (Table 3.4). These values are needed to convert the raw Δ_{47} value of the mass spectrometer into the absolute reference frame so that measurements can be compared to other analyses produced by other laboratories in a common reference system.

Table 3.4: Theoretical calculated values of equilibrium CO_2 clumping based on a fourth-order polynomial calculated from zero-point energies and normal mode wave numbers, modified from Wang et al. (2004).

Temperature (°C)	$\Delta_{47\text{-RF}}$ (‰)
0	1.0705
8	1.0208
10	1.0089
25	0.9252
27	0.9147
50	0.8050
1000	0.0266

Figure 3.11 shows data for equilibrated and heated gases produced at the University of Wollongong. Raw values of Δ_{47} and δ^{47} have been plotted against a common working gas for all samples (OzTech gas). Data for all temperatures have been assigned a common slope as non-linearity effects are expected to be equivalent at any given time and set of conditions at all Δ_{47} values, see Table 3.5. Minor variations in slope can be attributed to the physical limitation of the inability to analyse multiple samples simultaneously. Some error is also introduced through sample preparation and measurement precision limitations. Additionally equilibration temperatures that vary significantly from the extraction laboratory temperatures, namely 10 and 50 °C, have the potential for larger errors due to re-equilibration at an intermediate temperature (Dennis et al., 2011).

The measured equilibrated (EG) and heated gases (HG) results are then combined and used as an empirical transfer function (ETF) of;

$$\Delta_{47\text{-RF}} = 1.0006\ \Delta_{47[\text{EG vs WG}]0} + 0.8396 \qquad \textbf{Equation 3.2}$$

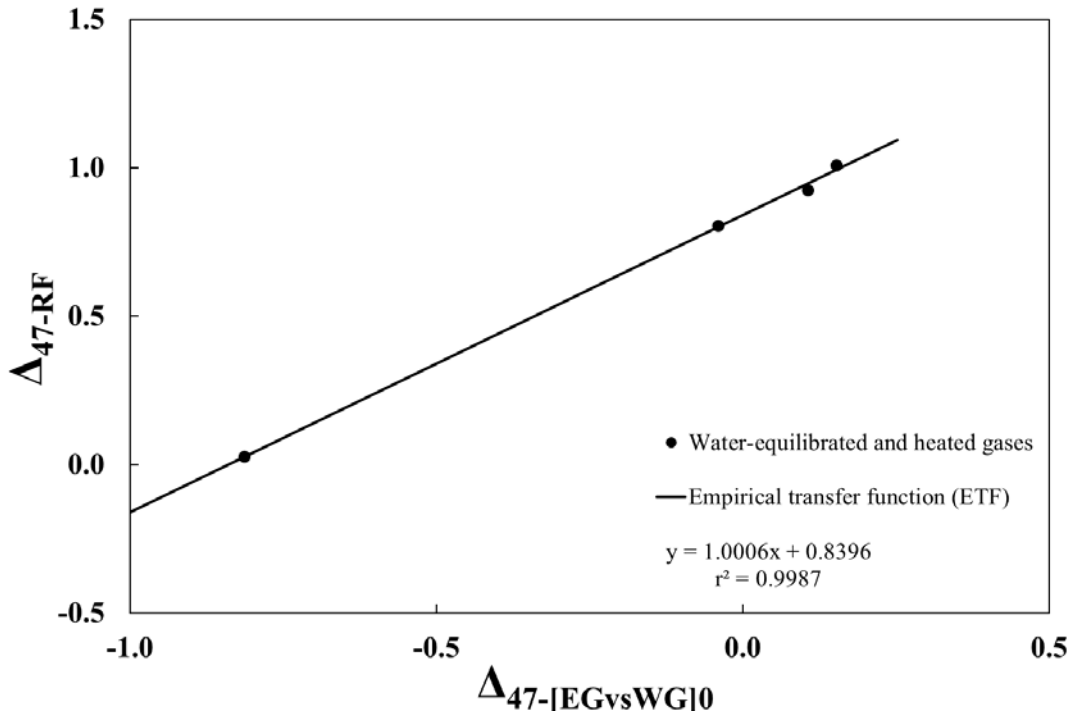

Figure 3.12: Intercepts of the $\Delta_{47[\text{EG vs WG}]0}$ values against the 'true' or theoretical value (Wang et al., 2004) an equilibrated CO_2 gas at a given temperature. This plot represents the empirical transfer function for the University of Wollongong clumped isotope laboratory.

Where the $\Delta_{47\text{-RF}}$ values of Wang et al. (2004) are plotted against the $\Delta_{47[\text{EG vs WG}]0}$ values of the EG and HG experiments to create an ETF with a slope and intercept incorporating all equilibrated temperatures.

This is very similar to the ETF produced by other clumped isotope laboratories using the same combination of water-equilibrated and heated gases. The above ETF (Equation 3.2) was used to correct all the sample data in this study, in order to report the Δ_{47} values and their calculated temperatures into the absolute reference frame (RF).

Calculated ETF's of the University of Wollongong, California Institute of Technology, Harvard University, Johns Hopkins University and Yale University range in slope between 1.0006 and 1.1548 and intercepts of between 0.8396 and 0.9539 utilising water-equilibrated temperatures of 0, 8, 10, 25 and 50 °C, and a heated gas equilibration temperature of 1000 °C. Empirical transfer functions vary between laboratories, this is due to instrument specific parameters such as; the ionisation source, the geometry of the gas inlet capillaries as well as their material (i.e. stainless-steel, fused silica, electro-polished nickel). Differences in inlet gas pressure can affect gas flow and cause variations in the Δ_{47} value. This can be minimised by keeping the bellows pressure constant for all gases analysed, as well as accurate capillary crimping to balance capillary flow rate between sample and reference gas. Additionally, minute differences in Faraday cup geometries have been postulated to be partly responsible for some of the non-linearity symptoms.

Empirical transfer functions of any clumped isotope laboratory will change over time as more replicates of equilibrated gas samples and heated gas samples are analysed and added to their respective temperature regression and changing the lope of the ETP accordingly. In some cases it may be more applicable to re-evaluate a EG and HG calibration and potentially restart the procedure if major instrumental component occurred such as; a source filament change, detector resistor change or venting of the flight tube changes or events have for vacuum system maintenance or similar actions.

Table 3.5: Water equilibrated (10, 25 and 50 °C) and heated gas (1000 °C) standard gases regression slopes and intercepts ($\Delta_{47[EGvsWG]\,0}$) used in generating the empirical transfer function in Table 3.6.

Temperature (°C)	$\Delta_{47[EG\ vs\ WG]}$ (‰)	$\delta^{47}{}_{RF[EG\ vs\ WG]}$ (‰)	Slope	Intercept ($\Delta_{47[EG\ vs\ WG]0}$)	r^2	Combined slope[a]
10[b]	0.0832	-15.6921	0.0044	0.1527		0.0044
25	0.0388	-18.2054	0.0047	0.1072	0.8121	
	0.0474	-18.1065				
	-0.0227	-17.9909				
	0.1187	5.9721				
	0.1512	5.6430				
50	-0.0061	2.1120	0.0052	-0.0399	0.9251	
	-0.0508	2.2251				
	-0.1423	-21.8485				
	-0.1684	-22.2970				
1000	-0.8089	-1.6538	0.0033	-0.8126	0.9781	
	-0.9695	-49.9271				
	-1.0004	-50.2613				
	-0.9814	-49.9560				
	-0.8189	-1.6538				
	-0.8207	-3.6543				
	-0.8081	-1.6334				
	-0.9621	-50.3295				
	-0.8357	-1.6705				
	-0.8239	-2.1284				

[a] Slope defining the non-linearity of the mass spectrometer, incorporating data from all four temperatures (10, 25, 50 and 1000 °C).

[b] Only one measurement at 10 °C was measured, therefore the slope of the equilibrated gas has been calculated using the combined slope of the remaining temperatures (25, 50 and 1000 °C)

Table 3.6: Equilibrated and heated gas calibration standards as used to generate the empirical transfer function of five different MAT253 instruments at the University of Wollongong, California Institute of Technology, Harvard University, Johns Hopkins University and Yale University, modified from Dennis et al. (2011).

Laboratory	Temperature (°C)	Intercept ($\Delta_{47[EGvsWG]0)}$ (‰)[a]	n[b]	Combined Slope[c]	r^2	Empirical transfer function	r^2
University of	10	0.1527	1	0.0044		$\Delta_{47\text{-RF}} = 1.0006\ \Delta_{47[EG\ vs\ WG]0} + 0.8396$	0.9987
Wollongong	25	0.1072	5		0.8121		
	50	-0.0398	4		0.9251		
	1000	-0.8126	10		0.9781		
California Institute	8	0.0788	6	0.0065	0.9859	$\Delta_{47\text{-RF}} = 1.1548\ \Delta_{47[EG\ vs\ WG]0} + 0.9343$	0.9986
of Technology	25	-0.0271	5		0.9417		
	50	-0.0957	7		0.9133		
	1000	-0.7869	9		0.9386		
Harvard University	10	0.0480	6	0.0091	0.9916	$\Delta_{47\text{-RF}} = 1.0105\ \Delta_{47[EG\ vs\ WG]0} + 0.9539$	0.9999
	25	-0.0216	9		0.9367		
	50	-0.1473	9		0.9375		
	1000	-0.9182	32		0.9167		
Johns Hopkins	0	0.1412	2	0.0059		$\Delta_{47\text{-RF}} = 1.0303\ \Delta_{47[EG\ vs\ WG]0} + 0.9194$	0.9997
University	27	-0.0077	6		0.8316		
	50	-0.1002	2				
	1000	-0.8686	4		0.9988		
Yale University	10	0.0812	4	0.0055	0.8086	$\Delta_{47\text{-RF}} = 1.0630\ \Delta_{47[EG\ vs\ WG]0} + 0.9227$	0.9999
	25	0.0013	3		0.8886		
	50	-0.1094	6		0.4155		
	1000	-0.8431	12		0.9206		

[a] Intercepts of the water-equilibrated and heated-gas line regressions at 0, 8, 10, 25, 27, 50 and 1000 °C respectively.
[b] Number of samples used in the equilibrated or heated-gas regressions.
c Combined slope to define non-linearity using equilibrated and heated gases from all temperatures.

3.8.3 Palaeotemperature determination

Temperature determination for the Δ_{47}-*T* calibration has been accomplished by using a combination of biogenic carbonate and synthetic carbonate precipitation experiments. Both of these data sets have been projected into the Ghosh et al. (2006a) and the Zaarur et al. (2013) reference frames. All standards and samples in this study have been analysed and calibrated to the absolute reference frame. The Dennis et al. (2011) calibration (Table 3.7) is based on a calibration range between 1 and 50 °C and uses only the synthetically precipitated carbonates of the Ghosh et al. (2006a) and Dennis et al. (2011) data.

Table 3.7: Δ_{47}-*T* calibration equations based on the original Ghosh et al. (2006a) synthetic calcite calibration.

Calibration Type	Equation
Original published calibration Ghosh et al. (2006a), in the Ghosh et al. reference frame.	$\Delta_{47} = 0.0592 * 10^6 * T^{-2} - 0.02$
Re-calculated synthetic calibration Dennis et al. (2011), in the absolute reference frame.	$\Delta_{47} = (0.0636 \pm 0.0049) * 10^6 * T^{-2} - (0.0047 \pm 0.0520)$

It has been established that biogenic carbonates generally agree with the synthetically precipitated carbonate calibration (Zaarur et al., 2013). Therefore they can be incorporated into the same calibration. It has been shown that these biogenic carbonates, with the exception of shallow-water corals (Saenger et al., 2012) show similar statistical variability and their incorporation would not significantly change the equilibration equation. However calibration uncertainty would be reduced with their combination providing the resulting calibration equations (Table 3.8).

The original calibration is in agreement to the revised calibration and to within 1 °C (between Δ_{47} values of 0.59 and 0.65 ‰). This is equivalent to temperatures between 25 and 39 °C. The difference between the two calibrations becomes more significant at high and low temperatures. Temperatures of materials growing at or below 16 °C experience an offset of >2 °C, equivalent to a Δ_{47} value of 0.68 ‰. The new revised calibration reduces this offset and allows for a wider range of Δ_{47} to be utilised.

Table 3.8: Δ_{47}-T calibration equations based on the updated combined synthetic calcite and biogenic carbonate calibration.

Calibration Type	Equation
Published combined synthetic calibration Ghosh et al. (2006a); Zaarur et al. (2011), in the Ghosh et al. reference frame.	$\Delta_{47(\text{Ghosh et al.})} = (0.0526 \pm 0.0025) * 10^6 * T^{-2} + (0.0520 \pm 0.0284)$
Published combined biogenic and synthetic calibrations, Ghosh et al. (2006a); Dennis et al. (2011); Zaarur et al. (2013), in the Ghosh et al. reference frame.	$\Delta_{47(\text{Ghosh et al.})} = (0.0539 \pm 0.0013) * 10^6 * T^{-2} - (0.0388 \pm 0.0155)$
Re-calculated combined biogenic and combined synthetic calibration of Zaarur et al. (2013), in the absolute reference frame.	$\Delta_{47(\text{abs})} = (0.0555 \pm 0.0027) * 10^6 * T^{-2} - (0.0780 \pm 0.0298)$

More recently, an additional synthetic calibration of high-temperature carbonates between 25-250 °C has been constructed by Kluge et al. (2015). This calibration provides a universal Δ_{47}-*T* calibration for phosphoric acid-digestions performed at >70 °C (Equation 3.3).

$$\Delta_{47(\text{abs})} = (0.98 \pm 0.01) * \left(\frac{-3.407*10^9}{T^4} + \frac{2.365*10^7}{T^3} - \frac{2.067*10^3}{T^2} - \frac{5.880*10^9}{T^4} \right) + (0.293 \pm 0.004)$$

Equation 3.3

However, this calibration does not take into account a combination of biogenic and synthetic calibrations and thus may not be a suitable calibration when used to interpolate clumped isotope palaeotemperatures of biogenic precipitated calcites. Additionally, the Kluge et al. (2015) calibration utilises a much greater calibration temperature range (25-250 °C), well outside the estimated formation temperatures of carbonates in this study (2-29 °C), potentially reducing the low-temperature sensitivity required for the majority of samples in this study. Furthermore, the Kluge et al. (2015) method uses a new acid-digestion method at 90 °C, intrinsically different to the common acid bath of previous calibrations.

An additional empirical calibration of the clumped isotope palaeothermometer using biogenically precipitated carbonate between 9 and 38 °C was constructed by Wacker et al. (2014) (Equation 3.4), providing suitable low-temperature sensitivity of the calibration. However, reactions are performed using a common acid bath at 90 °C.

$$\Delta_{47(\text{Ghosh et al.})} = (0.0327 \pm 0.0026) * 10^6 * T^{-2} + (0.3030 \pm 0.0308) \qquad \textbf{Equation 3.4}$$

In comparison, the Zaarur et al. (2013) calibration uses a combination of both biogenic and synthetic precipitated carbonate precipitated between 5 to 65 °C, as well as a similar acid-digestion temperature (25 °C) and purification technique to those used in this study.

Therefore, in this study we report our temperatures based on calibrated Δ_{47} values in the absolute reference frame (Dennis et al., 2011) using the re-calculated combined calibration of Zaarur et al. (2013), due to the greater temperature range used, compared to other calibrations, as well as the similarities in the sample acid-digestion, gas extraction and purification procedures used in this study. Additionally, the temperature range of Zaarur et al. (2013) fully encompasses the potential range of sample formation temperatures likely to be encountered in this study.

3.8.4 Internal carbonate reference standards

Throughout the analysis period, April 2014 to October 2014, standard carbonate samples were analysed to monitor mass spectrometer performance and as an intercomparrison between other laboratories that had also analysed the standard material. Two calcium carbonate standards were used, Carrara Marble (CM-1) and an in-house analytical grade $CaCO_3$ (AR). Reproducibility of carbonate CO_2 analysis was found to be 0.02, 0.05 and 0.009 ‰ (1σ) for $\delta^{13}C$, $\delta^{18}O$ and Δ_{47} respectively, for Carrara Marble (CM-1). The Carrara Marble standard produced Δ_{47} values of 0.434 ‰ (SE 0.005) corresponding to a temperature of 121.7 ± 2.7 °C. This compares well to results of other clumped-isotope laboratories such as Harvard University and the California Institute of Technology (Table 3.9)

Table 3.9 Carrara Marble standards in the absolute reference frame. With temperature calculated using the synthetic calibration of Ghosh et al. (2006) projected into the absolute reference frame by Dennis et al. (2011).

Laboratory	*n*	$\Delta_{47\text{-[SG vs WG]}}$	Δ_{47} (‰)	SE	Temperature (°C)
University of Wollongong	6	-0.402	0.434	0.005	121.7
California Institute of Technology	18	-0.402	0.392	0.007	127.1
Harvard University	40	-0.643	0.385	0.005	130.6
Johns Hopkins University	8	-0.581	0.403	0.006	121.8
Yale University	49	-0.445	0.400	0.004	123.3

Chapter 4: Cold-water carbonates

4.1 Introduction 86
4.2 Background 87
4.2.1 Natural ikaite formation 88
4.2.2 Geographic occurrence of ikaite and glendonite 90
4.2.3 Synthetic ikaite precipitation 93
4.2.4 Morphology of ikaite and its pseudomorphs 94
4.2.5 Stable isotopes of glendonites 96
4.3 Methods 97
4.3.1 Glendonite sample powder preparation 97
4.3.2 Polished block 98
4.4 Results 99
4.4.1 Sample material and site descriptions 99
4.4.2 Glendonite morphology and mineralogy 105
4.4.3 Growth zoning in glendonite 106
4.4.4 Glendonite trace-element composition 108
4.4.5 Glendonite mineralogy 109
4.4.6 Stable isotope results 110
4.5 Discussion 116
4.5.1 Sydney Basin 116
4.5.1 Tasman Basin 118
4.5.2 Kola Peninsula 119
4.5.3 Taymyr Peninsula 120
4.5.4 North American thinolite (Type A) pseudomorphs 120
4.5.5 Relationship of calcite to water of hydration and ambient pore water 121
4.6 Conclusions 123

4.1 Introduction

Glendonites are unique calcite ($CaCO_3$) structures that form as pseudomorphs after the metastable mineral ikaite, also known as calcium carbonate hexahydrate ($CaCO_3 \cdot 6H_2O$). A glendonite is not a primary mineral but a secondary substitution structure of the ikaite mineral. Ikaite forms by the precipitation of hydrated calcium carbonate at low to near-freezing temperatures (-1.9 to 7 °C) in highly alkaline (pH >10), organic carbon-rich and orthophosphate (PO_4^-)-rich waters. Glendonites form within the water column, at the sediment-water interface or within soft unconsolidated sediment. In this state the mineral ikaite is considered to be "metastable". If the temperature of the water is raised above ~7 °C the crystal lattice structure of the mineral is no longer stable and rapidly alters and recrystallises to an unhydrated form of carbonate, such as calcite, aragonite or vaterite crystal aggregates. During this process ikaite also loses its characteristic bipyramidal morphology. However, if the temperature conditions remain sufficiently low and stable while the formed ikaite crystal structure is buried within the surrounding sediment during dehydration, a glendonite pseudomorph may form from the ikaite mineral.

As ikaite is formed under a restricted range of chemical and physical conditions, with the formation of glendonite being the common outcome, the presence of glendonites has been used as a palaeoclimatic indicator of oceanic or estuarine temperatures (Pauly, 1963; Suess et al., 1982; Marland, 1975; Bischoff et al., 1993; De Lurio and Frakes, 1999; Selleck et al., 2007). The aim of this thesis study is to further characterise the transformation conditions of ikaite into its pseudomorph as glendonite. Specifically, the aim is to pinpoint the formation temperature of the glendonite calcium carbonate structure through the use of clumped-isotope palaeothermometry. For example, are the original cold temperature isotopes preserved in glendonite calcite or are the derived clumped-isotope temperatures indicative of later higher temperature diagenesis?

Ikaite itself is unstable at room temperatures and quickly dehydrates. It is not readily amenable to clumped-isotope analysis, as the water of crystallisation would be lost in a vacuum system and/or undergo oxygen-isotope exchange with evolved CO_2 during the phosphoric acid reaction. However, ancient samples of glendonite are available and are well documented in the geological record in many countries, in a variety of different geological settings and in highly diverse depositional environments. Australia provides a unique opportunity to study glendonites due to their common occurrence in Permian sedimentary sequences on the east coast of the continent, such as the Sydney and Tasman Basins. Additional samples are available from around the world and provide to a broad range of ambient conditions, environmental settings, ages and burial histories.

4.2 Background

Cold-water carbonates are associated with Permian to recent glacial marine sedimentary deposits and the presence of glendonites has been used as an important indicator for the presence and distribution of polar water conditions (Suess et al., 1982).

The water-saturated calcium carbonate precipitation system is controlled by both pressure and temperature. Accordingly, this may be an indicator of burial and formation. Marland (1975) used synthetically precipitated calcium carbonate hexahydrate to investigate the formation conditions of ikaite and the conditions at which the mineral dehydrates to aragonite and calcite (Figure 4.1). The indicated region of 'favourable' conditions for ikaite formation coincides well with the reported conditions of natural ikaite occurrence (De Lurio and Frakes, 1999).

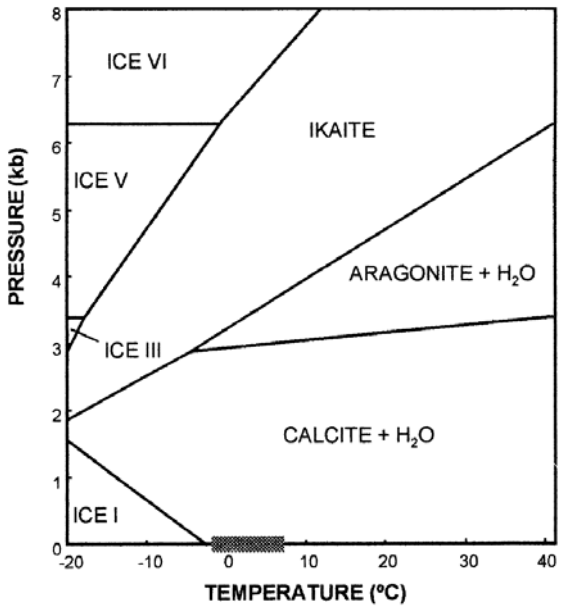

Figure 4.1: Pressure-temperature phase relations in the freshwater-saturated calcium carbonate system. Naturally observed ikaite occurs between -1.9 and 7 °C (shaded). In order for ikaite precipitation to occur, both high alkalinity conditions to achieve super saturation and elevated phosphate levels must be present to reduce calcite/aragonite precipitation. Modified from Marland (1975) by Bischoff et al. (1993a) and De Lurio and Frakes (1999).

During ikaite dehydration the mineral may lose up to two thirds of its total volume, assuming no carbonate or calcium is lost or added to the system and the mineral does not

self-degrade. This creates a highly porous calcium carbonate lattice structure. This is expressed in Equation 4.1 (Huggett et al., 2005).

ikaite ⇔ aragonite or calcite + water

$CaCO_3 \cdot 6H_2O \Rightarrow CaCO_3 + 6\ H_2O$

100 volumes ⇒ 32.3 volumes + 94.5 volumes

Equation 4.1 - Adapted from Huggett et al., (2005)

It should be noted that ikaite does not exclusively transform into calcite or aragonite ($CaCO_3$) but may also form other minerals such as vaterite (μ-$CaCO_3$), as found by synthetic precipitation experiments (Marland, 1975; Shaikh and Shearman, 1986; Bischoff et al., 1993). Other minor substitutions by magnesium, iron, strontium and manganese for calcium have also been noted; however, the concentrations of these elements are quite minor in comparison to the dominant calcite or aragonite mineral phase in natural samples (Huggett et al., 2005).

4.2.1 Natural ikaite formation

The ikaite mineral structure was first described as a precursor for the mineral gaylussite (Freiesleben, 1827). The term 'glendonite' was first introduced by David et al. (1905) and later further characterised by the discovery of the connection between ikaite and glendonite after the finding of marine ikaite minerals in the cold waters of the southwest Greenland fjord region of Ika (now Ikka), at Ivigtut (Pauly, 1963; Suess et al., 1982). However, ikaite was previously known as a synthetic compound, although unnamed, in laboratory experiments (Pelouze, 1865), created at near freezing temperatures from calcium carbonate bearing waters as a metastable compound. Other occurrences of 'unusual calcite pseudomorphs' were noted in mid Cenozoic mudstones in the Pacific North-West of the USA (Boggs, 1972). At the time, there was much speculation in regard to the composition of the precursor material for glendonites, including calcite and aragonite ($CaCO_3$), gypsum ($CaSO_4 \cdot 2H_2O$) and glauberite ($NaSO_4 \cdot CaSO_4$).

Ikaite formation typically occurs near the water-sediment interface in marine settings in sediments with a high degree of alkalinity. This is mainly due to the tendency of these environments to have very high organic matter contents and reduced oxygen concentrations, thereby creating anoxic conditions. Ikaite growth is also usually related to a high content of fine-grained inorganic constituents in the sediment; thus ikaite is commonly associated with dark mudstones and shales, again an indication of reduced conditions in the sediment with low oxygen levels (De Lurio and Frakes, 1999). The presence of sufficiently high concentration of orthophosphate (>3.0 ppm P_2O_5 and 2.0 ppm PO_4^-, respectively) in the water acts as an inhibitor of calcite and aragonite growth (below 21 °C) but does not affect the precipitation rate of ikaite (Brooks et al., 1950). This facilitates the formation of ikaite in favour of calcite and aragonite. In addition, Burton and Walters (1989) noted the significance of pH in the phosphate inhibition of calcite and aragonite precipitation rates in seawater, supporting the work of Brooks et al. (1950).

Recently, two biochemical processes have been described for the formation of marine, sedimentary ikaite and allow a classification of ikaite formation as either organotrophic or methanotrophic sulfate reduction (Teichert and Luppold, 2013). Organotrophic conditions are the most common ikaite forming conditions globally, with methanotrophic ikaite formation only being documented in two instances (Schubert et al., 1997; Kodina et al., 2001, 2003) and once for glendonites (Greinert and Derkachev, 2004). However the exact geochemical and ambient conditions required for ikaite formation, and likewise for glendonites, are not fully understood. There is still debate whether the defining formation parameter of ikaite is solely temperature dependence or if additional specific chemical and biogenic conditions are necessary.

Ikaite occurrence in sea ice has only been discovered recently and little is known about the physico-chemical processes involved in ikaite precipitation in sub-zero temperatures. Laboratory precipitation experiments have shown that ikaite is produced under varying conditions of salinity, pH, temperature and phosphate concentrations. This showed that pH and salinity are the controlling factors of ikaite formation in sea ice. Additionally, phosphate (PO_4^-) was shown not to be crucial in the formation as previously postulated (Hu et al., 2014). This is further confirmed by experiments of ikaite precipitation and dissolution in seawater-derived brines. Results indicate that the saturation state as well as the salinity and temperature of the brine control the precipitation kinetics of the ikaite mineral (Papadimitriou et al., 2014).

4.2.2 Geographic occurrence of ikaite and glendonite

Ikaite commonly occurs in high latitude marine environments where it grows at near-freezing temperatures in association with organic carbon-rich sediments (Pauly, 1963, Suess et al., 1982). The glendonite pseudomorph commonly forms the distinct prismatic 'star' shaped glendonite structures (Figure 4.3). Continental ikaite occurrences are also possible in high-latitude, seasonally cold, lacustrine and other terrestrial water bodies, where the mineral is deposited by direct precipitation of a Ca-rich water source into a highly alkaline organic-rich body of water. Non-marine ikaite formation does not require the near-freezing conditions of marine ikaite due to the high alkalinity. However these conditions form more massive mineral aggregates than their marine counterparts.

Ikaite in Ikka Fjord (Pauly 1963) occurs in near-freezing (3 to 7 °C) temperatures on the sea floor. Column shaped deposits of the mineral were found from 0.5 m to 20 m below the sea surface and some formations were up to 10 m across. This material was initially termed "calcium-hexahydrate" and was theorised to be a carbonate compound.

Subsequently natural modern samples of ikaite were found in Bransfield Strait, Antarctic Peninsula (Suess et al., 1982). Here, samples of large euhedral crystals were found at depths of 1950 m below sea level at near-freezing bottom water temperatures at the sediment-water interface. Initial samples were collected at 205 and 714 cm in a 1200 cm sediment core. Samples of the ikaite mineral upon extraction were amber and translucent in colour. Within hours the colour and consistency of the mineral changed with increasing temperature. The resulting disintegrated mineral changed into a sludge containing white calcite crystals. This showed the meta-stability of ikaite and the dehydration of the calcium carbonate hexahydrate mineral to calcium carbonate with increasing temperature.

That ikaite grows displacively at the water-sediment interface in marine environments was shown by the work of by Kaplan (1979) and Schmitz (1999). Thus the presence of glendonite pseudomorphs after ikaite has been used as a diagnostic tool for marine cold-bottom waters at ancient high latitude marine sites around the world. This was further confirmed by Selleck et al. (2007) using glendonites from both the Permian-Triassic marine sediments in the Sydney Basin and Late Neogene estuarine and lacustrine samples from Kola Peninsula, Oregon and Nevada. Their analyses showed that while Holocene glendonites may provide a reliable isotopic signature reflecting palaeoenvironmental conditions, the older diagenetically altered material has been subjected to secondary calcite substitution and thus produces a less clear isotopic signal.

Bischoff et al. (1993) found natural samples of ikaite along the southern shoreline of Lake Mono, California, USA. Low temperature shoreline springs mix in small amounts with lake waters

associated with organic-rich sediments and relatively high orthophosphate-ion contents. This allows the formation of ikaite and its later conversion to the pseudomorph glendonite as the precipitation environment conditions change and dehydration of the mineral occurs. In this continental formation the resulting glendonite pseudomorphs are termed thinolites. These are typically found as tufa or skerry mounds and are common in the Early Quaternary material (Shearman and Smith, 1985; Shearman, 1998). The Mono Lake thinolite is also similar to thinolite from Pyramid Lake, Nevada (Whiticar and Suess, 1998).

Glendonites in the Eromanga Basin, South Australia, provide additional evidence of seasonal freezing temperatures in the higher latitudes during the Early Cretaceous (Frakes and Francis, 1988, 1993; Frakes et al., 1995; De Lurio and Frakes, 1999). This finding further supports the applicability of the presence of ikaite and its glendonite pseudomorph as a palaeoclimatic indicator for glacial and polar water conditions.

As diverse as these depositional environments of ikaite may be, they are all primarily characterised by cold alkaline conditions facilitating the preferential precipitation of ikaite, as opposed to aragonite and calcite that are more soluble at lower temperatures.

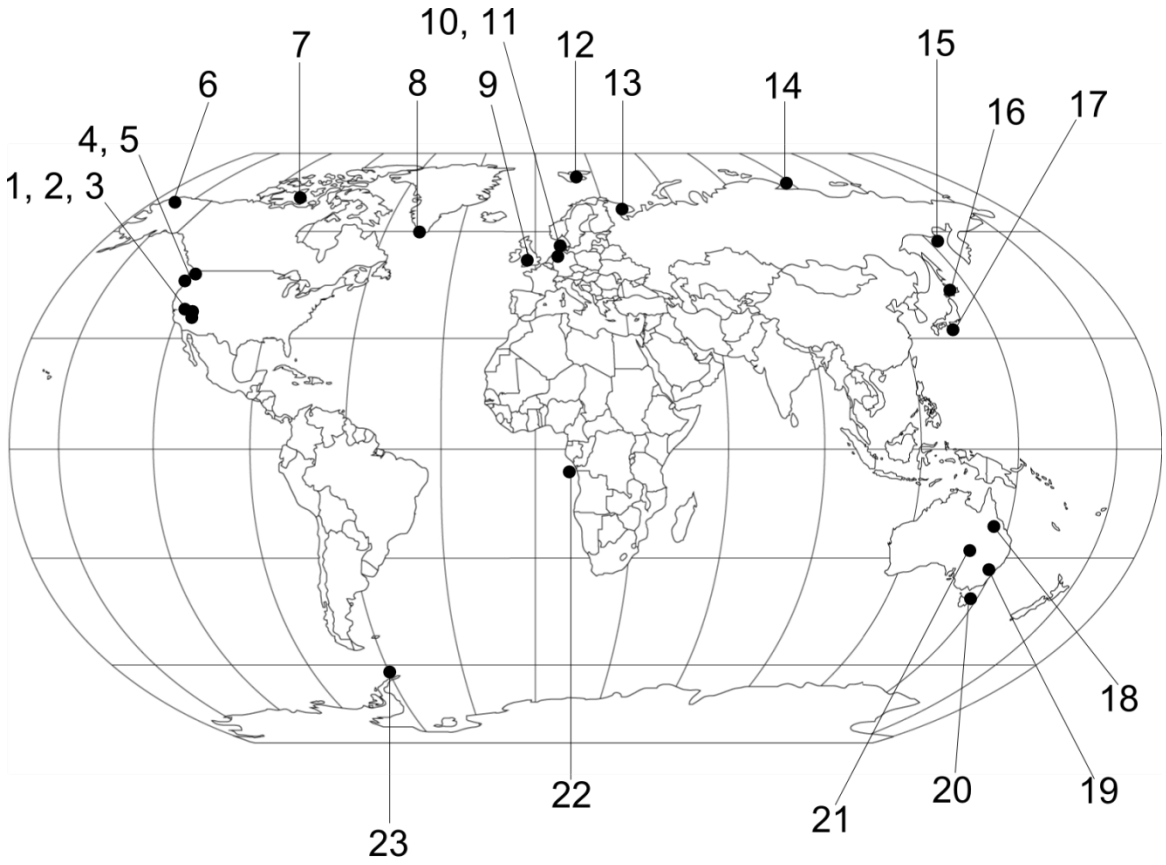

1	Mono Lake, California, USA	Late Neogene	(Whiticar and Suess 1998)
2	Pyramid Lake, Nevada, USA	Late Neogene	(Whiticar and Suess 1998; Selleck et al. 2007)
3	Alkali Lake, Oregon, USA	Late Neogene	(Selleck et al. 2007)
4	Olympic Peninsula, Washington, USA	Tertiary	(Whiticar and Suess 1998)
5	Astoria, Oregon, USA	Miocene	(Boggs 1997)
6	Arctic Alaska, USA*	Recent	(Whiticar and Suess 1998)
7	Arctic Canada	Recent	(Whiticar and Suess 1998)
8	Ikka Fjord, Greenland*	Recent	(Burchardt et al. 2001)
9	River Tyne, England, United Kingdom	Recent	(Whiticar and Suess 1998)
10	Denmark	Eocene	(Huggett et al. 2005)
11	Lower Saxony, Germany	Early Jurassic	(Teichert and Luppold 2013)
12	Spitzberg, Svalbrad Peninsual, Norway	Tertiary	(Whiticar and Suess 1998)
13	Kola Peninsula, Russia	Late Neogene	(Selleck et al. 2007)
14	Laptev Sea, Russia*	Recent	(Schubert et al. 1997)
15	Sea of Okhotsk	Recent	(Greinert and Derkachev 2004)
16	Hokkaido Isand, Japan	Recent	(Whiticar and Suess 1998)
17	Nankai Trough, Japan*	Recent	(Stein and Smith 1986)
18	Bowen Basin, NSW, Australia	Permian	(Huggett et al. 2005)
19	Sydney Basin, NSW, Australia	Permian	(Selleck et al. 2007)
20	Tasman Basin, Tasmania, Australia	Permian	(Selleck et al. 2007)
21	Eromanga Basin, NSW, Australia	Cretaceous	(De Lurio and Frakes 1999)
22	Zaire Fan, Congo*	Recent	(Jansen et al. 1987; Zable and Schulz 2001)
23	Bransfield Strait, Antarctica*	Recent	(Suess et al. 1982)

Figure 4.2: Global glendonite and ikaite occurrences, showing the dominant high latitude polar, sub-polar to temperate geographic distribution of glendonites. Ikaite occurrence is denoted by *.

4.2.3 Synthetic ikaite precipitation

Since the discovery of ikaite various laboratory experiments have attempted to synthetically precipitate ikaite crystals under controlled conditions, in an attempt to understand the complex equilibrium processes involved in ikaite precipitation, such as alkalinity, temperature and phosphate concentrations.

Laboratory-based experiments by Brooks et al. (1950) precipitated synthetic ikaite at 27 °C from water with high orthophosphate levels that inhibited the formation of calcite and aragonite. In addition, very low CO_2 levels were induced to mimic deep water carbon dioxide depleted waters to facilitate the formation of the mineral. These results confirmed the initial assumptions of ikaite forming conditions to be highly anoxic and rich in organic material favouring the formation of calcium carbonate hexahydrate over other carbonate minerals.

Later studies by Marland (1975) produced synthetic calcium carbonate hexahydrate by reversing reactions of calcium carbonate and water in pressure vessels at sub-zero temperatures. It was shown that ikaite is stable at pressures as low as 5.08 kb at 25 °C. This showed that ikaite stability increases with decreasing temperature and increasing hydrostatic pressure. However ikaite is highly under-saturated and only forms a metastable mineral state. Ikaite is unable to form a stable lattice structure at these cold temperatures and typically reverts to a more stable form of calcium carbonate, such as calcite or vaterite, when water temperature changes; thus temperature alone cannot cause preferential formation of ikaite over calcite and aragonite.

Experimental ikaite synthesis by Bischoff et al. (1993) utilised similar precipitation techniques to those of Johnston et al. (1916). Ikaite crystals were precipitated from solutions at 0 to 24.5 °C over a six to eight hour period. Various other components were added to monitor their effect on the formation, solubility and reaction kinetics. This showed that ikaite solubility increases with lower temperature. As previously postulated, the presence of orthophosphate inhibits the formation of more stable forms of calcium carbonate and therefore preferentially facilitates the formation of the metastable ikaite mineral.

4.2.4 Morphology of ikaite and its pseudomorphs

Ikaite is monoclinic and white in colour when pure (Figure 4.3). With the addition of secondary element substitution into the calcium carbonate hexahydrate lattice, colours can vary from white to off-white, yellow, fawn and pale brown. The colour is, therefore, not diagnostic and is also typically controlled by the surrounding sediments as well as the dissolved ionic load of the water column. The common ikaite crystal structure grows at a slow rate within the surrounding sediment under conditions of low-energy deposition. Alternatively, ikaite can also form directly in the water column (Sherman and Smith 1985).

Two distinct principal modes of occurrence determine the morphological structure of ikaite pseudomorphs (Selleck et al., 2007). Prior to this, three modes of occurrence were postulated by Huggett et al. (2005), however the second 'Type B' pseudomorph classification can be combined into the second displacive type that grows in-situ in the surrounding sediment.

Type A pseudomorphs are aggregates or 'tufa' that formed underwater. They were created by subsurface mineral springs that allowed crystals to grow into the water column unrestricted by sediments. Thinolites are abundant in areas containing groundwater with a high dissolved ion load in highly alkaline environments. This can occur in some lacustrine environments such as Mono Lake, California (Shearman, 1998; Council and Bennett, 1993; Whiticar and Suess, 1998), Alkali Lake, Oregon (Selleck et al., 2007) and Pyramid Lake, Nevada (Whiticar and Suess, 1998; Selleck et al., 2007). Other ikaite formation environments include sub-aerially exposed springs such as the mineral springs at Hokkaido, Japan (Ito, 1966, 1998). However, more common occurrences are in marine environments with sub-aqueous springs, such as at Ikka Fjord, Greenland (Buchardt et al., 1998, 2001). Thinolite 'tufa' deposits grow as single crystals, twin structures and interpenetrating aggregate group clusters. These crystal aggregates range up to 15 cm in size with typically smaller crystals than the single crystals (Huggett et al., 2005).

Type B pseudomorphs are usually found in aggregate or single spire forms. A sigmoidal bi-pyramidal shape is common in individual crystals, these typically grow displacively into the surrounding sediments. Typical sizes range from 5-15 cm in length and 1-3 cm wide, exhibiting a rhomboid cross-section. Other crystal growths exhibit a spherical stellate cluster structure with a star-like nature growing displacively in the surrounding sediment. These are equivalent to examples found in Bransfield Strait, Antarctica (Suess et al., 1982), jarrowite from the Tyne River, England, UK (Whiticar and Suess, 1998), glendonites from the Bowen, Eromanga and Sydney Basins (Huggett et al., 2005; De Lurio and Frakes, 1999; Selleck et al. 2007, respectively), gennoishi from the Nankai Trough, Japan (Stein and Smith, 1986) and the Sea of Okhotsk (Greinert and Derkachev, 2004). One of the more recent documentations of glendonite

occurrences stem from north-west Germany in association with Early Jurassic methane seeps (Teichert and Luppold, 2013).

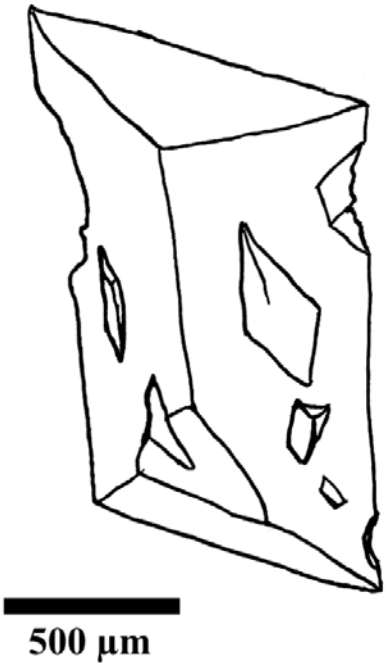

Figure 4.3: Ikaite crystal showing pyramidal crystal habbit, forming a square bi-pyramidal sigmoidal crystal. The crystal usually carries imperfections such as chipped corners and gouges. Stylised diagram from Buchardt et al. (2001).

The surface morphology of the pseudomorph is typically ridged and uneven. This was initially thought to be an artefact of the ikaite growth phenomenon. However laboratory growth experiments by Shaikh and Shearman (1986) have shown that this surface etching results from the environmental conditions of formation and is a direct effect of the dehydration of the ikaite mineral to calcite (Huggett et al., 2005).

At present calcite is the only known form of calcium carbonate that forms the pseudomorph structure of ikaite in the natural environment. However from laboratory growth trials by Shaikh and Shearman (1986) and Bischoff et al. (1993), adapting the precipitation method of Brooks et al. (1950) and Marland (1975), it was found that ikaite breaks down to both calcite and vaterite. Depending on the experimental conditions used by Bischoff et al. (1993) and Shaikh and Shearman (1986), calcite or vaterite were found to be present in excess, respectively. Natural samples collected by Stein and Smith (1985) exhibited decomposition to calcite and aragonite mixtures.

4.2.5 Stable isotopes of glendonites

The isotopic analysis of glendonites has been limited to conventional stable isotope analyses of carbon ($^{13}C/^{12}C$) and oxygen ($^{18}O/^{16}O$). There have not been any attempts to quantify the formation temperatures of glendonite using the clumped isotope Δ_{47} signature of the pseudomorph calcite. A summarised account of stable isotope data exists from studies by Selleck et al. (2007) in their comparison of isotopic compositions of glendonites around the world to the environmental conditions in which they formed.

Calcite pseudomorphs that grow displacively within the surrounding sediment in marine environments such as in the Bransfield Strait (Suess et al., 1992), Sea of Okhotsk (Greinert and Derkachev, 2004) the Nankai Trough (Stein and Smith, 1986) and the Zaire Fan (Jansen et al., 1987; Zabel and Schultz, 2001) all exhibit a very small range in $\delta^{18}O$ values of +2.92 ± 0.62 ‰ VPDB. However these glendonites display a broader range in $\delta^{13}C$ values of -25.36 ± 4.13 ‰ VPDB (Selleck et al., 2007). This has been attributed to source water mixing of "heavy" low temperature seawater with "lighter" methane oxidation sourced carbonate.

Pseudomorphs from non-marine terrestrial environments, such as from Mono lake, Pyramid Lake, and Alkali Lake, display distinctly different isotopic compositions from other glendonite pseudomorphs. Isotopic compositions of samples from these lacustrine environments appear to be controlled by the isotopic composition of the local meteoric waters. They display slightly negative $\delta^{18}O$ values and significantly enriched $\delta^{13}C$ values, indicating less influence from methane oxidation derived carbonate (Whiticar and Suess, 1998; Selleck et al., 2007).

Glendonite samples from Ikka Fjord display highly depleted $\delta^{18}O$ values of -10 ± 2 ‰ VPDB (Burchardt et al., 2001). This has been postulated to result from a mixing of meteoric, seawater and submarine spring water, creating a wide range of oxygen isotope values. The relatively restricted range in $\delta^{13}C$ values of 6.25 ± 0.32 ‰ VPDB suggests a very minor influence of methane oxidation on the isotopic composition of Ikka Fjord glendonites (Burchardt et al., 2001).

Australian samples from the Eromanga Basin exhibit $\delta^{18}O$ values similar to samples from the Kola Peninsula, Denmark and the United Kingdom. The isotopic composition of the glendonites would suggest that the precipitation water was significantly lower in $\delta^{18}O$ values than modern sea water. However, this would only be true if preserved samples represent a primary calcite pseudomorph after ikaite and no additional sources of calcite had an influence upon the isotopic composition post-deposition (De Lurio and Frakes, 1999).

4.3 Methods

Analysis of glendonite sample powders for mineralogical composition by X-ray diffraction (XRD), trace element analysis and clumped isotope analysis follow the same procedures as outlined in Chapter 3. Additional, glendonite specific, sample preparation methods are described below. Petrographic thin sections were not able to be made due some glendonite material being highly broken (only fragment picking was possible).

4.3.1 Glendonite sample powder preparation

Selected glendonite samples were first washed with Milli-Q water to free the mineral from any contamination by dust and detrital matter from elongated storage. It is suspected that some of the mineral specimens were coated in an oil or wax substance for visual preservation as museum display specimens. Specimens suspected of being coated in these substances were additionally washed with a 3 % peroxide solution (H_2O_2) to remove additional organic contaminants. Additionally, museum samples were also treated with a 50 % isopropyl alcohol (2-propanol) solution for 5 minutes in a sonicator to dissolve and agitate any oils coating the sample, which in museum specimens is common for presentation and display purposes. Further to this, mineral specimens not enclosed in matrix sediment or rocks were treated with a 2 % HCl solution for 5 minutes in a sonicator to dissolve any secondary carbonate. Samples were triple rinsed between treatment steps and air dried before being oven desiccated for 30 minutes at 60 °C to remove any adhering water from the cleaning process to ensure a clean dry sample for crushing (Tripati et al. 2010).

Sample material was prepared for gas extraction and isotopic analysis in two forms. Crushing of small samples (<10 g) into a powder was achieved by manual hand grinding of glendonite specimens in an agate or stainless steel mortar and pestle. Samples were cut into sections and different regions were sampled by breaking the structure apart using hand tools and working from the outside in. Fragments were then treated using the above cleaning regime and dried. Hand grinding was done in a wet state with ethanol (95 % un-denatured ethyl alcohol) as a cooling fluid to reduce the chance of frictional heating while grinding which may alter the isotopic temperature signature of the sample. Wet grinding residue was then collected and the ethanol was allowed to evaporate. Samples were then dried further by placing them in a desiccator for 48 hours or oven drying at 60 ºC for 2 hours. All samples were placed in plastic flip-top sample vials and stored in a desiccator prior to analysis to minimise moisture build up in the samples.

4.3.2 Polished block

As dehydration of the ikaite mineral (calcium carbonate hexahydrate – $CaCO_3.6H_2O$) to calcium carbonate occurs forming the glendonite pseudomorph there is potential for zoning to occur as the ikaite lattice structure loses water molecules and forms the characteristic irregular highly angled tapering spire structure. Due to this feature it was determined that a cut and polished cross-section specimen should be prepared to examine if there are morphological changes within the crystal structure across the glendonite calcite structure. In addition, any changes in morphology would be then sub-sampled to investigate if there are any changes in formation temperature as the dehydration of ikaite to calcite occurs within the crystal lattice structure.

A large glendonite specimen was used to maximise the physical area to be examined. The glendonite's exact location is unknown due to poor records at the time of collection, however the specimen is known to originate from the Glendon region in New South Wales, Australia, the first locality in the country where these structures were identified.

The single spire was cut along its short axis using a diamond cutting saw to divide the sample. One half was then polished and the other half was crushed for isotopic analysis. The section destined for polishing was hand polished on a grinding wheel with various grit grinding powders to achieve the desired texture. The sample was then mounted on a viewing platform and photographs taken as well as analysis under reflected light on a petrological microscope.

4.4 Results

4.4.1 Sample material and site descriptions

Samples were obtained from various locations around the world to investigate formation temperatures from an assorted range of (palaeo)latitudes and ages to understand the chemical composition of glendonites on a global level. Five type A glendonite specimens were available from the Bol'shaya Balakhnya River located on the Taymyr Peninsula (Taymyrskiy Autonomous Okrug), Eastern-Siberian Region, Russia, and from the Olenitsa River in the Kola Peninsula on the White Sea Coast, Murmanskaja Oblast, Northern Region, Russia. Three type B specimens from Alkali Lake, Nevada were avaliable along with one thinolite specimen from Mono Lake, Oregon, United States of America. The bulk of the glendonite specimens used in this study originated from the Sydney Basin and the Tasman Basin, Australia; these represent type A pseudomorphs and were obtained from exposed sedimentary units as well as drill core specimens. The samples from all regions were provided by Paul Carr and Bruce Selleck in 2012.

4.4.1.1 Australia (Figure 4.4 and 4.5)

All Australian samples were obtained from local sources in association with work by Selleck et al. (2007) as well as some museum specimens. Specimens from the initial discovery site at Glendon in the Hunter Valley, NSW, Australia, were collected along with examples from other major glendonite containing formations within Australia as mentioned by Carr et al. (1989). Within the Sydney Basin there are various sedimentary units that contain abundant glendonites. The Basin is part of the extensive Sydney-Gunnedah-Bowen Basin spanning from central Queensland through New South Wales and comprises relatively flat-lying undeformed marine and non-marine strata of Late Carboniferous to Triassic age, as well as some minor volcanic units of slightly younger age.

The glendonites obtained were typically bulk samples from the Mulbring Siltstone of the Sydney Basin sedimentary sequence. These units represent deposition under a shallow marine low-energy environment. Glendonites occur as large single crystal or cluster type C (Huggett et al., 2005) pseudomorphs. The samples are massive and many exhibit one primary prismatic axis with some examples showing two axes of growth (Figure 4.4).

Specimens from the Wandrawandian Siltstone, Huskisson, Southern Sydney Basin (H-1 to H-4B and WH) exhibit well-formed glendonites in fine-grained organic muds with abundant

brachiopods. The Wandrawandian Siltstone at Kinghorn Point, Sydney Basin (KP) exhibits a few glendonites of poor quality in association with abundant concretions. The specimens exhibit fractures and are possibly reworked. They are probably related to early post-depositional deformation in the marine depositional environment. Similar specimens from the Wesley Park Sandstone (WB), Werri Beach, Southern Sydney Basin, represent outcrop samples with bulk secondary spar calcite infill. Glendonites and concretions are rare and small in these sandy facies. Additionally, some glendonite specimens were sourced from a diamond drill hole (Tunbridge RG145) through the Quamby Formation, Tasman Basin. These glendonites occur in a shallow marine depositional environment similar to those found in the Sydney Basin. Both glendonite specimens and associated secondary calcite are present within the cores. All of the Sydney Basin and Tasman Basin glendonites are Permian in age, i.e. from 299 to 251 Ma.

These materials were previously examined by Selleck et al. (2007) to assess their applicability as records of ancient cold water conditions. Their work focused on a range of material from within the Sydney Basin (Late Carboniferous to Triassic marine and non-marine strata). Within the Sydney Basin six major glendonite-bearing intervals have been identified (Carr et al., 1989). However all localities share several characteristic features. The glendonites tend to be restricted to several horizons within each stratigraphic sequence, which tend to be dark grey, carbonaceous marine strata. The glendonites occur in bioturbated mudstone, siltstone and less commonly fine-grained sandstone. Generally glendonite formation is associated with deep water facies on the open continental shelf in a slowly deposited sedimentary phase that provided calm conditions for the mineral to form.

Figure 4.4
Glendonite – GL-1
Glendon, Hunter Valley, N.S.W, Australia.
5cm scale bar, 1cm subdivisions.

Figure 4.5
Glendonite – GL-1 (cut surface)
Glendon, Hunter Valley, N.S.W, Australia.
5cm scale bar, 1cm subdivisions.

4.4.1.1 Olenitsa River, Kola Peninsula, Russia (Figure 4.6, 4.7 and 4.8)

The Kola Peninsula is located in far northern Russia bordering the Arctic Ocean. It forms the bulk of the Murmansk Oblast region in the northwest of the country, occupying an area of approximately 100,000 square kilometres. The area is almost exclusively located within the Arctic Circle, at 66.5° north of the equator. The peninsula is situated on the north eastern portion of the Baltic Shield and has undergone multiple episodes of Quaternary ice sheet depression, uplift and subsequent isostatic readjustment. The lithology is mainly Precambrian metamorphosed mafic and ultramafic igneous units and incorporated sedimentary successions including minor limestone (Mitrofanov et al., 2002).

The Olenitsa River drains in a southerly direction into the White Sea. Samples were collected offshore by dredging unconsolidated sediments producing pristine glendonite specimens with little to no additional adhered clastic sedimentary material. The sample location coordinates suggest the samples originate directly in front of the mouth of the Olenitsa River approximately 2 km offshore.

Figure 4.6
Glendonite - OR-1A/B
Olenitsa River, Kola Peninsula, Russia.
5cm scale bar, 1cm subdivisions.

Figure 4.7
Glendonite - OR-2A/B
Olenitsa River, Kola Peninsula, Russia.
5cm scale bar, 1cm subdivisions.

Figure 4.8
Glendonite - OR-3 within concretion
Olenitsa River, Kola Peninsula, Russia.
5cm scale bar, 1cm subdivisions.

4.4.1.2 Bol'shaya Balakhnya River, Taymyr Peninsula, Russia (Figure 4.9 and 4.10)

The Taymyr Peninsula is also located on the Arctic Ocean in northern Russia. This area forms the most northerly point of Eurasia. The peninsula is situated between the Yenisei Gulf of the Kara Sea and the Khatanga Gulf of the Laptev Sea. The peninsula and most of the Kara and Laptev Sea are frozen for ten months of the year with summer non-freezing conditions only occurring for short periods of time in the coastal regions (Zhang et al., 2013). The Bol'shaya Balakhnya River is located in the Eastern-Siberian Region, on the Taymyr Peninsula (73°37'N, 107°5'E). The river is only active in the summer months between June and September forming a vast braided river system. Samples were collected from soft unconsolidated sea mud in the central portions of the Bol'shaya Balakhnya River near the main outflow area. Samples from the river are believed to be of Quaternary age however an exact determination has not been made (Selleck et al., 2007). Both specimens from the Bol'shaya Balakhnya River are contained within a clastic matrix rock, likely a carbonaceous mudstone which will also be investigated isotopically.

Figure 4.9
Glendonite - BR-1
Bol'shayaBalakhnya River, Taymyr Peninsula, Siberia, Russia.
5cm scale bar, 1cm subdivisions.

Figure 4.10
Glendonite - BR-1
Bol'shayaBalakhnya River, Taymyr Peninsula, Siberia, Russia.
5cm scale bar, 1cm subdivisions.

4.4.1.3 Alkali Lake, eastern Oregon, USA (Figure 4.11)

Alkali Lake is an evaporative seasonal lake in Lake Country, eastern Oregon, located 1320 m above sea level and comprising an area of approximately 2300 square kilometres. Alkali Lake has a maximum depth of approximately 80 metres but as it is a seasonal lake this has dried

considerably over time and has led to the formation of various thinolite deposits on the lake shoreline and within the lake bottom sediments.

Three thinolite specimens are available from Alkali Lake; these were collected from the lake shoreline in unconsolidated sediment in the condition shown by Figure 4.11. Samples are estimated to be of Pleistocene age and are approximately 30,000 years old (Selleck et al., 2007). Thinolite specimens exhibit a simple square bipyramidal prism tapering at both ends to a point. On some examples small secondary pyramid spires grow at acute angles from the centre outwards as shown by Figure 4.11. The external surface appears uneven and highly pitted, while in some areas the specimen appears to exhibit angular scales tapering in the direction of the spires. Some adhered fine-grained sediment is also evident, these were removed prior to analysis. The external colouration is light brown to fawn, with lighter areas being almost beige to off yellow. Internally, a more uniform light brown is present with alternating lighter and darker areas due to concentration of various crystal sizes as a product of mineral growth at the time of formation. The internal structure of the thinolite appears to mimic the external prismatic structure and appears to be layered outwards.

Figure 4.11
Thinolite – AL-1A/B/C
Alkali Lake, Lake Country, East Oregon, USA.
5cm scale bar, 1cm subdivisions.

4.4.1.1 Mono Lake, California, USA (Figure 4.12)

Mono Lake is a hypersaline lake in the Sierra Nevada region in eastern California. Calcareous thinolite deposits occur on the lake shoreline as 2-5 m high tufa mounds up to 3 m in diameter. Tufa may also rise out of the shallow waters on the lakes edge. Deposition occurs sub-aqueously in the lake at submerged vents where Ca-rich groundwater and high bicarbonate lake water mix and calcite precipitation readily occurs (Bischoff et al., 1993). Sample material from Mono Lake

used in this study generally exhibits morphology of small prominent bipyramidal spires up to 2 cm in length protruding from a largely in massive structure of smaller 1-2 mm fragments (Figure 4.17). The thinolite tufa is of Early Holocene to late Pleistocene age, during this time the surrounding area has been hydrothermally active through localised volcanism (Whiticar and Suess, 1998).

Figure 4.12
Thinolite – ML
Mono Lake, California, USA.
10cm scale bar, 1cm subdivisions.

4.4.1.1 Pyramid Lake, Nevada, USA

This lake is part of a series of Pleistocene lakes and their present-day remnants. Pyramid Lake, as well as other lakes on the border between California and Nevada, comprise the western Great Basin Lakes. These lakes are rich in calcareous materials and readily precipitate calcareous tufa deposits as mounds, towers and shoreline layered deposits. Thinolite pseudomorph deposits are common up to 60 m above the present lake shoreline with mounds extending up to tens of metres in height (Bishoff et al., 1993). Samples of thinolite from Pyramid Lake, Nevada, were taken from shoreline deposits close to the modern shoreline (Selleck et al., 2007). These represent Quaternary thinolite deposits and have similarities to the thinolite deposits from Alkali Lake, Oregon, USA.

4.4.2 Glendonite morphology and mineralogy

From the variety of specimens from several localities and environments, it can be seen that mineral specimens exhibit a set of definable morphological characteristics. The overall shape, orientation, size and form may be varied but some fundamental comparisons of formation environment and morphology can be made.

The morphologies include a very simple aggregate crystalline structure in the thinolite sample (ML-1) from Mono Lake, California, USA (Figure 4.12). This shows no particular orientation or growth pattern which may suggest that the mineral was formed quickly and possibly did not experience as stable growth conditions as other specimens. Pseudomorphs exhibiting more stable growth conditions, such as material from Glendon (GL-1), exhibit significantly longer axis spires and conform more to their characteristic diamond cross section and bipyramidal morphology (Figure 4.4 and 4.5). Morphological description of other glendonite specimens from the Sydney Basin and Tasman Basin was not possible due to the high amount of attached clastic sediment.

The lacustrine glendonites from Alkali Lake, eastern Oregon and Pyramid Lake, Nevada, appear to display a very different set of morphological characteristics from the other depositional environments that have been examined (Figure 4.11). This coincides with previous accounts of type A pseudomorphs, precipitated from subaqueous springs. Samples sourced from Alkali Lake appear to be smaller in size compared to specimens from shallow marine and lacustrine environments. Diagnostic morphological characteristics are still present such as the long axial spine in a bi-directional orientation and diamond shaped cross-sectional profile. This characteristic morphology is also exhibited in the Pyramid Lake material. Again, the overall size of the mineral growth is comparatively small but the key diagnostic properties can be distinctly identified.

Specimens from the Kola and Taymyr Peninsulas, exhibit a very massive structure, with axis growth spires being short and compacted in appearance. The length to width ratio is low, resulting in an angular spiked sphere structure (Figure 4.6 to 4.8). This is a likely primary factor of the formation environment and depositional environment of the sample. These estuarine environments have more favourable growth environment for the glendonite mineral than do higher energy shallow marine environments.

4.4.3 Growth zoning in glendonite

As the glendonite calcite replaces the ikaite crystal structure there appears to be different zones within single crystal spires of the glendonite mineral structure. This can be seen in the large glendonite specimens from Glendon in the Hunter Valley, New South Wales Australia (Figure 4.13). The glendonite was cut through the major growth axis of a single bipyramidal spire. The cut surface was polished and photographs taken to reveal the boundaries between different crystal structures.

The outermost margins of the glendonite are well defined although with irregular colour variations. Sample GL-1 exhibits small patches of off white to yellow material around its perimeter, mostly concentrated at the spire apices on both ends of the structure. Inspection and spot tests of scrapings of both the lightly coloured material and the darker portions of the glendonite margin show that the lighter coloured areas are likely to be calcitic mud inclusions from the surrounding sediments in which the glendonite formed, due to the higher concentrations of quartz and kaolin in the sample and which are absent in the darker material (Figure 4.13).

Most of the Sydney basin samples, as well as samples from the Tasman Basin that were received in the form of drill core samples, represent in-situ bulk sediment samples. These were unable to be photographed in a suitable manner. Therefore sample photographs are not presented for these glendonite samples. However, the glendonites are easily distinguishable from the surrounding sediment.

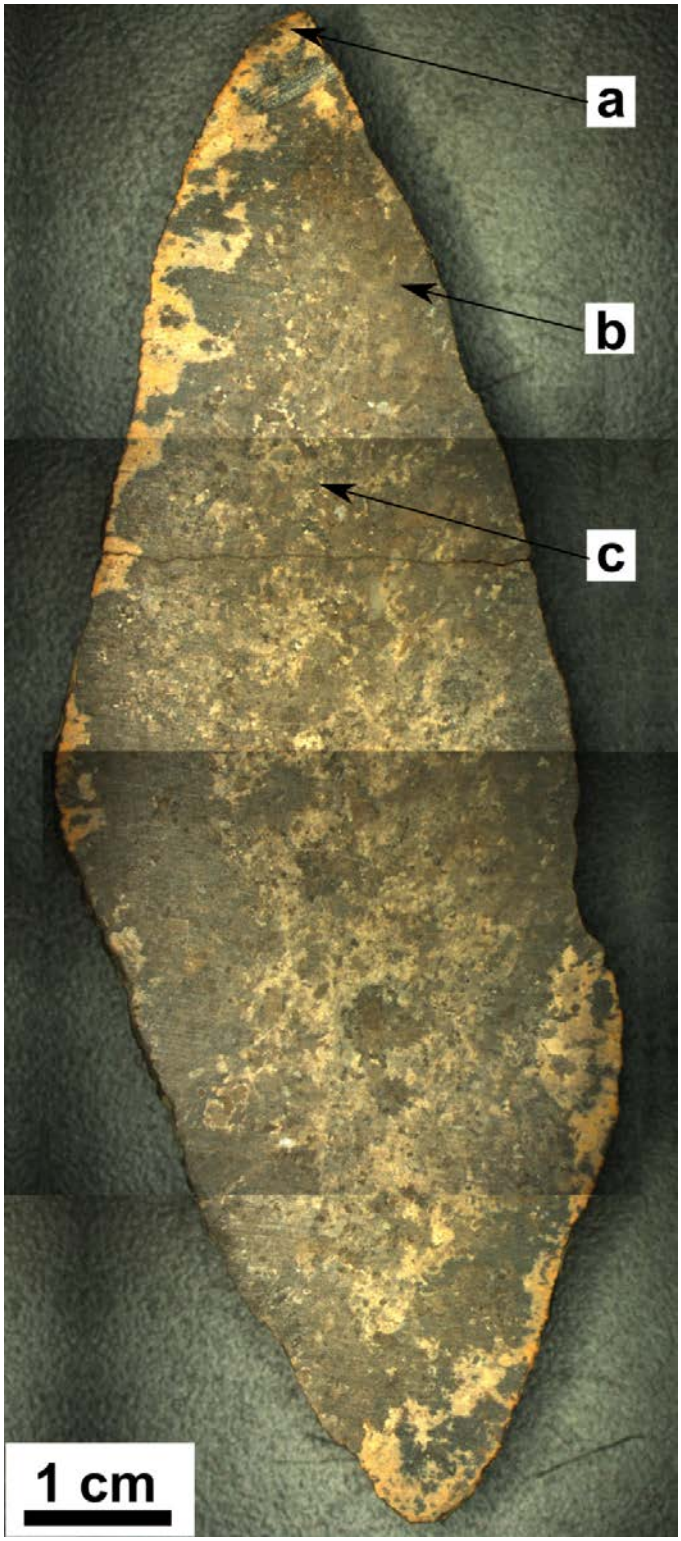

Figure 4.13: Glendonite, GL-1 from Glendon, NSW, Australia. Polished cross section, a) off white to pale yellow region of secondary calcareous mud, b) dark highly crystalline zone with large crystals up to 1 cm in length, c) internal zone with smaller crystals with some lighter coloration. The sample was previously broken (horizontal crack at label 'c') but reattached with resin, and polished.

4.4.4 Glendonite trace-element composition

The minor-element composition of glendonites is reported following ICP-MS analysis of 2% HNO_3 leachates. The data (Table 4.1) refer to the carbonate phase only, as other acid insoluble phases that may be present, such as quartz, gypsum or clay minerals do not contribute to the analysis.

Table 4.1: Minor-element composition of the carbonate fraction of glendonite samples. The compositions are shown as a molar fraction as well as their chemical formula in the form of (cation) CO_3.

Location	Sample Name	Calcium	Magnesium	Manganese	Iron	Aluminium	Formula
Glendon, Sydney Basin	GL-1	0.92	0.02	0.01	0.05	0	$(Ca_{0.92}Mg_{0.02}Mn_{0.02}Fe_{0.05})CO_3$
Huskisson, Sydney Basin	WH-1	0.96	0	0.01	0.03	0	$(Ca_{0.96}Mn_{0.01}Fe_{0.03})CO_3$
Huskisson, Sydney Basin	WH-2A	0.96	0.02	0	0.02	0	$(Ca_{0.96}Mg_{0.02}Fe_{0.02})CO_3$
Huskisson, Sydney Basin	WH-4	0.97	0.01	0	0.02	0	$(Ca_{0.97}Mg_{0.01}Fe_{0.02})CO_3$
Huskisson, Sydney Basin	WH-9b	0.94	0	0	0.04	0.02	$(Ca_{0.94}Fe_{0.04}Al_{0.02})CO_3$
Huskisson, Sydney Basin	H1-B	0.96	0.01	0.01	0.02	0	$(Ca_{0.96}Mg_{0.01}Mn_{0.01}Fe_{0.02})CO_3$
Huskisson, Sydney Basin	H4a	0.98	0	0	0.02	0	$(Ca_{0.98}Fe_{0.02})CO_3$
Kinghorn Point, Sydney Basin	KP7-B	0.96	0	0	0.02	0.02	$(Ca_{0.96}Fe_{0.02}Al_{0.02})CO_3$
Tunbridge, Tasman Basin	Tun541.7	0.94	0.03	0.01	0.02	0	$(Ca_{0.94}Mg_{0.03}Mn_{0.01}Fe_{0.02})CO_3$
Tunbridge, Tasman Basin	Tun637-dk	0.97	0	0.01	0.02	0	$(Ca_{0.97}Mn_{0.01}Fe_{0.02})CO_3$
Kola Peninsula, Russia	OR-1a	0.91	0.07	0	0.02	0	$(Ca_{0.91}Mg_{0.07}Fe_{0.01})CO_3$
Taymyr Peninsula, Russia	BR-1a	0.93	0.06	0	0.01	0	$(Ca_{0.93}Mg_{0.03}Fe_{0.01})CO_3$
Alkali Lake, USA	AL-1	0.95	0.01	0.03	0.01	0	$(Ca_{0.95}Mg_{0.01}Mn_{0.03}Fe_{0.01})CO_3$
Mono Lake, USA	ML-1	0.97	0.02	0	0.01	0	$(Ca_{0.97}Mg_{0.02}Fe_{0.01})CO_3$

The molar ratios were calculated from elemental concentrations (ppm) with appropriate dilution factors applied.

Samples from the Olenitsa River, Kola Peninsula and the Bol'shaya Balakhnya River, Taymyr Peninsula contain higher magnesium concentrations than samples from other depositional environments around the world. The former samples contain 6 to 7 mole percent Mg (Table 4.1). This phenomenon is likely to be an artefact of the depositional environment as well as the sedimentary sources. All glendonite specimens contain some iron to between 1 to 5 mole percent. Due to the formation of the original ikaite at the sediment water interface there is also potential for physical inclusion of other minerals and which can be assessed by X-ray diffraction.

4.4.5 Glendonite mineralogy

The XRD results of the glendonite samples show they are principally calcite (80.6 to 99.1 weight % $CaCO_3$, Table 4.2), with thinolite tufa-type (type A) pseudomorphs exhibiting generally lower calcite concentrations (and higher aragonite) than jarrowite-type (type B) glendonites. In addition, some samples have significant dolomite or magnesite contents. This appears to be a regional depositional artefact, not directly related to the formation mechanism. All samples appear to have minor inclusions of quartz and kaolinite from surrounding sediment. Both samples from the Olenitsa River, Kola Peninsula (OR-1a) and the Bol'shaya Balakhnya River, Taymyr Peninsula (BR-1a) contain magnesium carbonate up to 3.8% as well as some dolomite. Higher magnesium levels are also present in samples from Alkali Lake, containing up to 2.2% magnesium carbonate. Glendonite sample WH-9 showed a large amount of quartz uncharacteristic of a glendonite. Subsequently it was discovered that this material originally thought to be glendonite material was part of the surrounding clastic material in which the pseudomorph was precipitated.

Table 4.2: Mineralogical composition of glendonite samples. Based on XRD results of powdered samples. Compositions are shown as percentages of total sample composition of each mineral phase.

Location	Sample	Calcite $CaCO_3$	Dolomite $(Ca,Mg)CO_3$	Siderite $FeCO_3$*	Magnesite $MgCO_3$	Aragonite $CaCO_3$	Quartz SiO_2	Kaolin $Al_2Si_2O_5(OH)_4$	Gypsum $CaSO_4 \cdot 2H_2O$
Glendon, Sydney Basin	GL-1	80.6	9	0.6	0.7	3.4	1.6	0.7	3.4
Huskisson, Sydney Basin	WH-1	99.1	0.5	0.3	0	0	0	0.1	0
Huskisson, Sydney Basin	WH-2A	96.5	1.3	0.6	0	0	0.8	0.4	0.4
Huskisson, Sydney Basin	WH-4	92.8	1.5	0.7	0.1	0.9	3.0	0.4	0.6
Huskisson, Sydney Basin	WH9-B	30.8	0.6	0.6	0.5	3.6	55.0	6.4	2.6
Huskisson, Sydney Basin	H1-B	94.6	1.0	0.7	0.6	0	1.3	0.4	1.5
Huskisson, Sydney Basin	H4-A	95.6	0.8	0.6	0.8	0	1.4	0.3	0.5
Kinghorn Point, Sydney Basin	KP7-B	97.4	1.0	0.4	0	0	0.7	0.5	0
Tunbridge, Tasman Basin	Tun541.7	91.1	6.6	0.7	0	0	0.9	0.3	0.4
Tunbridge, Tasman Basin	Tun637-dk	97.1	0.5	0.5	0	0	1.0	0.3	0.6
Kola Peninsula, Russia	OR-1A	84.7	1.0	1.0	3.8	4.1	0.2	1.4	3.9
Taymyr Peninsula, Russia	BR-1A	85.5	0.9	1.0	2.4	4.2	0.3	1.7	4.0
Alkali Lake, USA	AL-1	84.6	0.9	0.9	2.2	4.6	0.4	2.5	4.0
Mono Lake, USA	ML-1	88.2	0.1	0.6	0.5	5.5	0.6	1.8	2.6

4.4.6 Stable isotope results

4.4.6.1 $\delta^{18}O$ and $\delta^{13}C$ results

Both thinolite tufa-type and jarrowite-type glendonites exhibit negative $\delta^{18}O$ values ranging between -1.68 and -10.95 ‰ and $\delta^{13}C$ values between +5.97 and -15.93 ‰ (Table 4.3). Slight differences in both oxygen and carbon isotope values were found in a few glendonite samples compared to the previous results of Selleck et al. (2007) on the same material. Samples from Tunbridge (TUN), Huskisson (H) and Werri Beach (WB) exhibited $\delta^{18}O$ and $\delta^{13}C$ values up to 1.5 ‰ lower than results obtained by Selleck et al. (2007). This is most likely due to small differences in bulk material subsampling and not a reflection of analytical precision. Additionally, glendonite sample powders analysed by Selleck et al. (2007) were roasted at 300°C prior to acid digestion to remove organic material. This step may also have introduced additional reordering of calcite molecules at the elevated temperatures, leading to the discrepancy in the $\delta^{18}O$ and $\delta^{13}C$ values. This heating step was not performed here due to the risk of reordering of isotopologues potentially resetting the clumped isotope temperature.

Thinolite samples exhibit distinctly enriched $\delta^{13}C$ values between +2.74 and +5.97 ‰. This is likely to indicate a difference in carbon source for the carbonate, likely attributed to methanogenesis by carbonate reduction (Whiticar and Suess, 1998). This coincides with both the Alkali Lake (AL-1) and Mono lake (ML-1) samples exhibiting the highest aragonite content 4.6 and 5.5 % respectively as well as a minor kaolin constituent. This is typical of terrestrial evaporite lakes and a common attribute of underwater springs (Bischoff et al., 1993). Jarrowite-type glendonites exhibit $\delta^{13}C$ values ranging from -1.03 to -15.93 ‰. This is primarily due to diagenetic remineralisation reactions, which can lead to the formation of ^{13}C-depleated waters. This may lead to the formation of isotopically light carbonate as exhibited in many of the marine glendonites. Additionally, these glendonites have a large geographical range and these differences are likely to be the result of differences in carbon sources in the respective environments and not an artefact of the mineral or pseudomorph formation process.

When the glendonites of this study are plotted as $\delta^{18}O_{carbonate}$ vs $\delta^{13}C_{carbonate}$ (Figure 4.14) and is compared to approximate regions of freshwater limestone, shallow and deep sea marine limestone and evaporitic limestone value ranges identified by Hudson (1977) and redrawn by Whiticar and Suess, (1998) various relationships become apparent.

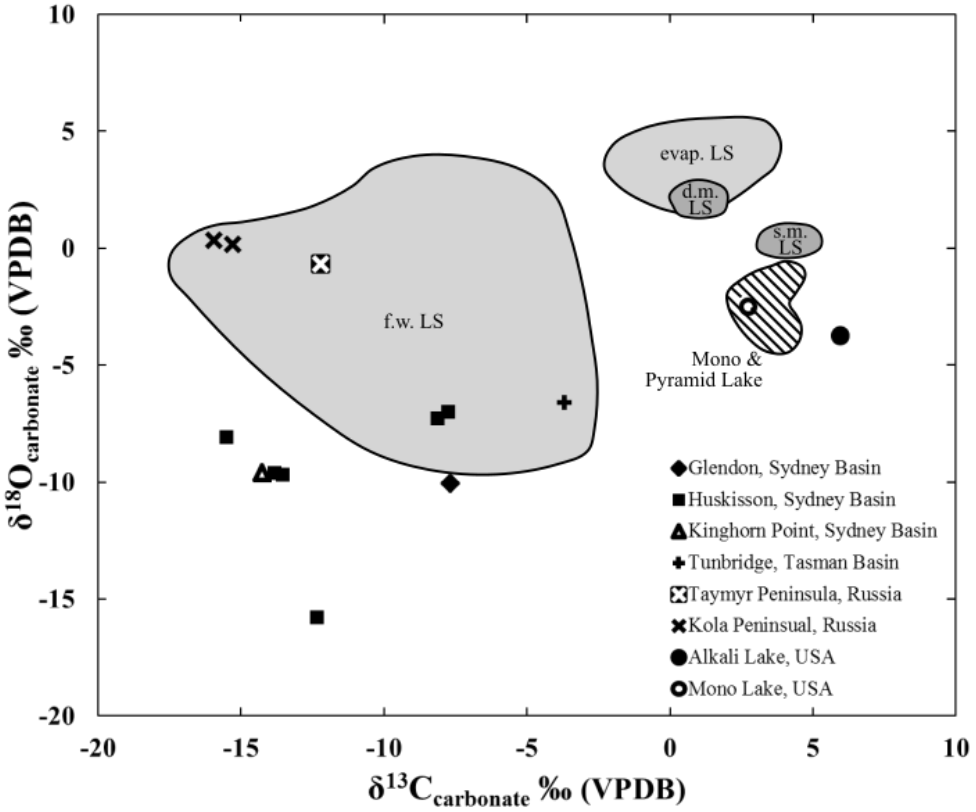

Figure 4.14 Conventional $\delta^{13}C_{carbonate}$ ‰ (VPDB) values plotted against $\delta^{18}O_{carbonate}$ ‰ (VPDB) values to show differences in relationships between glendonites from various geographic locations in relation to the generally accepted range of values for freshwater limestone (f.w. LS), deep marine and shallow marine limestone (d.m. and s.m. LS) and evaporative limestone (evap. LS) as postulated by Whiticar and Suess (1998).

None of the glendonites plot close to deep or shallow marine limestones. This is noteworthy as the vast majority of glendonites were thought to have formed in near-shore and shallow marine environments. Many glendonite samples lie within the region of freshwater limestones ^{13}C-^{18}O values, such as the Taymyr and Kola Peninsula as well as some of the Huskisson and Tunbridge Glendonites with no apparent causality. Other glendonite specimens from the same site and in close proximity border the freshwater-limestone values.

Interestingly, thinolite deposits from Alkali and Mono Lake plot close to the common values of evaporative limestone. These results also coincide with findings of Whiticar and Suess (1998) and Selleck et al. (2007).

Table 4.3 Clumped-isotope ($\Delta_{47\text{-RF}}$), calculated temperature (T) and $\delta^{13}C$ and $\delta^{18}O$ values for glendonites and associated calcite mineral samples.

Sample Site[a]	Sample	Sample Type[a]	Age[a]	*n*	$\Delta_{47\text{-RF}}$ (‰)	SD	δ_{47} (‰)	T[b] (°C)	±	This Study $\delta^{13}C_{(calcite)}$ VPDB (‰)	This Study $\delta^{18}O_{(calcite)}$ VPDB (‰)	Selleck et al. 2007 $\delta^{13}C_{(calcite)}$ VPDB (‰)	Selleck et al. 2007 $\delta^{18}O_{(calcite)}$ VPDB (‰)	$\delta^{18}O_{(water)}$[c] VSMOW (‰)
Glendon, Sydney Basin	GL-1	Bulk Glendonite	Permian	3	0.099	0.028	1.2	-18.4	3.9	-7.68	-10.06			
Huskisson, Sydney Basin	WH-1	Bulk Glendonite		3	-0.052	0.022	3.4	9.8	4.5	-8.13	-7.28			-7.1
Huskisson, Sydney Basin	WH-2A	Bulk Glendonite		3	-0.047	0.026	-4.6	1.9	4.8	-13.82	-9.60	-13.53	-9.76	-9.3
Huskisson, Sydney Basin	WH-2B	Bulk Glendonite		3	-0.148	0.024	-4.3	23.3	4.9	-13.54	-9.69	-13.53	-9.76	
Huskisson, Sydney Basin	WH-4	Bulk Glendonite		3	-0.047	0.011	-4.6	1.9	2.0	-15.52	-8.08	-12.92	-8.12	-7.8
Huskisson, Sydney Basin	WH-5	Bulk Glendonite		3	-0.126	0.032	4.0	26.8	8.8	-7.74	-7.01			
Huskisson, Sydney Basin	WH-5d	Secondary Calcite		3	0.141	0.025	2.9	-23.2	3.4	-9.82	-6.38			
Huskisson, Sydney Basin	H1-B	Bulk Glendonite		2	0.152	0.037	-9.1	-31.8	4.7	-12.35	-15.77	-9.00	-21.40	
Huskisson, Sydney Basin	H4-A	Secondary Calcite		4	-0.285	0.032	-1.3	66.1	11.3	-13.92	-6.16	-14.28	-8.13	-6.0
Kinghorn Point, Sydney Basin	KP-7B	Bulk Glendonite		3	0.047	0.027	-4.8	-14.4	4.1	-14.26	-9.60	-16.35	-9.30	-9.3
Kinghorn Point, Sydney Basin	KP-7B-lt	Secondary Calcite		2	0.229	0.025	-4.6	-38.7	2.8	-14.17	-9.70	-14.04	-10.74	
Tunbridge, Tasman Basin	TUN541.7	Bulk Glendonite		2	-0.240	0.019	8.3	65.2	6.7	-3.67	-6.62	-0.14	-6.76	-6.5
Tunbridge, Tasman Basin	TUN637-dk	Secondary Calcite		2	0.452	0.034	4.5	-57.5	2.8	-6.89	-7.90	-8.71	-8.74	
Taymyr Peninsula, Russia	BR-1a	Bulk Glendonite	Late Neogene	4	-0.024	0.022	6.2	6.5	4.1	-12.21	-0.69			-0.7
Kola Peninsula, Russia	OR-1a	Bulk Glendonite		3	0.119	0.020	3.7	-19.6	3.0	-15.93	0.32	-15.12	-0.99	
Kola Peninsula, Russia	OR-2a	Bulk Glendonite		3	0.091	0.014	4.1	-15.2	2.2	-15.27	0.14	-15.12	-0.99	
Kola Peninsula, Russia	MG-2a(m)	Matrix Rock		2	0.255	0.042	6.2	-36.1	4.6	-13.09	-0.10			
Kola Peninsula, Russia	MG-2a(s)	Bivalve Shell		2	0.192	0.030	16.8	-21.9	4.3	-1.03	-1.19	-0.87	-2.5	
Alkali Lake, USA	AL-1_1	Bulk Thinolite	Pleistocene	3	0.776	0.015	21.6	-76.9	1.0	+5.97	-3.75	+5.78	-6.25	
Alkali Lake, USA	AL-1_2	Bulk Thinolite		3	0.789	0.035	21.7	-77.7	2.3	+5.96	-3.71	+5.78	-6.25	
Mono Lake, USA	ML-1	Bulk Thinolite		3	0.242	0.024	19.2	-27.3	3.0	+2.74	-2.49			

[a] Specimen collection information from Selleck et al. (2007).
[b] Temperature determinations were made by applying the Zaarur et al. (2011) calibration.
[c] $\delta^{18}O_{(water)}$ ‰ (VSMOW) is calculated from plausible Δ_{47} temperatures and the $\delta^{18}O_{(calcite)}$ ‰ (VPDB) from the glendonite samples using the palaeotemperature equation of Kim and O'Neil (1997).

4.4.6.2 Δ_{47} , palaeotemperature results and calculated $\delta^{18}O_{(water)}$ of the host water

Glendonite deposits

The glendonites in the Wandrawandian Siltstone, Warden Head, Australia (WH2A and WH-2B), produce Δ_{47} values of -0.047 ± 0.026 and -0.052 ± 0.022 corresponding to temperatures between 1.9 ± 4.8 °C and 9.8 ± 4.5.°C, respectively. Samples from areas of greater burial depths and thus higher potential for recrystallisation display formation temperatures that lie well outside the known formation temperature limits of the parent ikaite mineral. This is observed in samples from the Tunbridge Drill Hole, Tasman Basin, and the Wandrawandian Siltstone, Kinghorn Point (KP), as well as Warden Head (WH-5). The Tunbridge Drill Hole glendonite gives a formation temperature of 65.2 ± 6.7 °C, whereas associated calcite spar shows an extrapolated formation temperature equivalent to -57.5 ± 2.8 °C.

Samples H4-A, H1-B, KP-7B and KP-7Blt cannot be considered for palaeotemperature determination. The Δ_{47} formation temperature calculations yielded values of 66, -31, -14 and -38 °C, respectively. This suggests that the samples may be contaminated or that the individual bulk samples were not subsampled correctly and surrounding carbonate containing sediment was incorporated into the sample. Abnormally high temperatures may be plausibly related to burial and diagenetic effects and will be considered separately.

Samples WH-5d and TUN637-dk are associated with calcite spar samples in close proximity to the glendonite material. These spar calcites all exhibit formation temperatures distinctly lower than their associated glendonites. TUN637-dk, an amber coloured calcite associated with glendonites contained within the Tunbridge Drill Hole, gives a temperature of -57.5 ± 2.8 ºC. In comparison, glendonite (TUN541.7) gives a temperature of 65.2 ± 6.7 ºC. This is quite a large discrepancy in formation temperature for two calcite minerals supposedly formed at the same time under a similar temperature regime. Similarly, white calcite spar from the Wandrawandian Siltstone, Huskisson, Australia (WH-5d), provide a calculated Δ_{47} temperature of -23.2 ± 3.4 ºC. The associated glendonite calcite (WH-5) gives a formation temperature of 28.6 ± 8.8 ºC.

Glendonite pseudomorph structures formed at or near the sediment-water interface or growing in-situ in soft sediment form their own specific subgroup in terms of their formation temperature ranges. Some locations provide plausible glendonite formation temperatures, such as the Bol'shaya Balakhnya River in Russia (BR-1a), produce a Δ_{47} value of -0.024 ± 0.022 ‰ corresponding to a calculated glendonite formation temperature of 6.5 ± 4.1 °C.

Thinolite tufa deposits

Three samples from a single collection site at Alkali Lake were available for analysis, two of which were analysed. Only one large crystal aggregate specimen was available from Mono Lake. This was subsampled and a homogenised powder used for subsequent palaeotemperature analysis. A further sample from Pyramid Lake was also available. However the sample size only allowed one replicate to be made which was lost during the sample extraction process due to a vacuum leak and subsequent contamination of the sample.

Thinolite samples from Alkali Lake and Mono Lake both exhibit high Δ_{47} values. This, in conjunction with high δ^{47} values, resulted in Δ_{47} values of 0.783 ± 0.025 ‰ and 0.242 ± 0.024 ‰ corresponding to abnormally low calculated formation temperatures of -77.3 ± 2.2 °C and -27.3 ± 3.0 °C, respectively. These formation temperatures are unrelaistically low, well outside the known formation range of ikaite (-1.9 to 7 °C; De Lurio and Frakes, 1999) and well outside the known temperature minimum of the surrounding environment, and beyond the temperature-calibrated range of Δ_{47} values.

Calculated $\delta^{18}O$ of host waters

Appling a conventional inorganic palaeotemperature equation, such as Kim and O'Neil et al. (1997), to ascertain the isotopic ($\delta^{18}O$) value of the precipitating host water to the glendonites in this study shows a noticeable difference between modern glendonites and older Permian glendonites.

The Late Neogene glendonite from the Tyamyr Peninsula gives a $\delta^{18}O$ value of -0.7 ‰. This reflects the average isotopic value of the ocean at the time of formation, previously thought to be ~1 ‰. This shows that the relatively young glendonites of the Tyamyr Peninsula preserve the isotopic composition the ambient sea water, with a possible very small component of river water, at the time of ikaite precipitation and the $\delta^{18}O$ value is maintained post burial.

Permian glendonites from the Sydney Basin exhibit calculated $\delta^{18}O_{water}$ values between -6.0 and -9.3 ‰. These low values potentially indicate isotopic exchange with meteoric water, after burial, and are not the isotopic composition of the initial precipitating sea water. However, it may also be an artefact of the pore water of the ikaite mineral remaining after dehydration of the parent mineral, as suggested by Rickaby et al. (2006) and Lu et al. (2012).

The $\delta^{18}O$ values of the calculated host water of the Sydney Basin glendonites appear to have some relationship with calculated formation temperatures from Δ_{47} values. However, the relationship is not well defined. Tasman Basin glendonites display similar $\delta^{18}O$ values although the calculated formation

temperature is very high and thought to be associated with some degree of post burial diagenesis (Figure 4.15).

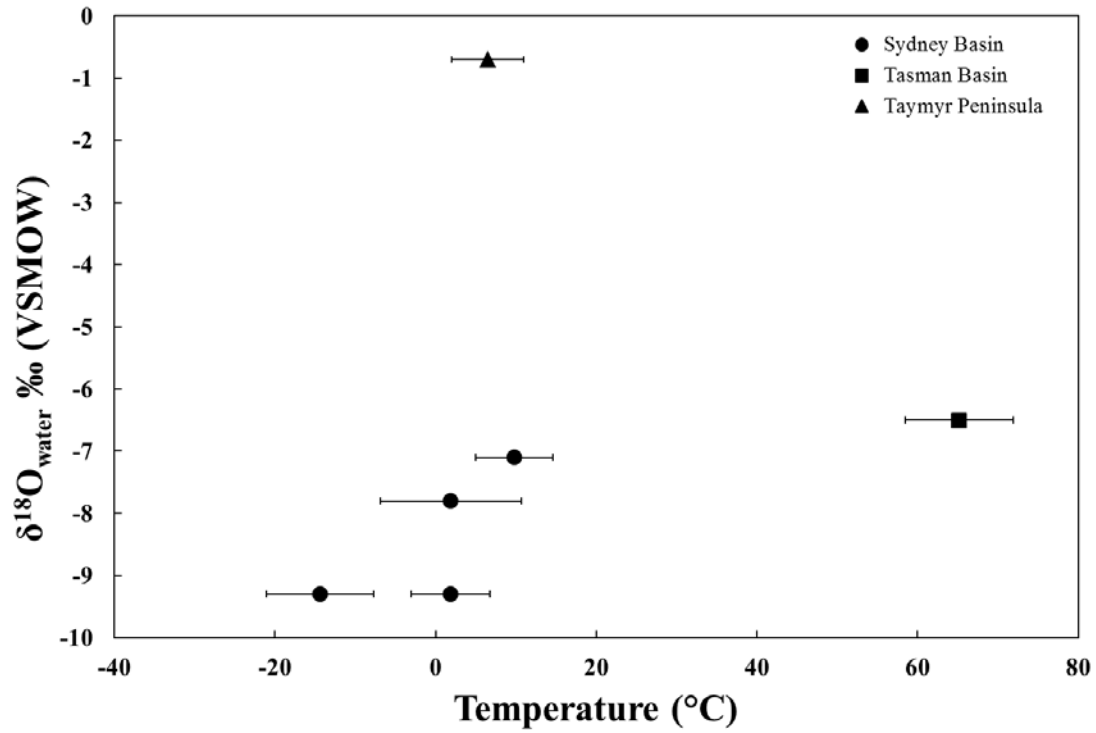

Figure 4.15. Glendonite $\delta^{18}O_{water}$ (±1σ) (VSMOW) values of the precipitating host water calculated from Δ_{47} values plotted in relation to the calculated temperatures formation temperatures (°C) calculated from Δ_{47} values of glendonites from the Sydney Basin, Tasman Basin and Taymyr Peninsula.

Glendonites from the Taymyr Peninsula, Russia appear to be very different in their $\delta^{18}O_{water}$ values. This is largely due to their geographical location being significantly different to the glendonites from the Sydney and Tasman Basins in Australia.

4.5 Discussion

This section provides a synthesis of glendonite morphology and growth zonation. This is then compared to minor-element and mineralogical composition of the various specimens and contrasted to the environment of precipitation. Finally the isotopic composition and the calculated Δ_{47} formation temperatures of the glendonite specimens will be discussed. This will be related to the known precipitation temperatures of the precursor ikaite mineral in the relevant environment. This will indicate if the determined formation temperature of the glendonite pseudomorph is likely to be representative of the formation temperature of the ikaite mineral and if this temperature can accurately indicate the presence of cold water conditions within the glendonite formation environment. This will be discussed in relation to the geographic areas in which glendonites in this study formed.

4.5.1 Sydney Basin

4.5.1.1 Glendon, Mulbring Siltstone: the type locality

The name "glendonite" was originally given to the ikaite pseudomorph after its rediscovery in Glendon, NSW, Australia, by David et al. (1905) following the original noted occurrence by Dana (1849). Later work by Carr et al. (1989) and Selleck et al. (2007) suggested, by analogy, that the occurrence of glendonites in this region is clear evidence of sub-polar cold water conditions within the Sydney Basin during the Permian period.

Glendonite specimens from Glendon, NSW, were analysed using clumped-isotope palaeothermometry to identify the formation temperature of the glendonite pseudomorph in the Glendon area. The materials analysed appear to exhibit a formation temperature of -18.4 ± 3.9 °C, substantially lower than the known ikaite formation temperature range of -1.9 to 7 °C (De Lurio and Frakes, 1999). This suggests that the burial history of the Glendon area in the Sydney Basin has had a secondary effect on the isotopic composition of the calcite pseudomorph in place of the ikaite. The highly negative formation temperature suggests a secondary calcite substitution or alteration during burial, increasing both the Δ_{47} and bulk δ_{47} value through the presence of methane enriched pore water. This would yield more negative formation temperatures when applying the clumped isotope palaeothermometer, providing unreliable formation temperature estimates. The secondary calcite alteration and precipitation is likely due to the Permian glendonite specimens from the Singleton/Glendon area within the Sydney Basin being exposed to diagenetic alteration for much longer time periods than more modern (Quaternary) specimens, such as those from the Kola and Taymyr Peninsula (Bischoff et al., 1993; Selleck et al. 2007), or near-modern glendonites.

It was initially considered that diagenesis may only affect the outermost zones of the glendonite structure and be related to morphological differences between specimens. However, zonation experiments were also conducted on a glendonite specimen from Glendon in the Sydney Basin (GL-1), see Section 4.4.1. This involved subsampling two distinctly different zones in the glendonite specimen. It was theorised that the outer margins might yield more enriched Δ_{47} values than the inner regions. These results proved to be inconclusive, both subsamples from a glendonite spire (outer and inner) exhibit the same Δ_{47} composition as a bulk glendonite sample that had been homogenised. These results have not been reported here and will require further investigation.

These findings suggest that glendonites from the Glendon area have undergone some burial alteration through secondary calcite substitution and do not allow the accurate determination of formation temperatures due to the mixing of primary and secondarily precipitated isotopically enriched calcite.

4.5.1.2 Huskisson, Wandrawandian Siltstone

The specimens from the Wandrawandian Siltstone, Huskisson, exhibit varied calculated Δ_{47} temperatures, ranging from -23.2 ± 3.4 °C to 26.8 ± 8.8 °C. However, only WH-1, WH-2A and WH-4 can be considered as plausible formation temperatures of the glendonite pseudomorph. These span a temperature range from 1.9 ± 2.0 °C to 9.8 ± 4.5°C. This range is comparable to the known ikaite formation temperatures from the Bransfield Strait and the Ikka Fjord of -1.9 to 7 °C (De Lurio and Frakes, 1999). The specimens that produced plausible glendonite formation temperatures lie within a suite of other specimens that did not produce plausible temperature results. This indicates that not all glendonite specimens will be amenable to clumped isotope analysis to find their formation temperature, even if they are present within the same geographic area or within the same geological unit.

Other glendonites and their associated co-precipitated calcite from the Wandrawandian Siltstone (WH-5 and WH-5d, respectively) did not produce usable palaeotemperature estimates. Glendonite WH-5 is highly porous (Selleck et al. 2007) and is likely to contain diagenetically precipitated secondary calcite. This precipitation is likely to have occurred in an environment with higher ambient temperature subsequent to the primary glendonite formation. Analysis of the mixed glendonite calcite and later infill precipitated calcite using clumped isotopes provides an intermediate temperature (26.8 ± 8.8 °C). This likely reflects later diagenesis; the calculated temperature may be plausible or induced by progressive recrystallisation over a lengthy period. If the latter, the calculated temperature may be geologically meaningless. The associated secondary calcite (WH-5d) provided a formation temperature result (-23.2 ± 3.4 °C) well below that known for ikaite precipitation. The calculated temperature is not related to the ikaite mineral formation temperature or the formation of the

pseudomorph and likely represents an artefact of the enriched host water carbonate precipitation during burial.

The additional glendonite H1-B and secondary calcite spar H4-A samples both contain at least 1.4 % quartz as well as minor gypsum which may be an artefact of secondary recrystallisation as well as possible fluid migration through the deposit. Both Δ_{47} temperatures appear to be highly improbable and suggest that this glendonite and the associated calcite are not a product of primary calcite substitution from ikaite. It is likely that these glendonites have experienced later recrystallisation and/or secondary calcite precipitation.

4.5.1 Tasman Basin

Glendonite specimens from the Tasman Basin were all extracted as drill core samples from the Tunbridge Drill Hole (Selleck et al. 2007). All specimens were encased in dark siltstone of the Quamby Formation, part of the Permian Parmeener Supergroup in the Tasman Basin. Glendonite material from the Tunbridge Drill Hole (RG145) and associated amber calcite spar, exhibit vastly different Δ_{47} values and thus highly different formation temperatures. The glendonite (TUN541.7) exhibits a formation temperature of 65.2 ± 6.7 °C (Table 4.3). This is quite a high formation temperature for the pseudomorph, well outside the assumed glendonite formation temperature ranges and is a plausible diagenetic temperature. Associated amber calcite (TUN637-dk) is probably a secondary precipitation (Selleck et al., 2007) and not directly associated with the glendonite formation. It produced a formation temperature of -57.5 ± 2.8 °C a highly negative formation temperature for a marine calcite (Table 4.3). This may suggest that fluid migration as a result of the faulting within the Quamby Formation has caused diagenetic alteration. The Tasman Basin glendonite sample is likely to contain secondarily precipitated calcite with formation temperatures reflecting the localised burial history, not the initial pseudomorph formation temperature. Glendonite sample TUN541.7 (541.7 m depth) was collected from a siltstone-dominated shallow marine environment. This area has undergone substantial burial since its Permian formation, through basalt flows as well as undergoing major seismic activity displayed by deep thrusting and near-surface flower thrust faulting (Blackburn, 2004). The Tunbridge RG145 drill hole has a maximum depth of ~900m encompassing the Parmeener Supergroup overlying a major basal Permian unconformity, with overlying Jurassic dolerite (Blackburn, 2004). The extensive burial diagenesis of the Parmeener Supergroup and the glendonites contained within it has led to the clumped isotope analysis displaying an elevated formation temperature of 65.2 ± 6.7 °C. Additional calcite precipitation as vein deposits is likely to have occurred after glendonite burial and is likely to be a result of secondary precipitation from fluid migration through the siltstone of the Quamby Formation. The diagenetically precipitated material

exhibits highly depleted Δ_{47}. In addition, the $\delta^{18}O$ and $\delta^{13}C$ values of the bulk isotopic composition of the glendonite vary by ~4 ‰ compared to results found by Selleck et al. (2007). This may be related to the large temperature discrepancy, but is likely to be an artefact of sample homogeneity. Samples from Huskisson (H1-A and H4-B) and Kinghorn Point (KP-7B and KP-7Blt) suffered significant damage during storage complicating the sampling procedure. This may have led to the incorporation of external calcite-rich sediment into the sample powder in addition to glendonite calcite. This may explain the unexpectedly enriched Δ_{47} values resulting in a highly negative calculated formation temperatures.

4.5.2 Kola Peninsula

Glendonites from the Olenitsa River in the Kola Peninsula formed in estuarine conditions at the mouth of the river as it enters the White Sea. Specimens were expected to yield formation temperatures similar to glendonite formation temperatures from the Taymyr Peninsula, Sydney Basin and the Tasman Basin. However, there appears to be a significant Δ_{47} enrichment in the isotopic composition of the OR and MG glendonites. This translates to glendonite formation temperatures between -19.6 ± 3.0 °C and -15.2 ± 2.2 °C. This is significantly lower than the currently known glendonite formation temperature range. The Olenitsa River specimens (OR-1 and OR-2) display relatively high magnesite content in their mineral phases, 3.8 mol % and 2.4 mol %, Mg respectively (Table 4.3). Their kaolinite contents (1.4 % and 1.7 %, respectively) were also greater than in other glendonite specimens such as those from the Sydney and Tasman Basin in Australia. In addition, these specimens also contain some aragonite, 4.1 mol % and 4.2 mol %. This suggests that there may have been some calcium carbonate recrystallisation as well as possible secondary mineral incorporation during ikaite dehydration and infilling of the porous calcite mineral structure. The $\delta^{18}O$ and $\delta^{13}C$ values of the Kola Peninsula glendonites are comparable to the values reported by Selleck et al. (2007).

Another glendonite specimen was sourced from the Kola Peninsula (MG; exact location not known); this included a glendonite sample with associated surrounding carbonate sediment and an accompanying bivalve mollusc shell. Both the glendonite and the associated bivalve shell did not provide plausible formation temperatures. The bivalve shell was highly enriched in Δ_{47} (0.192 ± 0.030 ‰) and resulted in a calculated temperature of -21.9 ± 4.3°C. Conventional $\delta^{18}O$ and $\delta^{13}C$ values for both the bivalve shell and glendonite correspond well to those found by Selleck et al. (2007), however this is only an indication that the clumped isotope values may show a representative formation temperature. However, other specimens and standard material in the same extraction and purification runs provided good results.

4.5.3 Taymyr Peninsula

The glendonite specimen from the Taymyr Peninsula, Russia, produced very different isotopic results to the glendonite pseudomrphs from the Kola Peninsula. The Taymyr specimen originated from the Bol'shaya Balakhnya River which is much larger both in width and depth, than the Olenitsa River. The glendonite (BR-1) provided a Δ_{47} value of -0.024 ± 0.022 corresponding to a formation temperature of 6.5 ± 4.1 °C. This formation temperature plausibly represents the approximate glendonite formation temperature after the dehydration of ikaite in an estuarine environment. The glendonite calcite in the BR sample is massive in nature suggesting that it has suffered little secondary mineral precipitation. Therefore the isotopic composition is not likely to have been contaminated with secondary precipitated calcite during burial. The conventional $\delta^{18}O$ and $\delta^{13}C$ values of BR are comparable to the values of glendonites found in the Kola Peninsula by Selleck et al. (2007). However, no specimens from the Taymyr Peninsula were previously analysed or documented in the literature. Glendonites from the Kola Peninsula appear to have been subject to post-depositional secondary carbonate precipitation, significantly altering their isotopic composition as well as affecting the calculated Δ_{47} clumped isotope temperature. This suggests that the Taymyr Peninsula glendonites appear to be more suited as palaeotemperature indicators of cold water conditions in the Late Neogene compared with their Kola Peninsula counterparts.

4.5.4 North American thinolite (Type A) pseudomorphs

Glendonite pseudomorphs deposited from surface springs and sub-lacustrine springs, such as in the highly alkaline lakes of North America, exhibit intrinsically different formation temperatures to any other glendonite calcite sample analysed in this study. Thinolites are ikaite pseudomorphs that have formed as tufa-type deposits from surface springs as well as sub-aqueous groundwater springs in lacustrine environments. Ikaite is only rarely found in lakes, typically precipitating in the winter months and forming tufa deposits in summer (Council and Bennett, 1993). Thinolite samples in this study analysed by clumped isotope palaeothermometry exhibit high Δ_{47} values of 0.776 and 0.789 ‰, respectively. This corresponds to highly negative formation temperatures of between -76.9 ± 1.0 to -77.7 ± 2.3 °C (Table 4.3), for deposits from Alkali Lake. The Alkali Lake thinolite specimens all contain some aragonite (4.6 %) as well as gypsum (4.0 %; Table 4.2), the product of summer evaporation of saline water. The highly negative temperatures may indicate later precipitation of calcium carbonate after ikaite dehydration which may have formed under supersaturated conditions of enriched carbonate. Alternatively, additional precipitation of calcite may have occurred in subsequent growth years during multiple wetting and drying cycles in summer and winter. This is a potential

source of the enriched Δ_{47} values which will exhibit a highly negative formation temperature well outside the average annual lake water temperatures.

The thinolite from spring deposits of Mono Lake provide Δ_{47} value of 0.242 ± 0.024 ‰, corresponding to a negative formation temperature of -27.3 ± 3.0 °C (Table 4.3). Ambient modern temperatures of the springs range from 8 to 18 °C, with an average lake water temperature of approximately 5.0 °C (Council and Bennett, 1993; Bischoff et al., 1993; Whiticar and Suess, 1998). Recently Mono Lake has also reduced in size due to the diversion of associated tributaries. This has resulted in an increase in lake water salinity to approximately 97 ‰ today (Bischoff et al., 1993). Mono Lake exhibits high levels of alkalinity due to its high concentrations of Na^+, CO_3^{2-}, Cl^- and SO_4^{2-} in both the spring waters as well as in the mixed lake water (Bischoff et al., 1993). The presence of high levels of orthophosphate ions inhibiting the precipitation of calcite and aragonite allows the hydrated ikaite mineral to be precipitated at these thermal spring sites. The large discrepancy between the average lake and spring temperatures and the clumped isotope calcite formation temperature suggests that another more influential factor is controlling the Δ_{47} composition and is significantly enriching the precipitated calcium carbonate. This may be a result of later precipitation of additional calcite crystals in the dehydrated ikaite lattice structure if the precipitated ikaite mineral remained under the surface of the water. This is supported by small amount of aragonite (5.5 %) present in the Mono Lake thinolite (Table 4.3). However, if the ikaite were exposed then evaporation and/or the additional dissolved ions may have affected the clumped isotope signature of the analysed thinolite calcium carbonate. This is similar to the proposed phenomenon occurring within Alkali Lake.

4.5.5 Relationship of calcite to water of hydration and ambient pore water

The relationship between ikaite, its water of hydration and the surrounding ambient pore water have been documented through laboratory experiments and measurements of naturally precipitated ikaite crystals (from the Zaire Fan; Rickaby et al., 2006 and the Antarctic Peninsula; Lu et al., 2012) and their respective hydration waters and associated pore water isotopic values. Laboratory synthesis experiments show that ikaite hydration waters dependably record the $\delta^{18}O$ composition of the ambient pore water of precipitation (Rickaby et al. 2006). If ikaite forms authigenically then the $\delta^{18}O$ value of the hydration water closely represents the $\delta^{18}O$ value of the surrounding pore-water (Lu et al., 2012). In addition $\delta^{13}C$ value of ikaite was found to accurately reflect the $\delta^{13}C$ values of the dissolved inorganic carbon (DIC) of the pore water. These results suggest that ikaite $CaCO_3$ is able to closely reflect both the isotopic composition of its hydration water and can also be utilised to infer the $\delta^{18}O$ of

the palaeo-porewater. This relationship appears to be temperature sensitive in ikaite formed between 2 and 4m below the sediment-water interface (Lu et al. 2012); at greater depths this may not be true.

Analyses in this study show that Late Neogene glendonites from the Tyamyr Peninsula retain their calculated $\delta^{18}O_{(water)}$ value of the palaeo-porewater, whereas Permian glendonites from the Sydney Basin, Australia exhibit lower $\delta^{18}O$ values, suggesting that long-term burial in this area and subsequent uplift has facilitated isotopic exchange with meteoric water.

The relationship between ikaite and ambient pore-water has only been investigated for relatively modern (Holocene) tufa deposits. The effect of long-term burial diagenesis and the chemical exchange with water of hydration on the isotopic composition if ikaite and its recorded formation temperature are still largely unknown. However, the relationship of pore water to ikaite $CaCO_3$ is established and indicates that isotopic exchange between different water sources after ikaite dehydration is minimal. Therefore there are grounds to assume that, under some circumstances, the calculated glendonite formation temperatures from clumped isotope palaeothermometry may be reliable.

4.6 Conclusions

This study was undertaken to assess the suitability of the glendonite pseudomorph (after ikaite) as a potential palaeoenvironmental indicator. The occurrence of the glendonite pseudomorph within the geological record is indicative of cold-water environments between approximately ~1.9 to 7 °C (De Lurio and Frakes, 1999), as shown by modern occurrence and laboratory growth experiments of ikaite. Pseudomorphs from various environments were analysed for their formation temperature using clumped isotope palaeothermometry. The calculated temperature should reflect the temperature of the ambient environment during the dehydration of the ikaite (calcium carbonate hexahydrate) to its pseudomorph calcite (calcium carbonate) state. Formation temperatures between 1.9 ± 2.0 °C to 9.8 ± 4.9 °C were found in glendonite specimens from the Sydney Basin in the Wandrawandian Siltstone. Glendonites from other regions such as the Taymyr Peninsula in Russia provided temperatures of 6.5 ± 4.1 °C. These calculated temperatures correlate reasonably well, within the margins of error, to the known range of ikaite precipitation and glendonite formation temperatures. Lacustrine spring thinolite samples exhibited unexpectedly enriched Δ_{47} values, producing highly negative formation temperatures, suggesting other precipitation dynamics influenced the isotopic composition of pseudomorphs from these environments. These temperatures were calculated using the Zaarur et al. (2011) temperature equation. This function was utilised due to its inclusion of biogenic and inorganic calcite as well as its total range of inorganic calcite temperature precipitation reactions included in the palaeotemperature equation. In addition, the instrumentation and extraction procedure is similar to the one used in this study.

Results show that deep burial conditions and sites of post depositional fluid migration through sedimentary facies have the potential to greatly alter the Δ_{47} values and associated calculated formation temperatures of the calcite pseudomorphs. This is evident from deeply buried (>500m) glendonites in the Sydney Basin and the Tasman Basin (H4-A and TUN541.7 respectively) that indicate formation temperatures above 65 °C, well outside the known precipitation range of the precursor mineral ikaite. However, due to the known burial diagenesis of the samples, the calculated temperature is probably a reflection of recrystallisation temperature during burial. Glendonites from the Sydney Basin (WH-5) indicated an elevated temperature of 26.8 ± 8.8 °C but not to the same extent as other glendonites in the same sedimentary succession. Glendonites in these locations also exhibit large amounts of associated secondary calcite precipitation as well as a highly crystalline morphology. This suggests that both fluid migration and increases in burial depth and thus pressure have led to substantial recrystallisation. This has led to resetting the clumped isotope signature of the associated glendonites, producing atypically high calculated formation temperatures for the glendonite pseudomorphs. Thus glendonite specimens from deeply buried sequences do not necessarily provide

suitable material for the investigation of clumped isotope (original) formation temperatures, although some calculated temperatures are plausibly appropriate for diagenesis.

Tufa (Type A) glendonite pseudomorph deposits, such as the bipyramidal thinolites from Alkali Lake (AL) and the larger aggregate thinolite from Mono Lake (ML), do not produce realistic palaeotemperatures using the clumped isotope method. This is likely caused by the high alkalinity of these lakes and their high concentrations of orthophosphates and organic material. These precipitation environments also experience high evaporation rates and rapid degasing of precipitation fluids which leads to a substantial enrichment in the Δ_{47} value. This will probably occur during evaporation of lake water during the warmer months. Additionally, due to the high porosity of the dehydrating calcium carbonate hexahydrate, void crystal lattice spaces have a higher likelihood to be in-filled by secondary calcite after the initial precipitation. Thus the overall isotopic composition of the thinolite crystal exhibits a highly enriched Δ_{47} value and thus a very low calculated precipitation temperature.

The bulk mineral composition (i.e. purity) of the glendonite does not appear to have any direct effect on the calculated formation temperature. However, the presence of clastic silicate minerals indicates if the crystal lattice or the pore space of the calcite mineral were infilled during precipitation and subsequent burial. This gives an indication of burial diagenesis, an indication of evaporation as well as burial secondary calcite precipitation. The specimens in this study that exhibited significant amounts of incorporated minerals such as quartz, gypsum and kaolin also exhibited highly elevated Δ_{47} values of the carbonate and subsequently highly negative and implausible formation temperatures for glendonites in their respective environments.

The $\delta^{18}O_{water}$ calculated for the glendonites in this study gave several plausible values. We show that Late Neogene glendonites retain the $\delta^{18}O$ value of the precipitating host seawater, whereas Permian glendonites exhibit lower $\delta^{18}O_{water}$ values, suggesting that long-term burial facilitates isotopic exchange with meteoric water.

In conclusion, during the formation of the glendonite pseudomorph (i.e. the ikaite dehydration), the specimen's burial history and its preservation in the geological record is a highly complex combination of processes. Several factors have to be considered to determine if the calculated clumped isotope palaeotemperature estimates are plausible. The presence of glendonites provides a general indicator of cold water temperatures in their precipitation environment during the dehydration of ikaite to the calcite pseudomorph. Through the use of clumped-isotopes, some formation temperature conditions of naturally occurring glendonites were estimated. Thinolite calcium carbonate deposits associated with lake springs analysed by clumped isotope palaeothermometry do not yield expected or plausible formation temperatures of their natural environment. This is due to other ambient factors such as degassing and evaporation altering the Δ_{47} signal. Glendonites from the marine environment have the potential to yield clumped isotope palaeotemperature results that

conform to the accepted formation temperatures of the calcite pseudomorph. However, this is only true if the glendonite has not experienced any significant burial diagenesis through recrystallisation of the calcite mineral by fluid migration and or during deeper burial, i.e. significant temperature increase.

From the results it appears that glendonites do have the potential to indicate past climate conditions within the sedimentary geologic record. Specimens from the Sydney Basin, Tasman Basin and the Taymyr Peninsula provide calculated clumped isotope formation temperatures between 1.9 and 9.8 °C. This compares well to the currently known 1.9 to 7 °C range of ikaite occurrence. This confirms that the ikaite pseudomorph forms naturally within the previously postulated formation temperatures. However, the formation of glendonites involves a complex array of variables and conditions that determine the isotopic composition of the precipitated pseudomorph. An increase in temperature by post-depositional burial as well as low-grade metamorphic processes has the potential to cause calcite recrystallisation at elevated temperatures. This resets the original clumped-isotope Δ_{47} value of the calcite and will yield a substantially higher overestimated formation temperature. Post-depositional secondary calcite precipitation from fluid migration or evaporation precipitating in the porous cavities of the pseudomorph structure also has the potential to substantially alter the calculated clumped isotope formation temperature. Therefore, if glendonites are to be utilised as a palaeotemperature indicator, specimens with deep burial histories or potential metamorphism as well as specimens that exhibit significant secondary crystalline calcite precipitation in pore spaces should be avoided.

Chapter 5: Cave Systems of Riversleigh, Queensland

5.1 Introduction 128
5.2 Background 129
5.2.1 Carbonate karst chemistry 130
5.2.2 Speleothem morphology 132
5.2.3 The geology of the Riversleigh area 133
5.2.4 Dating of the Riversleigh deposits 135
5.3 Methods 137
5.3.1 Sample collection and preparation 137
5.3.2 Thin sections 138
5.3.3 Isotopic analysis 138
5.4 Results and discussion 139
5.4.1 Carbonate facies descriptions 139
5.4.1.1 Neville's Garden site (NG) 139
5.4.1.2 Godthelp Hill area 147
5.4.1.3 Bitesantennary site (BC) 159
5.4.1.4 Cleft of Ages site (CA), White Hall site (WH), Oncoid site (OS) and Ringtail site (RT) 169
5.4.2 Clumped-isotope Δ_{47} palaeotemperature determinations 176
5.4.2.1 Neville's Garden site 177
5.4.2.2 Inabayence and Camels Sputum sites 177
5.4.2.3 Stalagmite site 178
5.4.2.4 Bitesantennary site 178
5.4.2.5 Cleft of Ages, Oncoid and White Hall sites 179
5.4.2.6 Ringtail site 180
5.4.3 Enriched Δ_{47} values and associated highly negative temperatures 181
5.4.4 Calculated $\delta^{18}O$ of host waters 183
5.5 Conclusions 186

5.1 Introduction

Karst environment cave systems are one of the most important accumulators of terrestrial fossil material with depositional environments such as sink holes, underground pools, streams, tufa terraces, calcite-lined rim pools and calcite encrusted ponds. These structures have the ability to trap a variety of organisms and preserve them in a rapid depositional environment resulting in a high diversity of well-preserved fossil specimens. Karst environments have the ability to provide high-resolution geochemical, geochronological and isotopic calcite precipitation records and provide some of the most comprehensive terrestrial climate records. A fundamental problem associated with investigating Earth-surface temperatures is that carbonate cave deposits do not always precipitate in equilibrium with the surrounding environment. This leads to isotopic fractionation through evaporation and gas exchange with cave air and may have adverse effects on the isotopic signature.

The limestone karst landscape of Riversleigh, north-western Queensland, provides conditions that enable the formation of carbonate deposits as stalagmites, flowstones, cave pearls, calcite rafts and travertine rim pools. These cave systems encompass faunal and environmental changes over the last 25 million years. The diverse range of speleothem material available provides an ideal opportunity to compare and contrast different carbonate precipitates in association with fossil material that may aid in the broader understanding of carbonate cave systems and the faunal assemblages within them.

Initial applications of the carbonate clumped-isotope method to carbonates precipitated at equilibrium can be analysed in a straightforward manner. By contrast, non-equilibrium precipitated carbonate deposits such as stalagmites have provided formation temperatures significantly different to carbonate precipitated in associated speleothem deposits in close proximity. These calculated temperatures are typically up to 6 to 8 °C higher than the accepted and recorded calcite precipitation temperature (Daëron et al., 2011). This chapter aims to compare equilibrium to non-equilibrium carbonate precipitation temperatures in a karst system to identify the average ambient temperature in the Oligo-Miocene period in the Riversleigh area.

5.2 Background

Precipitated cave deposits and formations are collectively referred to as speleothems (Hill and Forti, 2003) and refer to a mode of occurrence and morphology rather than a specific mineral composition. Speleothem deposits may be carbonates, sulfates and halides, as well as other rarer soluble materials. This chapter focuses on the carbonate minerals within the limestone karst and cave systems of Riversleigh.

Carbonate minerals constitute >95 % of all cave mineral deposits, the majority being calcite and aragonite. The calcite mineral deposits are either massive aggregates or exhibit trigonal or rhombohedral crystal habits. Other possible associated carbonate-based minerals include hydromagnesite ($Mg_5(CO_3)_4(OH)_2 \cdot 4H_2O$), a hydrated magnesium carbonate mineral that is commonly the diagenetic product of brucite and serpentinite. This mineral is the primary constituent of 'moon milk' in cave systems rich in magnesium. Dolostone is another speleothem rock type formed from dolomite ($CaMgCO_3$) as shown in Figure 5.1 (Leighton and Pendexter, 1962).

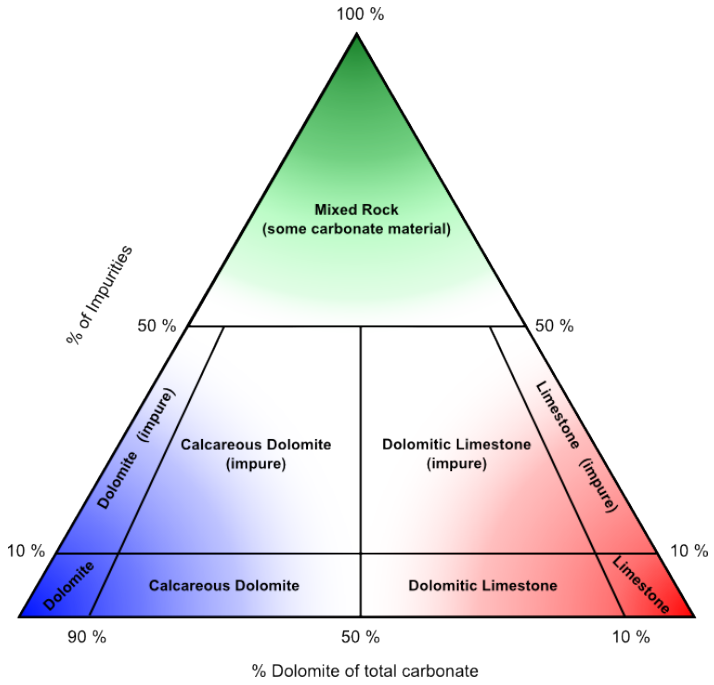

Figure 5.1: Classification of bulk carbonate rock composition, showing the dolomite content (in %) of total carbonate and the proportions of impurities. The composition name should be stated if the impurities are known. Modified from Leighton and Pendexter (1962).

5.2.1 Carbonate karst chemistry

Speleothems form in subsurface cavernous space in which both water and air exist and constant chemical exchange takes place between them. Water leaching through the surrounding bedrock of the cave will dissolve several components (Equation 5.1). This solubility potential is dependent on the amount of carbon dioxide gas in solution as well as the source of the water and the ambient temperature. The saturated solution then flows through the bedrock until it reaches an open cavity where there is a potential for the CO_2 in solution to exchange with the air, leading to supersaturation of the solution. This in turn will cause precipitation of the dissolved solutes as carbonates in various morphologies depending on the interaction between the air and water. This precipitation accumulation may continue at a micro scale for many thousands of years creating a layered sequence of carbonate precipitation within the cave deposit with potential to record the changes in chemical composition and physical parameters of the cave system over time.

$$HCO_3^- + H^+ \rightarrow CO_2 + H_2O$$ **Equation 5.1**

This deposition occurs at various rates in different cave systems and is controlled by many factors but is primarily a function of the dissolution rate and the precipitation rate of calcite from a saturated solution, as described by Plummer et al. (1978).

$$R = k^4(HCO_3^-)_S\,(Ca^{2+})_S - k_1\left(H^+\right)_S - k_2\left(H_2CO_3^*\right)_S - k_3$$

$$R = \alpha\,(c - c_{eq})$$ **Equation 5.2**

where, c is the real calcium concentration in solution in $mmolL^{-1}$ and c_{eq} is the equilibrium concentration in relation to calcite, α is the kinetic constant, which is dependent on temperature, the pCO_2 and the V/A volume of the solution to surface area of deposition and localised flow conditions (Equations 5.2 and 5.3).

From this principle, it is implied that precipitation of calcite is driven by the same reactions as chemical dissolution; however, the supersaturation of calcite in solution caused by degassing of CO_2 allows the reverse reaction to occur leading to precipitation of calcite on the cave floor.

This precipitation reaction and calcite deposition also controls cave deposit growth rates. If cave water flow is laminar, the above equation (5.3) is used to calculate a deposition rate. If flow is turbulent, through dripping from cave ceilings, the average growth rate is defined by Dreybrodt (1988, 1999).

$$R_{AV} = (c\text{-}c_{eq}) \left[1 - \exp\left(-\frac{T\alpha}{\delta}\right)\right] \delta / T \qquad \textbf{Equation 5.3}$$

where, c is the real calcium concentration in solution in $mmolL^{-1}$ and c_{eq} is the equilibrium concentration in relation to calcite, α is the kinetic constant, δ is the thickness of the flow and T is intervals of time (Figure 5.2).

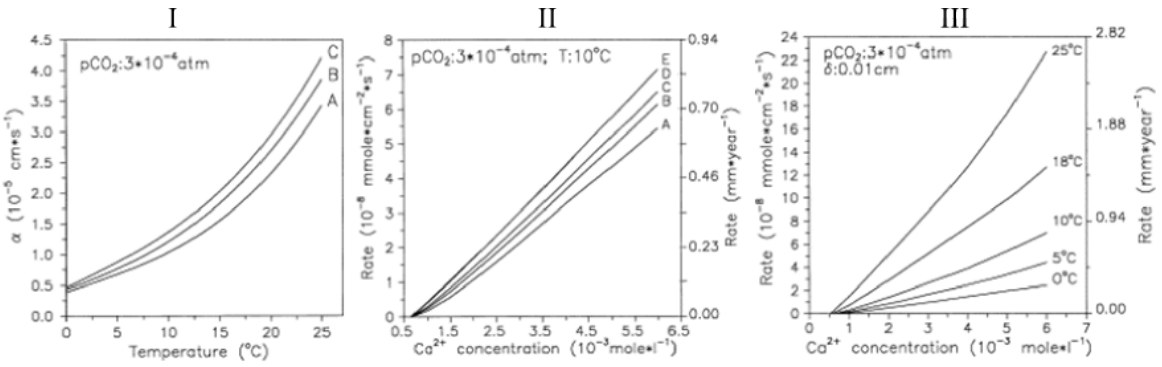

Figure 5.2: (I) Values of α in relation to temperature for various flow thicknesses δ, (A) δ=0.005cm, (B) δ=0.0075cm and (C) δ=0.01cm, for laminar flow. (II) Precipitation rates for various flow thicknesses δ, (A) δ=0.005cm, (B) δ=0.0075cm, (C) δ=0.01cm, (D) δ=0.02cm, (E) δ=0.04cm, as a function of calcium concentration (c) for laminar flow. (III) Deposition rates for various boundary-layer thicknesses in turbulent flow in a depth of 2 cm (Baker et al., 1998).

From this it can be seen that precipitation rates of calcite in caves cannot be derived from simple calculation of solution chemistry. This is due to the change in bulk solution flow dynamics as well as the slow dissolution reaction of bicarbonate and acid to carbon dioxide and water. The geological setting of the cave system, bulk solution chemistry, surface area to volume ratios and reaction surfaces of the precipitating solution play a more crucial role in the formation of cave deposits as well as the nature of the flow conditions experienced (Dreybrodt, 1999). Additional external factors in aerially exposed caves, for example precipitation and evaporation, and associated parameters such as air movement and biotic influences such as flora and fauna, are important.

5.2.2 Speleothem morphology

Speleothems occur in several forms and morphologies depending on the movement of water, the intensity and saturation of the solution and the air flow in the cave system that is in contact with the water. Speleothems may be classified into four main form categories based on water interaction type; dripping water (dripstones; stalactites and stalagmites), flowing water (flowstones), seeping water (cave crystals/speleoforms; helictites, outopholites and anthodites) and standing water (concretions and spar; White, 2012).

Dripstones encompass the most recognised form of stalagmites and stalactites and which form by water percolating vertically into a cave along fractures and joints in the bedrock. Stalactites form by slow dripping water from the cave ceiling thence carbonate precipitation to form a ring and later dome shaped structure as the water runs off. At the cave floor where water lands, a secondary precipitation occurs as not all calcite is precipitated on the ceiling; this is referred to as a stalagmite. A stalagmite and stalactite may coalesce to form a single structure (column) which becomes a secondary flowstone (Frisia and Woodhead, 2012).

Flowstone forms as a thin but broad sheet-like deposit on cave walls and floors. Flowstone forms by carbonate deposition from flowing water originating from cracks and horizontal fractures in the cave wall or floor allowing the water to flow laterally over a large area. These thin sheet flows ultimately contribute the majority of carbonate within speleothems and commonly appear as drapery, curtains or simple broad ground coverings. Depending on the specific solution and sediment load of the water at the time of precipitation these structures may also be laminated in different colour bands showing changes in cave water origin or different dissolution characteristics.

Low-flow **seepage** through bedrock may precipitate crusts and small crystal aggregates on cave walls. Due to the high solute load of the water and the evaporation of this supersaturated solution, it is typical for aragonite to be formed rather than calcite. These formations are referred to as frostwork or anthodites. An additional type of speleothem seepage product are helictites which form when there is an insufficient flow rate to form droplets. This results in a tube-like helical structure which grows from the tip (Hill and Forti, 2003).

Standing-water speleothems have a typical rounded structure and exhibit the growth habit of their component materials (White, 2012). Formation morphologies include cave pearls and pool spars. Cave pearls form by precipitating a near-spherical calcite layer around a central nucleus. This may be a sand grain, calcite crystal, or biogenic material such as animal remains. The water body in which the precipitate is submersed must be under constant motion to prevent the pearls

becoming attached. The constant precipitation and overturning of the structure forms a layered calcite concretion, which ranges in size from millimetres to approximately 15 cm in diameter, commonly in large groups of similar sized pearls.

Standing water in cave pools will become supersaturated by the degassing of CO_2 if no additional inflow of water is present. This may form calcite crystals at the air to water interface. These may aggregate to form floating calcite rafts which sink to the bottom of the pool and aggregate as stacked calcite plates. However, calcite crystal formation is not limited to the water surface. Most standing cave pools exhibit calcite spar formation within the water body, as the calcite may nucleate underwater. Their crystal structures may be mass aggregates of small layered crystals or near to perfect hexagonal scalenohedral crystals (White, 2012).

5.2.3 The geology of the Riversleigh area

The vertebrate fossil deposits at Riversleigh are located in northwestern Queensland, Australia, approximately 200 km south-west of the Gulf of Carpentaria between the Nicholson and Gregory Rivers and approximately 420 km north of the town of Mt. Isa (Figure 5.3).

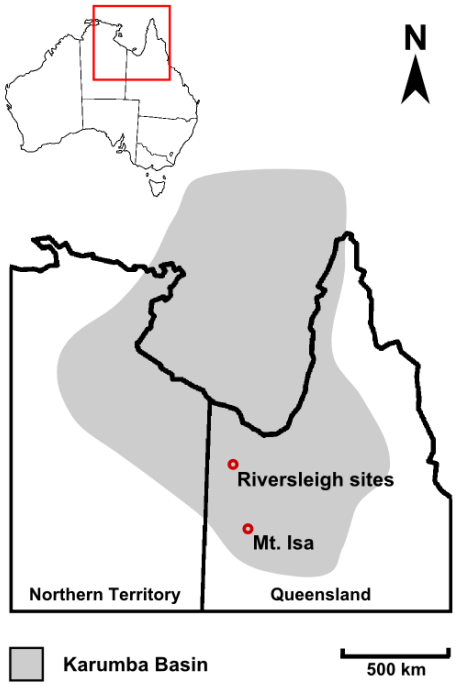

Figure 5.3: Locality map of the Riversleigh fossil sites showing the extent of the Karumba Sedimentary Basin, northwest Queensland.

The regional geology can be summarised as the following succession (Figure 5.4). The basement comprises the Lawn Hill Platform (upper McNamara Group; Lawn Hill Formation and Riversleigh Siltstone) of Proterozoic age, overlain by the dolomitic Thorntonia Limestone of Cambrian age. The latter locally contains chert nodules, minor phosphatic units, and a chert breccia/conglomerate unit at its upper unconformable boundary. Overlying this are basal sediments of the Oligo-Miocene Carl Creek Limestone. The Carl Creek Limestone is the confining unit for a large proportion of the Riversleigh fossil sites including the four main terrestrial and cave-fill depositional systems (informally named A, B, C and D).

The Carl Creek Limestone (Telford, 1967, Archer et al., 1986; 1986, Megirian, 1992) forms an outcrop area of 25 km^2 within the drainage basin of the Gregory, Nicholson and O'Shanassy Rivers. There are several lithologies including interbedded sand and conglomerate within the dominant limestone. In the following sections, details of the field relations and petrology of sampling sites are presented.

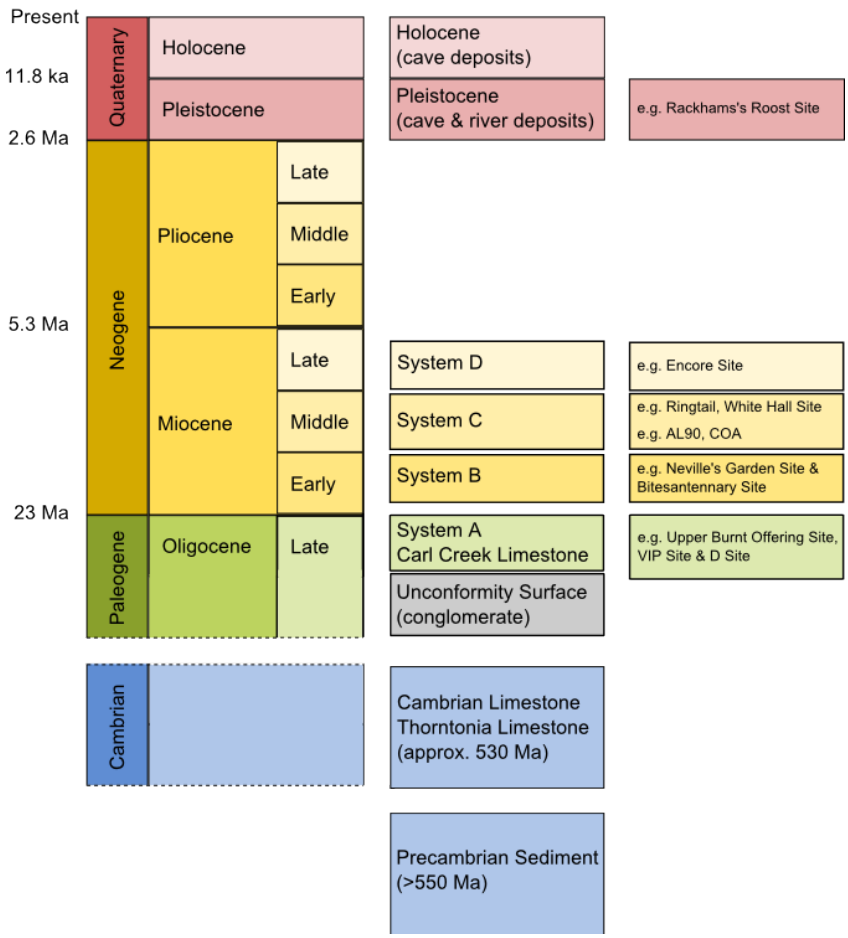

Figure 5.4: Summary stratigraphic diagram of the Riversleigh deposits. The most fossil-rich deposits are represented by System A, B, C and D limestone as well as younger cave deposits and other fill deposits. Modified from initial findings by Archer et al. (1994) and updated with information by Woodhead et al. (2014).

5.2.4 Dating of the Riversleigh deposits

All dates presented are taken from previous work on the Riversleigh fossil assemblages. These have been compiled since the initial discovery of the site in the 1960s and described in many fundamental scientific papers by Archer, Hand and Godthelp. Since the initial discovery of the Riversleigh fossil area, including the renowned D Site area in 1963 by Telford, subsequent visits starting in 1976 by Archer recognised increasingly more diverse environments. Dating of the Riversleigh fossil material has been attempted by both radiometric methods and biocorrelation, with varying rates of success (Archer et al., 1994).

Numerical dating using radiometric methods is the most accurate and precise method of determining the actual age of a particular fossil or sediment. Typically usable elements for radiometric dating are uranium, potassium or for more modern samples carbon or lead. For example, the sample's stratigraphic association must be certain, there should be no contamination or diagenetic alteration, and the rock needs to have formed within a closed geochemical system (Geyh and Schleicher, 1990).

Unfortunately, there is limited opportunity to apply most radiometric methods to the Riversleigh fossils and their surrounding geological materials. Many of the limestone deposits contain only minor amounts of the appropriate radioactive elements. Recently further possibilities have been proposed, such as ^{10}Be dating, and U-Pb dating of stalagmites and other speleothem deposits.

The other most common technique of determining the age of the Riversleigh deposits has been by bio-correlative methods. Various terrestrial and fresh water species are able to be utilised in the bio-correlation method of the Riversleigh fauna from other international fossil occurrences that have been extensively categorised by numerical dating techniques (Archer et al., 1994; 2006). Bio-correlation of the Riversleigh fossils has been made using bats (i.e. *Brachipposideros*), diprotodontids (i.e. *Ngapakaldia*) an the potoroid kangaroo (*Wakiewakie lawsoni*) (Travouillon et al. 2006, Archer et al., 2006). However these can only be used to determine relative age references and must be supported by numerical dating.

The recent work by Woodhead et al. (2014) produced a radiometrically-dated chronologic sequence for the Riversleigh fossil area. Results show that previous bio-correlation dating was largely successful and the U/Pb dates closely reflect those previously postulated for various faunal assemblages (System A, B, C and D), see Figure 5.5. In this study, we apply the newly derived dates to the various sites from which clumped isotope temperatures were calculated.

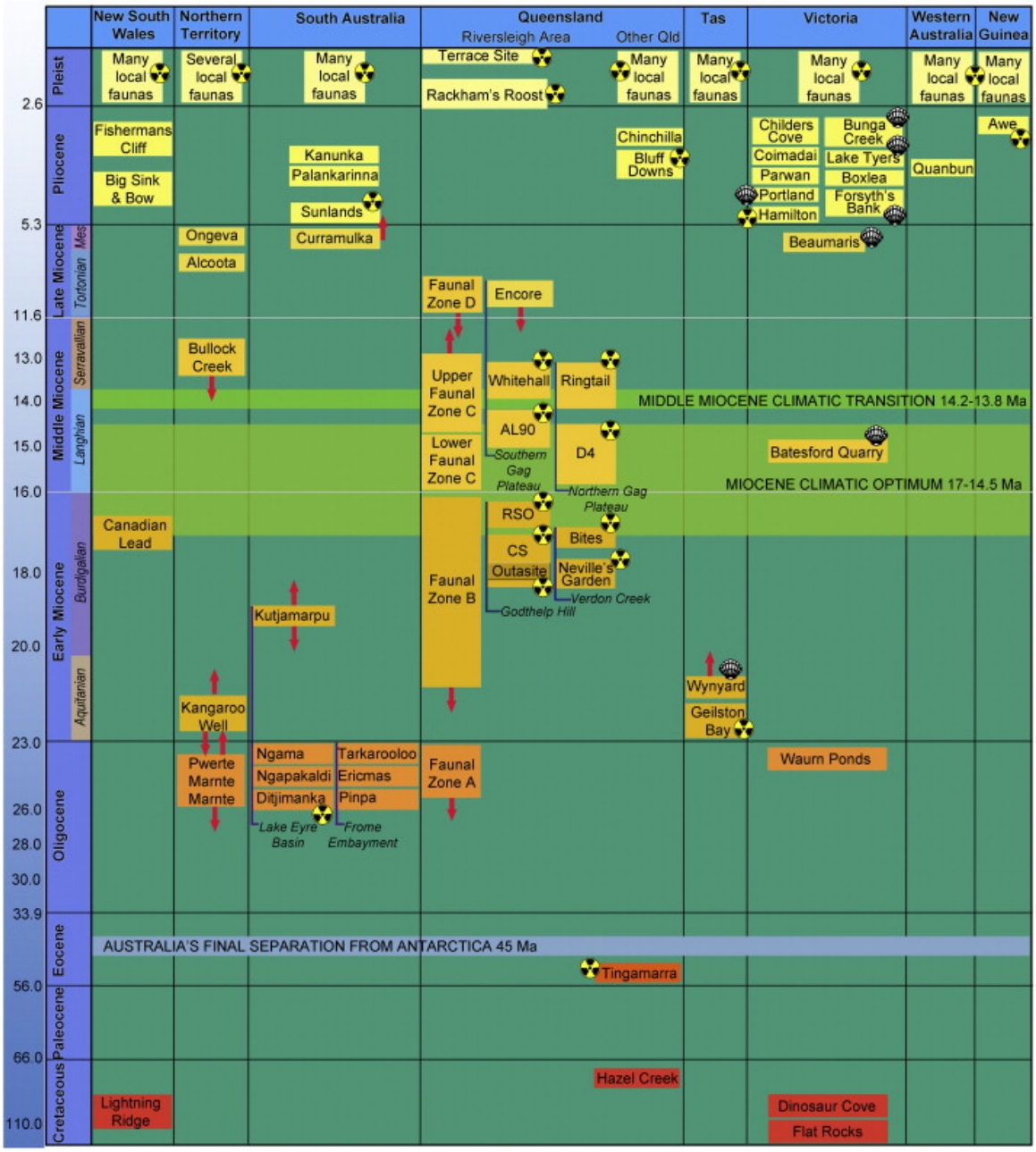

Figure 5.5: Stratigraphic age relationships of the Riversleigh Oligocene, Miocene and Plio-Pleistocene deposits. Deposits are dated on the basis of marine bio-correlation (shell symbol) and vertebrate stage-of-evolution bio-correlation. The radiometric dates derive from U/Pb dates of carbonate material (radiation symbol) from Woodhead et al. (2014).

5.3 Methods

5.3.1 Sample collection and preparation

Samples were collected at various sites in the Riversleigh area including the Neville's Garden (System B), Bitesantennary (System B), Camels Sputum (System B), Inabayence (System B), Stalagmite (System B), Cleft of Ages (System C), White Hall (System C), Oncoid (System C) and Ringtail (System C) see Figure 5.6. These encompass two of the main system types in the Riversleigh area in addition to cave deposits and fissure fills.

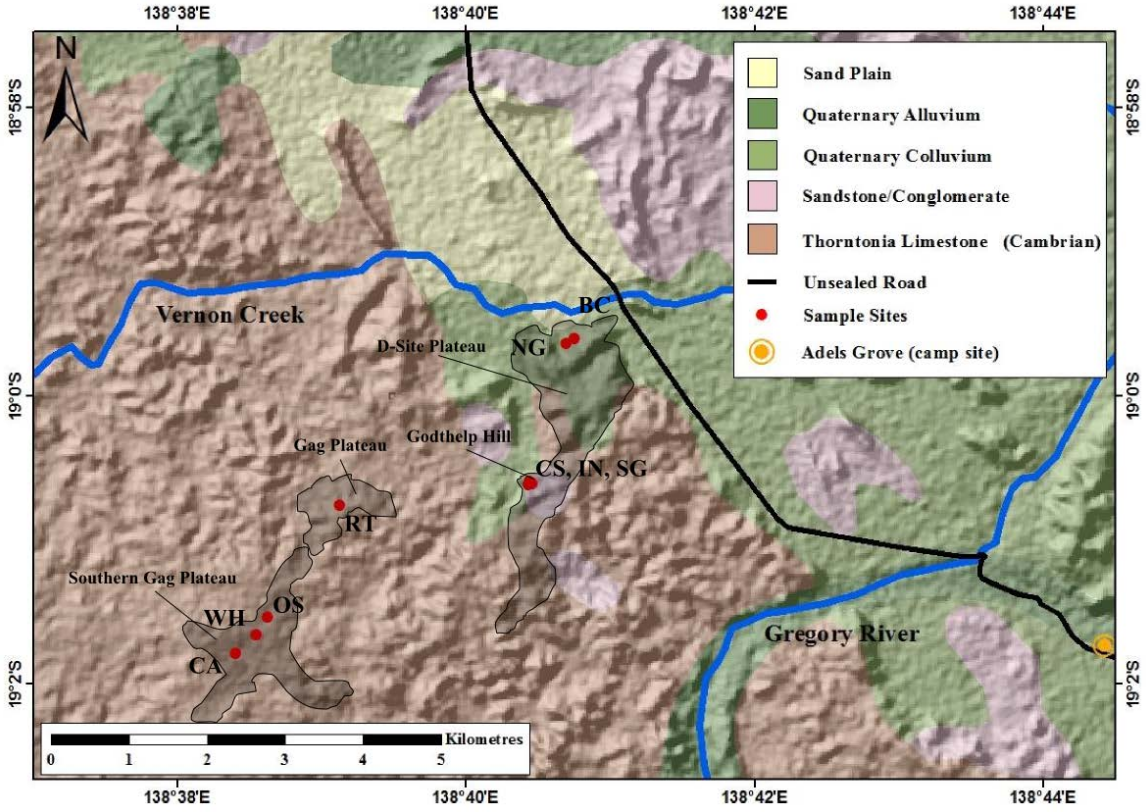

Figure 5.6: Riversleigh area map showing the major geological outcrop units (see legend), System B (AL-90, CA - Cleft of Ages site, WH - White Hall site, OS – Oncoid site, and RT – Ringtail site) and System C (NG – Neville's Garden site, BC – Bitesantennary site, CS – Camels Sputum site, IN – Inabayence site and SG – Stalagmite site). The grey overlay indicates the areas of the Oligo-Miocene karst deposits.

The samples were named and numbered in the field and their positions photographed to provide orientation and relation to adjacent samples and site-specific depositional characteristics. All material was later catalogued and described by depositional environment. The relative depths and

thicknesses of rock features and excavation pits were noted in the field through measurements and schematic sketches later digitised into overview. A handheld GPS unit (Global Positioning System) was used in the field to record the location and elevation of the sampling sites.

In the preparation laboratory, samples were cleaned and scrubbed with distilled water to remove any loose debris and accumulated dust or other surface contaminants. This initial preparation step, and further photography, allowed additional features of the field samples to be identified previously not noticed in the field such as lamination structures, intra-matrix clasts, and orientations of prominent features.

5.3.2 Thin sections

A total of 29 thin sections (30 µm thick) were produced by standard methods at the University of Wollongong (UOW). These included examples from all rock types, and were examined by petrographic microscope and point counter. The rocks were classified according to Leighton and Pendexter (1962) using the point count method combined with XRD analysis and minor-element data from ICP-MS analysis. Additionally, the thin sections were viewed under ultraviolet light in order to identify areas with abundant organic matter.

5.3.3 Isotopic analysis

A variety of materials from Riversleigh were analysed isotopically. These include shells, bones and teeth. Speleothem samples were taken as bulk whole-rock powders as well as sub-sampled from larger complex structures. Bone samples were pre-treated in 0.1M acetic acid for 3 days to remove adhering carbonate from the surrounding matrix. Sample pre-treatment for all Riversleigh carbonate specimens remained as previously described in Chapter 3.

The isotopic analysis method was the same as for other carbonate samples (Chapter 3). However, due to the increased magnesium contents of some of the speleothem samples, the acid-digestion reaction time was increased from ~12 hours to 18 hours or 24 hours to insure all carbonate material was fully reacted with phosphoric acid. Reaction temperatures remained unchanged as well as the acid volume to carbonate ratio.

Bone material was also subjected to lengthened H_3PO_4 reaction times up to 48 hours due to the low proportion of calcium carbonate in the bone mineral lattice structure (~3-7 % w/w). The bone samples proved difficult to extract due to the relatively high sample powder amounts needed to yield sufficient carbon dioxide. Samples between 100-200 mg were commonly utilised.

5.4 Results and discussion

Each study site within the Riversleigh area is described in terms of its stratigraphy, carbonate micro-facies structure and depositional history. A combination of hand sample, thin section, mineralogy and minor-element analyses characterise each site. Within each site, materials such as bone fragments and various calcite macro-structures were examined for their palaeotemperature through 'clumped' isotope analysis to define the depositional environment. The sampled field sites are described in stratigraphic order, starting with those from faunal zone (or system) B, followed by the younger sites from system C (Figure 5.5).

5.4.1 Carbonate facies descriptions

5.4.1.1 Neville's Garden site (NG)

The Neville's Garden site, part of the Riversleigh System B faunal assemblage is thought to have been an exposed pool with associated cave structures, as confirmed by the finding of cave straws and travertine pool rim structures in the surrounding rock and amongst the fossils in 1988 by Neville Whitworth (Archer et al., 1994, p. 167). Two small stalagmites found in the immediate area provide further evidence of an associated cave structure. Fossils from the Neville's Garden site indicate the complexity of the surrounding environment, with a variety of organisms preserved together. Various forest animals such as the marsupial lion (*Wakeleo* sp.) the herbivorous diprotodontid marsupial (*Neohelos* sp.) as well as various smaller creatures such as the omnivorous musky rat-kangaroo (*Hypsiprymnodon bartholomaii*), possums and the toothed platypus (*Obdurodon* sp.) occur (Archer et al., 1994). It is possible that the Bitesantennary site (also System B) which today lies on the opposite side of the hill may have been connected through subterranean caves and flow paths.

The Neville's Garden excavation pit has a thick basal limestone unit (Figure 5.7), the lower extent of which is unknown. Overlying this is a well laminated 5cm thick flowstone thinning towards one end of the excavation pit to less than 2 cm in thickness. The layering of the flowstone appears to conform to the surface of the underlying cave base material. The flowstone unit is interbedded with the underlying cave limestone in the thicker part of the sequence and displays a fragmented and irregular contact (left side of Figure 5.7 showing the mixing between the cave base and flowstone layers). Overlying the flowstone unit is a mottled cave-fill deposit, off white to pale

yellow in colour with dark brown oxidised mottles. Within this layer secondary calcite nodules occur with fracture-fill calcite crystals.

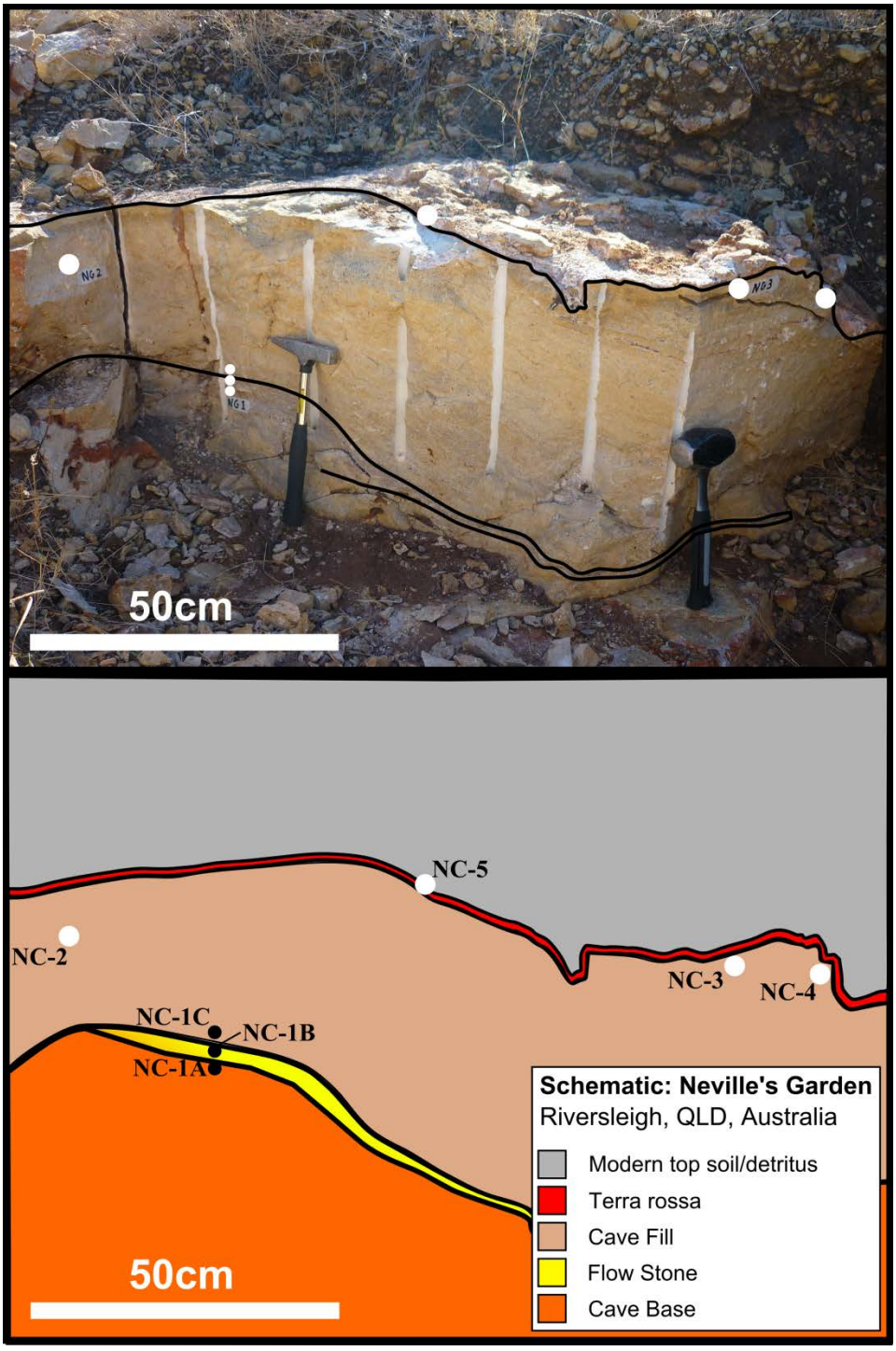

Figure 5.7: Photograph and sketch of the Neville's Garden site showing the cave base material NG-1A with the overlying flowstone NG-1B and overlying cave fill material NG-1C and NG-3. Overlying these layers is the red/brown terra rossa layer. Superimposed on this are modern soil and rock detritus. The photograph is taken facing south into the plateau.

Overlying the cave-fill is a partially consolidated younger fine-grained red/brown mudstone possibly Holocene in age or a late stage depositional feature if the flow rates of the cave waters slowed and the source became fluvial as more lithic material accumulated over the consolidated speleothem material.

If the Neville's Garden site is a combination of cave fill and travertine rim pool deposits with associated flowstone laminates it is possible that the environment developed as a late-stage cave collapse with subsequent change in the upper lithology to a lithic mudstone deposit. However this mudstone deposit may also have formed purely as a product of change in sediment load of the water flow from a lithic source. The nature of the travertine rim pool type deposition structure would contain the fine-grained muds which settled out into finely laminated sheets of red/brown oxidised upper sheets of the speleothem deposits.

Flowstone NG-1 was subdivided into three subsections (NG-1A, 1B, 1C); A – below the flowstone, B – flowstone and C – above the flowstone. The basal layer of Neville's Garden NG-1A indicates a cave base limestone, containing 75.8 % calcite, 4 % aragonite, 3.3 % quartz and 12.2 % kaolinite in addition to minor constituents of other carbonates (Table 5.1A). The high content of non-calcareous clastic material (quartz and kaolinite) indicates that the cave base may have had inputs from other sedimentary sources over its deposition cycle and may not solely be a speleothem deposit. Both overlying layers, NG-1 B and NG-1C, are composed of pure calcite with negligible clastic materials. This indicates that the flowstone (NG-1B) and superimposed cave fill (NG-1C) deposits are likely to be of speleothem origin.

Table 5.1: Neville's Garden site. (A) XRD mineral phase contents (wt %) of the homogenised sample powder; (B) ICP-MS carbonate cation substitution in molar percent, based on total molar concentration; (C) Carbonate classification through point count analysis from thin sections using the Folk (1959) system.

A

Sample Name	% Calcite ($CaCO_3$)	% Dolomite ($CaMgCO_3$)	% Magnesite ($MgCO_3$)	% Siderite ($FeCO_3$)	% Aragonite ($CaCO_3$)	% Quartz (SiO_2)	% Kaolinite ($Al_2Si_2O_5(OH)_4$)	% Gypsum ($CaSO_4 \cdot 2H_2O$)
NG-5	91.5	0.4	0.4	1.3	1.2	2.2	1.7	1.2
NG-3	97.8	0.3	0.6	0.7	0	0	0.4	0.3
NG-1C	98.8	0.5	0	0.4	0	0	0.2	0
NG-1B	98.2	0.6	0	0.3	0	0	0.3	0.6
NG-1A	75.8	0.2	0.5	0.5	4.0	3.3	12.2	3.5

B

Sample Name	% Ca	% Mg	% Fe	Formula
NG-5	0.97	0.00	0.03	$(Ca_{0.97}Fe_{0.03})CO_3$
NG-3	0.98	0.00	0.02	$(Ca_{0.98}Fe_{0.02})CO_3$
NG-1C	0.98	0.00	0.02	$(Ca_{0.98}Fe_{0.02})CO_3$
NG-1B	0.98	0.00	0.02	$(Ca_{0.98}Fe_{0.02})CO_3$
NG-1A	0.97	0.00	0.03	$(Ca_{0.97}Fe_{0.03})CO_3$

C

	Maxtrix		Allochems					
Sample Name	% Micrite	% Sparite	% Oolites	% Bones	% Molluscs	% Pellets	% Lithic fragments	Carbonate Classification (Folk 1959)
NG-5	48.75	55.0	0	0	0	0	1.25	Intrasparite
NG-3	43.0	55.64	0	0	0	0	1.36	Intrasparite
NG-1C	45.0	52.25	0	0	0	0	2.75	Intrasparite
NG-1B	0	100.0	0	0	0	0	0	Crystalline sparite Limestone
NG-1A	37.0	50.51	0	0	0	0	12.49	Intrasparite

NG-1A

The basement material (NG-1A) at the Neville's Garden site is an intrasparite with lithic fragments (Table 5.1C). It is mostly crystalline calcite spar cement with small areas of micrite banding. Some lithic fragments are also present in addition to larger (1-5 mm) micrite clasts. Throughout the sample, and at the outcrop scale, large pores (0.5-5 cm) occur (Figure 5.8). These contain red/brown oxidised staining around the edges and penetrate the surrounding spar and micrite calcite up to 1 cm (Figure 5.8).

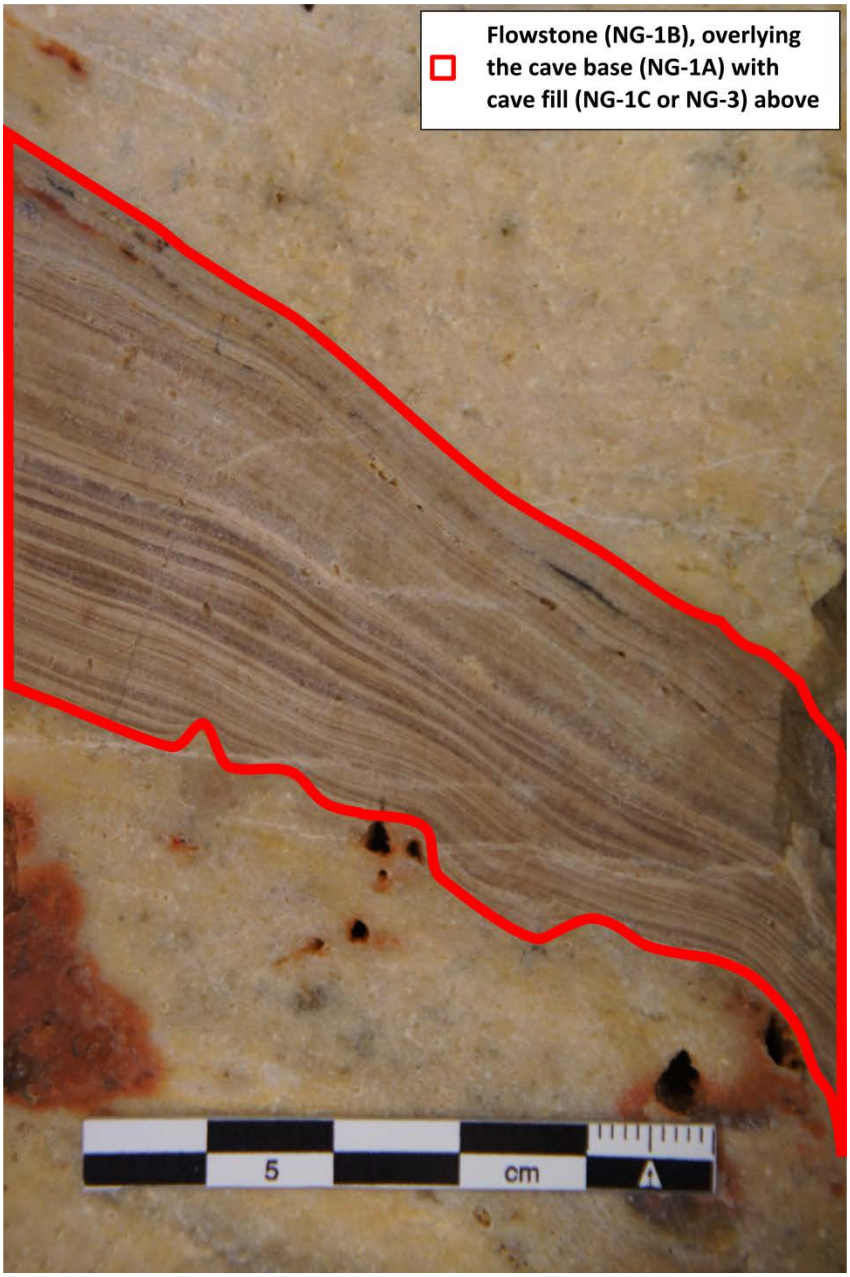

Figure 5.8: NG-1 flowstone; flowstone layering overlying a cave base limestone with later cave-fill deposit above. From the lower part of the Neville's Garden site. 5cm scale bar, 1 cm subdivisions.

NG-1B

The flowstone at Neville's Garden (NG-1B) is a finely laminated structure that extends throughout the excavation pit area (Figure 5.9). It ranges from a 30 cm thick unit at the initial pit outcrop thinning to approximately 3cm thick and incorporates material from the underlying NG-1A cave base. Flowstone laminations are between 1 mm to 0.1 mm in thickness alternating in colour from off white to light brown.

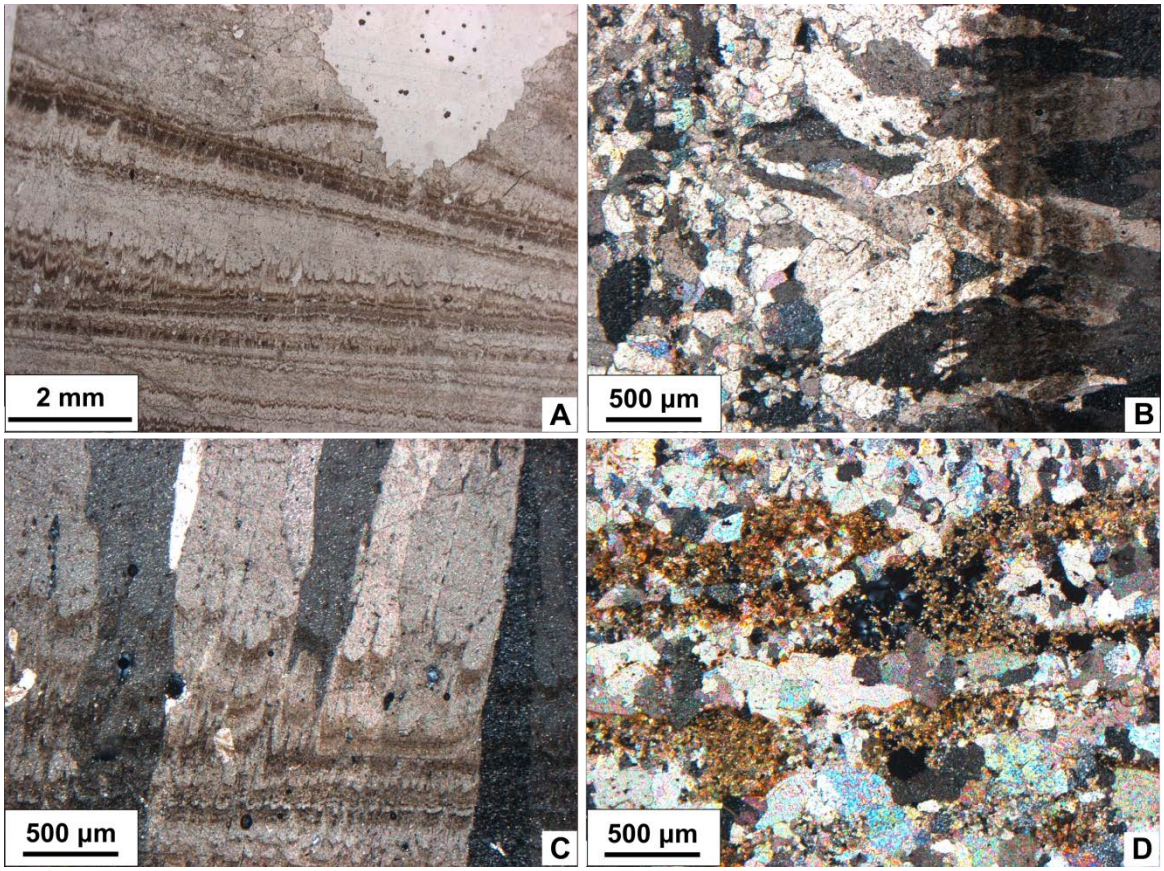

Figure 5.9: NG-1B (A) Flowstone showing lamination and growth lines from bottom to top (plane-polarised light); (B) Flowstone in polarised light showing crystal size changes along the growth lines of the lamination structures from right to left (cross-polarised light); (C) Growth lines in a flowstone speleothem, red/brown lines may indicate iron oxide staining or possible bacterial lamination of flowstone formation surface. Calcite crystals grow across some of these features (cross-polarised light); (D) NG-3 Intrasparite, near to equal amounts of spar and micrite matrix with some lithic fragments, shows layering of micritic and spar calcite (cross-polarised light). All sections are oriented with the original vertical component towards the top of the page.

NG-1C and NG-3

The upper layer comprises the main cave-fill layer NG-3 (Figure 5.10) which is similar to NG-1C from the lower portion of the layer. This unit is an intrasparite with some detrital carbonate fragments (1.36 - 2.75 %). The carbonate fraction is composed primarily of calcite with minor dolomite and siderite (Table 5.1A). NG-3 also shows bedding in the form of alternating spar calcite and micrite layers (Figure 5.9D). The micrite matrix exhibits minor oxidisation producing

red/brown staining of spar crystals. The upper portions of the cave fill are interbedded with NG-5 as shown in Figure 5.10, in conjunction with chert nodules.

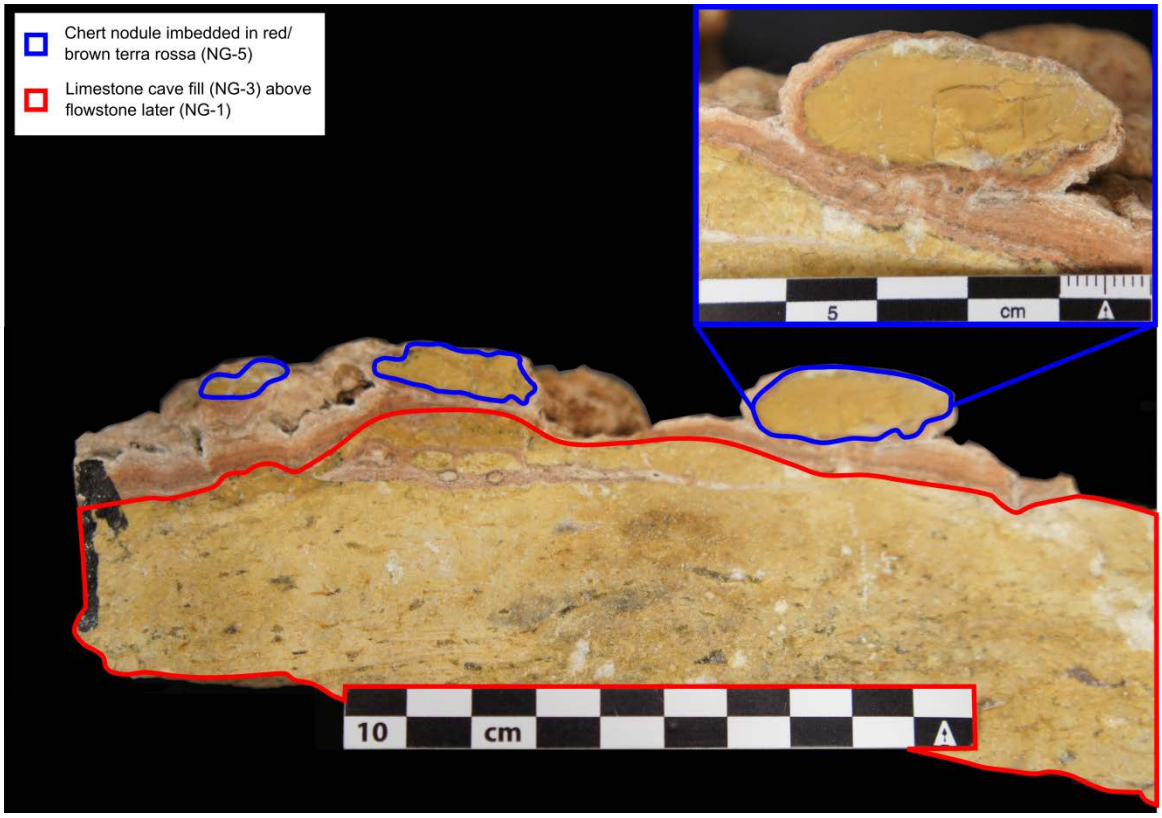

Figure 5.10: NG-3 limestone cave fill. The upper portion contains chert nodules with red/brown terra rossa fine-grained mudstone. 10cm scale bar, 1cm subdivisions.

NG-5

The top layer of the Neville's Garden site (NG-5), termed terra rossa (Archer pers. com. 2011) is a fine-grained mudstone laminate forming the upper layer of the Neville's Garden excavation pit (Figure 5.11) and has been described as Holocene in age (Archer et al., 1989). It exhibits an intricate morphology of small cracks and fissures with some interconnection. NG-5 is largely composed of calcite (91.5 %, Table 5.1A), with minor quartz, kaolinite and gypsum (2.2, 1.7 and 1.2 %, respectively). This indicates a clastic sedimentary source for these materials in addition to the chemically precipitated calcite layering present (Figure 5.11). The minor-element analysis of the carbonate fraction indicates 3 % iron, typical of freshwater carbonate systems, which commonly precipitate siderite ($FeCO_3$), whereas marine carbonate precipitation commonly favours some Mg substitution within the carbonate lattice (Table 5.1B). Some aragonite is also

present suggesting that the calcite infill is a secondary feature and may have been deposited long after the initial deposition of the limestone cave.

Figure 5.11: Terra rossa, overlying NG-3. Vertical view onto an exposed bedding plane showing the morphology of small mud-cracks.

5.4.1.2 Godthelp Hill area

This area is located to the south of the Bitesantennary area on the northern margin of the D Site plateau; sites include Camels Sputum (CS), Inabeyance (IN) and Stalagmite (SG). The Godthelp Hill area is composed of System C lithology with some cave and fissure fill deposits, these are early Miocene in age (17.85 ± 0.78 Ma, Woodhead et al., 2014). The main deposits appear to be lens shaped pool or pond deposits formed by infilling of water bodies by lime-rich sediment and bone material from the various fauna inhabiting the area. These lenses appear to grade laterally into the surrounding limestone material. However distinct contacts and discontinuities are difficult to categorise (Archer et al., 1994). The System B lithology at Godthelp Hill can be classified as lacustrine lenses and travertine pool deposits containing only non-aquatic life forms. This is possibly because the small pool and pond water bodies are too restrictive in size to accommodate large numbers of aquatic fauna and thus these smaller water bodies are more associated with foreign species (Archer et al., 1994).

Camels Sputum site (CS)

The Camels Sputum site represents one of the deepest and most extensive pit excavations on the Godthelp Hill site. The apparent gradient of the land surface surrounding the site is quite low with an approximate slope of 20-30º. Due to this, the Camels Sputum extraction pit is long and narrow, exposing a succession of layered carbonate sedimentary units. The total exposure of the excavation is approximately 2 m high and 2 m wide into the north face of Godthelp Hill (Figure 5.12).

The Camels Sputum site is dominated by massive yellow to off-white limestone interbedded with lighter coloured and crystalline limestone deposits in layers of varying thicknesses. Intra-formational clasts of similar material are common as well as larger bone fragments in distinctly cleaner carbonate layers with minimal clay and silt fractions. This may indicate a relatively low-energy depositional environment due to the highly crystalline nature of the calcite as well as the well preserved nature of the shell and bone fragments contained within them exhibiting clean breaks with distinct angular surfaces, indicating largely undisturbed isolated post-burial conditions.

Archer et al. (1994) suggested a low energy post-depositional environment such as deep cave pools. As organisms died and fell into the cave pool possibly from unstable banks and even surface cave roof collapse, biogenic material would fall to the bottom of such cave pools and undergo relatively undisturbed deposition.

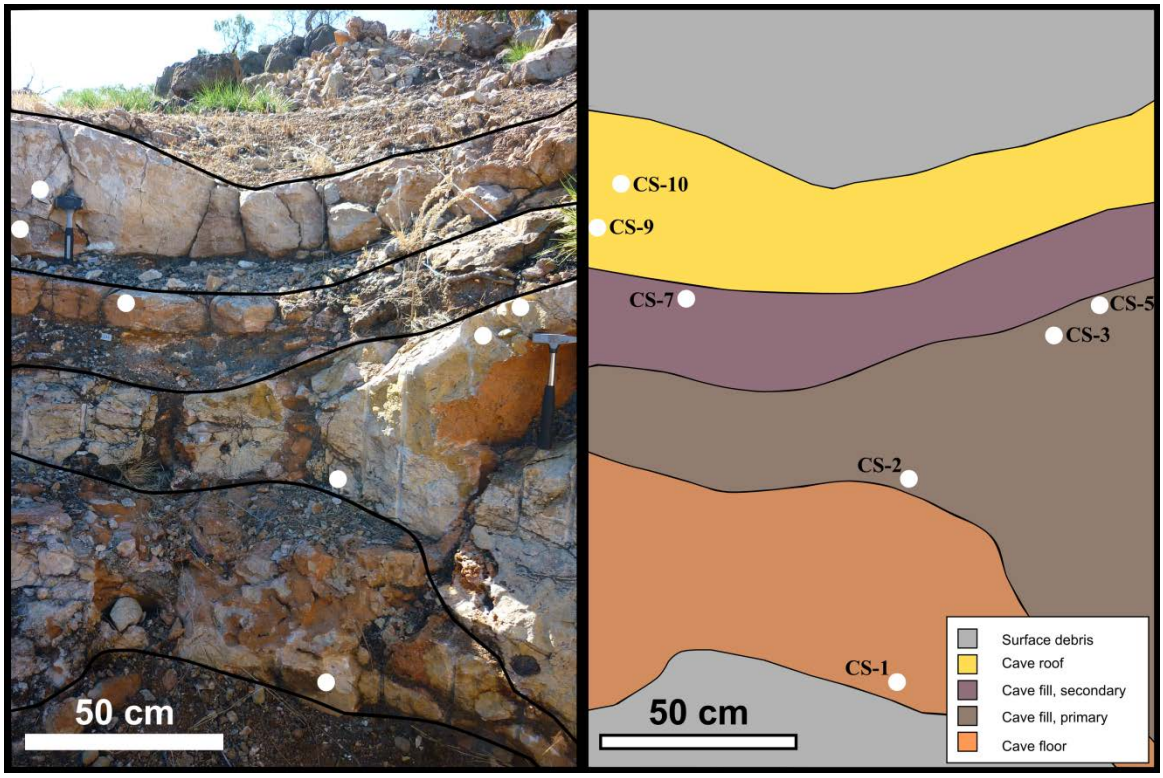

Figure 5.12: Photograph and sketch of the Camels Sputum site showing the cave roof, primary and secondary cave fill and cave floor structures. The surface and basal debris is not related to the lithology of the site. The photograph is taken facing southeast into the plateau.

Table 5.2: Camels Sputum site. (A) XRD mineral phase content (wt%) of the homogenised sample powder; (B) ICP-MS carbonate cation substitution in molar percent, based on total molar concentration; (C) Carbonate classification through point count analysis from thin sections using the Folk (1959) system.

A

Sample Name	% Calcite ($CaCO_3$)	% Dolomite ($CaMgCO_3$)	% Magnesite ($MgCO_3$)	% Siderite ($FeCO_3$)	% Aragonite ($CaCO_3$)	% Quartz (SiO_2)	% Kaolinite ($Al_2Si_2O_5(OH)_4$)	% Gypsum ($CaSO_4 \cdot 2H_2O$)
CS-10	98.4	0.7	0	0.5	0	0	0.3	0
CS-9	96.6	0.7	0	1.1	0	0	0.3	1.3
CS-7	98.6	0.7	0	0.5	0	0	0.2	0
CS-5	93.5	0.7	0.4	1.1	0	4.0	0.4	0
CS-3	62.7	0.5	1.0	0	0.6	34.7	0.5	0
CS-2	98.3	0.9	0	0.5	0	0.1	0.3	0
CS-1	92.0	0.5	0.3	0.4	2.0	1.9	2.2	0.6

B

Sample Name	% Ca	% Mg	% Fe	Formula
CS-10	1.00	0.00	0.00	$CaCO_3$
CS-9	0.99	0.00	0.01	$(Ca_{0.99}Fe_{0.01})CO_3$
CS-7	1.00	0.00	0.00	$CaCO_3$
CS-5	0.99	0.00	0.01	$(Ca_{0.99}Fe_{0.01})CO_3$
CS-3	0.99	0.00	0.01	$(Ca_{0.99}Fe_{0.01})CO_3$
CS-2	1.00	0.00	0.00	$CaCO_3$
CS-1	1.00	0.00	0.00	$CaCO_3$

C

	Maxtrix		Allochems					
Sample Name	% Micrite	% Sparite	% Oolites	% Bones	% Molluscs	% Pellets	% Lithic Fragments	Carbonate Classification (Folk 1959)
CS-10	0	98.75	0	0.5	0	0	0.75	Crystalline calcite
CS-9	0	99.5	0	0	0	0	0.5	Crystalline calcite
CS-7	0	99.0	0	0	0	0	1.0	Crystalline calcite
CS-5	62.25	29.0	0	0	1.75	5.75	1.25	Fossiliferous pelmicrite
CS-3	56.75	26.5	0	1.5	2.75	0	12.5	Unsorted lithic biosparite
CS-2	0	99.25	0	0	0	0	0.75	Crystalline calcite
CS-1	63.25	32.25	0	1.5	0.25	0	2.75	Massive intramicrite limestone

CS-1

The basal layer at Camels Sputum (CS-1) is an intramicrite unit, exhibiting a dominant micritic matrix with spar nodules, highly jointed with calcite spar fracture fillings (Table 5.2A, C). Large clasts (up to 2 mm) of micrite occur, some with associated red/brown iron oxide staining around the contact margins with the spar calcite cement. Quartz grains as well as minor kaolinite (1.9 and 2.2 %, respectively, Table 5.2A) are uncommon but appear as angular to sub-angular with yellow staining in the calcite spar fissure fills (Figure 5.13).

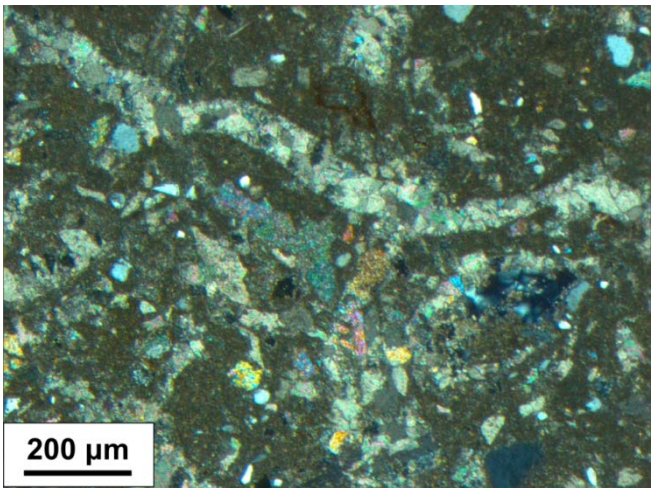

Figure 5.13: CS-1 intramicrite, showing micrite matrix with clasts and vein fill of spar crystals. There are some detrital quartz grains and bone and shell fragments (cross-polarised light). The section is oriented with the original vertical component towards the top of the page.

CS-3

CS-3 is an unsorted lithic biosparite containing shell and bone fragments, lithic fragments and detrital grains (1.75, 12.5 %, respectively, Table 5.2C). The carbonate in the Camels Sputum site is fairly pure with minor magnesium and iron substitution. Shell and bone material is primarily encased in micrite matrix but the internal structures of the gastropods (Figure 5.14A) are typically filled with spar calcite. This spar calcite is likely to be secondary infill whereas darker micrite fill within gastropods near the opening may be a primary deposition product. Many gastropods and bivalve fragments and whole specimens are incorporated in larger micritic clasts with spar calcite cement between larger (2 cm) fragments and quartz grains and some fine-grained red/brown mud laminae. Pellets are also common matrix constituents and are imbedded within the later spar calcite cement (Figure 5.14B).

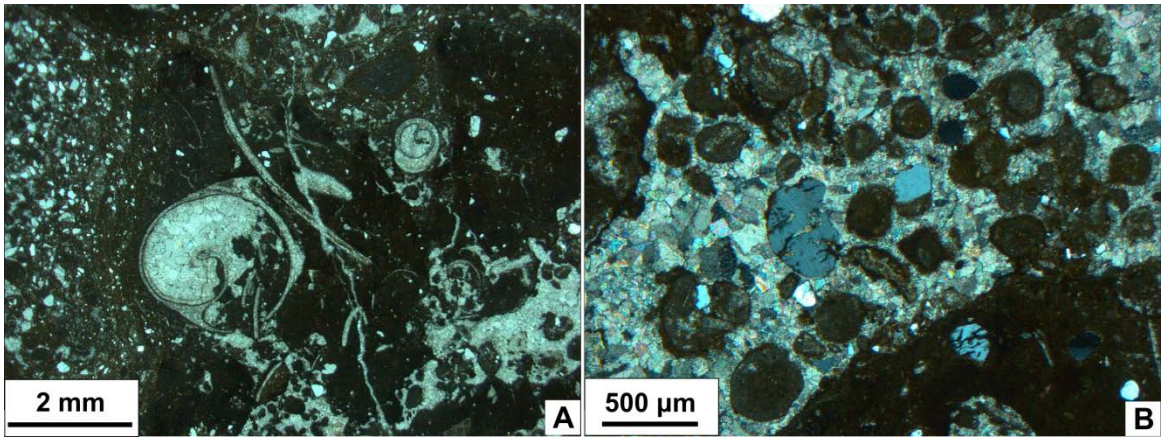

Figure 5.14: CS-3 unsorted lithic biosparite, (A) showing two gastropod shells and bivalve shell fragments with micrite matrix and spar cement infill (plane-polarised light). (B) Showing spar cement fill incorporating quartz fragments and pelletal material (cross-polarised light). Sections are oriented with the original vertical component towards the top of the page.

CS-5

CS-5 lies 10cm above CS-3 and is quite similar in morphology. It can be classified as a fossiliferous pelmicrite, containing some mollusc shell material (Table 5.2C). The sample is largely composed of micrite clasts which contain most of the fossil shell material. These are held in a spar calcite framework with high abundance of pellets as well as some quartz grains. Lithic constituents in the micrite clasts are angular to sub-rounded in appearance suggesting rapid burial. Whereas quartz grains are sub-rounded to sub-angular suggesting higher energy deposition environments and longer sediment transport distances. Pellets are very common in the inter clast areas, and range from 100 to 500 µm in diameter, in association with spar cement and quartz grains (Figure 5.15). Calcite spar framework binds the sample and is typically crystalline with few pore spaces creating a tightly packed well consolidated fossiliferous limestone.

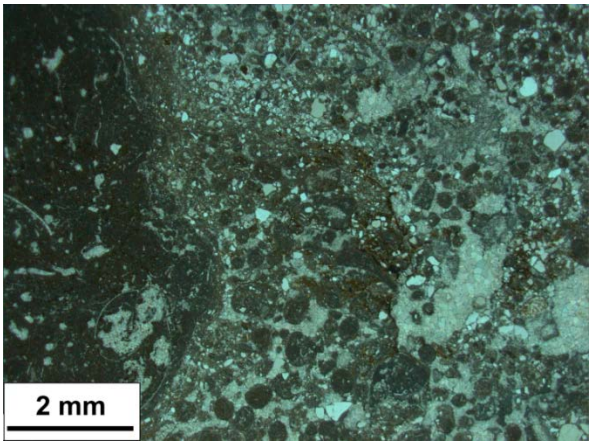

Figure 5.15: CS-5 fossiliferous pelmicrite, showing large fossiliferous micrite fragment on left, incorporating a gastropod as well as fragmented bivalve shell. Some spar infilling is also present. Pellets are common as well as smaller lithic micrite fragments. The cement is a essentially spar calcite with some fine-grained mud surrounding some pellets (plane-polarised light). The section is oriented with the original vertical component towards the top of the page.

CS-7

Sample CS-7 represents a secondary cave fill deposit of high calcite purity (Table 5.2), with no apparent major foreign clay or quartz constituents or cation substitution within the carbonate lattice (Table 5.2). Thin section analysis shows a spar dominated habit with crystals of over 2 mm in length (Figure 5.16).

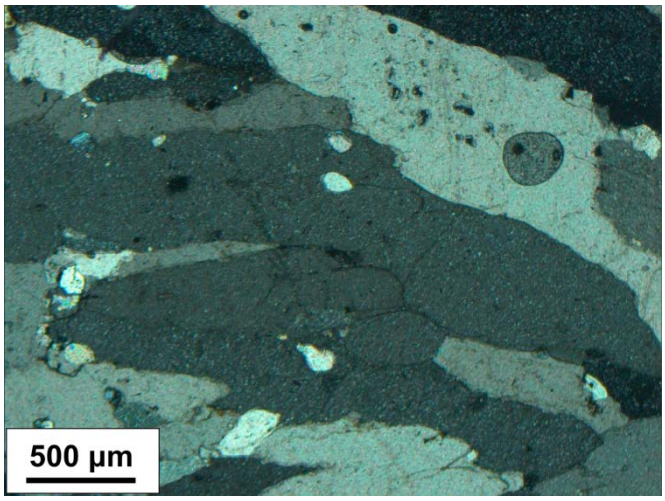

Figure 5.16: CS-7 Crystalline calcite, showing large calcite spar grains (cross-polarised light). The section is oriented with the original vertical component towards the top of the page.

CS-9 and 10

A stalagmite was found within the Camels Sputum site (Figure 5.17A and B), it shows a well-developed crystalline structure of pure calcite (99.5% spar calcite Table 5.2A, C), growth lines are pronounced with dark irregular staining across the crystal growth habit. Individual crystals range from 5mm up to 10mm in length (Figure 5.17A and B). Pores are present through the sample but are likely to be an artefact of thin section preparation.

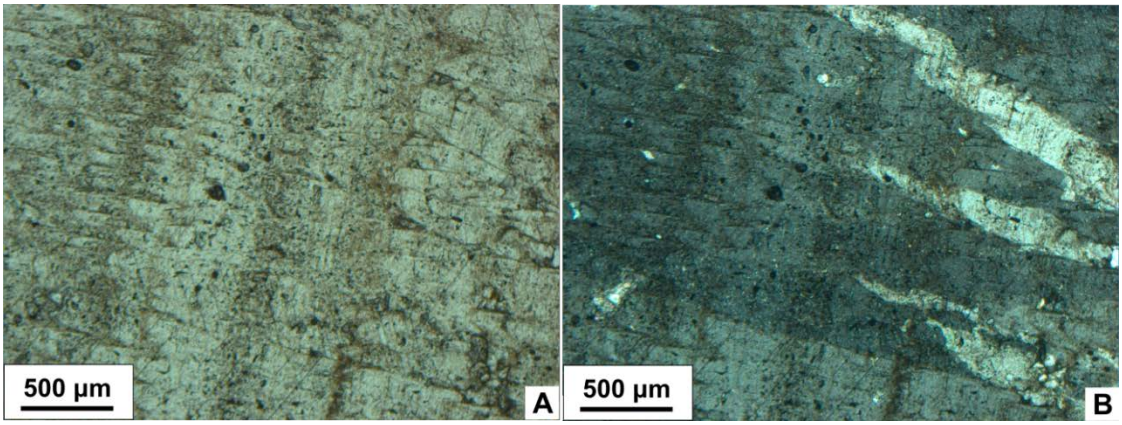

Figure 5.17: CS-9 Crystalline calcite; stalagmite structure; (A) interlocking calcite crystal structure showing stained growth lines (plane-polarised light); (B) crystal structure shown growing through stained growth lines (cross-polarised light). Sections are oriented with the original vertical component towards the left of the page.

Inabayence site (IN)

The Inabayence site is located to the north of the Camels Sputum site and represents a highly crystalline spar limestone cave-fill deposit of System B faunal assemblage of Late Miocene age (17.75 ± 0.78 Ma, Woodhead et al. 2014). It is one of the more recently expanded excavation pits in the Riversleigh area with a large amount of the fossil material yet to be identified or in the process of biostratigraphic analysis. Lower layers of the Inabayence site are more bone-rich and form distinct pool or lens shape beds within the surrounding limestone (Figure 5.18). These beds appear to be semi rounded in shape and grade laterally into the surrounding bedrock, confirming findings by Archer et al. (1994, 2006).

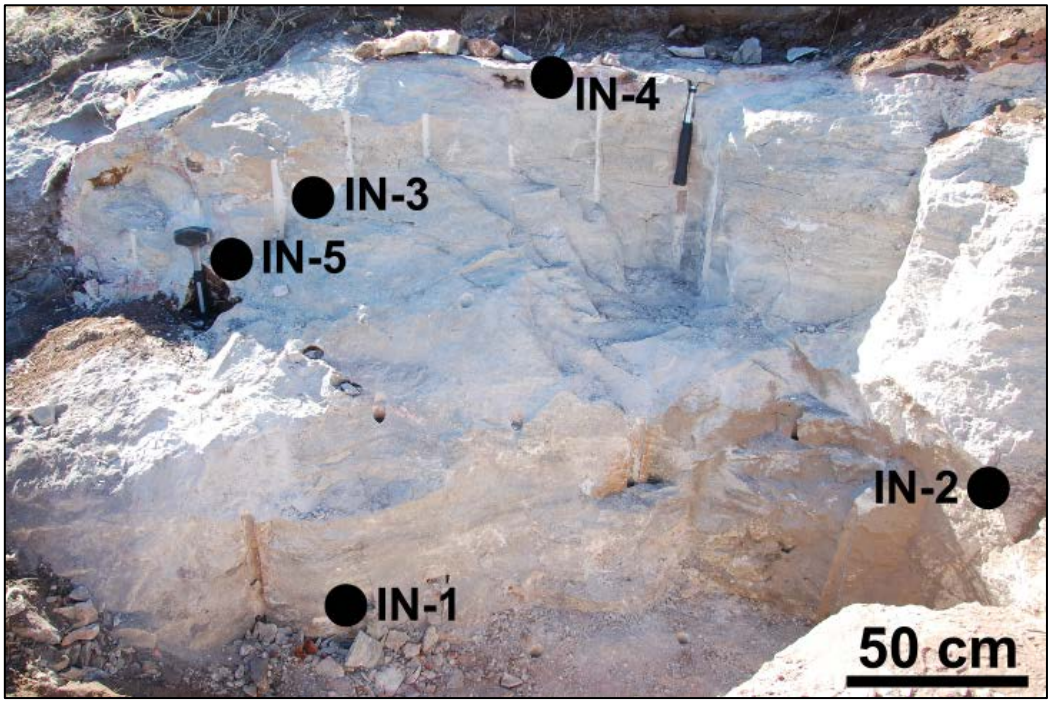

Figure 5.18: Photograph of the Inabayence site, showing the sample locations in the two-stage excavation pit. The sketch is drawn facing southeast into the plateau.

IN-1

The lowest layer in the Inabayence site is a massive calcite limestone (IN-1, 99.7% Table 5.3A). It is largely micritic with some calcite crystal fragments, sub-rounded to well-rounded in appearance. No bedding or grading is apparent (Table 5.3C) and the sample is part of the basement limestone of the Godthelp Hill area. Outcrops of this unit are meagre although similar

limestones occur in all areas of the Godthelp Hill area, such as the basement material found at Camels Sputum.

Table 5.3: Inabayence site, (A) XRD mineral phase content (wt%) of the homogenised sample powder; (B) ICP-MS carbonate cation substitution in molar percent, based on total molar concentration; (C) Carbonate classification through point count analysis from thin sections using the Folk (1959) system.

A

Sample Name	% Calcite ($CaCO_3$)	% Magnesite ($MgCO_3$)	% Aragonite ($CaCO_3$)	% Quartz (SiO_2)	% Kaolinite ($Al_2Si_2O_5(OH)_4$)	% Gypsum ($CaSO_4 \cdot 2H_2O$)
IN-4A	99.8	0	0	0	0.2	0
IN-3	95.9	0.3	2.6	0.1	1.1	0
IN-5	99.8	0	0	0	0.2	0
IN-2	99.8	0	0	0	0.1	0
IN-1	99.7	0	0	0	0.2	0

B

Sample Name	% Ca	% Mg	% Fe	Formula
IN-4A	0.99	0.00	0.00	$(Ca_{0.99}Al_{0.01})CO_3$
IN-3	1.00	0.00	0.00	$CaCO_3$
IN-5	0.97	0.00	0.00	$(Ca_{0.97}Al_{0.03})CO_3$
IN-2	1.00	0.00	0.00	$CaCO_3$
IN-1	0.99	0.00	0.01	$(Ca_{0.99}Fe_{0.01})CO_3$

C

Sample Name	Maxtrix		Allochems					Carbonate Classification (Folk 1959)
	% Micrite	% Sparite	% Oolites	% Bones	% Molluscs	% Pellets	% Lithic Fragments	
IN-4A	100.0	0	0	0	0	0	0	Crystalline calcite spar
IN-3	100.0	0	0	0	0	0	0	Crystalline calcite spar
IN-5	70.0	23.0	0	0	0	0	7.0	Lithic intrasparite
IN-2	99.25	0	0	0	0	0	0.75	Crystalline calcite spar
IN-1	69.25	22.25	0	0	0	0	8.5	Lithic intrasparite

IN-2

Samples were taken in an upward succession with IN-2 forming the basal layer of the depositional lens composed of calcite and a smaller amount of lithic derived clay, the latter likely originated from sediment-laden water flowing into the pool or carried by wind (Figure 5.19).

The lower layers of the site (IN-2) contain large well preserved fossil bone material, although not captured in thin sections. The upper layers of the Inabayence site are also highly fossil-rich and represent a shallow pool or depression within the ancient cave system which had a high potential for accumulation of fossil material.

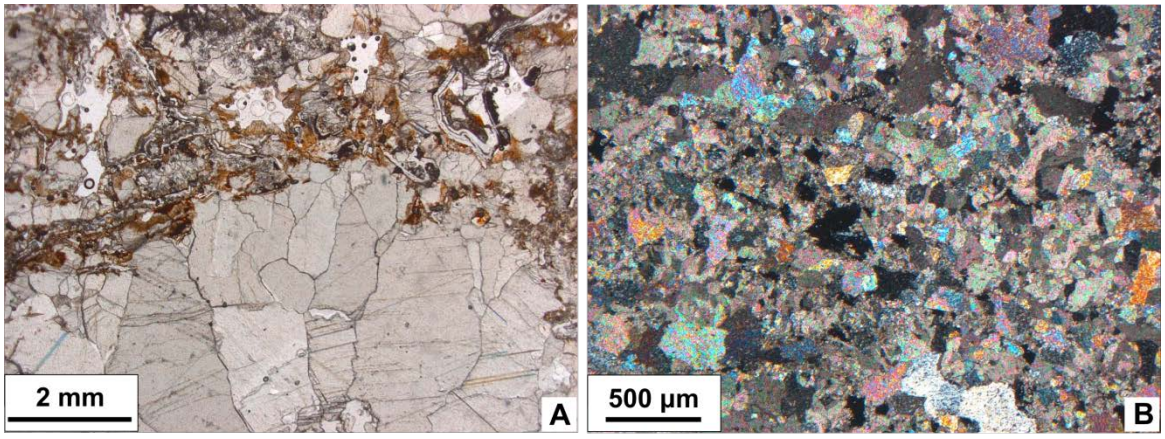

Figure 5.19: (A) IN-2; Crystalline spar calcite with mud lamination around disjointed crystals with some fine crystalline calcite vein precipitation (plane-polarised light); (B) IN-3; Finely crystalline spar calcite with no apparent matrix cement; the framework contains many pores (cross-polarised light). Sections are oriented with the original vertical component towards the top of the page.

IN-4 (Calcite Fraction; A and Mud lamination fraction; B)

The upper portion of the deposit (IN-4B) contains a red/brown mudstone layer, 1 to 2cm in thickness, with thin bedding-parallel veins of calcite (Figure 5.20). The IN-4B layer is a laminate deposit of the underlying IN-4A layer. Sample IN-4A can be classified as a lithic intrasparite, largely composed of calcite (83.3%) with some quartz and kaolinite (7.4 and 2.9 % respectively, Table 5.3C) comprising 8.5 % of the detrital framework material. Some alteration of the original source material has occurred with 4.9 % aragonite present (Table 5.3C). Lithic fragments range in size from 1 to 5 mm micrite clasts, these are bound by a crystalline spar matrix (Figure 5.20). Some micrite fragments contain iron oxidation staining. Laminae appear as white very finely crystalline sheets forming small crystals up to 50 µm in length occasionally bordering larger micrite clasts but appear random throughout the micrite matrix within the sample.

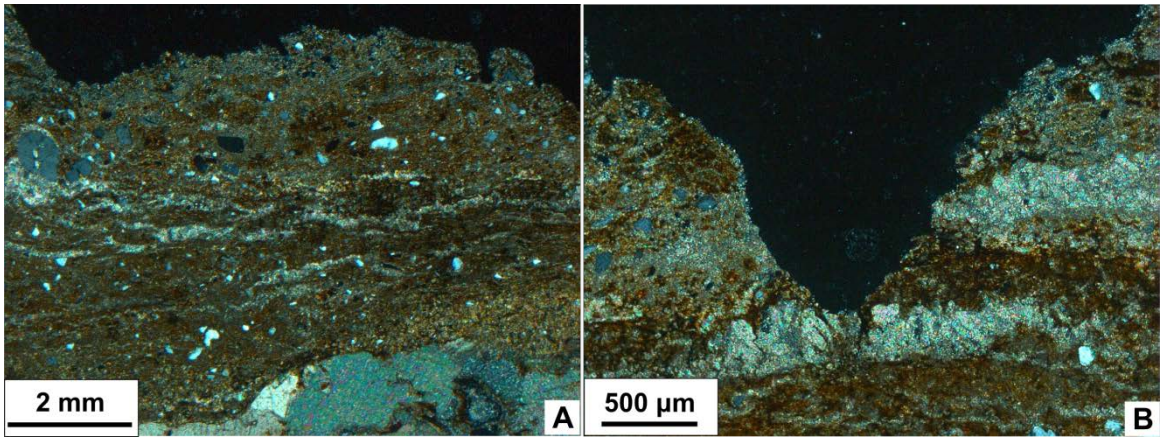

Figure 5.20: IN-4B (A) Uppermost layer of the Inabayence site; showing fine laminations of detrital silt and mud, some quartz grains are present (A: cross-polarised light). (B) Shows thicker veins of crystalline calcite interbedded with finer mud sediments (B: cross-polarised light). Sections are oriented with the original vertical component towards the top of the page.

IN-5 Calcite Pore Fill

Within the Inabayence excavation pit there are many distinct secondary calcite cavity pore fills. Structures such as IN-5 are common throughout the Riversleigh limestone and cave deposits and are considered to be secondary pore fill crystalline calcite deposits. Stratigraphically IN-5 lies below IN-3, and was collected after the initial samples were taken in sequence. Mineral fraction analysis reveals these pore fill structures to be pristine calcite (99.8 %) with only a minor kaolinite clay component (0.2 %, see Table 5.3C). Pores are filled by calcite crystals growing in from the pore margins into the centre. Crystal sizes range from a very fine to 1 to 5 mm crystals in the centre. Many of these structures are interconnected by fractures as well as distinct flow channels through the rock. These form calcite vein type structures. These are similar to the previously described pore fill calcite structures. However vein structures exhibit an overall finer crystal size around the margins with smaller crystals up to 1 mm in length. This is likely due to the more disturbed nature of a vein structure as it is being deposited with moving water not allowing for larger more pristine crystal growth.

Stalagmite site (SG)

This site contains a near-horizontal exposed section through a large stalagmite at the lower end of the Camels Sputum trench and close to the Inabayence Site. The surrounding material has been dated from flowstone material at the Camels Sputum site to 17.85 ± 0.78 Ma (i.e. System B, Woodhead et al., 2014). Three samples of the stalagmite were collected (SG-1, 2 and 3; Figure 5.21). The external stalagmite calcite was highly weathered and porous (SG-3). Inner calcite of SG-1 and SG-2 exhibited a pure crystalline spar calcite structure with minimal to no weathering.

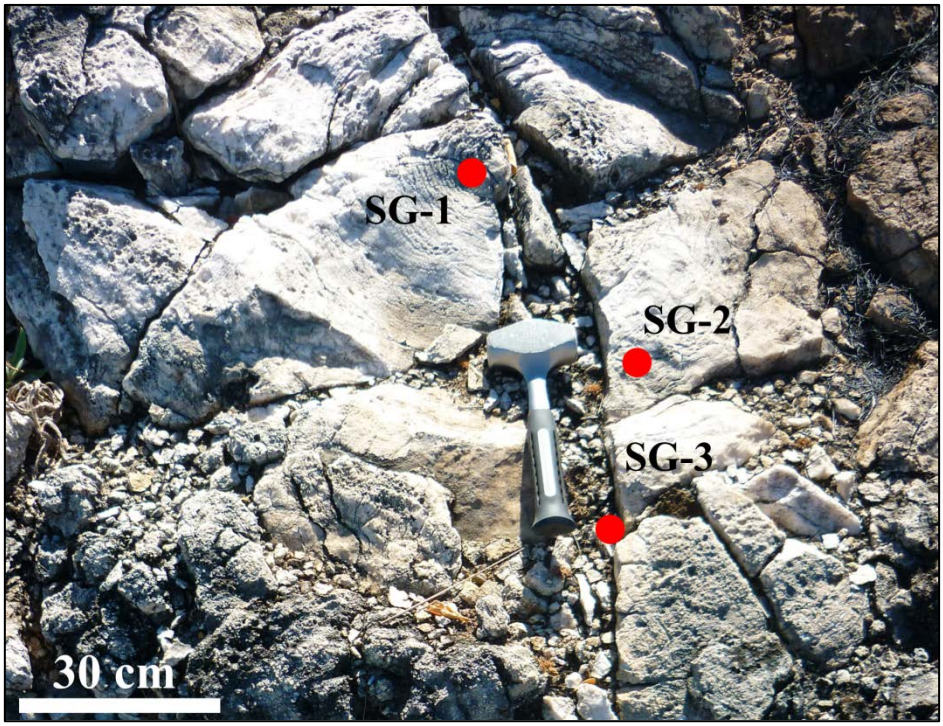

Figure 5.21: Stalagmite site (SG), showing sampling sites of the stalagmite from the oldest to youngest precipitating layer (SG-1 to 3). The photograph is orientated facing south into the plateau; the surface of the outcrop is nearly horizontal.

5.4.1.3 Bitesantennary site (BC)

The Bitesantennary site is located at the north-eastern margin of the D-Site plateau, it comprises mainly B system lithology of early Miocene age (17.11 ± 0.78 Ma Woodhead et al., 2014), confirming the relative biostratigraphic age of the early Miocene deposits of Archer et al. (1994, 2006). These deposits have been previously described as the 'Carl Creek Limestone' and 'D-site equivalents' (Archer et al., 2004; 2006). These limestone units unconformably overlie a calcareous conglomerate and sandstone unit at the top of the Cambrian Thorntonia Limestone. The carbonate cemented conglomerate contains many chert nodules of various sizes and abundances likely sourced from the Thorntonia Limestone. The underlying sandstone layer may also be a product of physical weathering of the chert nodules released by dissolution from the Cambrian limestone (Figure 5.22).

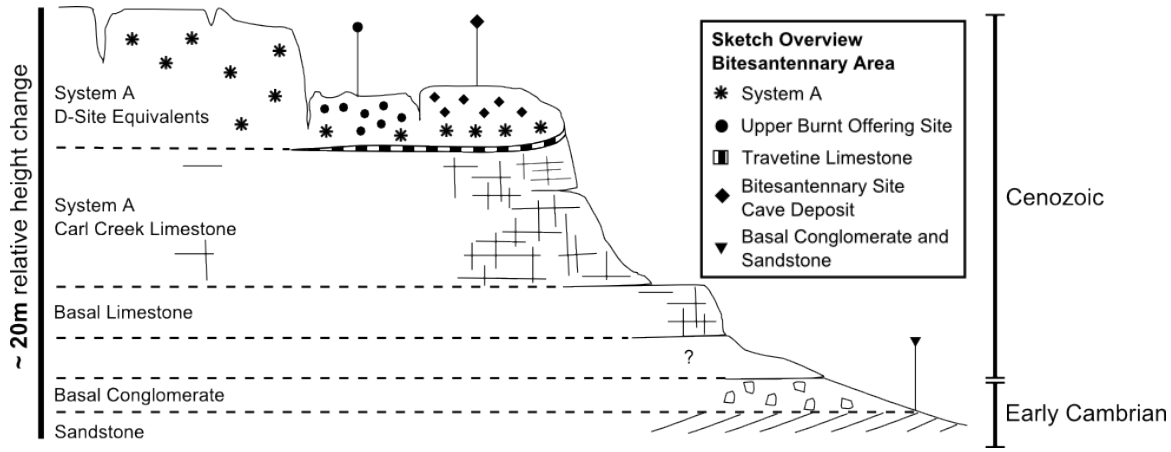

Figure 5.22: Diagrammatic profile of the Bitesantennary site, showing stratigraphic layers, incorporating the early Cambrian sandstone and conglomerate layers, the overlying Carl Creek Limestone and the Oligo-Miocene System A unit in conjunction with the System B cave deposits of the Bitesantennary Site (BC). Modified from Archer et al. (1994).

The area is exposed as a hill section with various limestone deposits outcropping from the lower area (Low Lion Site) to the top of the first plateau (Bitesantennary Site) and up onto the ridge (Neville's Garden site), as illustrated in Figure 5.23. The Bitesantennary site has been previously interpreted as a pool deposit in an open early Miocene cave within a wet rainforest environment (Archer et al., 1994; 2006). It has been suggested that these deposits are inset into travertine limestone. These cavernous facies are commonly phreatic with many passages and caves linked subterraneally. Cave roof collapse is common in near-surface karst systems and has allowed surface access to the cave, facilitating a larger number of bat species which occupied these

environments, such as the leaf-nosed bat (*Hipposideros* sp.) and the carnivorous ghost bat (*Macroderma* sp.). More rarely other mammals, reptiles and amphibians, such as the marsh frog (*Lymnodynastes* sp.), may have fallen into the cave system from the surface or have been transported to the cave by bats or predatory birds (Archer et al., 1989).

During the course of the cave development, cave pools accumulated on the floor and subsequently accumulated bone-rich carbonate forming the cave fill deposit. In the sampling expedition of 2011, carbonates were collected from several environments within the Bitesantennary area to further investigate the different cave deposits in this area and establish their usefulness in isotopic analysis for palaeotemperature reconstruction (Figure 5.23).

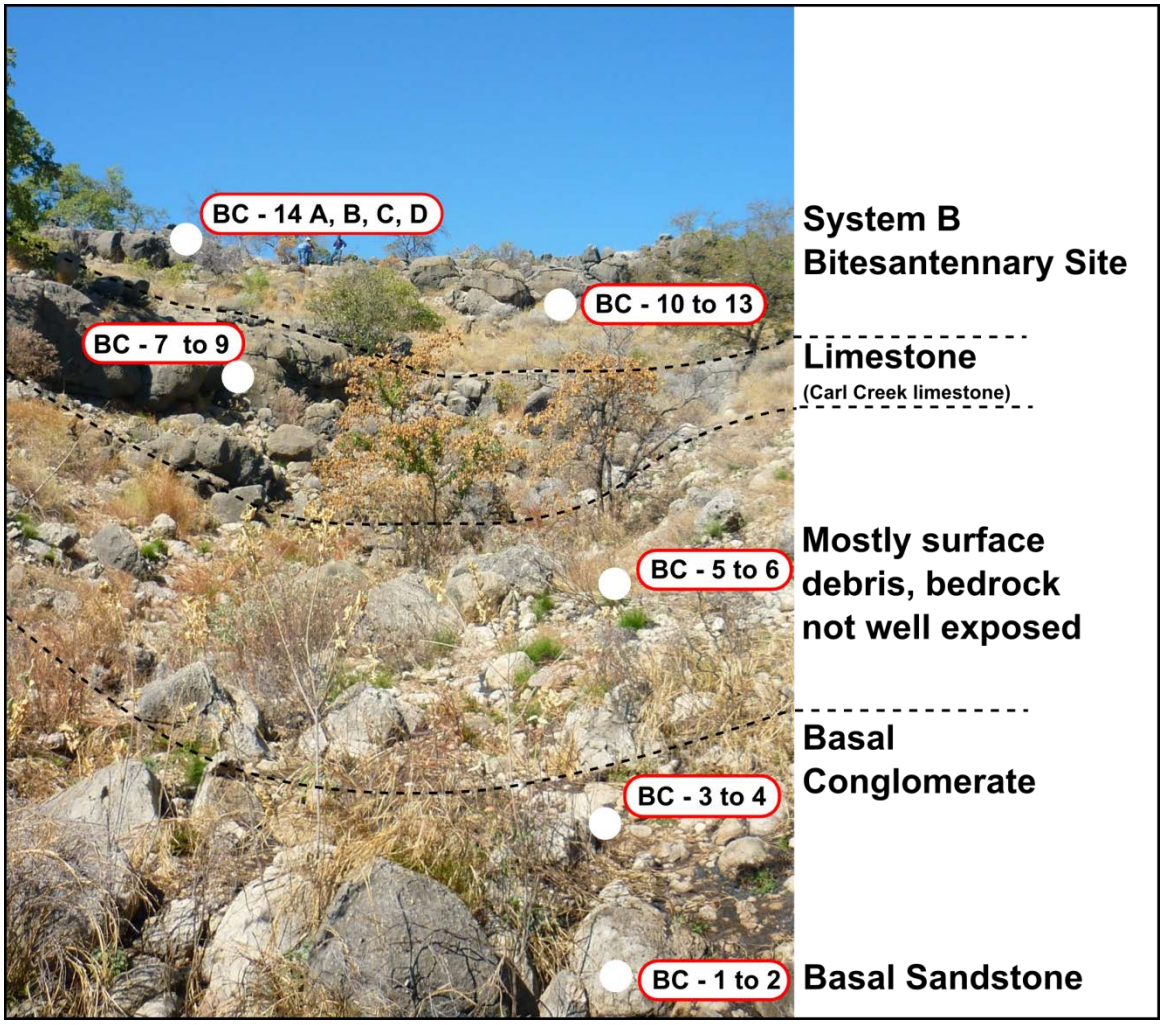

Figure 5.23: View of the Bitesantennary area, showing the approximate stratigraphic boundaries as depicted in Figure 5.22. The approximate sample locations are marked showing their spatial relationship to the appropriate stratigraphic layer. The photograph is taken from the base of the Bitesantennary area, and the view is to the southeast and uphill. The person at the top of the hill is approx. 1.8 m tall. The scale is distorted at the bottom of hill due to the gradient.

Carbonates BC-5, BC-9 and BC-10 represent massive equilibrium deposits formed underwater as structureless pond or cave-pool fill material. These samples have the highest potential to produce reliable Δ_{47} palaeotemperatures. Other calcite deposits such as BC-12 and BC-14 may have been equilibrium deposited in shallow cave pools. However, analysis of small cave pearls and their included nucleus may cause additional complications.

Table 5.4: Bitesantennary site (A) XRD mineral phase contents (wt%) of the homogenised sample powder; (B) ICP-MS carbonate cation substitution in molar percent, based on total molar concentration; (C) Carbonate classification through point count analysis from thin sections using the Folk (1959) system.

A

Sample Name	% Calcite ($CaCO_3$)	% Dolomite ($CaMgCO_3$)	% Magnesite ($MgCO_3$)	% Siderite ($FeCO_3$)	% Aragonite ($CaCO_3$)	% Quartz (SiO_2)	% Kaolinite ($Al_2Si_2O_5(OH)_4$)	% Gypsum ($CaSO_4 \cdot 2H_2O$)
BC-14B	95.4	0.6	0	0	0	0.2	2.8	1.1
BC-14A	97.9	0.8	0	0	0	0.1	0.8	0.5
BC-10	99.7	0.2	0	0	0	0	0	0.1
BC-5	92.4	0.6	0.9	0.4	2.4	1.3	1.6	0.4
BC-3	82.3	0.5	0.7	0.4	1.7	10.6	2.7	1.1
BC-1	40.1	0.2	2.5	0	0	57.2	0	0

B

Sample Name	% Ca	% Mg	% Fe	Formula
BC-14B	0.97	0.00	0.03	$(Ca_{0.97}Fe_{0.03})CO_3$
BC-14A	0.98	0.00	0.02	$(Ca_{0.98}Fe_{0.02})CO_3$
BC-10	0.98	0.00	0.02	$(Ca_{0.98}Fe_{0.02})CO_3$
BC-5	0.98	0.00	0.02	$(Ca_{0.98}Fe_{0.02})CO_3$
BC-3	0.97	0.00	0.03	$(Ca_{0.97}Fe_{0.03})CO_3$
BC-1	0.98	0.00	0.02	$(Ca_{0.98}Fe_{0.02})CO_3$

C

	Matrix		Allochems					
Sample Name	% Micrite	% Sparite	% Oolites	% Bones	% Molluscs	% Pellets	% Lithic Fragments	Carbonate Classification (Folk 1959)
BC-14D	69.75	14.0	5.25	5.0	1.0	0	5.0	Sparse biomicrite
BC-14B	9.75	19.25	66.0	0.5	0.75	0	3.75	Packed oomicrite
BC-14A	31.5	28.25	32.25	3.0	5.0	0	0	Packed oomicrite
BC-12	26.0	65.5	0	0.25	0	3.25	5.0	Sparse pelmicrite
BC-9	19.25	76.75	0	0.75	0	0.25	3.0	Sparse biomicrite
BC-7	14.5	71.25	0.25	3.5	1.5	3.75	5.25	Sparse biomicrite
BC-5	13.0	77.75	0	1.75	0	0	7.5	Fossiliferous micrite
BC-3	13.5	55.75	0	0.5	1.25	0	29.0	Limestone conglomerate
BC-1	45.0	27.25	0	0	0	0	27.75	Immature quartz sandstone

BC-1 and BC-3

Sample BC-1 is immature quartz sandstone with calcite cement with 40% calcite and 57% quartz (impurities) from XRD analysis (Tables 5.4A and C). The thin section analysis of BC-1 (Figure 5.23) shows that it is a poorly sorted fine- to medium-grained carbonate-quartz sandstone. Most grains are sub-angular to well-rounded with some more scattered well-rounded quartz grains present in a poorly sorted pattern.

Bedding in the sandstone is indicated by cleaner sand laminae and changes in grain size to thinner calcareous laminae. Quartz appears to be the dominant framework grain with some strained metamorphic quartz from older parent rock sources. Less dominant grain fractions appear to be metaquartzite, chert, fine-grained sandstone rock fragments as well as some micritic fragments and recrystallized shell fragments. Some larger (4-6 mm) micritic limestone fragments are present show patchy recrystallization and scattered quartz grains. Many of the detrital rock fragments are iron oxide stained. Most of the sample is bound by an iron-stained clay and micrite matrix. Porous areas of the sample show microspar and spar calcite cement with some spar calcite concretions being more crystalline (Figure 5.24 A and B).

Overlying the carbonate-quartz sandstone (BC-1) is the limestone conglomerate layer BC-3 with clast sizes ranging from 5mm to 50mm. From the mineral phase analysis it can be observed that it is largely calcite/aragonite based (~84 %), with some quartz (10.6 %) and kaolinite (2.7 %) fractions (Table 5.4A). The clasts are predominantly micritic limestone fragments but also include rarer siltstone and fine-grained sandstone fragments (Figure 5.24C and D). Clasts are irregular to rounded in shape and some are cut by irregular microspar fractures. A few clasts show signs of dissolution at the margins passing into an iron oxide clay matrix. The matrix is very fine grained <0.625 mm muddy micrite with common very angular to sub-rounded to well-rounded quartz. Other framework grains include stained fine-grained metaquartizite and fine-grained micrite and spar (Figure 5.22). The pores are filled with calcite crystals showing a crystal size increase from microspar to spar towards the centre. These two samples represent long-term erosion products reworked from the underlying Cambrian Thorntonia Limestone.

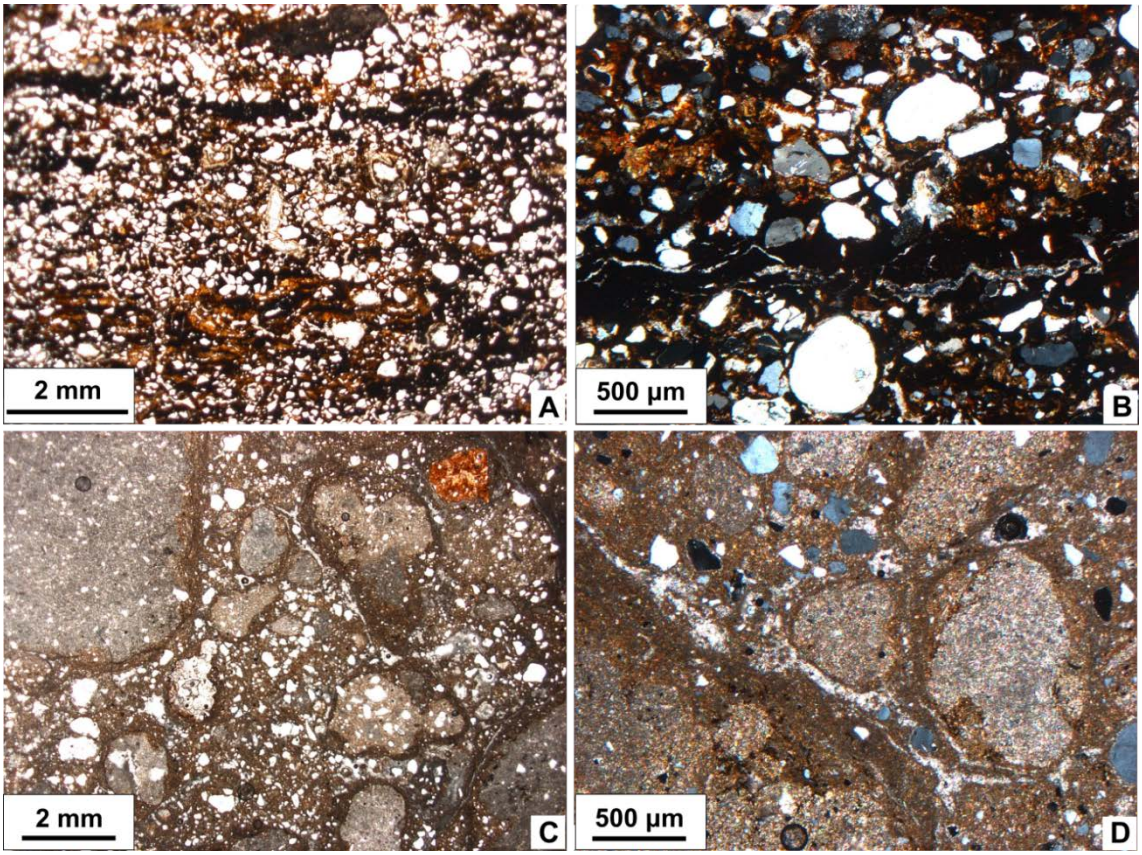

Figure 5.24: Bitesantennary thin section photographs. (A, B) BC-1 Immature quartz sandstone (A; plane-polarised light), showing the bedding of the sandstone as well as lamination of quartz grains in iron oxide mud and micrite matrix (B; cross-polarised light); (C, D) BC-3 Limestone conglomerate (C; plane-polarised light) showing micrite clasts and quartz grains in micritic and oxidised clay matrix and calcite spar fracture fill (D; cross-polarised light). Sections are oriented with the original vertical component towards the top of the page.

BC-5

Sample BC-5 material is fossiliferous intramicrite (Table 5.4), containing detrital fragments up to 20 mm in diameter, composed of micrite and spar fragments, as well as less abundant quartz grain and lithic fragments. Both shell and bone fragments are present in low abundances. The matrix of the sample is largely pure spar calcite material, with only minor iron constituents (2 %, Table 5.4), with pores also spar in-filled showing finer grained microspar lining the pore structure and larger grain sizes of crystals in the centre (Figure 5.25). Some pores are rimmed by iron oxide staining on the finer grained micrite; this also applies to some of the micritic fragments and clasts within the framework. Fractures within the rock form dendritic channels across the sample intersecting between grains and between the fractured grains calcite spar infill can occurs.

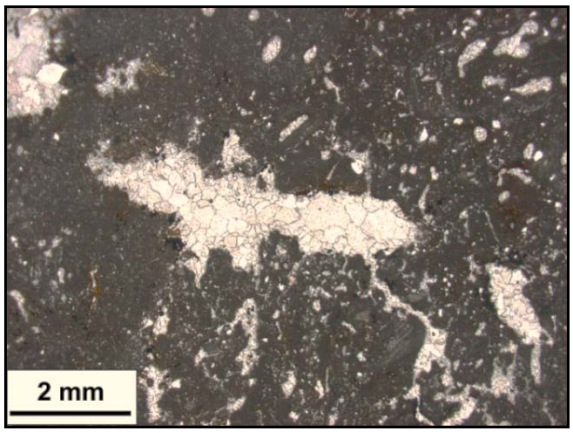

Figure 5.25: BC-5 Fossiliferous micrite, showing calcite pore fill. The matrix is mainly micritic with some quartz and shell fragments (plane-polarised light). The section is oriented with the original vertical component towards the top of the page.

BC-7 and BC-9 (Carl Creek Limestone)

In contrast to the previous fossiliferous micrite (BC-5), stratigraphically higher samples appear to be sparse biomicrite, micritic matrix dominant with various degrees of iron oxide staining. Some fractures are micrite infilled and exhibit less red oxidation than others. Both BC-7 and BC-9 contain large spar calcite void fillings layered over fine-grained clay (Figure 5.26A and B), growing from the bottom to top in various channels, possibly as small flow channels or solution pipes within the cave system. The brown biomicrite contains higher amounts of lithic constituents whereas the white calcite is relatively pure (Table 5.4A-C).

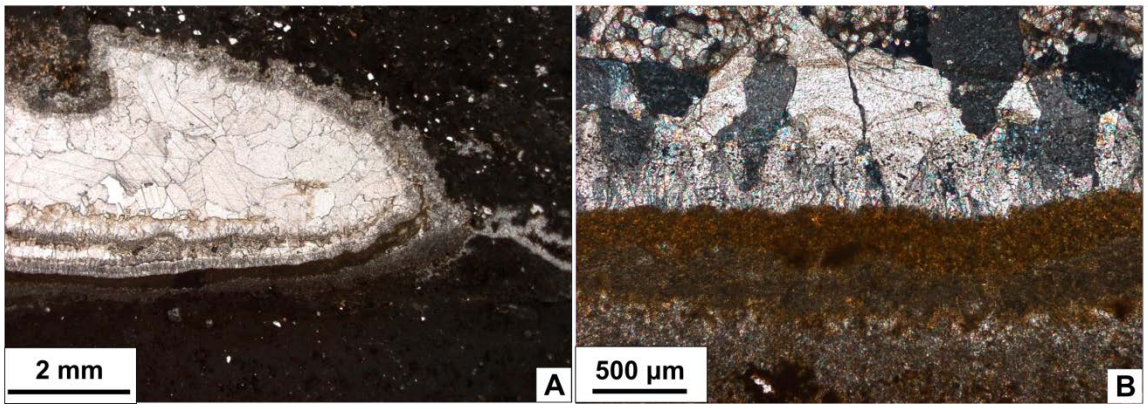

Figure 5.26: BC-9 spar calcite on clay base. The spar calcite crystals are coarser towards the centre of the flow channel or pipe (A: plane-polarised light, B: cross-polarised light). Sections are oriented with the original vertical component towards the top of the page.

BC-12

Sample BC-12 shows spar calcite cement and micrite matrix with abundant pelletal material (Figure 5.27). Large micritic fragments up 8mm are also present. The fragments are sub-rounded to sub-angular with distinct dissolution edges and oxide staining around the fragments. Spar calcite commonly envelopes larger micrite fragments and as seen in Figure 5.27 also cuts some fragments along fracture lines. This may indicate some compaction and/or material reworking has occurred after initial fragment deposition and prior to lithification. Due to the large amount of organic material and lithic fragments the carbonate fraction was not analysed for Δ_{47}.

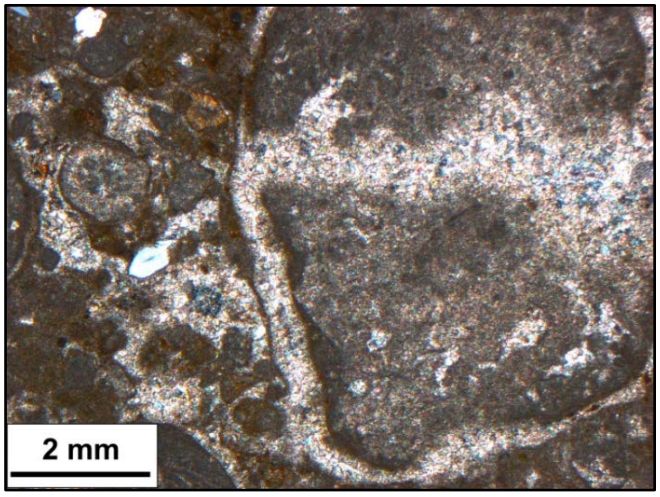

Figure 5.27: BC-12 Micrite matrix and spar calcite cement supported micrite fragments. Spar calcite veins transverse micrite fragments with oxidised micrite fragment boundaries (cross-polarised light). The section is oriented with the original vertical component towards the top of the page.

BC-14

The upper portion of the Bitesantennary site is largely composed of ooids (sample BC-14) interpreted as cave pearls (Figure 5.28A). Thin section locations and Δ_{47} sampling sites are shown in Figure 5.28. Cave pearls are deposited in ponded water and deposit fine layers of calcium carbonate (Figure 5.28B) onto a nucleus of either detrital calcite, bone fragments, pellets or lithic fragments. Laminae range in thickness from >100 μm to 2 mm in some ooids. Inner layers are coarser grained and are finer outwards, laminations tend to exhibit darker colouration in the fine-grained portion possibly due to some oxidation of iron oxide as well as that fine-grained micrite is denser and may appear darker in thin section. From the thin section analysis, various nuclei of these ooid structures are present; mostly calcite and lithic fragments (Figure 5.28C and D). The

ooids are primarily incorporated in a spar calcite cement with some micrite fragments (Figure 5.28E). In association with this, various bone fragments are also present with pores in-filled with large calcite spar crystals (Figure 5.28F). Throughout the sample various other fragments of quartz and chert are present, these are sub rounded to angular and up to 500 µm.

The BC-14 cave pearl layer, a succession of multiple deposition events of cave pearl beds can be observed (Figure 5.29). Two main layers of cave pearls are present with large ooids in the upper regions bound by a micritic matrix; ooids are larger in size upwards and are bound by a spar cement. This pattern repeats below in the same manner, indicating multiple cave pool and cave pearl deposition events. In addition, large limestone fragments are present in association with the larger cave pearls. Underlying the cave pearl layers is a more massive limestone. It contains some lithic clasts of chert and quartzite as well as small bone fragments. These fragments are contained in a micrite matrix with some spar cement and pore infill (Figure 5.29). No bedding is apparent in this layer and it may be part of the underlying more massive limestone such as in BC-12.

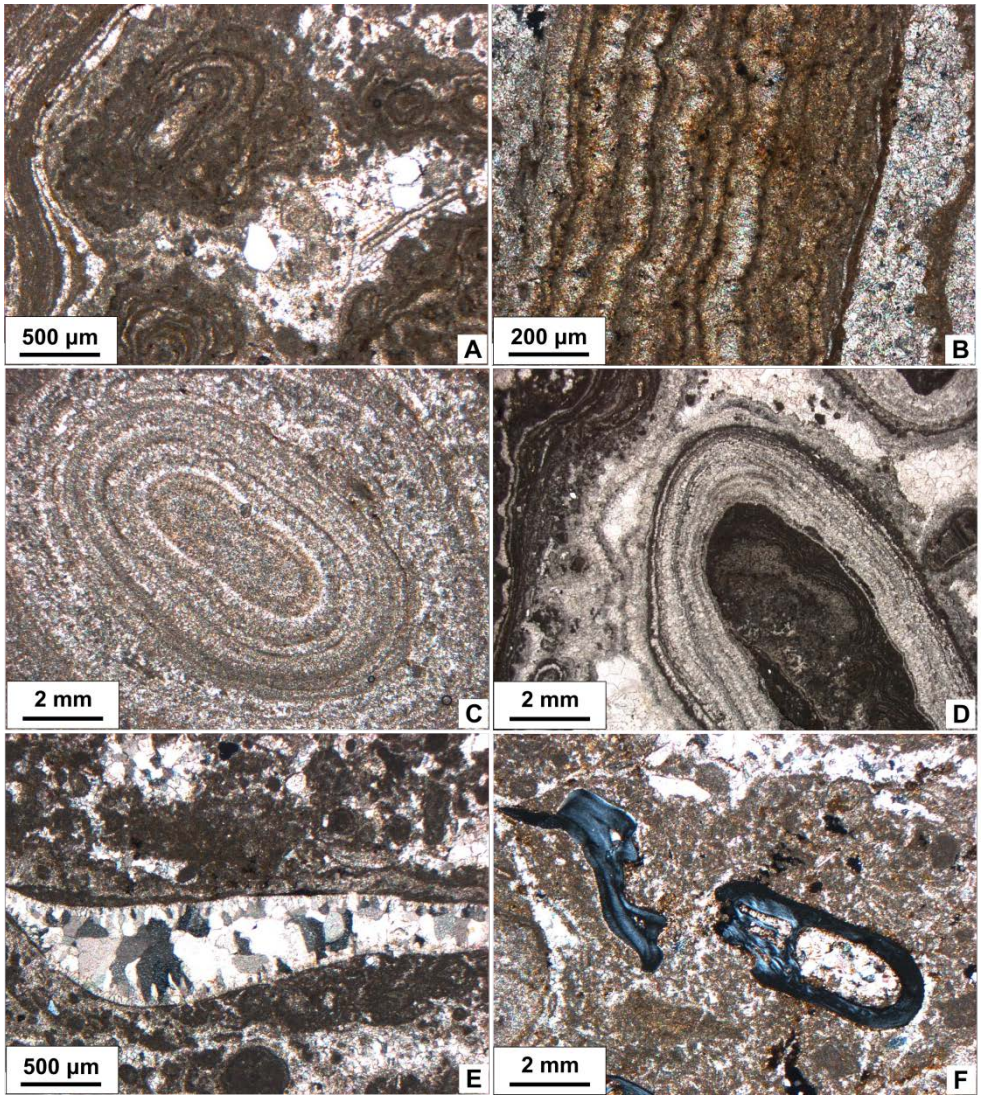

Figure 5.28: BC-14 Oosparite - cave pearl deposit in thin section. (A, B, C, D) Oolite cave pearls showing muddy micrite in thin concentric layers; (E) Spar calcite that has infilled a dissolution hollow; (F) Bone fragment with calcite infill. (A, B, E: cross-polarised light; C, D, F: plane-polarised light). Sections are oriented with the original vertical component towards the top of the page.

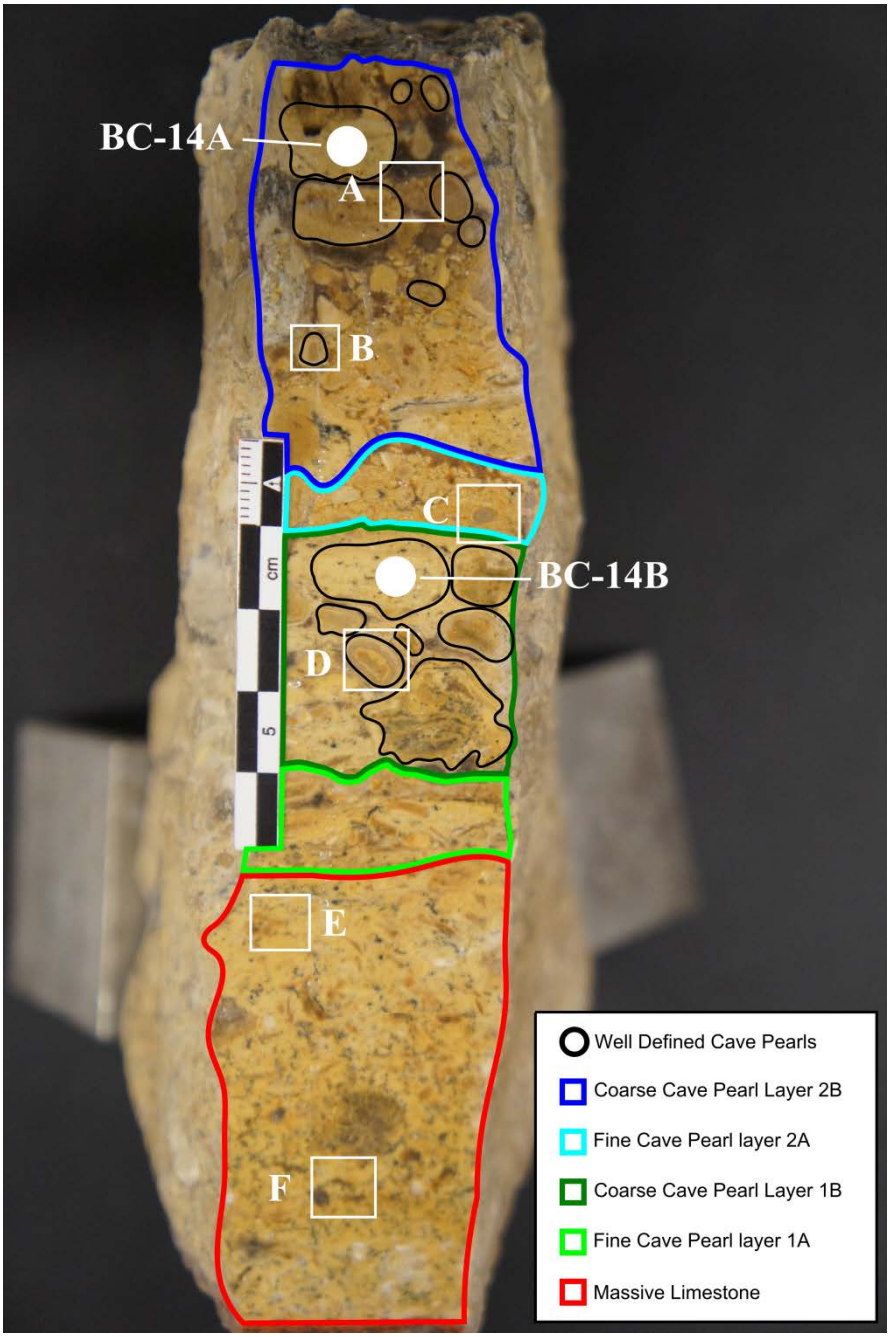

Figure 5.29: BC-14 cave pearl layer deposit, showing well defined cave pearls in two distinct layers (Layer 1 and 2), cave pearls are smaller nearer the base, forming two distinct zones of coarse and fine cave pearls in each layer (Zone A and B). Cave pearl layers grade into a massive fine-grained micritic limestone. White circles show Δ_{47} sampling sites, white boxes and letters correspond to areas covered by thin section in Figure 5.28. 5cm scale bar, 1 cm subdivisions.

5.4.1.4 Cleft of Ages site (CA,) White Hall site (WH), Oncoid site (OS) and Ringtail site (RT)

The Cleft of Ages site, White Hall site, Oncoid site and Ringtail site are located in close proximity to the AL-90 site on top of the ridge in the southern Gag Plateau. All the sites in this area represent small cave fill formations and structures within the Carl Creek Limestone. These deposits represent mid to late Miocene age caves of the System C faunal assemblages, from the White Hall site at 13.72 ± 0.12 Ma to the younger Ringtail site at 13.56 ± 0.66 Ma (Woodhead et al., 2014). These areas were first discovered in 1990 from preliminary surveys of the Gag Plateau. The area is rich in teeth from wombats, kangaroos and diprotodontids. In addition, the first preserved plant material of the Riversleigh fossil area was found adjacent to the Cleft of Ages site in association with a partially preserved *Neohelos* sp. (diprotodontid) jawbone (Archer et al., 2004).

Cleft of Ages site (CA)

The Cleft of Ages site is composed of an approximately 1 m thick layer of white to off-white speleothem (of uncertain geometry) with associated clastic detrital fragments (Figure 5.30). The outcrop contains many large pores and interconnecting channels that have been filled by secondary unconsolidated sediments as well as an overlying top soil and organic matter.

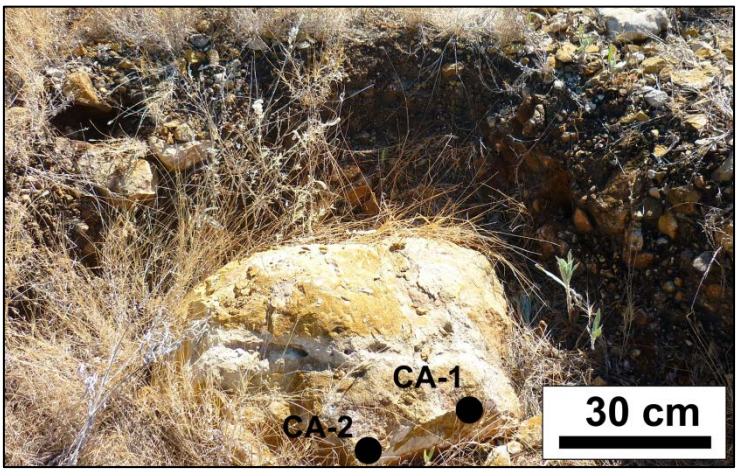

Figure 5.30: Cleft of Ages site sample outcrop, showing the exposed fossiliferous limestone and sample locations. Photograph is orientated facing northeast.

Both whole-bone structures and many small fragments occur in small concentrated areas throught the sample site. Most are small mammals and rodents as well as some avian species, identification of which is problematic as complete skeletons are rare. In addition large numbers of small bat bones were found; however, these are highly fragmented possibly indicating reworking and transport from other areas into this accumulating layer (Archer et al., 1998). Fragments are typically between 2 and 5 mm in size, sub-angular to sub-rounded in shape.

The sample of the Cleft of Ages calcite appears to contain many well rounded to rounded metaquartz grains; the bulk of the sample is micrite matrix supported (Table 5.5), and poorly sorted with rounded quartz grains appearing in a non-uniform pattern. This sparse biomicrite contains highly crystalline portions commonly associated with larger bone fragments (Figure 5.31), brown to yellow discolouration is common throughout the samples as are small black to dark brown organic plant fragments.

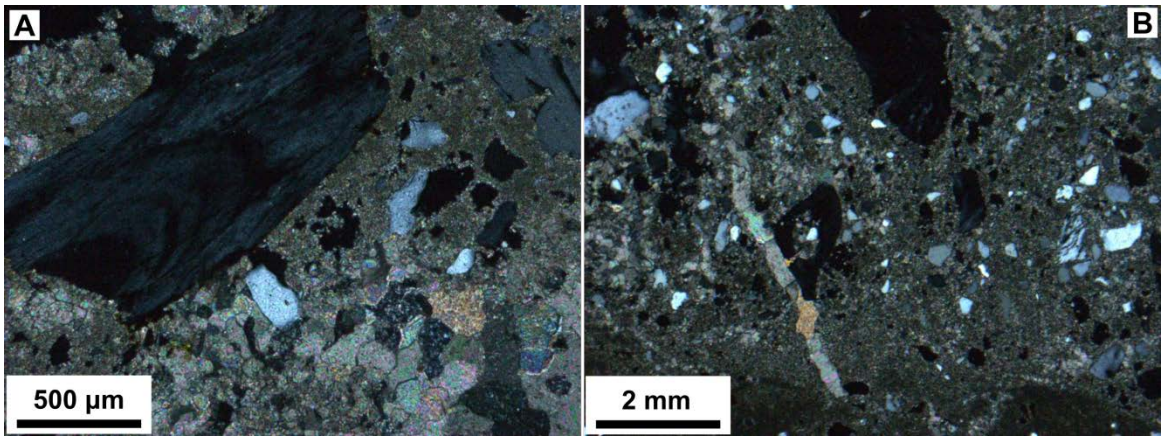

Figure 5.31: CA-2; (A) Sub-rounded bone fragment in micrite matrix in association with spar calcite (cross-polarised light); (B) Rounded quartz grains in micrite matrix in association with bone fragments and a calcite vein (cross-polarised light). Sections are oriented with the original vertical component towards the top of the page.

White Hall site (WH)

White Hall site is very similar to the Cleft of Ages site due to its close proximity as well as similar rock structure and morphological features and age (13.72 ± 0.12 Ma, Woodhead et al., 2014). The site is located approximately 300 m to the south east of the Cleft of Ages site, due to the limited excavation of the White Hall site at the time of sampling a useful field photograph is not provided. This area contains highly crystalline chemically precipitated limestone in various pond

or pool type deposits with a distinct crystal structure grading within the pool deposits (Figure 5.32).

Table 5.5: Cleft of Ages, White Hall, Oncoid and Ringtail sites. (A) XRD mineral phase contents (wt%) of the homogenised sample powder; (B) ICP-MS carbonate cation substitution in molar percent, based on total molar concentration; (C) Carbonate classification through point count analysis from thin sections using the Folk (1959) system.

A

Sample Name	% Calcite ($CaCO_3$)	% Dolomite ($CaMgCO_3$)	% Magnesite ($MgCO_3$)	% Siderite ($FeCO_3$)	% Aragonite ($CaCO_3$)	% Quartz (SiO_2)	% Kaolinite ($Al_2Si_2O_5(OH)_4$)	% Gypsum ($CaSO_4 \cdot 2H_2O$)
CA-1	95.6	0.5	0.5	0.5	1.7	0.3	0.5	0.4
CA-2	86.8	0.3	0.0	1.0	0.0	10.7	1.2	0.0
WH-1	99.0	0.6	0.0	0.2	0.0	0.0	0.2	0.0
WH-4	98.1	0.7	0.0	0.4	0.0	0.0	0.3	0.5
WH-5	97.2	0.8	0.0	0.5	0.1	0.0	0.5	0.9
OS-1	95.9	0.5	0.9	0.7	0.9	0.0	0.7	0.4
OS-2	94.7	0.8	0.4	1.7	0.0	2.0	0.3	0.0
OS-3	89.4	0.8	0.8	0.7	4.4	0.1	1.9	2.0

B

Sample Name	% Ca	% Mg	% Fe	Formula
CA-1	0.99	0.00	0.01	$(Ca_{0.99}Fe_{0.01})CO_3$
CA-2	0.98	0.00	0.02	$(Ca_{0.98}Fe_{0.02})CO_3$
WH-1	1.00	0.00	0.00	$CaCO_3$
WH-4	1.00	0.00	0.00	$CaCO_3$
WH-5	1.00	0.00	0.00	$CaCO_3$
OS-1	0.99	0.00	0.01	$(Ca_{0.99}Fe_{0.01})CO_3$
OS-2	0.99	0.00	0.01	$(Ca_{0.99}Fe_{0.01})CO_3$
OS-3	0.99	0.01	0.00	$(Ca_{0.99}Mg_{0.01})CO_3$

C

	Maxtrix		Allochems					
Sample Name	% Micrite	% Sparite	% Oolites	% Bones	% Molluscs	% Pellets	% Lithic Fragments	Carbonate Classification (Folk 1965)
CA-1	0	100.0	0	0	0	0	0	Spar calcite
RT-1	8.5	25.0	4.25	0	62.0	0	0.25	Sorted biosparite
RT-2	77.5	11.0	0	0.25	10.5	0	0.75	Fossiliferous biomicrite
WH-1	0	100.0	0	0	0	0	0	Spar calcite
WH-4	86.0	13.5	0	0	0	0	0.5	Dismicrite
WH-5	0	100.0	0	0	0	0	0	Spar calcite
OS-2	11.5	31.75	52.5	2.5	0	0	1.75	Packed oosparite

In the samples selected from the White Hall site, two main deposition processes are present. Sample WH-1 a highly crystalline calcitic limestone containing many individual crystal aggregates and structures such as small calcite blocks up to 2 cm in size. Grading is well developed with calcite forming fine-grained microspar layers on top with more crystalline calcite below, with crystals up to 6 mm in length. Graded calcite rafts and cave pool deposits are predominant (Figure 5.32).

Figure 5.32: WH-1; crystalline spar calcite and microspar cement. Calcite raft grading is apparent from tightly bound microspar on top into larger crystals of calcite on the bottom. Nearer the bottom of the illustration, more calcite microspar has infilled around the larger crystals (plane-polarised light). Section is oriented with the original vertical component towards the top of the page.

Calcite cave rafts, such as the ones found at White Hall (WH-5), display a highly crystalline structure with distinct orientation and grading throughout the small 2-3 cm long structure. Rafts such as this are found layered within the deposit with the more crystalline side facing downwards with the fine-grained portion uppermost. These fine-grained layers are typically between 0.5 and 1 mm in thickness and form at the surface of cave pools and still standing bodies of water as an evaporite crust. Larger crystals then begin to form downward into the water column. Once the weight of the accumulated crystal structure becomes too great the calcite crystal aggregate will break off and typically settle onto the bottom of the cave pool (Figure 5.33).

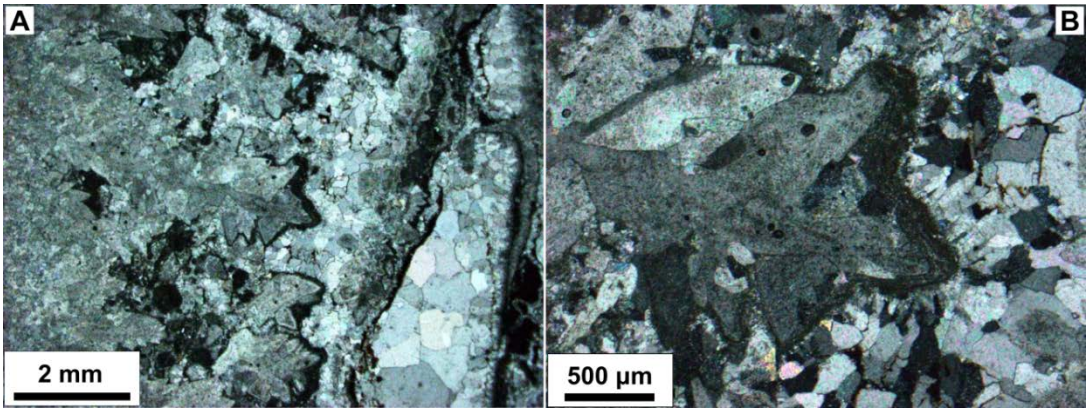

Figure 5.33: WH-5 showing A: Crystalline spar calcite with, B: microspar cement and dark micrite infill (A, B: cross-polarised light). Sections are oriented with the original vertical component towards the top of the page.

Oncoid site (OS)

Oncoid site is in close proximity to both the Cleft of Ages site and the White Hall site. The former contains no vertebrate remains but is notable for the presence of well developed cave pearls whose nuclei are predominantly spar calcite with gastropods and minor bone (Figure 5.34A, C). The general carbonate composition is calcite with minor quartz (2 %, Table 5.5C).

Figure 5.34: Oncoid site sample outcrop, showing the exposed cave pearl bearing limestone with smaller pearls on top and larger cave pears below. Photograph is orientated facing northeast.

The limestone of the oncoid site is primarily composed of up to 52 % oolites in a micritic calcite matrix (Table 5.5A). Some quartz and clay also occur as oolite nuclei, whose morphology is sub-rounded to ovate in shape. Lamination is evident in distinct layers of alternating irregular bands of light and dark calcite precipitates. Light coloured precipitate is of sparite consistency with darker layers representing a more micritic nature as well as some organic matter (Figure 5.35A, B, C and D).

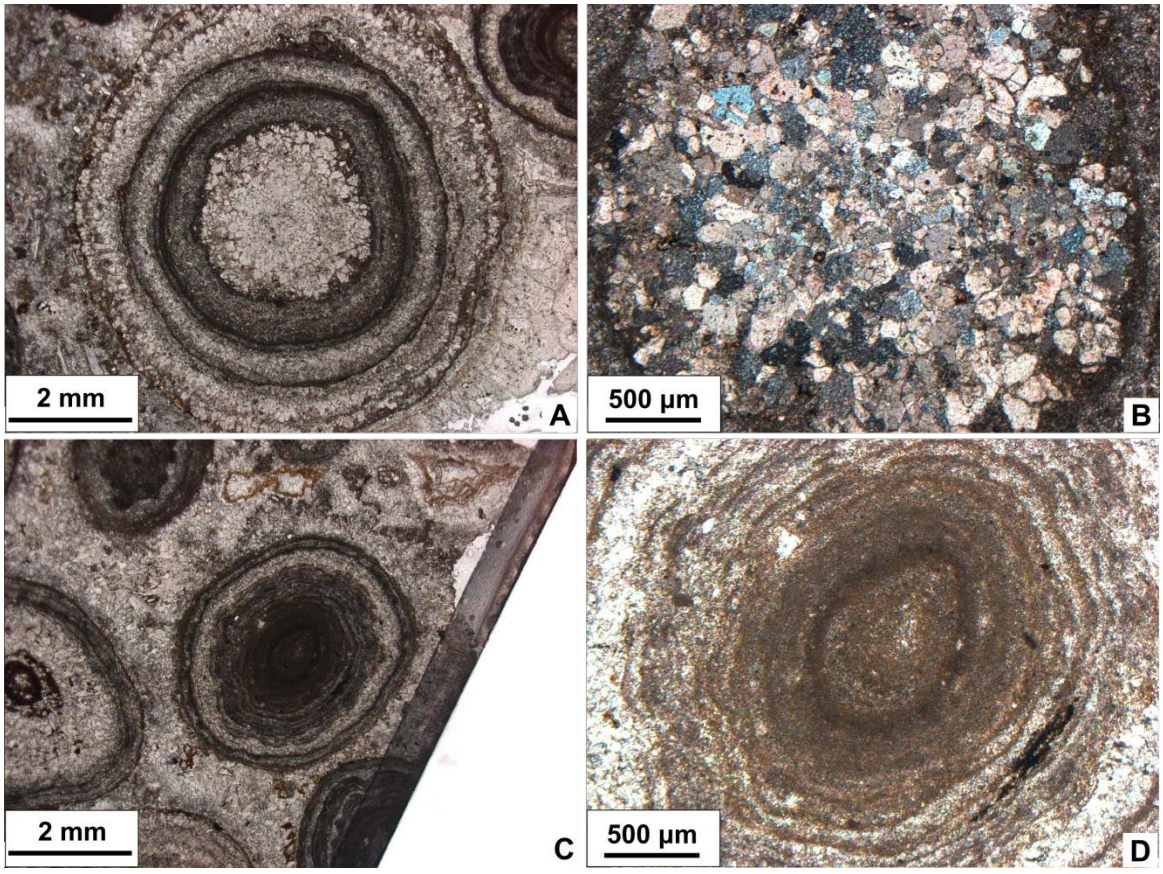

Figure 5.35: OS-1 and 3; Cave pearls encased in calcite spar cement. A and B: show a cave pearl containing a calcite spar core surrounded by finer-grained calcite growth layers stained with darker organic matter (A: plane-polarized light; B: cross-polarised light). OS-3; C and D: shows a cave pearl containing a lithic core surrounded by finer-grained calcite growth layers stained with darker organic matter (C and D: plane-polarised light). Sections are oriented with the original vertical component towards the top of the page.

Ringtail site (RT)

The Ringtail site is the youngest site in this study at 13.56 ± 0.66 Ma (Woodhead et al., 2014) forming the upper end member of the System C faunal assemblage, and located on the Gag Plateau to the west of Godthelp Hill. Due to the limited excavation of the Ringtail site at the time of sampling a useful field photograph is not provided. The site contains abundant well-preserved fossil material, such as bivalve and gastropod shells. The fossil material is micrite bound in association with prominent dark organic colouration. Lithic fragments such as quartz and clay detritus are also present in association with some fossils, suggesting a dynamic depositional environment with potential fluvial influences on the fossiliferous limestone (Figure 5.36).

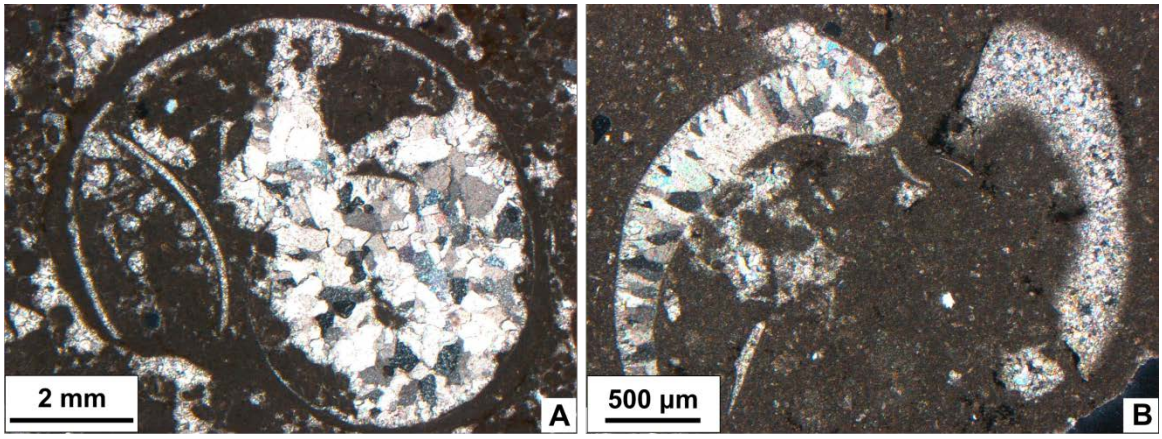

Figure 5.36: RT-1; A: shows a gastropod shell with spar calcite infill. B: shows a bivalved shell in micrite matrix (A and B: cross-polarised light). Sections are oriented with the original vertical component towards the top of the page.

5.4.2 Clumped-isotope Δ_{47} palaeotemperature determinations

From the carbonate facies previously described, particular samples from several environments were selected for palaeotemperature determination. The samples chosen did not exhibit any signs of significant diagenetic alteration. Various microcarbonate deposition structures such as cave pearls, calcite rafts and bulk cave wall and infill material were sampled to provide a large range of potential palaeotemperature indicator sites. Additionally, the selected materials are considered to be depositional structures within the cave system that precipitated calcium carbonate at or close to isotopic equilibrium. Some non-equilibrium precipitated stalagmite samples were also taken deliberately to compare with adjacent cave deposits. The results are reported in the same order as the previous presentations of each site.

Flowstones and their associated calcite deposits do not precipitate their calcite in thermodynamic (Δ_{47}) equilibrium (Affek et al., 2008). This is largely due to the nature of the deposition that it is not always in contact with the precipitation host water. The implication of this is that the palaeotemperature result may be an overestimate of actual ambient temperature for this type of calcium carbonate deposition (Daëron et al., 2011). It has been suggested that speleothems produce calculated Δ_{47} temperatures up to 8 °C above the actual ambient conditions in the cave system. This was shown in one of the first applications of the clumped isotope thermometer to speleothems from Soreq cave, Israel (Affek et al., 2008, 2014). Similar trends were reported for cave drip water experiments and equilibrium calculations by Daëron et al. (2011) on the Villars cave, France. Conversely, when deducing temperature from fluid inclusions the equilibrium relationships are not as previously expected and show an underestimation in carbonate formation temperature (Daëron et al., 2011).

It is likely that the former is the case observed from the speleothem carbonates (cave limestones, flowstone and stalagmites) at the Neville's Garden site as well as other sites in the Riversleigh area such as Inabayence, Camels Sputum Stalagmite site and the majority of the System C faunal assemblage deposits such as Cleft of Ages, White Hall and Ringtail sites. However, the magnitude of this offset cannot be accurately estimated for Riversleigh, since the cave systems are no longer active and water flow ceased many thousands of years ago. Therefore, palaeotemperatures from the Riversleigh speleothems must be scrutinised in a similar way to examples from Soreq and Villars cave systems. It cannot be assumed equilibrium precipitation conditions for the precipitated calcite in the deposited speleothem.

However, estimates can be made of the isotopic composition of the precipitating host water through the use of a conventional palaeotemperature equation such as from Kim and O'Neil (1997) or Coplen et al. (2007).

5.4.2.1 Neville's Garden site

The limestone samples from Neville's Garden provided Δ_{47} values of 0.661 ± 0.017 and 0.700 ± 0.008 ‰ corresponding to calculated carbonate formation temperatures of 35.6 ± 4.4 and 25.8 ± 1.9 °C (Table 5.6). Both these temperatures were calculated from limestone calcite directly below and above the precipitated flowstone at the base of the Neville's Garden site. The flowstone itself was not analysed by Δ_{47} palaeothermometry since it was likely not precipitated at equilibrium conditions and is most likely to exhibit significant disequilibrium fractionation. Both the upper and lower calculated formation temperatures are likely an overestimate of ambient temperature. Samples taken at the top of the Neville's Garden site do not yield plausible formation temperatures. This is likely due to additional factors of secondary calcite precipitation as well as organic matter contamination, this will be discussed in detail later.

5.4.2.2 Inabayence and Camels Sputum sites

The low energy (deep pool) depositional environment of Camels Sputum provided undisturbed burial conditions providing well preserved shell and bone fragments. The massive limestone precipitates of CS-2 produced a Δ_{47} value of 0.688 ± 0.020 ‰ corresponding to a calculated temperature of 28.6 ± 5.1 °C (Table 5.6). The neighbouring Inabayence site contained crystalline calcite flowstone precipitates (sample IN-2), this yielded a Δ_{47} value 0.692 ± 0.028 ‰ corresponding to a calculated temperature of 27.6 ± 6.9 °C and sample IN-5 exhibited a similar Δ_{47} value of 0.699 ± 0.006 ‰ with a calculated temperature of 26.0 ± 1.4 °C (Table 5.6). The calculated temperatures of the Inabayence site are similar to the calcite precipitation temperature calculated for Camels Sputum (CS-2). However, these three temperatures are likely overestimations of actual ambient temperature conditions of the System B faunal assemblage of the Riversleigh area, due to disequilibrium precipitation as discussed previously. If similar temperature offsets were assumed then these temperature may be meaningful. If such offsets were applied the calculated Innabayence and Camels Sputum temperatures would conform well to calcite precipitation temperatures such as the Bitesantennary calcites and White Hall pool carbonates of approximately 19 ± 4 °C (Table 5.6).

5.4.2.3 Stalagmite site

The stalagmite found in the vicinity of the Camels Sputum and Inabayence site provided three very different Δ_{47} values of 0.686 ± 0.020 to 0.960 ± 0.036 ‰ corresponding to calculated formation temperatures ranging from 29.2 to -22.2 °C (Table 5.6). Three temperature determinations were made on three zones of the stalagmite SG-1, SG-2 and SG-3. These samples were taken from the inside to outside respectively. The temperature calculated from the outside of the stalagmite is highly negative (-22.2 °C) well outside the likely temperature range of the environment during the Oligo-Miocene. This enrichment in the Δ_{47} value is likely to be the result of diagenesis of the external stalagmite calcite after burial or may be the result of incorporated organic material in the precipitated stalagmite calcite. Distinction between primary and secondary calcite proved difficult due to the highly crystalline nature of the material.

Formation temperatures calculated from Δ_{47} values from the inner core SG-2 and SG-3 (15.8 ± 5.0 and 29.2 ±4.4 °C, respectively) suggest that these areas have not been as affected by post burial recrystallisation as the external layer. Organic material appears to be absent from the internal areas of the stalagmite. This may indicate a change in precipitation chemistry or may be due to a change in cave water chemistry during the evolution of the cave system. Also, the outer margins appear highly bleached through rainwater percolation and are crumbly suggesting a significant amount of weathering and reprecipitation of calcite, resulting in highly enriched Δ_{47} values in the outer portions of the stalagmite.

As previously noted stalagmites are known not to precipitate at isotopic equilibrium in regard to the clumped isotope method. However, the calculated temperature of 29.2 ± 5.0°C for the central portion of the stalagmite is plausible given the lack of subsequent burial of the cave deposits. Nevertheless it is likely to still represent an overestimation of actual ambient environmental conditions.

5.4.2.4 Bitesantennary site

The Bitesantennary site is one of the largest in the Riversleigh area as well as one of the most complicated and dynamic. Various calcite cave deposits were collected, however, only a limited number of these were utilised. Most samples from the site were not suitable for palaeotemperature analysis due to their high organic content. Other specimens such as BC-1 to BC-4 contained larger amounts of lithic components and pre-date the karst cave systems. Pure calcium carbonate specimens from the Bitesantennary site BC-5 and BC-10 appear to produce similar plausible palaeotemperatures for calcite formation. These specimens represent massive calcite deposits from two distinct deposition events as shown in section 5.4.2.1. Clumped isotope measurements

were conducted on primary crystalline spar calcite precipitated at equilibrium in both occurrences. This produced Δ_{47} values of 0.728 ± 0.018 ‰ and 0.725 ± 0.025 ‰. These values represent an average value for the BC-5 and BC-10 samples of 4 replicate analyses on different calcite spar nodules within the bulk whole rock sample. The Δ_{47} values provide calculated calcite precipitation temperatures of 19.3 ± 4.0°C and 19.8 ± 5.6°C, respectively (Table 5.6). These samples are considered to be equilibrium precipitated calcite deposits within the karst cave system. Both samples contain multiple bone fragments and small gastropods. Therefore, it is assumed that the calcite spar analysed resembles co-precipitated calcium carbonate within a body of water within the cave system. The reported temperature is highly plausible for the early Miocene north-eastern margin of the D-Site plateau at Riversleigh. Since the carbonate precipitated at equilibrium, the calculated temperature can be considered as a plausible ambient temperature reflection of the surrounding environment during the Miocene. However, it is possible that some equilibrium fractionation has affected the temperature calculation. The higher errors take this into account and provide a conservative palaeotemperature estimate for the Bitesantennary site.

Additionally, a sample of calcite matrix dominated sandstone was analysed (BC-2). Due to the specimens deposition style the organic constituent was quite high. This is reflected in the elevated Δ_{47} value of 0.884 ± 0.024 ‰, this translates to a negative calculated formation temperature of -10.5 °C. This may be because the carbon dioxide gas purification method used in this study was not fully successful in removing all the organic components incorporated into the calcite material. The oxygen-18 and carbon-13 values are also substantially different to calcite specimens from the upper layers of the Bitesantennary site. The $\delta^{18}O$ value of BC-2 is up to 5 ‰ higher than other BC calcite samples, whereas $\delta^{13}C$ values are up to 13 ‰ different to other Bitesantennary specimens (Table 5.6).

5.4.2.5 Cleft of Ages, Oncoid and White Hall sites

The Cleft of ages site did not provide plausible carbonate formation temperatures. Both CA-1 and CA-2 samples produced highly enriched Δ_{47} values providing highly negative temperatures. This high enrichment will be discussed further in section 5.4.3.

OS-1 and OS-3 are both cave pearls that contained calcite nuclei. Only the precipitated layers of the cave pearl were analysed using the clumped isotope method. This provided Δ_{47} values of 0.673 ± 0.063 and 0.690 ± 0.017 ‰ corresponding to calculated temperatures of 32.4 ± 5.0 and 28.2 ± 4.3 °C (Table 5.6). Both these temperatures are likely to be an overestimate of the ambient environmental conditions, as suggested by Affek et al. (2008) and Daëron et al. (2011).

The White Hall site exhibits formation temperatures similar to Neville's Garden. Specimens from the White Hall site were thought to be equilibrium deposited calcite rafts and travertine rim pool precipitates. Calcite raft precipitates such as WH-1 display Δ_{47} values of 0.647 ± 0.018 corresponding to a calcite precipitation temperature of 39.2 ± 4.9 °C. This formation temperature is quite high for a calcite deposited at thermodynamic equilibrium with the surrounding cave water in comparison to other carbonate formation temperatures from the surrounding area, such as the equilibrium calcite depositions of the Bitesantenary site ~19.5 °C or elevated flowstone palaeotemperatures of Neville's Garden at 25 °C. Another White Hall specimen gave Δ_{47} values of 0.732 ± 0.021, from radial calcite clusters that have grown unrestrained within their precipitation waters, this yielded a more plausible calculated formation temperature of 18.2 ± 4.8 °C suggesting it may have precipitated at equilibrium.

5.4.2.6 Ringtail site

The Ringtail site represents an aquatic precipitated limestone, possibly a rim pool or small cave lake. Small bivalves, gastropods and small calcareous concretions are present in a spar calcite cement. The calcite cement of the Ringtail site was analysed by clumped isotope palaeothermometry and gave Δ_{47} values of 0.710 ± 0.023 ‰ corresponding to a calculated temperature of 23.2 ± 5.4 °C. This calculated temperature is plausible for the ambient conditions of the surrounding environment. Calcite at the Ringtail site has formed at equilibrium within the precipitating host water. However, as previously discussed it is possible that some disequilibrium precipitation has occurred.

5.4.3 Enriched Δ_{47} values and associated highly negative temperatures

Several of the Riversleigh cave deposits produced implausibly high Δ_{47} values, corresponding to highly negative extrapolated calculated carbonate formation temperatures. We consider two possible sources for this error.

Firstly, contamination may have resulted from organic material that was not able to be removed using the carbon dioxide purification method used in this study. This suggests that the amount of organic material in some samples was in excess of the capacity of the gas chromatography purification process. Alternatively, the organic matter contained within the Riversleigh deposits was more complicated than initially expected and did not respond well to the carbon dioxide purification procedure. The samples in the Cleft of Ages site contained organic matter in bands associated with iron staining. The samples Δ_{47} value is enriched (0.809 ‰) and thus produces an implausibly low calculated formation temperatures of 2.5 °C for the sample (Table 5.6). The upper layer of cave-fill limestone of the Neville's Garden site (NG-3) contained large organic fragments, as indicated by thin section (Figure 5.10). Sample NG-3 produced a Δ_{47} value of 0.845 corresponding to a low formation temperature of -4.0 °C, not a plausible limestone precipitation temperature. Additionally the upper portion of the NG site was contaminated with red brown iron staining possibly in association with algal colonies forming banded organic layers, these were also analysed by Δ_{47} palaeothermometry but did not yield plausible calculated temperatures. Cave pearls found in the upper reaches of the Bitesantennary site (BC-14), as well as one of the cave pearls from the Oncoid site (OS) contained organic material (Figure 5.32). Organic constituents are present in concentric layers within the cave pearl incorporated in conjunction with calcite; this forms bands of brown to grey staining in the cave pearls. Cave pearls of the Bitesantennary site BC-14A,B produced implausible calculated formation temperatures of -3.0 and -19.4 °C (Table 5.6).

Secondly, some organic matter present within the calcite may also react with H_3PO_4 during sample gas preparation and producing CO_2 which is mixed with carbonate-derived CO_2. This has the potential to highly enrich the Δ_{47} signal which may be part of the reason that some of the Riversleigh speleothems produce calculated formation temperatures of between 29 and -22 °C. This phenomenon of organic matter reacting with the phosphoric digestion acid may also be occurring in other samples in this study including some of the glendonites. Further analysis and refinement of purification techniques such as the addition of peroxide or methanol treatments may be necessary to resolve some of the uncertainties. However, sample integrity must be maintained to reduce the possibility of isotopic fractionation and alteration.

Table 5.6: Clumped isotope results for the Riversleigh area fossil sites, tabulated in stratigraphic order. The Δ_{47} values are presented in the absolute reference frame of Dennis et al. (2011), Temperatures are calculated using the clumped isotope palaeotemperature equation of Zaarur et al. (2014). All Δ_{47} and conventional $\delta^{13}C_{VPDB}$ and $\delta^{18}O_{VSMOW}$ values are standardised against high purity Oztech gases, Carrara marble (CM-1) and laboratory standard analytical grade calcium carbonate with known isotopic compositions. Measurements were replicated 2 to 4 times per sample.

Site	Faunal System	Sample	*n*	$\Delta_{47\text{-RF}}$ ‰	SD	δ_{47} ‰	(°C)	±	$\delta^{13}C_{calcite}$ VPDB ‰	$\delta^{18}O_{calcite}$ VPDB ‰	$\delta^{18}O_{water}$ VSMOW ‰*
Ringtail		RT-1	3	0.71	0.023	5.2	23.2	5.4	-8.38	-5.95	-5.8
Oncoid		OS-1	2	0.673	0.02	6.2	32.4	5	-7.3	-6.22	-6.1
		OS-3	4	0.69	0.017	8	28.2	4.3	-5.75	-5.67	-5.6
White Hall		WH-1	3	0.647	0.018	3.7	39.2	4.9	-7.58	-8.14	-8.0
		WH-2	3	0.825	0.029	3.9	-0.4	5.2	-7.88	-7.80	
		WH-4	3	0.819	0.038	3.3	0.7	7.1	-8.08	-8.14	
	System C	WH-5	3	0.732	0.021	3.1	18.2	4.8	-8.23	-8.18	-8.0
Cleft of Ages		CA-1	3	0.809	0.025	4.4	2.5	4.8	-8.18	-7.02	
		CA-2	3	2.647	0.036	6.4	-126	1	-7.02	-7.95	
Bitesantennary		BC-14B	2	0.941	0.041	6.5	-19.4	6	-7.1	-6.10	
		BC-14A	2	0.839	0.047	7.6	-3.0	8.3	-6.04	-5.94	
		BC-10	3	0.725	0.025	5.5	19.8	5.6	-7.61	-6.42	-6.2
		BC-5	3	0.728	0.018	4.4	19.3	4	-7.88	-7.23	-7.0
		BC-2(calcite)	2	0.884	0.024	22.4	-10.5	3.9	5.44	-2.60	
Stalagmite		SG-3	2	0.96	0.036	5.3	-22.2	5.1	-5.97	-6.81	
		SG-2	2	0.743	0.02	5.6	15.8	4.4	-7.54	-6.35	-6.2
		SG-1	3	0.686	0.02	4.9	29.2	5	-7.44	-7.15	-7.0
Camels Sputum		CS-10	1	0.824	0.025	6	-0.3	4.6	-7.27	-6.34	
		CS-2	3	0.688	0.02	4.3	28.6	5.1	-7.96	-7.23	-7.1
Inabayence	System B	IN-5	3	0.699	0.006	5.6	26	1.4	-4.15	-9.57	-9.3
		IN-3	2	0.796	0.017	3.4	5.1	3.4	-8.21	-7.98	
		IN-2	3	0.692	0.028	4.9	27.6	6.9	-7.46	-7.13	-7.0
Neville's Garden		NG-3	2	0.845	0.026	3.7	-4.0	4.6	-8.05	-7.83	
		NG-1C	3	0.7	0.008	2.6	25.8	1.9	-8.46	-8.35	-8.1
		NG-1A	3	0.661	0.017	7.5	35.6	4.4	-6.25	-5.65	-5.6

*$\delta^{18}O_{water}$ ‰ (VSMOW) is calculated from plausible Δ_{47} temperatures and the $\delta^{18}O_{(calcite)}$ ‰ (VPDB) from the Riversleigh samples using the palaeotemperature equation of Kim and O'Neil (1997).

5.4.4 Calculated $\delta^{18}O$ of host waters

The $\delta^{18}O$ value of the precipitating host water of some of the Riversleigh deposits was calculated based on plausible calculated Δ_{47} temperatures and the $\delta^{18}O_{calcite}$ ‰ (VPDB) of the carbonate sample using the calcite palaeotemperature equation of Kim and O'Neil (1997).

Carbonates of the System C faunal assemblage of the Early Miocene (~16-23 Ma) exhibit $\delta^{18}O_{water}$ values of between -5.6 and -8.0 ‰ (Figure 5.37). Additionally, faunal system C temperatures are generally lower than system B faunal assemblage deposits. Carbonate deposits of the System B faunal assemblage of the Middle Miocene (~13-16 Ma) exhibit calculated $\delta^{18}O$ values between -5.6 and -9.3 ‰ (Figure 5.37). Faunal system B occupies a narrower and slightly higher average temperature range than the system C faunal assemblage deposits.

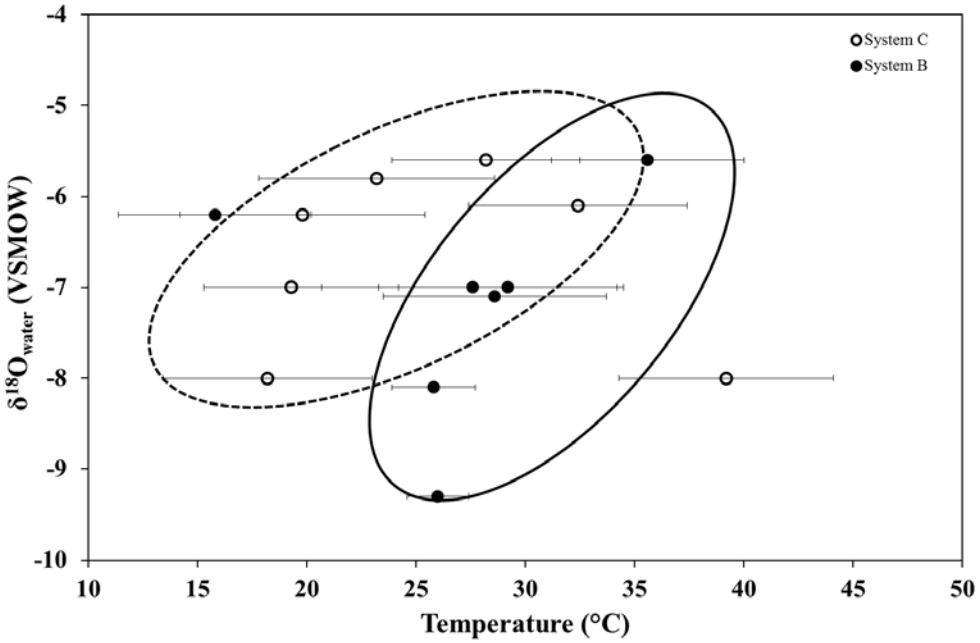

Figure 5.37: Riversleigh $\delta^{18}O$ (±1σ) (VSMOW) values of the precipitating host water calculated from Δ_{47} values plotted in relation to the calculated temperatures formation temperatures (°C) calculated from Δ_{47} values of Riversleigh carbonate samples from Faunal Systems C and B. Ellipses, in solid black and dashed black, show the approximate grouping for faunal systems C and B.

There is little difference in the average value between the two assemblage systems; however, due to the large uncertainty of both the Δ_{47} derived temperature of some of the samples as well as the uncertainty of the palaeotemperature equation used there is no clear basis to suggest that there is a significant difference in host water isotopic composition within the Riversleigh area. This is

further illustrated by figure 5.37 where the calculated $\delta^{18}O_{(water)}$ values of the Riversleigh carbonates are plotted against the calculated formation temperature. There is a large proportion of overlap between the two faunal systems. However, there appears to be an observable difference between the two systems both in average temperature and $\delta^{18}O_{water}$ values (Figure 5.#). This is illustrated by the solid and dotted ellipses showing the approximate grouping of the two faunal systems and how they relate to one another.

These relationships show that there appears to be a minor trend that suggests an elevated local average annual palaeotemperature in the Early Miocene (Faunal system B), associated with extensive rainforest habitats (Travouillon et al., 2009) and subsequently lower average annual temperature in the Mid Miocene (Faunal system C), associated with a dryer savannah-dominated landscape (Megirian et al., 2004). This coincides with long-term global cooling and drying trend of the Miocene (Woodhead et al., 2014). This may be a localised phenomenon and may only be appropriate for the immediate geographical area. A wider study area as well as a broader time period should be considered before any tangible extrapolations can be made using this data to elucidate the palaeoenvironmental evolution of the Riversleigh fossil area.

5.4.5 Conventional $\delta^{13}C$ and $\delta^{18}O$ analyses

Conventional $\delta^{13}C_{carbonate}$ and $\delta^{18}O_{carbonate}$ ‰ (VPDB) values show that there are distinct differences in isotopic composition between different excavation sites in the Riversleigh fossil area. Excavation sites such as White Hall and Inabayence share relatively similar $\delta^{13}C$ and $\delta^{18}O$ values, ranging from ~-7.4 to -8.2 ‰ (VPDB) and ~-7.2 to 8.3 ‰ (VPDB) respectively, although they originate from different faunal systems and are geographically disconnected. The Cleft of Ages excavation site is geographically no more than 10 meters to the north of White Hall, occupying the same faunal system, and has a relatively similar isotopic composition. The Bitesantennary site has a fairly narrow range of $\delta^{18}O$ values, between ~-6.0 and -7.2 but varies up to 2 ‰ in $\delta^{13}C$. Also, this excavation area should be isotopically similar to the other system C sites, such as Cleft of Ages and White Hall. However Figure 5.38 shows a distinct offset between these sites.

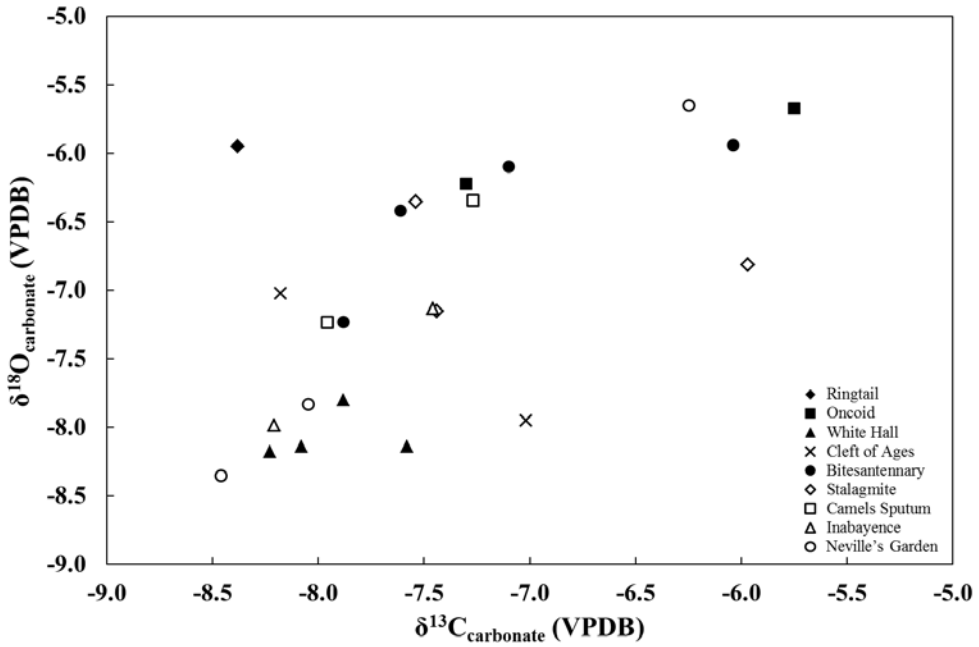

Figure 5.38: Conventional $\delta^{13}C_{carbonate}$ ‰ (VPDB) values plotted against $\delta^{18}O_{carbonate}$ ‰ (VPDB) values showing the differences between the various Riversleigh fossil sites.

The faunal system B excavation sites show similar discontinuous relationships. However, sites in close geographic proximity such as Stalagmite and Camels Sputum are isotopically similar. Whereas other sites such as Neville's Garden have widely distributed isotopic values and no clear pattern is observed. This may in part be due to the different sample types analysed from the various extraction sites and not essentially be related to the age of the deposit and therefore may not represent a change in either source water isotopic composition change nor a change in the biogenic carbonate availability of the environment in the Riversleigh fossil area.

5.5 Conclusions

Previous studies using clumped isotopes to investigate the palaeotemperatures of speleothems have met with temperature discrepancies between inter-cave precipitation structures as well as calibration issues when comparing ancient material to modern cave precipitates and their associated drip waters. These studies have focussed on stalagmites and flowstones that are known to precipitate calcium carbonate that is not in isotopic thermodynamic equilibrium. Therefore, these specimens exhibit clumped isotope precipitation temperatures up to 8 °C higher than the actual ambient conditions of the precipitating environment.

The Riversleigh fossil area is part of a large inactive near-surface carbonate karst system of Oligo-Miocene age, where various types of cave deposits are found in association with the largest diversity of the megafauna species in Australia. In this study clumped isotopes were used to quantify equilibrium precipitated calcite concretions and subaqueous precipitated spar calcite and non-equilibrium precipitated calcite deposits such as calcite rafts, pool stones, cave pearls, travertine rim pool precipitates as well as the common cave features such as stalagmites and flowstones. Equilibrium precipitated calcites appear to produce reliable ambient temperatures of 19.6 ± 4.8 °C, plausible for the environment in the Oligo-Miocene period in the north-east of Australia. These were attained from flowstones at the Bitesantennary site at Riversleigh. Non-equilibrium precipitates produce precipitation temperatures, up to ~7.3 °C higher than calcites precipitated at equilibrium. Such non-equilibrium precipitates included the stalagmite (SG-1) displaying up to a 10 °C temperature discrepancy. Cave deposits at the Camels Sputum (CS) and Inabayance (IN) sites exhibit a temperature discrepancy of between ~7 to 9 °C. Other specimens produced temperatures up to 20 °C higher than equilibrium, such as the calcite rafts at the White Hall site (WH) and flowstones from Neville's Garden (NG). However, these originate from depositional environments where excessive evaporation and degassing of precipitation water was highly plausible.

Some specimens analysed in this study produced irregular clumped isotope compositions, exhibiting highly enriched Δ_{47} values greatly above the normal natural limits. This was due to organic matter influences during the acid-reaction and gas purification process. The sample gas purification procedure developed for the clumped isotope method at the University of Wollongong was applied to all samples from the Riversleigh caves. However, certain specimens containing large amounts of organic matter yielded highly enriched Δ_{47} results. This indicated that the sample gas purification method may not applicable to all samples and may only have a limited potential for removing enclosed organic constituents in calcium carbonate precipitated speleothem

specimens. Results presented in Chapter 6 exhibit similar problems of highly enriched Δ_{47} values due to organic content that was unable to be removed using the developed carbon dioxide gas purification protocol. Alternatively, organic matter in the sample powders produced additional CO_2 in reaction with phosphoric acid, enriching the Δ_{47} anomaly and thus producing highly improbably low calculated formation temperatures.

In summary, the Riversleigh cave deposits and the associated fossil material are able to further elucidate the palaeoenvironmental conditions of the Oligo-Miocene period and give insight into the ambient environmental conditions of the past habitats of some Australian megafauna assemblages. The Riversleigh cave systems have been inactive for a long time preventing the calibration of ancient samples to modern equivalents. This reduces the accuracy and applicability of the determined palaeotemperatures. However, we have successfully shown that the site is able to produce usable calcite formation temperatures if the deposition mechanisms, depositional history and degree of organic material contamination are known.

Chapter 6 : Sydney Harbour: temperate or tropical waters ?

6.1 Introduction 190
6.2 Background 192
6.2.1 Calcification physiology 193
6.2.2 Dissolved inorganic carbonate (DIC) source 194
6.2.3 Shell sampling strategies 194
6.2.4 Clumped isotopes and biogenic carbonates 195
6.3 Methods 199
6.3.1 Specimen classification and nomenclature 199
6.3.2 Shell carbonate sampling and preparation 201
6.3.3 ^{14}C dating by AMS 202
6.3.4 Isotopic analysis 202
6.4 Results and discussion 203
6.4.1 Shell taxonomy and descriptions 203
6.4.2 Significance of species diversity 211
6.4.3 Shell ages and ^{14}C dating 215
6.4.4 Conventional $\delta^{13}C$ and $\delta^{18}O$ results 216
6.4.5 Clumped-isotope analysis 218
6.4.6 Isotopic shell zone partitioning 219
6.4.7 Temperatures calculated from $\delta^{18}O$ 220
6.5 Conclusions 223

6.1 Introduction

Bivalve and gastropod shells have the potential to provide information about their physiologies, calcification and ambient environmental conditions through the isotopic composition of their precipitated carbonate shells. The use of bivalves and gastropods and their applicability for palaeoenvironmental studies has been well established over many years by the carbonate-water oxygen isotope method. However molluscs remain a relatively underrepresented category within 'clumped' isotope analyses. Recent studies by Came et al. (2007, 2014), Eagle et al. (2013), Henkes et al. (2013) and Petrizzio et al. (2014) have calibrated the clumped isotope palaeothermometer using marine molluscs and brachiopods. These studies have shown a distinct carbonate precipitation disequilibrium between molluscs and brachiopods compared to some other biogenic carbonate-secreting organisms such as foraminifers and deep-sea corals. This may indicate a distinct dissolved inorganic carbon (DIC) fractionation mechanism within the calcified shell that has yet to be fully explained. This discrepancy is further supported by Zaarur et al. (2011) in work on terrestrial snails. These indicate calcification temperatures at higher than ambient conditions, possibly reflecting the organism's internal temperature at the time of calcification, not that of the surrounding environment. However, there are also uncertainties from a combination of discrepancies of vital effects in conjunction with intra-laboratory scale compression of the Δ_{47} palaeotemperature method, as well as compositional non-linearity effects between different analytical instruments.

This study aims to further investigate molluscan isotopic characteristics through the use of various extant gastropod and bivalve species from a range of Sydney Harbour Holocene deposits. These will be analysed for their isotopic composition to seek any changes in ambient conditions in Sydney Harbour (Lat. 34°S) water during the Holocene. These results, if successful, will indicate if higher latitude Australian waters have significantly changed during the last 11.8 ka to allow the habitation of tropical marine mollusc species further south than previously considered. The investigation focusses on material collected in the 1920s to early 1930s when dredge samples were taken from the *Triton* site in Sydney Harbour and the Port Jackson area within the greater Sydney Harbour basin. Material was originally collected and catalogued by the Australian Museum to extend the known assemblage of Australian marine shells in the NSW region. Within this assemblage various species from previously known substantially different habitats, with different temperature regimes, were identified. Species conventionally found in lower latitudes of the tropical Indo-Pacific region were identified alongside the more common specimens from the region. These findings were the impetus for undertaking this investigation.

Mollusc samples were scrutinised for their correct taxonomic naming and corrections made according to the World Register of Marine Species (2012). Specimens were described and categorised according to observed morphology, and their typical habitats were identified. Previous work on these shell samples included ^{14}C dating as well as $\delta^{13}C$ analysis by accelerator mass spectrometry (AMS), conducted in 2005 by the Australian Nuclear Science and Technology Organisation (ANSTO). In addition, conventional stable isotope analysis of $\delta^{13}C$ and $\delta^{18}O$ were made using isotope ratio mass spectrometry (IRMS) at the University of Wollongong (UOW). Subsequently shell specimens were pre-treated for further chemical analysis and sectioned into various portions to further analyse the various species for their formation temperature by clumped isotope mass spectrometry using a MAT253 IRMS at the UOW.

6.2 Background

This section explores the previous applications of marine and freshwater bivalves and gastropods, as well as terrestrial examples, in palaeotemperature investigations. This provides a synthesis of their past use in palaeothermometry and their future applicability and usefulness as a proxy for the investigation of palaeotemperatures in various environments.

Marine molluscs secrete and deposit carbonate (MCO_3) minerals in isotopic equilibrium with their surrounding water. This is typically in the form of calcium carbonate ($CaCO_3$); mainly aragonite with minor calcite constituents depending on the species (Bøggild, 1930). The isotopic composition ($\delta^{18}O$) of the shell is dependent on both the isotopic composition of the host water from which it is being precipitated and the formation temperature at which the precipitation occurs. It was realised by Epstein et al. (1951, 1953) that shell deposition occurred over a wide range of temperatures and that this produces different isotopic compositions. Therefore, if the isotopic composition of the shell has not changed with time through diagenesis, the growth temperature of a shell specimen, such as a fossil or a modern specimen, can be determined by analysing the isotopic composition of the precipitated calcium carbonate, provided the $\delta^{18}O$ value of the host water is known or can be estimated.

The first isotope palaeothermometer for carbonates was published by Epstein et al. (1953), based on isotopic values from live mollusc shells and their growth water. Later studies by McCrea (1965), O'Neil et al. (1969), Horbie and Oba (1972), Erez and Luz (1983), Chivas et al. (2002) and Wanamaker et al. (2004) all draw their basis from this work. Subsequently, these temperature relationships and have been extensively used to categorize the formation temperature of various carbonate-secreting organisms. More recently clumped-isotope palaeothermometry has been utilised by Came et al. (2007, 2014), Eagle et al. (2013), Henkes et al. (2013) and Petrizzio et al. (2014) to further constrain the uncertainties of using molluscs as palaeotemperature indicators. These studies span a wide range of environments from marine and estuarine to freshwater and lacustrine, as well as terrestrial settings globally. Applying these relationships to geological settings can elucidate environmental temperature regimes, as well as giving indications about the isotopic composition of the precipitating host water.

6.2.1 Calcification physiology

Bivalves and gastropods have long been used in this type of palaeoenvironmental reconstruction due to their abundance in the natural environment, their occurrence in highly diverse environments and their sequential deposition of skeletal biogenic carbonate during growth. Analysis of the geochemical processes and contributing factors of calcareous shell formation have been explored, with species-specific vital effects becoming better understood as more diverse species are examined. It is imperative to be able to distinguish between physiological and environmental factors to accurately utilise the isotopic composition of carbonates as an environmental proxy. Therefore it is increasingly important to understand the physiology and ecology of the calcifying organism. In addition, factors such as the source of oxygen and carbon in inorganic bicarbonate, air, water and food of the organism becomes increasingly significant. Understanding these 'vital' effects is an important step in understanding the usefulness of bivalves and gastropods for palaeotemperature investigations (McConnaughey et al., 1997).

Molluscs and brachiopods have shell skeletons composed of calcite, aragonite, or a mixture of both. Intra-shell carbonate precipitation is difficult to measure due to the small fluid volume size, therefore accurate geochemical sampling is difficult. However some studies have shown that only minor differences in isotopic composition exist between inner shell fluids and ambient waters. pH plays an important role in the calcification chemistry and is the main driver for CO_2 absorption and CO_3^{2-} accumulation within the shell (McConnaughey et al., 2008).

Calcification is also significantly governed by the growth rate of the organism. This may result in shell growth being moderated by various ambient environmental conditions (Prendergast and Stevens, 2014). Under favourable conditions, molluscs precipitate carbonate in regular intervals. Over the life of the organism distinct growth bands are formed. Growth is periodic and mediated by the ambient conditions of the environment. Shells may also show seasonal banding in their carbonate growth lines. Therefore the ambient conditions are primarily incorporated through the isotopic composition when optimal growth conditions occur. This implies that material analysed may exist in an environment with much larger ambient condition ranges (i.e. temperature, salinity or pH), than is indicated by the isotopic composition of the carbonate shell (Schöne, 2008).

6.2.2 Dissolved inorganic carbonate (DIC) source

Both ambient inorganic carbon and respired carbon dioxide contribute to the calcareous shells of molluscs. In work by McConnaughey et al. (2008) it was suggested that terrestrial 'air-breathing' organisms construct their carbonate shells from respired carbon dioxide. Whereas aquatic species derive their carbonate from the ambient carbonate found in their surrounding aquatic habitat. Land-dwelling organisms have limited sources of fixed carbon that are readily available for incorporation into their shells.

Isotopic variations within the molluscan shell have also been described from marine and freshwater environments. In some cases, the isotopic composition of the shell can provide a salinity indication proxy (Mook and Voegl, 1968; Mook, 1971). Meteoric dissolved inorganic carbon (DIC) will have a much higher $\delta^{13}C$ value in comparison to more negative marine values. Mixing of meteoric and marine waters can also have a profound effect on the carbon isotopic composition (McConnaughey et al., 2008). This can provide an estimate for freshwater input and potential correction for palaeotemperature estimates. This process is very important in 'conventional' oxygen isotope measurements of fossil materials due to the limiting factor being the need to know the isotopic composition of the host water.

Land snails generally contain higher $\delta^{13}C$ values due to the increased amount of enriched respired CO_2 present within the shell. However ambient air does provide a source for some of the shell material. Air-breathing snails appear to record insights into their diets better in shell carbonate rather than in their organic matter (McConnaughey et al., 2008), whereas aquatic species appear to preserve ambient DIC isotopic conditions better in shell carbonate and more readily preserve isotopic information of diet in their organic portions (O'Donnell et al., 2003).

6.2.3 Shell sampling strategies

Selection of carbonate material from mollusc shells for isotopic analysis encompasses two distinct approaches, with varying degrees of applicability. Firstly, sampling of individual growth layers of the carbonate shell in various thicknesses and intervals may be made to ascertain the various isotopic conditions throughout the life cycle of the organism. This has been the convention for many studies primarily focussed on conventional oxygen isotopic signatures of the calcareous material in relation to water temperature, salinity and to a lesser extent carbon isotopic signatures in relation to dissolved inorganic carbon (DIC) and dissolved organic carbon (DOC) sources

(Wefer and Berger, 1991). This may also indicate changes within the organisms' environment such as marine or terrestrial influences of host waters and evaporation rates.

Alternatively, the bulk (homogenous) sample analysis of shell carbonate is a better reflection of total life cycle average conditions of a particular specimen. This is achieved by crushing the whole shell or large portions into a homogeneous powder for the subsequent analysis. Equally specimens may be subdivided to preserve some morphological structure for later analysis by sectioning the material, such as halving the shell or analysing specific growth regions. This retains the average chemical composition of the shell but reduces the need for total sample destruction. This is a more relevant method of carbonate sampling if seasonal change is of less importance than the sum of the conditions the organism underwent during its life. This is a more common method to use in fossil material when the exact age of a sample is not known and seasonal variation is negated by the accuracy and precision of the dating method used for the specimen (i.e. conventional ^{14}C dating techniques).

The latter of the two methods described is a more appropriate method for most clumped isotope analyses. The nature of the clumped-isotope measurement requires extensively long analysis cycles of up to 4 hours (Eiler, 2007, 2013), and therefore requires a larger amount of solid sample. Sampling of individual growth bands of the mollusc shell would be impractical (for small shells) and may decrease analysis precision, by restricting the maximum integration time and maximum counting time per shell sample.

6.2.4 Clumped isotopes and biogenic carbonates

The clumped isotope Δ_{47}-temperature relationship for modern biogenically precipitated carbonates generally obeys the inorganic calibration of carbonates reported by Ghosh et al. (2006) and the later calibration by Dennis and Schrag et al. (2010). The clumped isotope method has been successfully used to reconstruct palaeotemperatures and isotopic compositions of ancient sea water (Came et al., 2007; Finnegan et al. 2010; Keating-Bitonti et al., 2011) from mollusc specimens. To make more accurate palaeotemperature assessments, empirical calibration of biogenic carbonate material is necessary. Such calibrations have been produced for corals (Ghosh et al. 2006; Thiagarajan et al., 2011), fish otoliths (Ghosh et al., 2007), foraminifers and coccoliths (Tripati et al., 2010) from natural waters with known ambient growth conditions (Henkes et al., 2013). Investigations on aragonitic mollusc shells by Came et al. (2007), Keating-Bitonti et al. (2011) and Csank et al. (2011) found that the resultant calibration closely

approximates the inorganic calcite calibration line (Figure 6.1). They reported possibilities of some potential vital effects but their results were inconclusive on this subject.

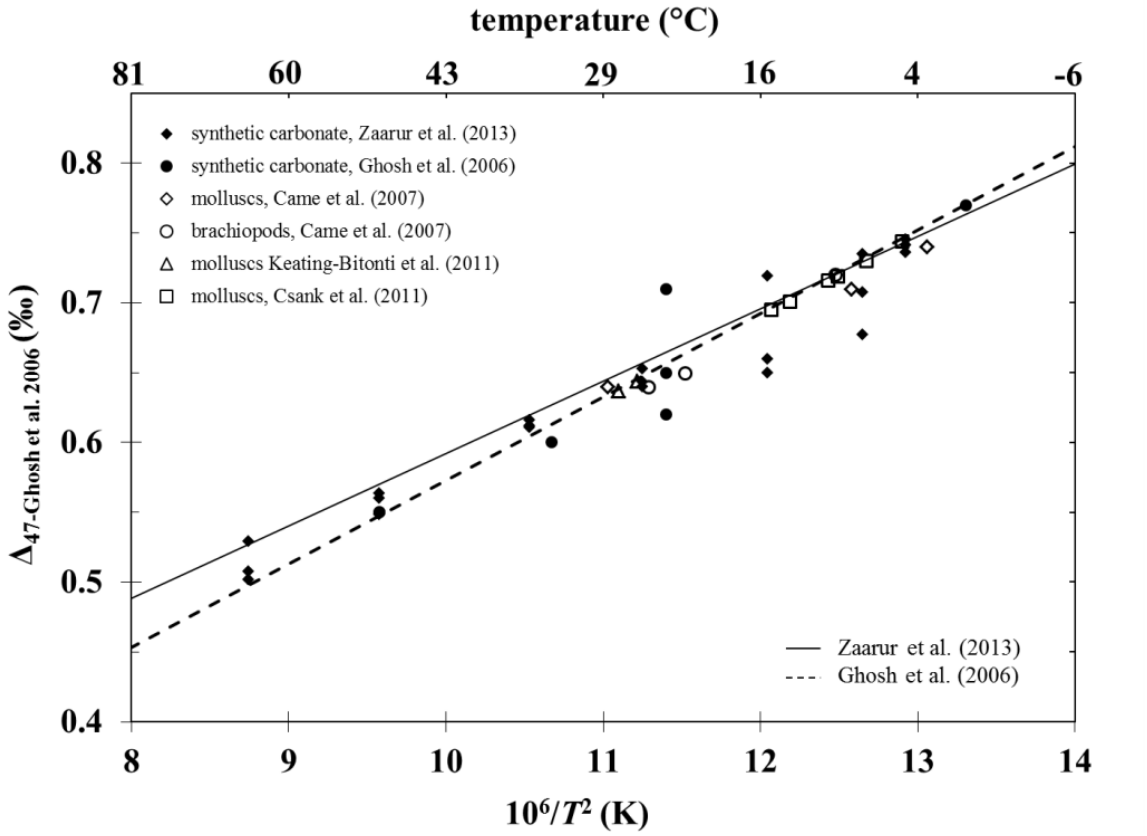

Figure 6.1: Δ_{47} measurements by Came et al. (2007), Keating-Bitonti et al. (2011) and Csank et al. (2011) on mollusc shells and their respective growth temperatures. Δ_{47} values are plotted using the empirical calibration by Ghosh et al. (2006). The plotted lines represent the empirical calibration (Ghosh et al., 2006) and the revised synthetic calibration (Zaarur et al., 2013).

Later investigations by Henkes et al. (2013) and Came et al. (2014) showed that the temperature sensitivity of mollusc and brachiopod shells appears to be significantly lower than those of corals, fish otoliths, foraminifers and coccoliths (Figure 6.2). This suggests unknown mineral-DIC fractionation between the mollusc and brachiopod shells and the other biological organisms.

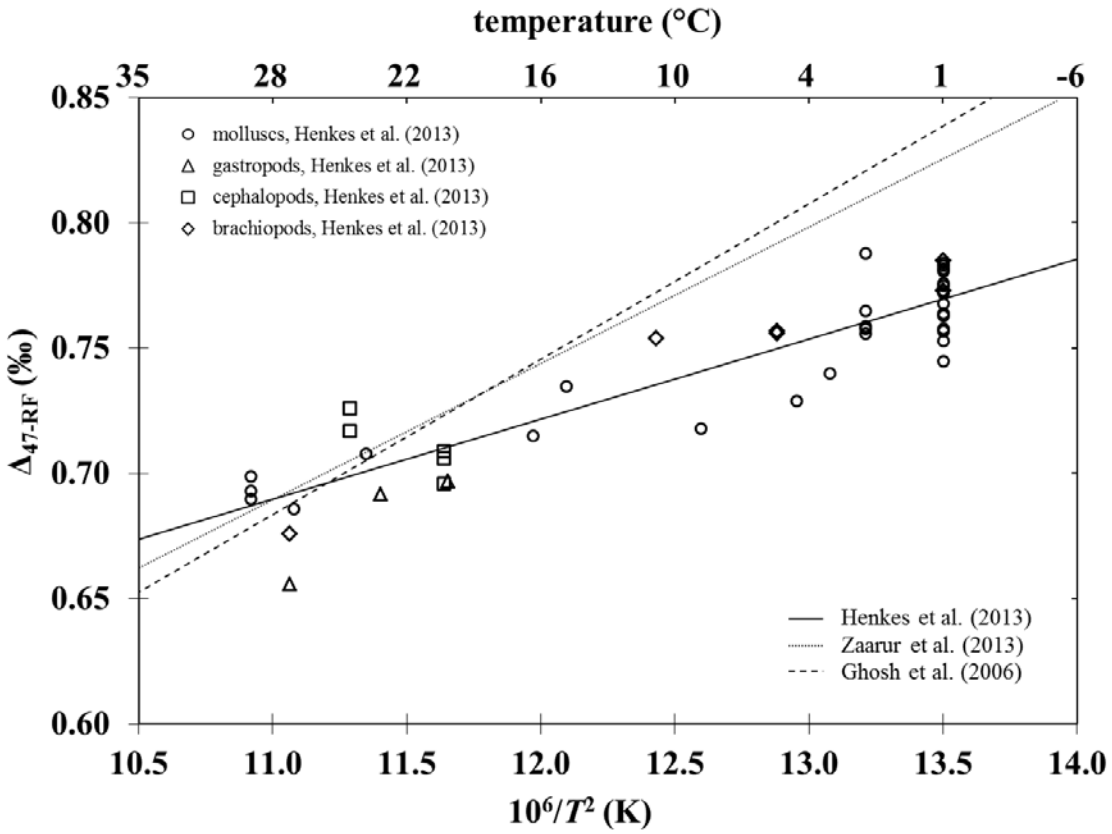

Figure 6.2: Δ_{47} measurements by Henkes et al. (2013) on bivalve, gastropod, cephalopod and brachiopod shells and their respective growth temperatures. The Δ_{47} values are plotted into the absolute reference frame scale (RF) (Dennis et al., 2011). The lines represent the Ghosh et al. (2006) empirical calibration, the Zaarur et al. (2013) revised synthetic calibration and the Henkes et al. (2013) calibration for shell data at various temperatures.

This latest investigation yielded an empirical calibration line of $\Delta_{47} = 0.0327 \times 10^6/T^2 + 0.3286$, with an r^2 value of 0.84 (Henkes et al., 2013) (Figure 6.2). This palaeotemperature equation exhibits approximately half the temperature sensitivity of other biogenic and inorganic synthetically precipitated carbonates. These discrepancies have been attributed to incorporation of amorphous calcium carbonate during the analysis process and differences in the pH of the precipitation fluid within the shell. This was further confirmed by Came et al. (2014) and their revised biogenic palaeotemperature equation $\Delta_{47} = 0.0478\pm0.0099 \times 10^6/T^2 + 0.1203\pm0.1203$ with an r^2 value of 0.91.

Additionally, investigations using aragonitic land snails show that calculated calcification temperatures appear higher than the average annual temperature and even higher than the most active growth season (Zaarur et al., 2011). Results indicate that shell aragonite material is formed at equilibrium, and represents the snails' internal body temperature at the time of shell

calcification in the growth season. This further confirms results by McConnaughey et al. (2008) that terrestrial gastropods calcify their shells from carbon and oxygen acquired primarily through respiration sourced from their diets. Therefore, ambient conditions do not appear to have a significant effect on the calcification temperatures and isotopic composition of terrestrial snail shells. Whereas aquatic species exhibit formation temperatures based on the ambient environment through DIC sources from their surrounding aqueous environment, allowing external shell precipitation dynamics to dominate the isotopic signature of the precipitated shell.

The most recent Δ_{47} bivalve mollusc temperature calibration indicates a lower sensitivity than the earlier calibrations of inorganic calcite, corals, foraminifers and coccoliths. However, the calibration agrees more closely with the recent Δ_{47}-temperature relationships from mollusc and bivalves (Petrizzio et al., 2014).

6.3 Methods

6.3.1 Specimen classification and nomenclature

Shell specimens collected from Sydney Harbour were dredged, by the vessel *Triton*, from shell beds on the harbour floor between 1928 and 1929. The shells are beautifully preserved with their original colour and minimal breakages. Upon collection the shells were recognised as being largely tropical species, not currently present at such latitudes (34°S). The shells were presumed to be 'old' with later dating confirming this.

Most of the shell specimens were first classified and catalogued in the 1970s after their collection, with some of the most recent taxonomic determinations conducted in the late 1990s. Various tools can be utilised to classify shells effectively, however in conchology, which relies solely on shell morphological and geometric features, the determinations can be misleading and have the potential of multiple sources of error.

Historically shell classification involves the identification and comparison of various geometric and morphological features of the mollusc shell to previously described specimens through photographic references or collection reference assemblages. It is unclear from the information available from the Australian Museum what sources were initially used for the species name determination. However all species used in this study were taxonomically re-evaluated prior to any sample preparation or analysis. Sources used include various visual references such as Kira (1962), Wilson and Gilbert (1971, 1980), Abbott and Dance (1986), Wefer and Berger (1991), Lamprell and Whitehead (1992), Kobashi (2001) and Wilson (2002). In conjunction with these, electronic sources such as the work of Beechey (2012) and the World Register of Marine Species (2012) were used to confirm the determinations.

The illustrations in Figure 6.3 show a generalised schematic diagram of both gastropod and bivalve mollusc shells used in the classification and description process. Diagrams represent a generic anatomical representation of shell morphology, some species will have additional or fewer characteristics.

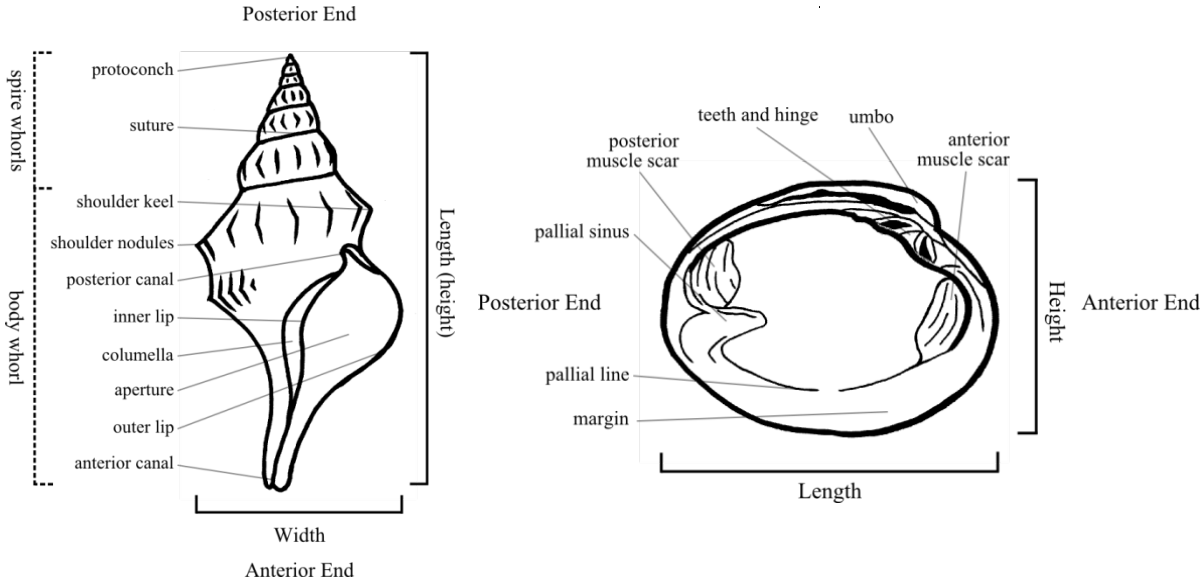

Figure 6.3: Schematic diagram of a typical mollusc gastropod (fusiform welk shell; left) and a typical mollusc bivalve (Venus clam shell; right).

Some shell specimens were in a damaged and broken state when received. This was potentially as a result of sample collection by initial dredging. However, shell specimens were likely to be damaged as a result of sample processing for the ^{14}C dating. All gastropod specimens exhibit an 8mm diameter circular hole in the final body whorl, cut for AMS dating. Bivalve shells were broken into fragments with an approximate 8 mm^2 fraction of the shell unaccounted for. This damage did not impede the identification or any further use of the shell material in this study.

6.3.2 Shell carbonate sampling and preparation

Shell samples were analysed by the bulk sampling analysis method, providing an average life cycle palaeotemperature signature of the shell's lifetime as discussed in Section 6.2.3. Shell samples were cut or broken into two portions to preserve part of the specimen for later review and other potential analytical techniques. Cutting was performed using a hand-held rotary drilling tool (Dremel©) with an attached cutting disc. The specimen was submerged in ethanol as a cooling fluid to reduce heat build-up in the sample, and to minimise the risk of isotopic heat fractionation in the sample.

Due to the need for large sample amounts, gastropods (G) were sub-sectioned into two main growth areas. The outer and inner lip including portions of the body whorl (G-a) and the apex spire or protoconch the first 3 to 4 whorls (G-b) as shown by Figure 6.4. Bivalves (B) were partitioned in a similar manner to the gastropods. Two main growth areas were sub-sectioned – the outer margin (B-a) and the hinge line and umbo region (B-b) as shown by Figure 6.4. The subsection proportions were kept as uniform a possible but varied slightly depending on the shell size.

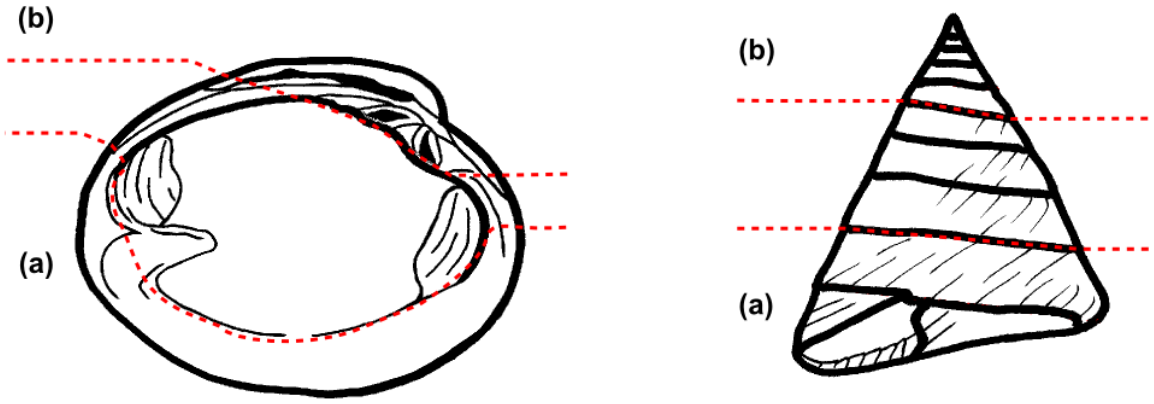

Figure 6.4: Schematic diagram of a bivalve (left) and gastropod (right) showing shell partitioning zones for isotopic analysis. Shells have been sub-sectioned into two zones (a) and (b).

Shell zoning in this arrangement was used to subdivide the shell into two distinct growth stages from the most recently precipitated carbonate zone (a), to the earliest precipitated carbonate in zone (b), the protoconch spire tip in the gastropod and the hinge line and umbo in the bivalve (Figure 6.4).

6.3.3 ^{14}C dating by AMS

Accelerator Mass Spectrometry (AMS) analyses were made from drilled subsamples of the shell material. Samples were drilled out of the main body whorl of the shell as a 7.5mm disk or equivalent size. These were then prepared as standard ANSTO AMS radiocarbon samples using methods described by Fink et al. (2004). Measurements were carried out at the Australian Nuclear Science and Technology Organisation (ANSTO), NSW, Australia (Chapter 3.5).

6.3.4 Isotopic analysis

6.3.4.1 $\delta^{13}C$ and $\delta^{18}O$

Conventional carbon and oxygen isotope measurements were made on the Sydney Harbour shells prior to commencement of this study. Analyses were conducted at the University of Wollongong's Geochemistry Laboratories in the School of Earth and Environmental Sciences. Analyses were made using standard stable isotope analytical methods. Shell material was subsampled in the same manner as ^{14}C dating material was taken from the shell specimens.

Fragments were ground into a fine powder and weighed out into analysis vials. Weights ranged from 0.4 to 2.3 mg. Samples were analysed on a Micromass PRISM III mass spectrometer with an additional multi-prep sample inlet system. Sample vials were individually evacuated and reacted with ~103 % H_3PO_4 (orthophosphoric acid) at 90 °C to liberate carbon dioxide from the carbonate for isotopic analysis. Reference standards of TTB-1 (China) ($\delta^{18}O_{VPDB}$ = -8.45 ‰), NBS-19 ($\delta^{18}O_{VPDB}$ = -2.20 ‰) and Chihuahua ($\delta^{18}O_{VPDB}$ = -11.68 ‰) were used as calibration standards as well as an inter-laboratory synthetic carbonate standard (AR).

Results for carbonate samples are reported in reference to VPDB (Vienna – Pee Dee Belemite) in per mil (‰) for $\delta^{13}C$ and VSMOW (Vienna - Standard Mean Ocean Water) in per mil (‰) for $\delta^{18}O$. Measurements were typically made in duplicate with some samples being replicated up to four times. Precision for $\delta^{13}C$ and $\delta^{18}O$ values was in the order of 0.1 ‰ for all sample material.

6.4 Results and discussion

In this section the results of the taxonomic investigation and species descriptions, ^{14}C dates and corresponding $\delta^{13}C$ and $\delta^{18}O$ values are described and discussed in relation to the shells typical habitat relative to their occurrence within Sydney Harbour and the implications of their occurrence. This will then be compared and contrasted to the findings of the clumped isotope Δ_{47} values and formation temperatures of the shells as well as results from the shell zone partitioning investigation. Comparisons between the typical habitual climate of the shell species and the inferred determined climatic regime will then be assessed in relation to the age of the organism. This information can then be contrasted to specimens living in Sydney Harbour today along with other extant species' shell material from the Australian Museum in other assemblages from Sydney Harbour to determine if the water temperature and climate regime of Sydney Harbour waters has changed during the Holocene. This section will also discuss the success of the clumped isotope technique on this type of sample material. The shortcomings of the technique are then outlined as well as recommendations for potential changes and modification to the method.

6.4.1 Shell taxonomy and descriptions

Collected shell material from Sydney Harbour was first catalogued in the 1970s, with some determinations being made in 1999. Since initial determinations were made various taxonomical changes have occurred resulting in species and genus name changes (see Table 6.1). Significant changes include the reclassification of *Cymatium dunkeri* Lischke 1868 to *Ranularia dunkeri* (Lischke, 1868), the reclassification of *Tonna dolium* Linne 1758 to *Tonna tessellata* Lamark 1816 and the major reclassification of genus *Strombus* such as *Strombus vomer vomer* Röding 1798 and *Strombus dilatatus dilatatus* Swainson 1821 to *Eurotomus vomer* (Röding, 1798) and *Dolomena dilatata* (Swainson, 1821), respectively.

Sample Number: C361481

Class: Bivalvia (Heterodonta)

Order: Veneroida

Super Family: Veneroidea

Family: Veneridae

Genus: *Tawera*

Species: *T. lagopus* (Lamarck 1818)

Refer to Figure 6.5 A,B and Table 6.1

(World Register of Marine Species, 2015)

Genus *Tawera* exhibits a strong sculpture with re-curved ridges and distinct radial striae in interstices, creating a highly textured shell (Figure 6.5 A,B). External colour is typically white to brown and interior is usually white with violet blotches at the rim and posterior and anterior muscle scars (Wilson and Gilbert, 1971). It inhabits littoral waters with sandy substrate up to 40 m depth and is distributed in Western Australia, South Australia, Victoria and New South Wales (Lamprell and Whitehead, 1992).

Sample Number: C355060

Class: Gastropoda (Caenogastropoda)

Order: Littorinimorpha

Super Family: Cypraeoidea

Family: Cypraeidae

Genus: *Erosaria*

Species: *E. eburnea* (Barnes 1824)

Refer to Figure 6.5 C,D and Table 6.1

(World Register of Marine Species, 2015)

Unaccepted synonymous name: *Cypraea eburnea* Barnes 1824

Erosaria eburnea is a cowrie shell found widely in the South Pacific Ocean, as far north as Palau and east to the Fijian islands. It exhibits a well-rounded shell with an aperture running the length of the shell, it is usually toothed and restricted (Figure 6.5 C,D). Shell texture is glossy smooth

with colour being highly variable from intricate reds to brown and yellows, some mottling and patterns do occur but are prone to fading with shell age (Wilson and Gilbert, 1971).

Sample Number: C360016

Class: Bivalvia (Heterodonta)

Order: Veneroida

Super Family: Veneroidea

Family: Veneridae

Genus: *Callista* (Notocallista)

Species: *C. kingii* Gray in King 1827

Refer to Figure 6.5 E,F and Table 6.1

(World Register of Marine Species, 2015)

Unaccepted synonymous names: *N. kingii* or *P. kingi* (Gray in King 1827)

Callista kingii displays a well-developed shell sculpture with indistinct irregularly spaced, deep concentric grooves and board ridges (Figure 6.5 E,F). Colour is typically off-white to cream with brown radial stripes, in some cases flecked. *C. kingii* usually inhabit intertidal waters with sandy substrates (Lamprell and Whitehead, 1992). Habitat extents range from South Australia, Victoria, New South Wales and as far south as Tasmania. These species can be viewed as more of a temperate climate snail due to their higher latitude distribution (Wilson and Gilbert, 1980).

Sample Number: C348717

Class: Gastropoda (Caenogastropoda)

Order: Neogastropoda

Super Family: Muricoidea

Family: Muricidae (Rapaninae)

Genus: *Pinaxia*

Species: *P. coronata* Adams 1853

Refer to Figure 6.5 G,H and Table 6.1

(World Register of Marine Species, 2015)

Pinaxia coronata is a species of the murex or rock snail family Muricidae. These inhabit shallow waters in low latitude tropical environments from the Philippines to Japan within the Indo-Pacific region. Size of *P. coronata* is typically small up to 2 cm in total length, sculpture is subtle with fine ridges narrowing towards the anterior. Specimen shell is thin and brittle with some breakage at the body whorl and the apical spire (Figure 6.5 G,H). Colour is characteristically off white with brown stripes depending on location (Abbott and Dance, 1986).

Sample Number:	C081953
Class:	Gastropoda (Caenogastropoda)
Order:	Littorinimorpha
Super Family:	Naticoidea
Family:	Naticidae
Genus:	*Mammilla*
Species:	*M. simiae* Deshayes 1838

Refer to Figure 6.5 I,J and Table 6.1

(World Register of Marine Species, 2015)

Mammilla simiae is found primarily in the waters of South-East Asia and Polynesia as well as South Africa, inhabiting tropical shallow marine environments. Shell sculpture is delicate, the very thin shell is slightly ovate with a low spire (Wilson and Gillett, 1971). Colour is dull off white with three irregular brown streaks. Specimen is undamaged with an overall length of 3 cm, body whorl 2 cm and spire 1cm. Colouring is well preserved, showing brown stripes orientated laterally (Figure 6.5 I,J).

Sample Number:	C098606
Class:	Gastropoda (Caenogastropoda)
Order:	Littorinimorpha
Super Family:	Stromboidea
Family:	Strombidae
Genus:	*Euprotomus*
Species:	*E. iredalei* Abbott 1960

Refer to Figure 6.5 K,L and Table 6.1

(World Register of Marine Species, 2015)

Unaccepted synonymous names: Strombus vomer vomer Roding 1798

E. aratum of the conch shells, inhabits tropical intertidal zones. *E. aratum* has a simple thick lip, spines are not present in this species. Shell sculpture is elongate with a pronounced shoulder keel and shoulder nodules. Specimen is damaged, apical spire, outer lip, and posterior and anterior canal are absent as well as body whorl suture line shows indications of disturbance (Figure 6.5 K,L). Colour has faded to a dull yellow cream to off white colour at the spire. Size is 6.5 cm in its damaged state so possibly longer up to 8 cm (Wilson and Gilbert, 1971).

Sample Number: C114412

Class: Gastropoda (Caenogastropoda)

Order: Littorinimorpha

Super Family: Stromboidea

Family: Strombidae

Genus: *Dolomena*

Species: *D. dilatata* (Swainson 1821)

Refer to Figure 6.5 M,N and Table 6.1

(World Register of Marine Species, 2015)

Unaccepted synonymous names: *Strombus dilatatus dilitatus* Swainson 1821

Dolomena dilatata is a tropical herbivorous snail, inhabiting sand to rubble substrates in the intertidal zone. *D. dilatata* is thinly structured with a prominent thicker widely flared lip. Colour is predominantly white with some striations of brown to yellow, deeper colour inside the lip of the whorl (Wilson and Gilbert, 1971).The sculpture exhibits a deep posterior canal grove that curves laterally across, prominent sharp shoulder keel on all whorls. Commonly occurring in central Indo-West Pacific regions and northern Queensland, Australia (Wilson, 2002). Shell has broken spire and anterior canal as well as some foreign discolouration of the shoulder nodules (Figure 6.5 M,N).

Sample Number: C349881

Class: Gastropoda (Caenogastropoda)

Order: Vetigastropoda

Super Family: Trochoidea

Family: Trochidae (Umboniinae)

Genus: *Monilea*

Species: *M. lentiginosa* Adams 1853

Refer to Figure 6.6 O,P,Q,R and Table 6.1

(World Register of Marine Species, 2015)

Monilea lentiginosa belongs to the very large and diverse top shell family Trochidae. The shell is conical in shape and sharply striate. Suture lines nearly indistinguishable from whorl sculpture striation. Specimen is largely unbroken, columella is absent, however outer lip is undamaged (Figure 6.6 O,P,Q,R). Colour is white with distinct narrow and board brown stripes from anterior to posterior of shell. *M. lentiginosa* are herbivorous molluscs and occur in large localised numbers, inhabiting central Indo-West Pacific regions on muddy to sandy substrates, now extinct from NSW and most of Australia (Beechey, 2012).

Sample Number: C405410

Class: Gastropoda (Caenogastropoda)

Order: Littorinimorpha

Super Family: Cypraeoidea

Family: Cypraeidae

Genus: *Contradusta*

Species: *C. walkeri* (Sowerby 1832)

Refer to Figure 6.6 S,T and Table 6.1

(World Register of Marine Species, 2015)

Unaccepted synonymous names: *Cyprae walkeri* Sowerby 1832

Contradusta is another genus of the Cypreidae family, the cowrie shells. Sculpture is pyriform in shape with long teeth flanking the aperture on both the inner and outer lip (Figure 6.6 S,T). Colouring is pale orange to yellow with large brown blotches. (Wilson and Gilbert, 1971) Typically occurs in the north Indian Ocean to central Indo-West Pacific and northern margins of Australia in tropical reef waters (Abbott and Dance, 1986).

Sample Number: C159311

Class: Gastropoda (Caenogastropoda)

Order: Neogastropoda

Super Family: Conoidea

Family: Terebridae

Genus: *Terebra*

Species: *T. cingulifera* Lamarck 1822

Refer to Figure 6.6 U,V and Table 6.1

(World Register of Marine Species, 2015)

Terebra cingulifera is a carnivorous auger or pencil snail. It exhibits a long slender shell body with many whorls that tapers to a sharp point, spiral and axial sculpture is well developed (Wilson, 2002). *T. cingulifera* inhabits the tropical waters of the Indo-West Pacific region almost exclusively; it has not been recorded in Australia (Beechey, 2012). Colour is typically an even light brown to yellow in a uniform pattern throughout the shell (Abbott and Dance, 1986). Specimen is slightly damaged, outer lip as well as anterior and posterior canals are broken, however colour is very well maintained and uniform (Figure: 6.6 U,V).

Sample Number: C071600

Class: Gastropoda (Caenogastropoda)

Order: Littorinimorpha

Super Family: Tonnoidea

Family: Ranellidae (Cymatiinae)

Genus: *Ranularia*

Species: *R. dunkeri* (Lischke, 1868)

Refer to Figure 6.6 W,X and Table 6.1

(World Register of Marine Species, 2015)

Unaccepted synonymous names: *Cymatium dunkeri* Lischke 1868

An example of the triton or trumpet snails, this species exhibits a very robust and thick shell construction with folds and ridges on the lip and whorl opening (Kira, 1962). Colour is a dull

white with light brown to yellow irregular bands (Wilson and Gillett, 1971), these appear more faded in the sample. Members of the genus *Ranularia* are typically large in size 6-10 cm in total length. In this case the specimen is unbroken and 5 cm in length, body whorl 3 cm and spire 2 cm (Figure 6.6 W,X), indicating it is of juvenile growth stage. *R. dunkeri* occurs within the Indo-West Pacific oceans reaching as far as southern Japan and New Caledonia, no previous Australian occurrences have been noted (Beechey, 2012).

Sample Number:	C074754
Class:	Gastropoda (Caenogastropoda)
Order:	Littorinimorpha
Super Family:	Tonnoidea
Family:	Tonniae
Genus:	*Tonna*
Species:	*T. tessellata* Lamarck 1816

Refer to Figure 6.6 Y,Z and Table 6.1

(World Register of Marine Species, 2015)

Unaccepted synonymous names: *Tonna dolium* Linne 1758

T. tessellate is a species of the carnivorous tun shells. These are generally large (up to 10 cm in length), thin walled almost spherical in appearance. External sculpture exhibits a heavily toothed outer edge and lip, long narrow spiral ribs widening towards the end of the apical whorls. Inter rib spacing narrows towards the posterior of the shell (Wilson, 2002). External colour is primarily off-white to light brown with distinct orange-brown spots, the toothed edge is white with interior whorls yellow in colour. Specimen is undamaged and 7 cm in length, with colouring well preserved (Figure 6.6 Y,Z). The genus is well represented in tropical and warm temperate seas in the Indo-West Pacific region (Wilson and Gilbert, 1971).

6.4.1.1 Summary

The majority of the shells from the *Triton* site in Sydney Harbour are commonly associated with more tropical marine conditions, such as far northern Australia, Polynesia and the Indo-west Pacific region around Indonesia. In addition certain species in this assemblage have been deemed extinct within Australian waters, such as *M. lentiginosa*. Other species from the *Triton* site have never been recorded in Australian waters prior to their discovery in Sydney Harbour, such as *R. dunkeri* and *T. cingulifera* (Beechey, 2012). Furthermore, species such as *P. coronata*, *C. walkeri* and *E. eburnea* have only been recorded outside Australia in sub-equatorial environments such as the Indo-West Pacific region. Therefore, there is a possibility that the ambient environmental conditions in Sydney Harbour may have been more tropical than they are today, which would have facilitated the above species to be present within the record.

6.4.2 Significance of species diversity

Many of the represented species are reported to be tropical to sub-tropical in habitual nature. Occupying the majority of the Indo-West Pacific realm such as *M. lentiginosa, T. cingulifera, D. dilatata* and *T. tessellata* to the outer margins of the West Pacific, such as *P. coronata* in southern Japan and the Philippines, *R. dunkeri* in New Caledonia, *C. eburnea* in areas of the South Pacific Ocean as far north as Palau and east as the Fijian islands, *C. walkeri* in the far North Indian Ocean and *M. simiae* in South-East Asia and large portions of Polynesia.

Many of the species are also present within Australia but are quite restricted to the northern margins of Western Australia, Queensland and the Northern Territory. All of which are tropical regions.

Both bivalve examples *C. kingii* and *T. lagopus* are largely found in Australian waters from Northern Queensland to Victoria and Tasmania in the south. These species can be considered more temperate water molluscs. However, this is may also be a product of the bivalves being a deep water to littoral species with movement of the organism being more common than with some of the other exclusively littoral and near shore dwelling species of gastropods.

The occurrence of all these species from seemingly more tropical habitat conditions raises the question of whether or not the average ocean temperature of Sydney Harbour has changed significantly since the start of the Holocene (~11.8 ka).

Table 6.1: Shells from *Triton* site, Sydney Harbour. Collected between 1928 and 1929 by dredging the sediment of the bottom of the water channel in Sydney Harbour and Port Jackson, Sydney, NSW, Australia. Shells were identified between 1970 and 1999 using available taxonomic dichotomous keys. Taxonomic names have been re-written to the current accepted status given by the World Register of Marine Species (2015).

Sample Code	Taxonomic Name as of March 2015 - (WoRMS, 2015)		Taxonomic Name (at time of initial identification)		Identifier	Year	Location	Co-ordinates (xx°xx'S, xx°xx'E)
C361481	*Tawera lagopus*	(Lamarck 1818)	*Tawera lagopus*	(Lamarck 1818)	Kerslake, J.	1980	Sydney Harbour	33°51'S, 151°14'E
C355060	*Erosaria eburnea*	(Barnes 1824)	*Cypraea eburnea*	Barnes 1824	Loch, I.	1980	Sydney Harbour	33°51'S, 151°14'E
C360016	*Callista kingii*	Gray in King 1827	*Notocallista kingii*	Gray in King 1827	Kerslake, J.	1980	Sydney Harbour	33°51'S, 151°14'E
C348717	*Pinaxia coronata*	Adams 1855	*Pinaxia coronata*	Adams 1855	Ponder, W.F.	1970	Sydney Harbour	33°51'S, 151°14'E
C081953	*Mammilla simiae*	Deshayes 1838	*Mammilla simiae*	Deshayes 1838	Kabat, A.	1990	Sydney Harbour	33°51'S, 151°14'E
C098606	*Euprotomus iredalei*	(Röding 1798)	*Strombus vomer vomer*	Roding 1798	Colman, P.H.	1974	Sydney Harbour	33°51'S, 151°14'E
C114412	*Dolomena dilatata*	(Swainson 1821)	*Strombus dilatatus dilatatus*	(Swainson 1821)	Loch, I.	1980	Sydney Harbour	33°51'S, 151°14'E
C349881	*Monilea lentiginosa*	Adams 1853	*Monilea lentiginosa*	Adams 1853	Loch, I.	1982	Port Jackson, Sydney	33°50'S, 151°27'E
C405410	*Contradusta walkeri*	(Sowerby 1832)	*Cypraea walkeri*	Sowerby 1832	Loch, I.	1999	Sydney Harbour	33°51'S, 151°14'E
C159311	*Terebra cingulifera*	Lamarck 1822	*Terebra cingulifera*	Lamarck 1822	Leroi, A.	1991	Sydney Harbour	33°51'S, 151°14'E
C071600	*Ranularia dunkeri*	Lischke 1868	*Cymatium dunkeri*	Lischke 1868	Beu, A.G.	1998	Sydney Harbour	33°51'S, 151°14'E
C074754	*Tonna tessellata*	(Lamarck 1816)	*Tonna dolium*	Linne 1758	Colman, P.H.	1980	Sydney Harbour	33°51'S, 151°14'E

Figure 6.5: Photographs of Sydney Harbour shells; A, B: *Tawera lagopus*, C, D: *Erosaria eburnea* E, F: *Callista kingii,* G, H: *Pinaxia coronate,* I, J: *Mammilla simiae,* K, L: *Euprotomus iredalei,* M, N: *Dolomena dilatata,* (all have 5cm scale bars with 1cm subdivisions).

Figure 6.6: Photographs of Sydney Harbour shells; O, P, Q, R: *Monilea lentiginosa,* S, T: *Contradusta walkeri,* U, V: *Terebra cingulifera,* W, X: *Ranularia dunkeri,* (O, P, Q, R, S, T, U, V, W, X have 5cm scale bars with 1cm subdivisions).Y, Z: *Tonna tessellata* (Z and Y have 10cm scale bars with 1cm subdivisions).

6.4.3 Shell ages and ^{14}C dating

The ages of the individual shells span approximately 6000 years within the Holocene (Table 6.2) from 7980 to 570 a BP (conventional radiocarbon years). This provides a suitable age range over which to potentially infer a palaeoclimatic change within the Sydney Harbour basin area within the scope of this study.

Table 6.2: Radiocarbon ages of shells from Sydney Harbour arranged in order of increasing age.

Sample Code	Species	ANSTO Code	$\delta^{13}C$‰ (VPDB)	% Modern Carbon		Conventional ^{14}C Age	
				% MC	1σ error	yr BP	1σ error
C361481	*T. lagopus*	OZH5011	-0.4	93.12	0.64	570	60
C355060	*E. eburnea*	OZH509	0.9	76.83	0.60	2120	70
C360016	*C. kingii*	OZH5010	0.7	62.90	0.54	3720	70
C348717	*P. coronata*	OZH507	0.2	57.03	0.48	4510	70
C081953	*M. simiae*	OZH503	0.6	55.11	0.50	4790	80
C098606	*E. iredalei*	OZH504	0.0	55.05	0.45	4800	70
C114412	*D. dilatata*	OZH505	0.2	52.59	0.53	5160	80
C349881	*M. lentiginosa*	OZH508	2.0	50.36	0.44	5510	70
C405410	*C. walkeri*	OZH5012	0.9	49.66	0.44	5620	80
C159311	*T. cingulifera*	OZH506	2.4	47.33	0.41	6010	70
C071600	*R. dunkeri*	OZH501	2.3	44.04	0.40	6590	80
C074754	*T. tessellata*	OZH502	0.5	37.03	0.36	7980	80

AMS ^{14}C analyses from ANSTO; conventional carbon dating analyses. The $\delta^{13}C$ value (±0.1) (‰ VPDB) is from the produced graphite and is commonly slightly different to that of the original carbonate, % Modern carbon (%MC), ^{14}C age (years BP), rounding as per Stuiver and Polach (1977), errors given to 1σ (SD).

Ranularia dunkeri, *Terebra cingulifera* and *Monilea lentiginosa* display significantly larger $\delta^{13}C$ values (>1.0‰) than other examples of shell within this assemblage. These species all occur at approximately the same time from 5510 ± 70 to 6590 ± 70 years ago (Table 6.2). The increase in $\delta^{13}C$ values in this particular part of the Holocene may be coincidental, however, when compared to shell formation temperature may give an indication of ambient temperature change within the surrounding environment.

6.4.4 Conventional $\delta^{13}C$ and $\delta^{18}O$ results

Over time the $\delta^{18}O$ value of the Quaternary ocean changes, typically between 1.0 and 1.2‰ across full glacial to interglacial cycles. This is documented through the use of various marine sediment cores and ice cores (i.e. Vostok ice core record, the NGRIP ice core record or the recent EPICA Dome C).The age of analysed molluscs from Sydney Harbour range from 570 to 7980 years, within marine isotope stage (MIS) 1, and a time when sea-level had stabilised (although perhaps 1 m higher than present at about 6000 years ago) and when seawater $\delta^{18}O$ was essentially constant.

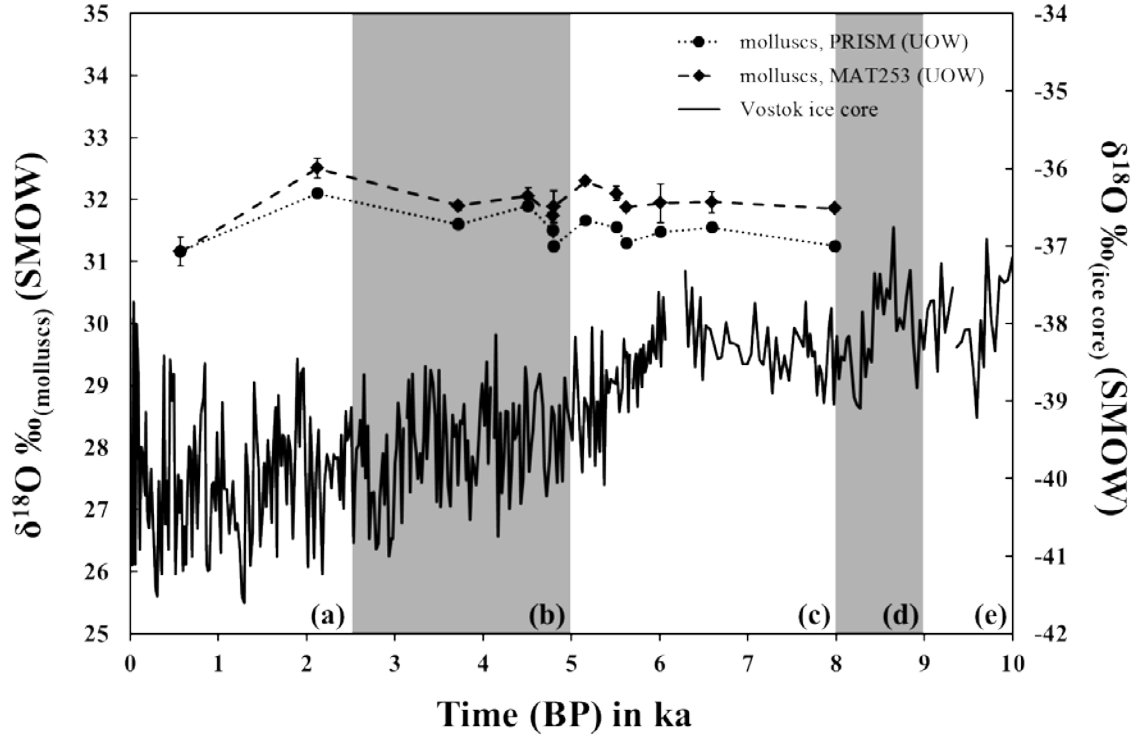

Figure 6.7: Mollusc $\delta^{18}O$ ‰ (±1σ) (VSMOW) for MAT253 and $\delta^{18}O$ ‰ (±0.1) (VSMOW) PRISM values in relation to the equivalent conventional ^{14}C age (ka BP) for the *'Triton'* site. Superimposed Holocene time intervals are provided; (a) Sub-Atlantic (2.5 ka – present), (b) Subboreal (5 ka – 2.5 ka), (c) Atlantic (8 ka – 5 ka), (d) Boreal (9 ka – 8 ka) and (e) Preboreal (10 ka – 9 ka) (Mangerud et al. 1974) using the NGRIP ice core record data of Vinther et al. (2009).

The variation in $\delta^{18}O$ in mollusc carbonate with age from Sydney Harbour does not conform to any appreciable trend with the ice core data (Figure 6.7). This may be due to various factors influencing carbonate formation. Likely causes are differences in vital effects of the individual species. Other possible contributing factors are terrestrial meteoric water runoff since the Sydney Harbour basin is fed by various freshwater streams linked to larger catchment areas. Furthermore,

the resolution of both these isotopic records must be taken into consideration. There is very little appreciable trend in the variation of the oxygen isotope record in the oceans at this time. Oxygen isotope values in the NGRIP ice core in this time frame fluctuate over a range of 4 ‰, whereas the oxygen isotope values from the analysed Holocene shells fluctuate over a range close to 2.0 ‰.

Table 6.3: Conventional stable-isotope results using both the PRISM IRMS (UOW) and the MAT253 (UOW) for all bivalves and gastropods from the *Triton* site'.

		PRISM (UOW)[a]				MAT253 (UOW)[b]			
Sample Code	**Species**	**δ^{13}C‰ (VPDB)**	**δ^{18}O‰ (SMOW)**	**δ^{18}O‰[c] (VPDB)**	**Temp.[d] °C**	**δ13C‰ (PDB)**	**δ18O‰ (SMOW)**	**δ18O‰[c] (VPDB)**	**Temp.[d] °C**
C361481	*T. lagopus*	2.0	32.1	1.2	16.2	0.9	31.2	0.4	20.2
C355060	*E. eburnea*	2.1	31.3	0.5	19.7	2.0	32.5	1.6	14.4
C360016	*C. kingii*	1.1	31.9	1.0	17.1	2.2	31.9	1.0	17.1
C348717	*P. coronata*	1.2	31.5	0.7	18.8	1.1	32.1	1.2	16.2
C081953	*M. simiae*	3.4	31.6	0.8	18.4	1.2	31.7	0.8	18.0
C098606	*E. iredalei*	0.7	31.3	0.5	19.7	0.9	31.9	1.0	17.1
C114412	*D. dilatata*	0.8	31.7	0.8	18.0	1.4	32.3	1.4	15.3
C349881	*M. lentiginosa*	3.6	31.5	0.7	18.8	2.4	32.1	1.2	16.2
C405410	*C. walkeri*	1.2	31.3	0.5	19.7	2.2	31.9	1.0	17.1
C159311	*T. cingulifera*	3.1	31.6	0.8	18.4	3.3	31.9	1.0	17.1
C071600	*R. dunkeri*	1.8	31.6	0.8	18.4	3.0	32	1.1	16.6
C074754	*T. tessellata*	1.0	31.2	0.4	20.2	1.2	31.9	1.0	17.1

[a] MAT253 prepared samples used acid-digestion reaction at 25 °C

[b] Precision for PRISM $\delta^{18}O$ values is ± 0.1 ‰ and ± 0.1 ‰ for $\delta^{13}C$. Note that these values represent a random drill sample of the shell. These samples were prepared using acid-digestion reaction at 90 °C

[c] $\delta^{18}O_{(water)}$ ‰ (VSMOW) is assumed to be 1‰ (Schrag et al., 2002)

[d] calculated from the $\delta^{18}O_{(calcite)}$ ‰ (VPDB) and $\delta^{18}O_{(water)}$ ‰ (VSMOW) using the palaeotemperature equation of Kim and O'Neil (1997) recast by Wanamaker et al. (2007).

6.4.5 Clumped-isotope analysis

Clumped isotope measurements were made along with the conventional carbon and oxygen isotope measurements. These were conducted to yield carbonate formation temperatures of the shell material. Three separate extraction sets were performed on all shell samples. During each of these extraction cycles the conventional $\delta^{18}O$ and $\delta^{13}C$ values generally coincide with the original results from the UOW analysis of 2005. However the results of the clumped isotope method provide highly inconsistent results in terms of the Δ_{47} values and the calculated formation temperature. It was initially postulated that the inconsistencies between the three extraction runs were due to machine error, errors in ratio calculation by the Isodat system as well as questions of acid purity and carbon dioxide gas purification procedures. However these concerns were all intensively scrutinised and not found to be at fault.

All clumped-isotope data for the Holocene shells appears to produce highly enriched $\Delta_{47(abs)}$ values, this translates to a highly negative calculated formation temperature using the temperature equation of Zaarur et al. (2011). Calculated temperatures for the shell material range between approximately -54 to 4 °C with extremely poor reproducibility of ±10 °C for most shell samples. Individual run reproducibility is acceptable between 0.0219 and 0.0620 ‰, however samples do not reproduce well between different extraction days using identical sample extraction procedures as well as purification techniques. All shell samples were analysed, extracted and purified in conjunction with other carbonate samples (glendonite and speleothem specimens) together with standard carbonate material (Carrara Marble (CM-1) and analytical grade calcite - AR), which provided reproducible, accurate and precise results.

It is likely that one major contributor to the highly enriched Δ_{47} values is the incorporation of unknown organic contaminants within the carbonate matrix. This would have the effect of greatly enriching the Δ_{47} value which would account for the highly negative formation temperatures calculated. Organic contaminates were supposedly eliminated or reduced by employing the carbon dioxide purification set as outlined in the method (see Chapter 3.7). However it is likely that the incorporated organic material was not fully removed by this process and continued to impact on the isotopic measurement of the Δ_{47} value.

During this study the entire suite of 12 shells specimens were analysed in 5 separate extraction batches. During this time the only parameter changed was the phosphoric acid used in the acid-digestion step of the extraction procedure. However, throughout the data acquisition there was no apparent consistent tend in the data. Δ_{47} values continued to vary in a random manner not associated with any factor associated with the extraction procedure, digestion acid used or gas

purification procedure employed. In some cases the gas purification step was removed, to examine if the gas chromatography operating process was contributing to the unreliability of the Δ_{47} data. However, this did not show any noticeable improvement.

A complete data table is not presented here due to the unreliability of the data and the obvious significant contamination of the original sample material. Future work will involve more rigorous contamination testing as well as refining the gas purification procedure used for biogenically precipitated carbonates, such as the bivalves and gastropods analysed in this investigation. This phenomenon requires further investigation, which lies outside of the scope of this thesis. Further characterisation of the incorporated organic material would need to be undertaken by closely analysing the extracted carbon dioxide gas fraction and the retained contaminants from the gas chromatography purification step. Additional analysis by GC-MS would allow the determination of these organic molecule contaminants. Dependent on these results the gas chromatography purification procedure would need to be refined and possibly extensively modified.

6.4.6 Isotopic shell zone partitioning

In this study shell specimens that were large enough and were able to provide sufficient sample material were subdivided into two zones. Zone A, composed of the last body whorle and the lip, and zone B, composed of the spire apex of the shell. This was done to investigate if shells exhibit differences in isotopic composition and formation temperature throughout their life cycle. Shell zonation experiments were conducted on three of the shells in the Holocene assemblage C098606, C159311 and C348717.

As previously stated, calculation of formation temperatures from these shells proved difficult (see Chapter 6.4.5). However, the Δ_{47} values are given for all three specimens for both growth zones. Conventional isotope measurements were able to be successfully made on both growth zone A and B on these shells with adequate precision for both $\delta^{18}O$ and $\delta^{13}C$, ±0.13 ‰ and ±0.05 ‰, respectively (see Table 6.4).

In both the C159311 and C348717 specimens zone B appears to most closely reproduce the random drill sample from the shell as analysed by the PRISM at UOW in 2005. However, in specimen C098606 this relationship appears to be reversed. Since the random drill samples were taken approximately in the middle of the shell body the PRISM isotope data may represent a mid-growth isotopic signature.

Table 6.4: Conventional stable-isotope results using both the PRISM IRMS (UOW) and the MAT253 (UOW) for all bivalves and gastropods from the '*Triton*' site for different growth zones.

			MAT253 (UOW) 2013[b]			PRISM (UOW) 2005[c]	
Sample[a]	**$\Delta_{47(abs)}$**	**SD**	**δ^{47}**	**$\delta^{13}C_{VPDB}$**	**$\delta^{18}O_{VSMOW}$**	**$\delta^{13}C_{VPDB}$**	**$\delta^{18}O_{VSMOW}$**
C348717A	0.340	0.056	22.5	-0.30	31.80	1.1	31.9
C348717B	0.907	0.032	23.0	1.10	31.97		
C098606A	0.228	0.025	21.8	0.83	31.73	0.65	31.25
C098606B	0.367	0.022	20.8	-0.03	31.48		
C159311A	0.873	0.026	25.5	3.50	32.14	3.60	31.60
C159311B	0.480	0.062	24.8	3.26	32.05		

a Specimens were sampled in two zones A and B

b Precision for MAT253 $\delta^{18}O$ values is ±0.13 ‰ and ±0.05 ‰ for $\delta^{13}C$.

c Precision for PRISM $\delta^{18}O$ values is ± 0.1 ‰ and ± 0.1 ‰ for $\delta^{13}C$. Note that these values represent a random drill sample from the shell.

Nevertheless, from these data it can be seen that there appears to be a distinct difference in the Δ_{47} value between the two sampled zones of the shells (Table 6.3). If formation temperatures could be accurately determined from these shells this may define changes in the ambient conditions of a shells environment during the phases of calcification of the shell. In addition, it has to be considered that both bivalves and gastropods primarily precipitate their carbonate shell in the warmer summer months. This coupled with the possible influx of meteoric water into confined shallow marine environments from coastal runoff adds an additional dimension of complexity to the palaeotemperature signature that can be derived from shallow marine molluscs.

6.4.7 Temperatures calculated from $\delta^{18}O$

Since clumped isotope palaeotemperatures were not able to be calculated from the Sydney Harbour shells from Δ_{47} values of the carbonates, we present potential formation temperatures calculated using the conventional isotope palaeothermometry equation of Kim and O'Neil (1997) recast by Wanamaker et al. (2007).

$$T°C = 16.9 - 4.69 \cdot [\delta^{18}O_{(calcite)}VPDB - \delta^{18}O_{(water)}VSMOW] + 0.17 \cdot [\delta^{18}O_{(calcite)}VPDB - \delta^{18}O_{(water)}VSMOW]$$

Equation 6.1

We assume a value of 1 ‰ as the standard seawater composition during the Holocene. Such seawater values were described by Schrag et al. (2002) and suggested as plausible by Wanamaker et al. (2007) when applying conventional palaeotemperature equations to pre-historic specimens where the original host water is no longer present.

In this study we present $\delta^{18}O_{(calcite)}$ from two different mass spectrometers (PRISM and MAT253) yielding two sets of $\delta^{18}O$ values for each of the shell specimens from Sydney Harbour. However, it should be noted that the two analysis set was performed on different portions of the shell. Therefore some differences in the $\delta^{18}O$ values were anticipated. Results presented in Table 6.3 demonstrate that $\delta^{18}O_{(calcite)}$ varies between 0.1 and 1.2 ‰ and 0.4 and 1.6 ‰, for each mass spectrometer respectively. These values corresponds to a variation in calculated temperatures of between ~0.4 and 5.3 °C (Table 6.2).

These calculated temperatures do not indicate higher than average sea water temperatures for Sydney Harbour between 570 and 7980 yr. BP. However as previously stated this may be due to the sampling strategy adopted by this study. Furthermore, both data sets show a significant discrepancy over the last ~2000 years. This is likely due to that the most recent shell specimens are both bivalve molluscs and are likely to produce isotopic values vastly different to the gastropods of older age in Sydney Harbour (Figure 6.8). Additionally, the crystalline structure of calcite/aragonite in gastropods and bivalves is vastly different due to their shell morphology, this may also have contributed to the inconsistencies (Dettman et al. 1999).

Partitioning results of individual shells showed a difference in isotopic composition between different parts of the same shell of up to 1.4 ‰. This may well have contributed to the variation in calculated temperature results seen in the shells from Sydney Harbour. The modern-day mean annual sea-surface temperature of Sydney Harbour is approximately 18 °C, comparing this to the calculated temperatures of the shells one can argue that certain shells appear to produce a higher temperature than others. At most an average increase of 1°C would be plausible across the range of species.

Furthermore, the inconsistency of results as well as the possible influence of organic matter is likely to have influenced the isotopic results. If these inconsistencies are addressed in the future there is possibility to more accurately determine the ambient water temperature of the shells.

No strong long term climate trend is evident from the data presented here. However, some argument can be had as to a shift in localised environmental conditions at 5000 years BP as indicated by a pronounced temperature fall and later rise over ~800 years of approximately 1.7°C (Figure 6.8).

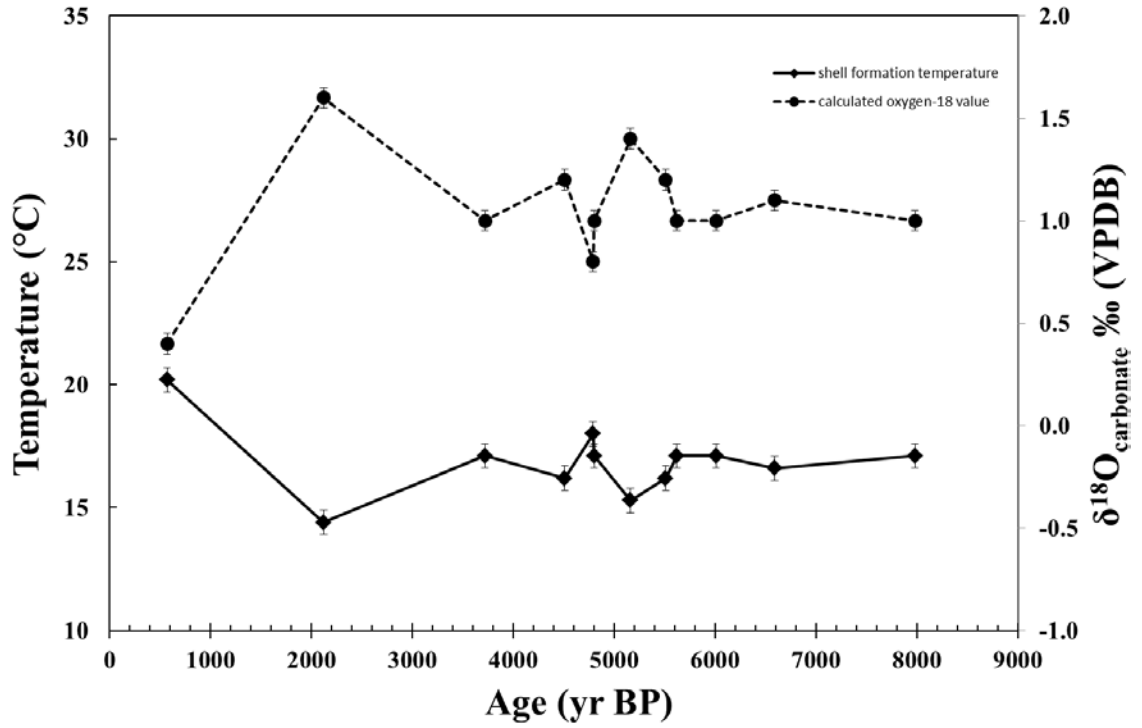

Figure 6.8 Calculated mollusc precipitation temperatures (°C ± 1σ) and calculated $\delta^{18}O_{water}$ ‰ (±1σ) (VSMOW) values from conventional $\delta^{13}C_{carbonate}$ and $\delta^{18}O_{carbonate}$ values in relation to the equivalent conventional ^{14}C age (ka BP) for the *'Triton'* site. Diamonds and solid line represent the calculated precipitation temperatures and circles and dashed line represent the $\delta^{18}O$ values.

6.5 Conclusions

The use of these marine Holocene mollusc shells as a palaeotemperature indicator using clumped-isotopes has not been successful. It was not possible to effectively and consistently measure the Δ_{47} value of the Holocene molluscs. This, therefore, did not allow the calculation of accurate carbonate formation temperatures. Through undertaking this study and choosing this sample set to apply the clumped-isotope thermometer we can conclude that marine molluscs in the Sydney Harbour basin have potential organic contamination that significantly alters the Δ_{47} value of their carbonate shell and does not allow the calculation of carbonate formation temperature using the clumped isotope palaeothermometer.

Due to the inconsistency of Δ_{47} results in this study it is thought that the carbon dioxide gas purification technique requires further scrutiny. The current purification protocol was not successful at completely removing additional organic contaminants from the biogenic carbonate shell powders used in the analysis. To further characterise this and to reduce the impact of this organic matter major modification to the extraction and purification procedure would need to be made, such as increasing the purification time, reducing the gas chromatography column temperature to aid in contaminant retention, reduction or increase in carrier gas flow as well as additional pre-treatment protocols to remove organic matter through bleaching and peroxide cleaning of carbonate powders.

Although no successful clumped-isotope measurements could be made on the mollusc shells it was still possible to determine bulk isotopic values using both the clumped-isotope method with the MAT253 instrument and earlier analysis using a conventional PRIMS IRMS setup for measuring conventional $\delta^{18}O$ and $\delta^{13}C$ values of carbonate shells. These were used calculate the $\delta^{18}O$ of the precipitating host water and carbonate formation temperature using a palaeotemperature equation. In addition to this, age determinations using radiocarbon dating were undertaken to give context to the $\delta^{18}O$ and $\delta^{13}C$ measurements.

It was found that shell zonation appears to have a minor effect on the bulk isotopic composition of different regions of a mollusc shell throughout its life cycle. This observation would require further investigation as well as increasing the number of samples to confirm that this phenomenon of changes between different zones in shell growth is consistent within a particular species. This is likely not to be a function of growth rate but more possibly a result of individual species vital effects which could change the oxygen and carbon isotopic composition of the precipitated shell.

Vital effects can also influence the clumped isotopic composition but further investigation into species specific vital effects is needed to fully understand this phenomenon. This difference in isotopic composition was also registered by the Δ_{47} values of the shells in this study but is unlikely to be reliable due to the low precision of the measurements as well as the significant fluctuation between sample replicates.

Calculated $\delta^{18}O_{(water)}$ of the host water of the Sydney harbour shells and subsequent calculation of formation temperatures using conventional palaeotemperature equations showed only a minor change in host water ambient temperature of ~1°C compared to the present environment. However, errors on individual measurements of the sample as well as uncertainty associated with the palaeotemperature equation make it difficult to provide any definitive temperature change indication. However, there does appear to be some charge in localised environmental conditions around 5000yr BP.

The literature suggests that molluscs have been shown to successfully produce reliable palaeotemperature measurements over various different environments using the clumped-isotope method. Most of these advancements have been made over the last 3 years, while this study was already underway. This is due to the clumped-isotope field still rapidly evolving and analytical techniques changing and improving. Recently Zaarur et al. (2011) and Henkes et al. (2013), as well as older work by Came et al. (2007), have provided well constrained clumped-isotope formation temperatures. However, there are many factors affecting the clumped-isotope measurement, all of which are intrinsically different and require more detailed analysis.

In summary, the use of clumped-isotopes in quantifying the formation temperature of the shell carbonate in molluscs is a highly complex problem and requires detailed study into the species specific disequilibrium effects. The clumped isotope technique is still in the early stages of development when compared to conventional isotope analysis. Further refinement of the analytical protocol for biogenically precipitated carbonate is needed to fully understand the complex disequilibrium effects and how these affect temperature. Specifically, to fully utilise the clumped isotope thermometer for mollusc carbonate shells, more refined purification techniques are required in the experimental method used in this study to remove additional organic contaminants that are significantly contributing to the large discrepancies in calculated formation temperatures of the Holocene shell samples used in this investigation.

Chapter 7: Synopsis

Understanding past environments and regional climatic change is critically reliant on robust estimates of past ambient air temperatures and regional rainfall. Although sedimentary records provide a reasonable indication of global climatic changes, understanding the effect of changing ocean-atmosphere dynamics on terrestrial environments remains largely problematic. Generally, terrestrial palaeoclimate archives such as lacustrine sedimentary cores, palaeosol and speleothem records commonly only offer indirect and ambiguous evidence for past climatic change when interpreted individually. Typically a suite of different palaeoenvironmental proxies is required to gain a comprehensive interpretation of long-term climate changes. Therefore it is imperative to develop analytical techniques that can independently provide robust estimates of past temperature regimes. This is especially important for terrestrial records due to their rarity.

Historically, conventional $\delta^{18}O$ measurements have been used to construct palaeotemperature equations from inorganic and biogenic precipitated calcium carbonate (Urey, 1947; McCrea, 1950; Epstein et al., 1953). However, $\delta^{18}O$ relationships to ambient temperature have a fundamental limitation in that they require both the isotopic composition of the precipitated carbonate and the precipitating host water to complete the palaeotemperature equation. Clumped isotope geochemistry builds upon conventional light-element gas-source stable-isotope mass spectrometry. Clumped isotope measurements are a measure of the affinity of heavy isotopes bonding ($^{13}C^{18}O^{16}O = {}^{47}CO_2$) in favour to bonding to lighter isotopes (such as in $^{12}C^{16}O^{16}O = {}^{44}CO_2$) in evolved CO_2 from carbonates (Eiler, 2007, 2011, 2013). This phenomenon of 'clumping' is represented as a deviation of ^{13}C-^{18}O-^{16}O abundance from its stochastic distribution (Δ_{47}). It is sensitive to the ambient temperature during carbonate precipitation but is independent of the bulk isotopic composition of the precipitating host water (Ghosh et al., 2006a,b). Therefore, palaeotemperatures can be deduced without knowledge of the past $\delta^{18}O$ value of the water, circumventing the primary limiting factor of conventional isotope palaeotemperature equations. If measured carefully, to a precision of ± 0.01 ‰, variations in Δ_{47} can provide ambient Earth-surface temperatures at resolutions of about ± 2 °C.

The use of clumped isotopes in geochemistry and in palaeoenvironmental studies has grown substantially since its initial application to the study of atmospheric gases (Eiler and Schauble, 2004). The method has grown into a sophisticated palaeotemperature analysis tool for carbonates (Ghosh et al., 2006a, Huntington et al., 2010, Dennis et al., 2012 and Zaarur et al., 2013).

This body of work describes the fundamentals of clumped isotope analysis, drawing upon past research to construct and optimise the clumped-isotope method to commission a new clumped isotope laboratory at the University of Wollongong. Carbon dioxide was extracted from carbonate powders using a glass vacuum extraction line with McCrea-type side-arm extraction vessels and cryogenic separation, similar to McCrea (1950), Swart et al (1991) and Ghosh et al. (2006a). This allows for the analysis of a range of sample sizes (2 mg to 20 mg, pure $CaCO_3$) as well as much larger samples where carbonate content may be as low as 7% (i.e. bone and soil). Powders were reacted with ~2mL of anhydrous H_3PO_4 (purified to 103% w/w) at 25 ± 0.1 °C in a temperature controlled circulating water bath for 12-16 hours. Purification of the extracted gas is performed using an Agilent® 7890A GC with fused-silica polystyrene-divinylbenzene capillary column (HP-PLOT-Q column with 530 µm internal diameter, 30 m long). Gas samples are entrained in an inert helium carrier gas stream (2 mL/min flow rate) and cryogenically cooled to -20 °C removing organic hydrocarbon and halocarbon contamination. The column, sample inlet and collection U-trap are baked to 150 °C for 40 min between samples. Samples were collected for approximately 40 minutes using a stainless steel U-trap and liquid nitrogen.

All gas samples and standards were analysed on a Thermo Fisher MAT253 with a customised inlet manifold. All analyses were made using Faraday cups measuring through 3 x 10^8 Ω (mass 44), 3 x 10^{11} Ω (mass 45), 10^{11} Ω (mass 46), 10^{12} Ω (mass 47, 48 and 49) resistors. Measurements were made with an acceleration potential of approx. 9.5 kV with the "sulfur-window" closed. Gas samples are introduced into the dual-inlet system through electroformed nickel capillaries to encourage uniform laminar flow. Each sample measurement consisted of 12 acquisitions of 10 cycles, each cycles comprises one set of 26 seconds integration of reference gas and sample gas. Between each acquisition an automatic pressure balance was performed to yield 8 V on mass 44 on both the sample and reference gas. A background measurement was performed before each acquisition. High voltage peak centring was conducted manually at the beginning of a measurement set and adjusted if required. This equates to an approximate analysis time of 4 hours per sample. Samples were standardised by comparison to international standard Carrara Marble 1 (CM-1) as well as NBS-19. Intra-laboratory analytical grade calcium carbonate (AR-$CaCO_3$) was used to monitor long-term analytical precision as well as CM-1. All clumped isotope measurement results are reported in the absolute reference frame (Dennis et al., 2011). An empirical transfer function (ETF) of $\Delta_{47\text{-RF}} = 1.0005\ \Delta_{47[\text{EG vs.WG}]0} + 0.8396$ was developed from head-space water-equilibrated gas samples from 10, 25 and 50 °C as well as heated gases at 1000 °C.

This study serves as a frontier to test the clumped isotope method on the cold-water carbonate glendonites, equilibrium precipitated speleothem cave deposits and Holocene marine molluscs. Through the investigation of ikaite pseudomorph structures we have confirmed the natural

formation temperature range of Permian glendonites of 1.9 ± 2.0 to 9.8 ± 4.9 °C, in the Sydney Basin, these temperature ranges conform well to the previously expected formation temperature range of 1.9 to7 °C (De Lurio and Frakes, 1999). Neogene glendonites from the Taymyr Peninsula, Russia gave temperatures of 6.5 ± 4.1 °C. Glendonite specimens from areas influenced by deep burial and substantial post-burial heating produced highly depleted Δ_{47} values and respectively high formation temperatures well outside the normal range. This may indicate that post-depositional heating of the calcite pseudomorph has the potential to be recorded by the clumped isotopic composition of the glendonite. Additionally, thinolite specimens or jarrow-type pseudomorphs associated with sub-aqueous precipitation or in association with lacustrine depositional settings produce highly enriched Δ_{47} values and therefore highly negative formation temperatures. This indicates that post-depositional evaporation and fluid migration can influence the clumped isotope palaeothermometer and affect the calculated palaeotemperature. The calculated $\delta^{18}O_{water}$ value of a Late Neogene glendonite indicates that its calcite preserves the $\delta^{18}O$ value of its precipitating seawater. Older Permian glendonites exhibit lower calculated $\delta^{18}O_{water}$ values indicative of post-depositional meteoric water exchange during burial.

In investigation of speleothem cave deposits from Riversleigh, Australia, showed that carbonate deposits formed in equilibrium with the precipitating cave water produce plausible calcite formation temperatures of ~19 °C from the broader Bitesantennary Area (Bitesantennary, Neville's Garden and Inabayence sites). These give an approximate indication of mean annual air temperature of the Mid-Miocene period. We note that stalagmite deposits appear to produce banded temperature differences within their deposition structure. Stalagmite calcite precipitates exhibit higher than expected formation temperatures of up to 8 °C higher than other surrounding equilibrium cave precipitates. In addition, calcite precipitates such as cave pearls and organic-rich dark flowstones that exhibit significant amounts of incorporated organic matter are difficult to analyse due to the high amount of contamination enriching the Δ_{47} signal. This contamination was not able to be successfully removed by gas chromatography purification. Therefore a different or refined cleaning and purification protocol must be developed in order to successfully analyse these types of deposits.

Molluscs and gastropods have previously been used in the development of the clumped isotope palaeothermometer. Bivalves and gastropods have yielded Δ_{47}-T calibrations with distinct offsets from inorganically precipitated calcite as well as other biogenically precipitated carbonate. A suite of mollusc and gastropod shells from Sydney Harbour, Australia, was analysed for their clumped isotopic composition to determine temperature variation over the course of the Holocene. Both conventional isotopic measurements as well as ^{14}C dating has been undertaken previously. The conventional $\delta^{18}O$ and $\delta^{13}C$ measurements were confirmed during the clumped isotope analysis. However, it was not possible to produce usable Δ_{47} palaeotemperature results of

the formation temperatures of these organisms. This is likely due to the incorporation of organic material into the specimens. Such contamination may be an artefact of the collection environment (i.e. marine oil from shipping in Sydney Harbour) or an artefact of post-collection (in museum) sample treatment with chloroform or formaldehyde.

In summary, this study has facilitated the application of the clumped isotope method to new sample materials. It has elucidated the formation temperature of the glendonite pseudomorph from the ikaite mineral in various geographical locations. This has confirmed the presence of polar cold-water temperatures in the Permian in the Sydney Basin, Australia as well as in the Taymyr Peninsula, Russia in the Permian and Neogene respectively. Equilibrium cave deposits of the Riversleigh fossil area, Australia have yielded palaeotemperature estimates for the Mid-Miocene period. In addition, non-equilibrium speleothem material exhibits calculated temperatures that are too high, in keeping with earlier from several caves elsewhere in the world.

References

Abbott, R.T., Dance, S.P. (1986). *Compendium of Seashells: A Color Guide to More Than 4,200 of The World's Marine Shells*. 1st ed. American Malacologists, Melbourne, Fla. pp 411.

Affek, H.P. (2012). Clumped isotope paleothermometry: principles, applications, and challenges. *The Paleontological Society Papers* **18**: 101-114.

Affek, H.P. (2013). Clumped isotopic equilibrium and the rate of isotope exchange between CO_2 and water. *American Journal of Science* **313**: 309-325.

Affek, H.P., Eiler, J.M. (2006). Abundance of mass 47 CO_2 in urban air, car exhausts, and human breath. *Geochimica et Cosmochimica Acta* **70**: 1-12.

Affek, H.P., Bar-Matthews, M., Ayalon, A., Matthews, A., Eiler J.M. (2008). Glacial/interglacial temperature variations in Soreq cave speleothems as recorded by 'clumped isotope' thermometry. *Geochimica et Cosmochimica Acta* **72**: 5351-5360.

Affek, H.P., Matthews, A., Ayalon A., Bar-Matthews, M., Burstyn, Y., Zaarur, S., Zilberman, T. (2014). Accounting for kinetic isotope effects in Soreq Cave (Israel) speleothems. *Geochimica et Cosmochimica Acta* **143**: 303-318.

Affek, H.P., Zaarur, S. (2014). Kinetic isotope effect in CO_2 degassing: Insight from clumped and oxygen isotopes in laboratory precipitation experiments. *Geochimica et Cosmochimica Acta* **143**: 319-330.

Agilent (2014). Agilent Technologies, GC & GC/MS Columns, viewed 17 January 2014, http://www.chem.agilent.com/en-US/products-services/Columns-Sample-Preparation/GC-GC-MS-Columns/Capillary/HP-PLOT-Q/Pages/default.aspx.

Andrews, S. (1998). Stratigraphy and depositional setting of the Upper McNamarra Group, Lawn Hill Region, Northwest Queensland. *Economic Geology* **93**: 1132-1152.

Appeltans, W., Bouchet, P., Boxshall, G.A., De Broyer, C., de Voogd, N.J., Gordon, D.P., Hoeksema, B.W., Horton, T., Kennedy, M., Mees, J., Poore, G.C.B., Read, G., Stöhr, S., Walter, T.C., Costello, M.J. (eds) (2012). World Register of Marine Species. Accessed at http://www.marinespecies.org on 2013-07-17.

Archer, M., Hand, S., Godthelp, H. (1986). Uncovering Australia's Dreamtime. Surrey Beatty & Sons Pty Ltd, Chipping North, NSW, Australia, pp.32.

Archer, M., Godthelp, H., Hand, S.J., Megirian, D. (1989). Fossil mammals of Riversleigh, northern Queensland: Preliminary overview of Biostratigraphy, correlation and environmental change. *Australian Zoologis*t. **25**: 29-65.

Archer, M., Hand, S. J. and Godthelp, H. (1994). Riversleigh: the story of animals in ancient rainforests of inland Australia. Reed Books. Chatswood, Australia. pp. 264.

Archer, M., Arena, D.A., Bassarova, M., Beck, R.M.D., Black, K., Boles, W.E., Brewer, P., Cooke, B.N., Crosby, K., Gillespie, A., Godthelp, H., Hand, S.J., Kear, B.P., Louys, J., Morrell, A., Muirhead, J., Roberts, K.K., Scanlon, J.D., Travouillon, K.J., Wroe, S. (2006). Current status of species-level representation in fauna from selected fossil localities in the Riversleigh World Heritage Area, northwestern Queensland. *Alcheringa: An Australian Journal of Palaeontology* **30**: 1-17.

Arena, D.A., Black, K.H., Archer, M., Hand, S.J., Godthelp, H., Creaser, P. (2014). Reconstructing a Miocene pitfall trap: Recognition and interpretation of fossiliferous Cenozoic palaeokarst. *Sedimentary Geology* **304**: 28-43.

Baker, A., Genty, D., Greybrodt, W., Barnes, W.L., Mockler, N.J., Grapes, J. (1998). Testing theoretically predicted stalagmite growth rate with Recent annual laminated samples: Implications for past stalagmite deposition. *Geochimica et Cosmochimica Acta* **62**: 393-404.

Beechey, D. (2012). *The Seashells of New South Wales*, Australian Museum, Accessed at http://seashellsofnsw.org.au/index.htm on 22/07/2013.

Bernasconi, S.M., Schmid, T.W., Grauel, A., Mutterlose, J. (2011). Clumped-isotope geochemistry of carbonates: A new tool for the reconstruction of temperature and oxygen isotope composition of seawater. *Applied Geochemistry* **26**: S279-S280.

Bernasconi, S.M., Hu, B., Wacker, U., Fiebig, J., Breitenbach, S.F.M., Rutz, T. (2013). Background effects on Faraday collectors in gas-source mass spectrometry and implications for clumped isotope measurements. *Rapid Communications in Mass Spectrometry* **27**: 603-612.

Bischoff, J.L., Fitzpatrick, J.A., Rosenbauer, R.J. (1993). The solubility and stabilization of ikaite ($CaCO_3 \cdot 6H_2O$) from 0° to 25° C: Environmental and paleoclimatic implications for Thinolite Tufa. *The Journal of Geology* **101**: 21-33.

Bischoff, J.L., Stine, S., Rosenbauer, R.J., Fitzpatrick, J.A., Stafford, T.W. Jr. (1993). Ikaite precipitation by mixing of shoreline springs and lake water, Mono Lake, California, USA. *Geochimica et Cosmochimica Acta* **57**: 3855-3865.

Bøggild, O.B. (1930). The shell structure of the Mollusks. *Det Kongelige Danske Videnskabernes Selskabs Skrifter. Naturvidenskabelig og Mathematisk Afdeling* **2**: 231-326.

Boggs, S. (1972). Petrography and geochemistry of rhombic, calcite pseudomorphs from mid-Tertiary mudstones of the Pacific Northwest, USA. *Sedimentology* **19**: 219-235.

Brand, U., Posenato, R., Came, R., Affek, H., Angiolini, L., Azmy, K., Farabegoli, E. (2012). The end-Permain mass extinction: A rapid volcanic CO_2 and CH_4-climatic catastrophe. *Chemical Geology* **322-323**: 121-144.

Brand, W.A., Assonov, S.S., Coplen, T.B. (2010). Correction for the ^{17}O interference in $\delta(^{13}C)$ measurements when analyzing CO_2 with stable isotope mass spectrometry (IUPAC Technical Report). *Pure Applied Chemistry* **82**: 1719-1733.

Bristow, T.F., Bonifacie, M., Derkowski, A., Eiler, J.M., Grotzinger, J.P. (2011). A hydrothermal origin for isotopically anomalous cap dolostone cements from south China. *Nature* **474**: 68-71.
Brooks, R., Clarke, L.M., Thurston, E.F. (1950). *Philosophical Transactions of the Royal Society* **243**: 145–167.

Buchardt, B., Israelson, C., Seaman, P., Stockman, G. (2001). Ikaite tufa towers in Ikka Fjord, Southwest Greenland: their formation by mixing of seawater and alkaline spring water. *Journal of Sedimentary Research* **71**: 176–189.

Buchardt, B., Seaman, P., Lindal, E., Stockman, G., Vous, M., Wilken, U. (1998). Ikaite from the type locality in South Greenland: formation of an unstable, low-temperature carbonate. *Nordic Geological Winter Meeting, Abstracts* **23**: 43.

Burton, E.A., Walters, L.M. (1989). The role of pH in phosphate inhibition of calcite and aragonite precipitation rates in seawater. *Geochimica et Cosmochimica Acta* **54**: 797-808.

Came, R.E., Eiler, J.M., Veizer, J., Azmy, K., Brand, U., Weidman, C.R, (2007). Coupling of surface temperatures and atmospheric CO_2 concentrations during the Palaeozoic era. *Nature* **449**: 198-201.

Came, R.E., Brand, U., Affek, H.P. (2014). Clumped isotope signatures in modern brachiopod carbonate. *Chemical Geology* **377**: 20-30.

Cao, X., Liu, Y. (2012). Theoretical estimation of the equilibrium distribution of clumped isotopes in nature. *Geochimica et Cosmochimica Acta* **77**: 292-303.

Carr, P.F., Jones, B.G., Middleton, R.G. (1989). Precursor and formation of glendonites in the Sydney Basin. *Australian Mineralogist* **4**: 3-12.

Carrapa, B., Huntington, K.H., Clementz, M., Bywater -Reyes, S., Quade, J., Schoenbohm, L., Canavan, R. (2014). Uplift of the Central Andes of NW Argentina associated with upper crustal shortening, revealed by multi-proxy isotopic analyses. *Tectonics* doi: 10.1002/2013TC003461.

Chivas, A.R., De Deckker, P., Wang, S.X., Cali, J.A. (2002). Oxygen-isotope systematics of the nektic ostracod *Australocypris robusta*. In *The Ostracoda - Applications in Quaternary Research*. (Eds, J.A. Holmes and A.R. Chivas) American Geophysical Union; Geophysical Monograph **131**: 301-313.

Cohen, K.M., Finney, S.M., Gibbard, P.L., Fan, J.-X. (2013). The ICS International Chronostratigraphic Chart. *Episodes* **36**: 199-204.

Coplen, T.B., De Bièvre, P., Krouse, H. R., Vocke R.D. Jr., Gröning, M., Rozanski, K. (1996). Ratios for light-element isotopes standardized for better interlaboratory comparison. *Eos, Transactions American Geophysical Union* **77**: 255.

Coplen, T.B., Kendall, C., Hopple, J. (1983). Comparison of stable isotope reference samples. *Nature* **302**: 236-238.

Council, T.C., Bennett, P.C. (1993). Geochemistry of ikaite formation at Mono Lake, California: Implications for the origin of tufa mounds. *Geology* **21**: 971-974.

Craig, H. (1965). The measurement of oxygen isotope paleotemperatures. In: Stable isotopes in oceanographic studies and paleotemperatures (Editor E. Tongiorgi), 161-182, CNR-Laboratorio di Geologica Nucleare, Pisa.

Csank, A.Z., Tripati, A.K., Patterson, W.P., Eagle, R.A., Rybczynski, N., Ballantyne, A.P., Eiler, J.M. (2011). Estimates of Arctic land surface temperatures during the early Pliocene from two novel proxies. *Earth and Planetary Science Letters* **304**: 291-299.

Cui, L., Wang, X. (2014). Determination of clumped isotopes in carbonate using isotope ratio mass spectrometer: Effects of extraction potential and long-term stability. *International Journal of Mass Spectrometry* **372**: 46-50.

Daëron, M., Guo, W., Eiler, J., Genty, D., Blamart, D., Boch, R., Drysdale, R., Maire, R., Wainer, K., Zanchetta, G. (2011). $^{13}C^{18}O$ clumping in speleothems: Observations from natural caves and precipitation experiments. *Geochimica et Cosmochimica Acta* **75**: 3303-3317.

Dale, A., John, C.M., Mozley, P.S., Smalley, P.C., Muggeridge, A.H. (2014). Time-capsule concretions: Unlocking burial diagenetic processes in the Mancos Shale using carbonate clumped isotopes, *Earth Planetary Science Letters* **394**: 30-37.

Dana, J.D. (1849). United States Exploring Expedition. During the Years 1838, 1839, 1840, 1841, 1842, Under the Command of Charles Wilkes, U.S.N. Vol X. Geology, C. Shearman, Philadelphia, USA.

David, T.W.E, Taylor, T.G., Woolnough, W.G., Foxhall, H.G. (1905). Occurrence of the pseudomorph glendonites in New South Wales. *Records of the Geological Survey of New South Wales* **8**: 162-179.

de Groot P.A. (2008). *Handbook of Stable Isotope Analytical Techniques*. Volume 2, Elsevier, Amsterdam, pp.1372.

Defliese, W.F., Hren, M.T., Lohmann, K.C. (2015). Compositional and temperature effects of phosphoric acid fractionation on Δ_{47} analysis and implications for discrepant calibrations. *Chemical Geology* **396**: 51–60.

De Lurio, J.L., Frakes, L.A. (1999). Glendonites as a paleoenvironmental tool: Implications for early Cretaceous high latitude climates in Australia. *Geochimica et Cosmochimica Acta*. **63**: 1039-1048.

Dennis, K.J., Schrag, D.P. (2010). Clumped isotope thermometry of carbonatites as an indicator of diagenetic alteration. *Geochimica et Cosmochimica Acta* **74**: 4110-4122.

Dennis, K.J., Affek, H.P., Passey, B.H., Schrag, D.P., Eiler, J.M. (2011). Defining an absolute reference frame for 'clumped' isotope studies of CO_2. *Geochimica et Cosmochimica Acta* **75**: 7117-7131.

Dennis, K.J, Cochran, J.K., Landman, N.H., Schrag, D.P. (2013). The climate of the Late Cretaceous: New insights from the application of the carbonate clumped isotope thermometer to Western Interior Seaway macrofossils. *Earth and Planetary Science Letters*, **362**: 51-65.

Dietzel, M., Tang, J.W., Leis, A., Kohler, S.J. (2009). Oxygen isotopic fractionation during inorganic calcite precipitation - effects of temperature, precipitation rate and pH. *Chemical Geology* **268**: 107-115.

Dreybrodt, (1988). *Processes in karst Systems: Physics, chemistry and geology*. Berlin and New York. Springer. pp.288

Dreybrodt, W. (1999). Chemical kinetics, speleothem growth and climate. *Boreas* **28**: 347-356.

Dux. F.W., Chivas, A.R., García, A. (2015). Trace-element and stable-isotope chemistry of gyrogonites of the euryhaline charophyte *Lamprothamnium*. *Aquatic Botany* **120**: 51-59.

Eagle, R.A., Schauble, E.A., Tripati, A.K., Tütken, T., Hulbert, R.C., Eiler, J.M. (2010). Body temperatures of modern and extinct vertebrates from ^{13}C-^{18}O bond abundances in bioapatite. *Proceedings of the National Academy of Sciences* **107**: 10377-10382.

Eagle, R.A., Tütken, T., Martin, T.S., Tripati, A.K., Fricke, H.C., Connely, M., Cifelli, R.L., Eiler, J.M. (2011). Dinosaur body temperatures determined from isotopic (^{13}C-^{18}O) ordering in fossil biomaterials. *Science* **333**: 443-445.

Eagle, R.A., Eiler, J.M., Tripati, A.K., Ries, J.B., Freitas, P.S., Heibenthal, C., Wanamaker, A.D. Jr., Taviani, M., Elliot, M., Marenssi, S., Nakamura, K., Ramirez, P., Roy, K. (2013). The influence of temperature and seawater carbonate saturation state on ^{13}C-^{18}O bond ordering in bivalve mollusks. *Biogeosciences Discussions* **10**: 157-194.

Eiler, J.M., Schauble, E.A. (2004). $^{18}O^{13}C^{16}O$ in Earth's atmosphere. *Geochimica et Cosmochimica Acta* **68**: 4767-4777.

Eiler, J.M. (2007). "Clumped-isotope" geochemistry – The study of naturally-occurring, multiply substituted isotopologues. *Earth and Planetary Science Letters* **262**: 309-327.

Eiler, J.M. (2011). Paleoclimate reconstruction using carbonate clumped isotope thermometry. *Quaternary Science Reviews* **30**: 3575-3588.

Eiler J.M. (2013). The isotopic anatomies of molecules and minerals. *Annual Review of Earth and Planetary Sciences* **41**: 411-414.

Eiler, J.M., Clog, M., Magyar, P., Piasecki, A., Sessions, A., Stolper, D., Deerberg, M., Schueter, H.-J., Schwieters, J. (2013). A high-resolution gas-source isotope ratio mass spectrometer. *International Journal of Mass Spectrometry* **335**: 45-56.

Eiler, J.M., Bergquist, B., Bourg, I., Cartigny, P., Farquhar, J., Gagnon, A., Guo, W., Halevy, I., Hofmann, A., Larson, T.E., Levin, N., Schauble, E.A., Stolper, D. (2014). Frontiers of stable isotope geoscience. *Chemical Geology* **372**: 119-143.

Emiliani, C., Cardini, L.,Mayeda, T., McBurney, C.B.M. and. Tongiorgi, E.,(1964). Palaeotemperature analysis of fossil shells of marine molluscs from the Arene Candide cave, Italy and the Haua Fteah cave, Cyrenaica. in H. Craig, S.L. Miller & G.J. Wasserburg (eds.). *Isotopic and cosmic chemistry*: North Holland,Amsterdam, 133-156.

Epstein, S., Buchsbaum, R., Lowenstam, H.A., Urey, H.C. (1951). Carbonate-water isotopic temperature scale. *Geological Society of America Bulletin* **62**: 417-426.

Epstein, S., Buchsbaum, R., Lowenstam, H.A., Urey, H.C. (1953). Revised carbonate-water isotopic temperature scale. *Bulletin of the Geological Society of America* **64**: 1315-1325.

Erez, J., Luz, B. (1983). Experimental paleotemperature equation for planktonic foraminifera. *Geochimica et Cosmochimica Acta* **47**: 1025-1031.

Fan, M., Hough, B.G., Passey, B.H. (2014). Middle to late Cenozoic cooling and high topography in the central Rocky Mountains: Constraints from clumped isotope geochemistry. *Earth and Planetary Science Letters* **408**: 35-47.

Fernandez, A., Tang, J., Rosenheim, B. (2014). Siderite 'clumped' isotope thermometry: A new paleoclimate proxy for humid continental environments. *Geochimica et Cosmochimica Acta* **126**: 411-421.

Ferry, J.M., Passey, B.H., Vasconcelos, C., Eiler, J.M. (2011). Formation of dolomite at 40-80 °C in the Latemar carbonate buildup, Dolomites, Italy, from clumped isotope thermometry. *Geology* **39**: 571-574.

Fichter, L.S., Poche, D. (1993). *Ancient Environments and the Interpretation of Geologic History*. 2nd Edition, Macmillan Publishing Company. pp.310

Fink, D., Hotchkis, M., Hua, Q., Jacobsen, G., Smith, A.M., Zoppi, U., Child, D., Mifsud, C., van der Gaast, H., Williams, A., Williams M. (2004). The ANTARES AMS facility at ANSTO. *Nuclear Instruments and Methods in Physics Research* **B 223–224**: 109-115.

Finnegan, S., Bergman, K., Eiler, J.M., Jones, D.S., Fike, D.A., Eisenman, I., Hughes, N.C., Tripati, A.K., Fischer, W.W. (2011). The magnitude and duration of Late Odovician-Early Silurian glaciation. *Science* **331**: 903-906.

Folk, R.L. (1959). Practical petrographic classification of limestones. *American Association of Petroleum Geologists Bulletin* **43**: 1-38.

Frakes, L.A., Francis, J.E. (1988). A guide to Phanerozoic cold polar climates from high-latitude ice-rafting in the Cretaceous. *Nature* **333**: 547-549.

Frakes, L.A., Alley, N.F., Deymoux, M. (1995). Early Cretaceous ice rafting and climate zonation in Australia. *International Geology Review* **37**: 567-583.

Francis, J.E., Frakes, L.A. (1993). Cretaceous climates. *Sedimentary Reviews* **1**: 17–30.

Frantz, C.M., Petryshyn, V.A., Marenco, P.J., Tripati, A., Berelson, W.M., Corsetti, F.A. (2014). Dramatic local environmental change during the Early Eocene Climatic Optimum detected using high resolution chemical analyses of Green River Formation stromatolites, *Palaeogeography, Palaeoclimatology, Palaeoecology* doi: 10.1016/j.palaeo.2014.04.001.

Friedman, I., O'Neil, J.R . (1977). Compilation of stable isotope fractionation factors of geochemical interest. *In*: Fleischer, M., ed., Data of Geochemistry. U.S. Geological Survey Professional Paper **440**: 1-11.

Frisia, S., Woodhead, J.D. (2012) Stalactites and Stalagmites. *Encyclopaedia of Caves*. Elsevier, Amsterdam. pp. 996.

Gabitov, R.I., Watson, E. B., Sadekov, A. (2012). Oxygen isotope fractionation between calcite and fluid as a function of growth rate and temperature: An in situ study. *Chemical Geology* **306-307**: 92-102.

Garzione, C.N., Auerbach, D.J., Smith, J.J-S., Rosario, J.J., Passey, B.H., Jordan, T.E., Eiler, J.M. (2014). Clumped isotope evidence for diachronous surface cooling of the Altiplano and pulsed surface uplift of the Central Andes. *Earth Planetary Science Letters* **393**: 173-181.

Geyh, M.A., Schleicher, H. (1990). '*Absolute age determination: physical and chemical dating methods and their application*'. Springer-Verlag: Berlin.

Ghosh, P., Brand, W.A. (2003). Stable Isotope Ratio Mass Spectrometry in Global Change Research. *International Journal of Mass Spectrometry* **228**: 1-33.

Ghosh, P., Adkins, J., Affek, H. P., Balta B., Guo, W., Schauble, E. A., Schrag, D., Eiler, J. M. (2006a). ^{13}C-^{18}O bonds in carbonate materials: A new kind of paleothermometer. *Geochimica et Cosmochimica Acta* **70**: 1439-1456.

Ghosh, P., Garzione, C., Eiler, J.M. (2006b). Rapid uplift of the Altiplano revealed through ^{13}C-^{18}O bonds in paleosol carbonates. *Science* **311**: 511-515.

Ghosh, P., Eiler, J.M., Campana, S.E., Feeney, R.F. (2007). Calibration of the carbonate 'clumped isotope' paleothermometer for otoliths. *Geochimica et Cosmochimica Acta* **71**: 2736-2744.

Godthelp, H., Archer, M., Hand, S.J., Plane, M.D. (1989). New potoroine from Tertiary Kangraoo Well Local Fauna, NT. And description of upper dentition of potoroine *Wakiewakie lawsoni* from Upper Site Local Fauna, Riversleigh. *Conference of Australasian Vertebrate Evolution, Palaeontology and Systematics*. Abstracts: p. 6.

Gonfiantini, R. (1978). Standards for stable isotope measurements in natural compounds. *Nature* **271**: 534-536.

Gonfiantini, R., Stichler, W., Rozanski, K. (1995). Standards and intercomparison materials distributed by the International Atomic Agency for stable isotope measurements. In: *Reference and intercomparison materials for stable isotopes of light elements. Proceedings of a Consultants Meeting held in Vienna*. TECHDOC-825. International Atomic Agency Vienna, Vienna: 13-29.

Grauel, A-L., Schmid, T.W, Hu, B., Bergami, C., Capotondi, L., Zhou, L., Bernasconi, S.M. (2013). Calibration and application of the 'clumped isotope' thermometer to foraminifera for high-resolution climate reconstructions. *Geochimica et Cosmochimica Acta*, **108**: 125-140.

Greinert, J., Derkachev, A. (2004). Glendonites and methane-derived Mg-calcites in the sea of Okhotsk, eastern Siberia.: implications of a venting-related ikaite/glendonite formation. *Marine Geology* **204**: 129-144.

Greybrodt, W. (2012). Speleothem Deposition. *Encyclopaedia of Caves*. Elsevier, Amsterdam. p.996.
Guo, W., Mosenfelder, J.L., Goddard, W.A.III., Eiler, J.M. (2009). Isotopic fractionations associated with phosphoric acid digestion of carbonate minerals: Insights from first-principles theoretical modelling and clumped isotope measurements. *Geochimica et Cosmochimica Acta* **73**: 7203-7225.

He, B., Olack, G.A., Colman, A.S. (2012). Pressure baseline corrections and high-precision CO_2 clumped-isotope (Δ_{47}) measurements in bellows and micro-volume models. *Rapid Communications in Mass Spectrometry* **26**: 2837-2853.

Henkes, G.A., Passey, B.H., Wanamaker, A.D.Jr., Grossman, E.L., Ambrose, W.G. Jr., Carroll, M.L. (2013). Carbonate clumped isotope compositions of modern marine mollusk and brachiopod shells. *Geochimica et Cosmochimica Acta* **106**: 307-325.

Henkes, G.A., Passey, B.H., Grossman, E.L., Shenton, B.J., Perez-Huerta, A., Yancey, T.E. (2014). Temperature limits for preservation of primary calcite clumped isotope paleotemperatures. *Geochimica et Cosmochimica Acta* **139**: 362-382.

Hill, C., Forti, P. (2003). Speleothems: Carbonate. In: *Encyclopaedia of caves and karst science*. Edr. John Gunn. Fitzroy Dearborn, New York, USA. pp. 690-693.

Hill, P.S., Tripati, A.K., Schauble, E.A. (2014). Theoretical constraints on the effects of pH, salinity, and temperature on clumped isotope signatures of dissolved inorganic carbon species and precipitating carbonate minerals. *Geochimica et Cosmochimica Acta* **125**: 610-652.

Hoefs, J. (1987). *Stable Isotope Geochemistry*, Springer Verlag. pp. 170-175.

Hoke, G.D., Giambiagi, L.B., Garzione, C.N., Mahoney, J.B., Strecker, M.R. (2014). Neogene paleoelevation of intermontane basins in a narrow, compressional mountain range, southern Central Andes of Argentina. *Earth and Planetary Science Letters* **406**: 153–164.

Horibe, Y., Oba, T. (1972). Temperature scales of aragonite-water and calcite-water systems. *Fossils* **23/24**: 69–79.

Hough, B.G., Fan, M., Passey, B.H. (2014). Calibration of the clumped isotope geothermometer in soil carbonate in Wyoming and Nebraska, USA: Implications for paleoelevation and paleoclimate reconstruction. *Earth Planetary Science Letters* **391**: 110-120.

Hu, Y.-B., Wolf-Gladrow, D.A., Dieckmann , G.S., Völker , C., Nehrke G. (2014). A laboratory study of ikaite (CaCO3·6H2O) precipitation as a function of pH, salinity, temperature and phosphate concentration. *Marine Chemistry* **162**: 10-18.

Hua, Q., Jacobsen, G.E., Zoppi, U., Lawson, E.M., Williams, A.A., Smith, A.M., McGann, M.J. (2001). Progress in radiocarbon target preparation at the ANTARES AMS Centre. *Radiocarbon* **43**: 275-282.

Huggett, J.M., Schultz, B.P., Shearman, D.J., Smith, A.J. (2005). The petrology of ikaite pseudomorphs and their diagenesis. *Proceedings of the Geologist's Association* **116**: 207-220.

Huntington, K.W., Eiler, J.M., Affek, H.P., Guo, W., Bonifacie, M., Yeung, L.Y., Thiagarajan, N., Passey, B., Tripati, A., Daëron, M., Came, R. (2009). Methods and limitations of 'clumped' CO_2 isotope (Δ_{47}) analysis by gas-source isotope ratio mass spectrometry. *Journal of Mass Spectrometry* **44**:1318-1329.

Huntington, K.W., Wernicke, B.P., Eiler, J.M. (2010). Influence of climate change and uplift on Colorado Plateau paleotemperatures from carbonate clumped isotope thermometry. *Tectonics* **29**: 1-19.

Huntington, K.W., Budd, D.A., Wernicke, Eiler, J.M. (2011). Use of clumped-isotope thermometry to constrain the crystalization temperature of diagenetic calcite. *Journal of Sedimentary Research* **81**: 656-669.

Ito, T. (1996). Ikaite from cold spring water at Shiowakka, Hokkaido, Japan. *Journal of Mineralogy, Petrology and Economic Geology* **91**: 209-219.

Ito, T. (1998). Factors controlling the transformation of natural ikaite from Shiowakka, Japan. *Geochemical Journal* **32**: 267-273.

Jansen, J.H.F., Woensdregt, C.F., Kooistra, M.J., Van der Gaast, S.J. (1987). Ikaite pseudomorphs in the Zaire deep-sea fan: an intermediate between calcite and porous calcite. *Geology* **15**: 245-248.

John, C.M., Vandeginste, V., Jourdan, A.-L., Kluge, T.M., Davis, S., Sena, C., Honig, M., Beckert, J. (2014). Carbonate reservoir analogues and clumped isotopes: How combined geometries and geochemistry of outcrops help reservoir management in the Middle East. *Society of Petroleum Engineers - International Petroleum Technology Conference* **1**: 533-539.

Johnston, J., Merwin, H.E., Williamson, E.D. (1916). The several forms of calcium carbonate. *American Journal of Science* **41**: 473-512.

Keating-Bitonti, C.R., Ivany, L.C., Affek, H.P., Douglas, P., Samson, S. (2011). Warm, not super-hot, temperatures in the early Eocene subtropics. *Geology* **39**: 771-774.

Keith, M.L., Anderson, G.M., Eichler, R. (1964). Carbon and oxygen isotopic composition of mollusk shells from marine and fresh-water environments. *Geochimica et Cosmochimica Acta*.**28**:1757-1786.

Kim, S., O'Neil, J.R., Hillaire-Marcel, C., Mucci, A. (2007a). Oxygen isotope fractionation between synthetic aragonite and water: Influence of temperature and Mg^{2+} concentration. *Geochimica et Cosmochimica Acta* **71**: 4704-4715.

Kim, S., Mucci, A., Taylor, B.E. (2007b). Phosphoric acid fractionation factors for calcite and aragonite between 25 and 75 °C: Revisited. *Chemical Geology* **246**: 135-146.

Kim, S., O'Neil, J. R. (1997). Equilibrium and nonequilibrium oxygen isotope effects in synthetic carbonates. *Geochimica et Cosmochimica Acta* **61**: 3461-3475.

Kira, T. (1962). *Shells of the Western Pacific in color*. Hoikusha. Osaka, Japan. pp. 224.

Kluge, T., Affek, H.P. (2012). Quantifying kinetic fractionation in Bunker Cave speleothems using Δ_{47}. *Quaternary Science Reviews* **49**: 82-94.

Kluge, T., Affek, H.P., Zhang, Y.G., Dublyansky, Y., Spötl, C., Immenhouser, A., Richter, D.K. (2014). Clumped isotope thermometry of cryogenic cave carbonates. *Geochimica et Cosmochimica Acta* **61**: 3461-3475.

Kobashi, T. (2001). Reevaluation of conflicting Eocene tropical temperature estimates: Molluskan oxygen isotope evidence for warm low latitudes. *Geology* **29**: p. 983.

Kodina, L.A., Tokarev, V.G., Vlasova, L.N., Bychkov, A.M., Mardanjan, I.Y. (2002) New findings of ikaite in the Kara Sea during R/V ''Akademik Boris Petrov'' Cruise 36, September 2001. *Reports on Polar and Marine Research* **419**: 164–172.

Kodina, L.A., Tokarev, V.G., Vlasova, L.N., Korobeinik, G.S. (2003). Contribution of biogenic methane to ikaite formation in the Kara Sea; evidence from the stable carbon isotope geochemistry: *Proceedings in Marine Science* **6**: 349–374.

Lamprell, K. and Whitehead, T., (1992). *Bivalves of Australia*. Crawford House Press. Bathurst, N.S.W. pp.182.

Land, L.S. (1980). The isotopic and trace element geochemistry of dolomite: The state of the art. *In*:, *Concepts and models of dolomitization.* Zenger, D.H. et al. (eds.). Society of Economic Paleontologists and Mineralogists Special Publication **28**: 87-110.

Leier, A., McQuarrie, N., Garzione, C., Eiler, J., (2013). Stable istope evidence for multiple pulses of rapid surface uplift in the Central Andes, Bolivia. *Earth Planetary Science Letters* **371-372**: 49-58.

Leighton, M.W. and Pendexter, C. (1962). Carbonate rock types. In: *Classification of carbonate rocks,* Ham, W.E. (Ed.), American Association of Petroleum Geologists Memoirs **1**: 33-61

Lu, Z., Rickaby, R.E.M., Kennedy, H., Kennedy, P., Pancost, R.D., Shaw, S., Lennie, A., Wellner, Anderson, J.B. (2012). An ikaite record of late Holocene climate at the Antarctic Peninsula. *Earth and Planetary Science* **325-326**: 108-115.

Ma, Q., Wu, S., Tang, Y. (2008). Formation and abundance of doubly-substituted methane isotopologues ($^{13}CH_3D$) in natural gas systems. *Geochimica et Cosmochimica Acta* **72**: 5446-5456.

Mangerud, J., Anderson, S.T., Berglund, B.E., Donner, J.J. (1974). Quaternary stratigraphy of Norden, a proposal for terminology and classification. *Boreas* **3**:109-128.

Marland, G. (1975). The stability of $CaCO_3 \cdot 6H_2O$ (ikaite). *Geochimica et Cosmochimica Acta* **39**: 83-91.

McCrea, J.M. (1950). On the isotopic chemistry of carbonates and a paleotemperature scale. *The Journal of Chemical Physics* **18**: 849-857.

McKinney, C.R., McCrea, J.M., Epstein, S., Allen, H.A., Urey, H.C. (1950). Improvements in mass spectrometers for the measurement of small differences in isotope abundance ratios. *Review of Scientific Instruments* **21**: 724-730.

Megirian, D. (1992). Interpretation of the Miocene Carl Creek Limestone, Northwestern Queensland. *The Beagle, Records of the Northern Territory Museum of Arts and Sciences* **9**: 219-248.

Merck (2014). ICP/MS Calibration Standards, Merck Millipore, Merck KGaA, viewed 20 May 2013, http://www.merckmillipore.com/australia/chemicals/icp-ms-calibration-standards/c_vOyb.s1L27oAAAEWuOEfVhTl.

Mitrofanov, F.P., Pozhilenko, V.I. , Arzamastsev, A.A., Fedotov, Z.A., Kolka, V.V., Korsakova O.P., Lyubtsov, V.V., Neradovsky, Y,N., Skuf'in, P.K., Smolkin, V.F., Vetrin, V.R., Zozulya, D.R. (2002). *Major geological sights of the Kola Peninsula*. 1st Edition, Eds. Mitrofanov F.P., Zozulya D.R. Geological institute, Kola Science Centre, Apatity, Russia, pp.160.

Mook, W G, Vogel, J.C., (1968). Isotopic Equilibrium between Shells and their Environment. *Science* **159**: 874.

Mook, W.G. (1971). Paleotemperatures and chlorinities from stable carbon and oxygen isotopes in shell carbonate. *Palaeogeography, Palaeoclimatology, Palaeoecology*.**9**: 245–263.
Muscheler, R., Kromer, B., Björck, S., Svensson, A., Friedrich, M., Kaiser, K.F., Southon, J. (2008).Tree rings and ice cores reveal ^{14}C calibration uncertainties during the Younger Dryas. *Nature Geoscience* **1**: 263-267.

O'Donnell, T.H., Macko, S.A., Chou, J., Davis-Hartten, K.L., Wehmiller, J.F. (2003). Analysis of $\delta^{13}C$, $\delta^{15}N$, and $\delta^{34}S$ in organic matter from the biominerals of modern and fossil *Mercenaria* spp. *Organic Geochemistry* **34**:165-183.

O'Neil, J.R. (1986). Theoretical and experimental aspects of isotopic fractionation. In *Stable Isotopes in High Temperature Geological Processes.* J.W. Valley, H.P. Taylor, Jr., and J.R. O'Neil (eds.). *Reviews in Mineralogy and Geochemistry* **16**: 1-40.

O'Neil, J.R, Clayton, R.N., Mayeda, T.K. (1969). Oxygen isotope fractionation in divalent metal carbonates. *The Journal of Chemical Physics* **51**: 5547-5557.

Papadimitriou, S., Kennedy, H., Kennedy, P., Thomas, D.N. (2014). Kinetics of ikaite precipitation and dissolution in seawater-derived brines at sub-zero temperatures to 265 K. *Geochimica et Cosmochimica Acta* **140**: 199-211.

Passey, B.H., Levin, N.E., Cerling, T.E., Brown, F.H., Eiler, J.M. (2010). High-temperature environments of human evolution in East Africa based on bond ordering in paleosol carbonates. *Proceedings of the National Academy of Sciences* **107**: 11245-11249.

Passey, B.H., Henkes, G.A. (2012). Carbonate clumped isotope bond reordering and geospeedometry. *Earth and Planetary Science Letters* **351–352**: 223-236.

Pauly, H. (1963). "Ikaite", a new mineral from Greenland. *Arctic* **16**: 263-264.

Pelouze, M.J. (1865). Sur une combination nouvelle d'eau et de carbonate de chaux. *Chemical Review* **60**: 429-431.

Peters, N.A., Huntington, K.W., Hoke, G.D. (2012). Hot or not? Impact of seasonally variable soil carbonate formation paleotemperature and O-isotope records form clumped isotope thermometry. *Earth and Planetary Science Letters* **361**: 208-218.

Peterson, S.V., Schrag, D.P. (2014). Clumped isotope measurements of small carbonate samples using a high-efficiency dual-reservoir technique. *Rapid Communications in Mass Spectrometry* **28**: 2371-2381.

Petrizzo, D.A., Young, E.D., Runnegar, B.N. (2014). Implications of high-precision measurements of ^{13}C-^{18}O bond ordering in CO_2 for thermometry in modern bivalved mollusc shells. *Geochimica et Cosmochimica Acta* **142**: 400–410.

Phipps, A.M., Hume, D.N. (1968). General purpose low temperature dry-ice baths. *Journal of Chemical Education* **45**: 664.

Plummer, L.N., Wigley, T.M.L., and Parkhurst, D.L. (1978). The kinetics of calcite dissolution in CO_2-water systems at 5 to 60 °C and 0.0 to 1.0 atm CO_2. *American Journal of Science* **278**: 179-216.

Prendergast, A.L., Stevens, R.E. (2014). Molluscs (isotopes): Analyses in environmental archaeology, In: *The Encyclopedia of Global Archaeology*. Clare Smith (eds.).Springer New York, pp. 5005-5010.

Quade, J., Breecker, D.O., Daëron, M., Eiler, J. (2011). The paleoaltimetry of Tibet: an isotopic perspective. *American Journal of Science* **311**: 77-115.

Quade, J., Garzione, C., Eiler, J. M. (2007). Paleoelevation reconstruction using pedogenic carbonates. *Reviews in Mineralogy & Geochemistry* **66**: 53-87.

Quade, J., Eiler, J. M., Daëron, M., Achyuthan, H. (2013). The clumped isotope geothermometer in soil and paleosol carbonate. *Geochimica et Cosmochimica Acta* **105**: 92-107.

RESTEK (2014) Restek Co., Rt®-Q-BOND Columns, viewed 17 January 2014, http://www.restek.com/catalog/view/7858.

Rickaby, R.E.M., Shaw, S., Bennitt, G., Kennedy, H., Zable, M., Lennie, A. (2006). Potential of ikaite to record the evolution of oceanic $\delta^{18}O$. *Geology* **34**: 497-500.

Rondeau, R.E. (1966). Slush baths. *Journal of Chemical and Engineering Data* **11**: 124.

Rosenheim, B.E., Tang, J., Fernandez, A. (2013). Measurement of multiply substituted isotopologues ('clumped isotopes') of CO_2 using a 5 kV compact isotope ratio mass spectrometer: Performance,

reference frame, and carbonate paleothermometry. *Rapid Communications in Mass Spectrometry* **27**: 1847-1857.

Rule, S., Brook, B.W., Haberle, S.G., Turney, C.S.M., Kershaw, A.P. (2012). The Aftermath of Megafaunal Extinction: Ecosystem Transformation in Pleistocene Australia. *Science* **335**: 1483–1486.

Saenger, C., Affek, H.P., Felis, T., Thiagarajan, N., Lough, J.M., Holcomb, M. (2012). Carbonate clumped isotope variability in shallow water corals: Temperature dependence and growth-related vital effects. *Geochimica et Cosmochimica Acta* **99**: 224-242.

Schauble, E.A., Ghosh, P., Eiler, J.M. (2004). Preferential formation of ^{13}C-^{18}O bonds in carbonate minerals, estimated using first principles lattice dynamics. *Geochimica et Cosmochimica Acta* **70**: 2510-2529.

Schmid, T.W., Bernasconi, S.M. (2010). An automated method for 'clumped-isotope' measurements on small carbonate samples. *Rapid Communications in Mass Spectrometry* **24**: 1955-1963.

Scholle, P.A. (1978). *A color illustrated guide to carbonate rock constituents, textures, cements, and porosities*. American Association of Petroleum Geologists. Tulsa, Oklahoma., USA, pp. 241.

Schrag, D.P., DePaolo, D.J. (1993). Determination of $\delta^{18}O$ of seawater in deep ocean during the Last Glacial Maximum. *Paleoceanography* **8***:* 1-6

Schrag, D.P., DePaolo, D. J., Richter, F.M., (1995). Reconstructing past sea surface temperatures: Correcting for diagenesis of bulk marine carbonate. *Geochimica et Cosmochimica Acta* **59**: 2265–2278.

Schrag, D.P., Adkins, J.F. McIntyre, K. Alexander, J.L. Hodell, D.A. Charles, C.D., McManus, J.F. (2002). The oxygen isotopic composition of seawater during the Last Glacial Maximum. *Quaternary Science Reviews* **21**: 331-342.

Schrag, D.P., Adkins, J.F., McIntyre, K., Alexander, J.L., Hodell, D.A., Charles, C.D., McManus, J.F. (2002). The oxygen isotopic composition of seawater during the Last Glacial Maximum. *Quaternary Science Reviews* **21**: 331-342.

Schubert, C.L., Nurnberg, D., Scheele, N., Pauer, F., Kriews, M. (1997).^{13}C isotope depletion in ikaite crystals: evidence for methane release from the Siberian shelves? *Geo-Marine Letters* **17**: 169-174.

Schöne, B.R., Surge, D. (2005). Looking back over skeletal diaries – high-resolution environmental reconstruction from accretionary hard parts of aquatic organisms. *Palaeogeography, Palaeoclimatology, Palaeoecology* **228**: 1-3.

Selleck, B.W., Carr, P.F., Jones, B.G. (2007). A review and synthesis of glendonites (pseudomorphs after ikaite) with new data: assessing applicability as recorders of ancient coldwater conditions. *Journal of Sedimentary Research* **77**: 980-991.

Sena, C.M., John, C.M., Jourdan, A.-L., Vandeginste, V., Manning, C. (2014). Dolomitization of Lower Cretaceous peritidal carbonates by modified seawater: constraints from clumped isotopic paleothermometry, elemental chemistry, and strontium isotopes. *Journal of Sedimentary Research* **84**: 552-566.

Shackleton, N. (1976). Oxygen Isotope Analyses and Pleistocene Temperatures Re-assessed. *Nature* **215**: 15-17

Shaikh, A., Shearman, G.J. (1986). Ikaite and the morphology of its pseudomorphs. In: *Proceedings of the International Meeting on the Geochemistry of the Earth Surface and Processes of Mineral Formation*, Granada, Spain, pp. 791-803.

Sharma, T., Clayton, R.N. (1965). Measurement of O18/O16 ratios of total oxygen of carbonates. *Geochimica et Cosmochimica Acta* **29**: 1347-1353.

Shearman, D. (1998). The Mono Lake tufas and ikaite columns of Ikka Fjord, Greenland. *Geoscientist* **8**: 4-5.

Shearman, D., Smith, A.J. (1985). Ikaite, the parent mineral of jarrow-type pseudomorph. *Proceedings of the Geologist's Association* **96**: 305-314.

Siegé, B. Hand, S.J., Archer, M. (1982). An Australian Miocene *Brachipposideros* (Mammalia, Chiroptera) related to Miocene representatives from France. *Palaeovertebrata* **12**: 149-172.

Sigma-Aldrich (2014). Sigma-Aldrich Co. LLC., Supel-Q™ PLOT, viewed 17 January 2014, http://www.sigmaaldrich.com/analytical-chromatography/analytical-products.html?TablePage=14540650.

Snell, K.E., Thrasher, B.L., Eiler, J.M., Koch, P.L., Sloan, L.C., Tabor, N.J. (2013). Hot summers in the Bighorn Basin during the early Paleogene. *Geology*. **41**: 55-58.

Stein, C.L. Smith, A.J. (1986). Authigenic carbonate nodules in the Nankai Trough, Site 583. *Initial reports of the deep sea drilling project* **87**: 659-668.

Stolper, D.A., Sessions, A.L., Ferreira, A.A., Santos Neto, E.V., Schimmelmann, A., Shusta, S.S., Valentine, D.L., Eiler, J.M. (2014). Combined ^{13}C-D and D-D clumping in methane: Methods and preliminary results. *Geochimica et Cosmochimica Acta* **126**: 169-191.

Stuiver, M., Polach, H.A. (1977). Discussion: Reporting of ^{14}C data. *Radiocarbon* **19**: 355-363.

Suess, E., Blazer, W., Hesse, K.F., Müller, P.J., Ungerer, C.A., Wefer, G. (1982). Calcium carbonate hexahydrate from organic-rich sediments of the Antarctic shelf: precursors of glendonites. *Science* **216**: 1128-1130.

Swainson, I.P., Hammond, R.P. (2001). Ikaite $CaCO_3 \cdot 6H_2O$: cold comfort for glendonites as paleothermometers. *American Mineralogist* **86**: 1530-1533.

Swanson, E.M. Wernicke, B.P., Eiler J.M., Losh, S. (2012) Temperatures and fluids on faults based on carbonate clumped-isotope thermometry. *American Journal of Science* **312**: 1-21.

Swart, P.K., Burns, S.J., Leder, J.J. (1991). Fractionation of the stable isotopes of oxygen and carbon in carbon dioxide during the reaction of calcite with phosphoric acid as a function of temperature and technique. *Chemical Geology* **86**: 89-96.

Tang, J., Rosenheim, B.E., Dietzel, M., Fernandez, A., Tripati, A.K. (2013) Evaluation of kinetic effect on clumped isotope fractionation (Δ_{47}) during inorganic calcite precipitation. *Mineralogical Magazine* **77**: 2308.

Tedford, R.H. (1967). Fossil mammals from the Carl Creek Limestone, northwestern Queensland. *Bulletin of the Bureau of Mineral Resources, Geology and Geophysics Australia* **92**: 217 -36.

Teichert, B.M.A., Luppold, F.W. (2013). Glendonites from an early Jurassic methane seep-Climate or methane indicators. *Palaeogeography, Palaeoclimatology, Palaeoecology* **390**: 81-93.

Thiagarajan, N., Adkins, J., Eiler, J.M. (2011). Carbonate clumped isotope thermometry of deep-sea corals and implications for vital effects. *Geochimica et Cosmochimica Acta* **75**: 4416-4425.

Thomas, R. (2013). *A practical guide to ICP-MS: A tutorial for beginners*. Third Edition. CRC Publishing Boca Raton, FL, United States of America.

Travouillon, K.J., Archer, M., Hand, S.J., Godthelp, F. (2006). Multivariate analyses of Cenozoic mammalian faunas from Riversleigh, northwest Queensland. *Alcheringa: An Australian Journal of Palaeontology* **30**: 323-349.

Tripati, A.K., Eagle, R.A., Thiagarajan, N., Gagnon, A.C., Bauch, H., Halloran, P.R., Eiler, J.M. (2010).$^{13}C–^{18}O$ isotope signatures and 'clumped isotope' thermometry in foraminifera and coccoliths. *Geochimica et Cosmochimica Acta* **74**: 5697-5717.

Tripati, A.K., Sahany, S., Pittman, D., Eagle, R.A., Neelin, J.D., Mitchell, J.L., Beaufort, L. (2014). Modern and glacial tropical snowlines controlled by sea surface temperature and atmospheric mixing. *Nature Geoscience* **7**: 205-209.

Urey, H. (1947). The thermodynamic properties of isotopic substances. *Journal of the Chemical Society*: 562-581.

Vandeginste, V., John, C.M., Cosgrove, J.W., Manning, C. (2014). Dimensions, texture-distribution, and geochemical heterogeneities of fracture - related dolomite geobodies hosted in Ediacaran limestones, northern Oman. *AAPG Bulletin* **98**: 1789-1809.

Van De Velde, J.H., Bowen, G.J., Passey, B.H., Bowen, B.B. (2013). Climatic diagenetic signals in the stable isotope geochemistry of dolomitic paleosols spanning the Paleocene-Eocene boundary. *Geochimica et Cosmochimica Acta* **109**: 254-267.

Vinther, B.M., Buchardt, S.L., Clausen, H.B., Dahl-Jensen, D., Johnsen, S.J., Fisher, D.A., Koerner, R.M., Raynaud, D., Lipenkov, V., Andersen, K.K., Blunier, T., Rasmussen, S.O., Steffensen, J.P., Svensson, A.M. (2009). Holocene thinning of the Greenland ice sheet. *Letter to Nature* **461**: 385-388.

Wainer, K.D., Genty, D., Blamart, M., Daëron, M., Bar-Matthews, H., Vonhof, Y., Dublyansky, E., Pons-Branchu, L., Thomas, P., van Calsteren, Quinif, Y., Caillon, N. (2011). Speleothem record of the last 180 ka in Villars cave (SW France): Investigation of a large ^{18}O shift between MIS6 and MIS5. *Quaternary Science Reviews* **30**: 130-146.

Wanamaker, A.D. Jr., Kreutz, K.J., Borns, H.W. Jr., Introne, D.S., Feindel, S., Funder, S., Rawson, P.D., Barber, B.J. (2007). Experimental determination of salinity, temperature, growth and metabolic effects on shell isotope chemistry of *Mytilus edulis* collected from Maine and Greenland. *Paleoceanography* **22**: PA2217, doi:10.1029/2006PA001352.

Wang, Z., Schauble, E.A., Eiler, J.M. (2004). Equilibrium thermodynamics of multiply substituted isotopologues of molecular gases. *Geochimica et Cosmochimica Acta* **68**: 4779-4797.

Wefer, G., Berger, W.H. (1991). Isotope paleontology: growth and composition of extant calcareous species. *Marine Geology* **100**: 207-248.

White, W.B. (2012). Speleothems: General Overview. In: *Encyclopaedia of Caves*. Elsevier, Amsterdam. pp. 996.

Whiticar, M.J., Suess, E. (1998). The cold water connection between Mono lake, California and the Bransfield Strait, Antarctica. *Aquatic Geochemistry* **4**: 429-454.

Wilson, B.R. and Gilbert, K. (1971).*Australian Shells: illustrating and describing 600 species of marine gastropods found in Australian waters*. Reed. Sydney. pp.162.

Wilson, B.R. and Gilbert, K. (1980). *Australian Shells: illustrating and describing 600 species of marine gastropods found in Australian waters*. Rev. Edition.Reed. Sydney. pp.152.

Wilson, B.R. (2002). *A handbook to Australian seashells*. New Holland. Sydney. pp.185.

Woodhead, J., Hand , S.J., Archer, M., Graham, I., Sniderman, K., Arena D.A.., Black, K.H., Godthelp, H., Creaser, P., Price, E. (2014). Developing a radiometrically-dated chronologic sequence for Neogene biotic change in Australia, from the Riversleigh World Heritage Area of Queensland. *Gondwana Research*, http:// dx.doi.org/10.1016/j.gr.2014.10.004.

WoRMS Editorial Board (2015). World Register of Marine Species. Available from http://www.marinespecies.org. Last accessed 2015-03-26.

Xia, J., Ito, E., Engstrom, D.R. (1997). Geochemistry of ostracode calcite: part 1. An experimental determination of oxygen isotopefractionation. *Geochimica et Cosmochimica Acta* **61**: 377-382.

Yeung, L.Y., Young, E.D., Schauble, E.A. (2012). Measurements of $^{18}O^{18}O$ and $^{17}O^{18}O$ in the atmosphere and the role of isotope-exchange reactions. *Journal of Geophysical Research* **117**: doi:10.1029/2012JD017992.

Yoshida, N., Vasilev. M., Ghosh, P., Abe, O., Yamada, K., Morimoto, M. (2013). Precision and long-term stability of clumped-isotope analysis of CO_2 using a small-sector isotope ratio mass spectrometer. *Rapid Communications in Mass Spectrometry* **27**: 207-215.

Zaarur, S., Olack, G., Affek, H.P. (2011). Paleo-environmental implication of clumped isotopes in land snail shells. *Geochimica et Cosmochimica Acta* **75**: 6859-6869.

Zaarur, S., Affek, H.P., Bradon, M.T. (2013). A revised calibration of the clumped isotope thermometer. *Earth and Planetary Science Letters* **382**: 47-57.

Zabel, M., Schulz, H.D. (2001). Importance of submarine landslides for non-steady state conditions in pore water systems: lower Zaire (Congo) deep-sea fan. *Marine Geology* **176**: 87-99.

Zhang, X., Omma, J., Peaseand, V., Scott, R. (2013). Provenance of Late Paleozoic-Mesozoic Sandstones, Taimyr Peninsula, the Arctic. *Geosciences* **3**: 502-527.

Appendix 1: ICP-MS tuning parameters

Table A1.1 Instrument analysis parameters for ICP-MS analyses.

Parameter	Value
Integration time	0.100 sec
Sample period	1.3300 sec
n (number of integrations)	200
Oxide (156/140)	0.819%
Doubly charged (70/140)	1.506%

Table A1.2 Relative standard deviation and background counts for ICP-MS analyses.

m/z	Symbol	Element	RSD%	Background
7	Li	lithium	3.26	2.3
59	Co	cobalt	2.31	3.6
89	Y	yttrium	1.9	2.3
140	Ce	cerium	2.21	5.5
205	Tl	thalium	2.77	8.7
156/140	-	oxide	11.94	-
70/140	-	doubly charged	8.7	-
55	Mn	manganese	5.27	2.1
48	Ca	calcium	7.26	2.9
238	U	uranium	97.51	9.8
138	Ba	barium	9.6	5.6
88	Sr	strontium	3.25	3
25	Mg	magnesium	6.71	2.4

* m/z refers to the mass/charge ratio used in the ICP-MS calculation

Table A1.3 Plasma condition parameters for ICP-MS analyses.

Plasma Condition	Value
RF Power	1500 W
RF Matching	1.75 V
Sample Depth	0.8 mm
Torch-H	(-)0.8 mm
Torch-V	(-)0.5 mm
Carrier Gas	0.9 L/min
Makeup Gas	0.2 L/min
Nebuliser Pump	0.1 rps
S/C Temperature	2°C

Table A1.4 Ion lens parameters for ICP-MS analyses.

Ion Lenses	Value
Extract 1	2.4 V
Extract 2	(-)134.5 V
Omega Bias-ce	(-)20 V
Omega Lens-ce	1.6 V
Cell Entrance	(-)28 V
QP Focus	2 V
Cell Exit	(-)26 V

Table A1.5 Octopole parameters for ICP-MS analyses.

Octopole Parameters	Value
OctP RF	156 V
OctP Bias	(-)6.2 V

Table A1.6 Q-pole parameters for ICP-MS analyses.

Q-Pole Parameters	Value
AMU Gain	127
AMU Offset	125
Axis Gain	0.9996
Axis Offset	0.01
OP Bias	(-)3 V

Table A1.7 Detector parameters for ICP-MS analyses.

Detector Parameters	Value
Discriminator	8 mV
Anolog HV	1750 V
Pulse HV	1240V

Appendix 2: MAT253 tuning parameters

Table A2.1 Tuning parameters for the MAT253.

Parameter		Unit	Value
Trap		V	90.7
Electron Energy		eV	84.701
Emission		mA	2.0
Extraction 1	Extraction	%	20.00
Extraction 2	Shield	%	87.99
X-Focus 1		%	20.342
X-Focus 2		%	-9.206
X-Deflection	(R-Plate)	%	51.50
Y-Deflection 1		%	14.2
Y-Deflection 2		%	-23.00
SE Suppression	(Einzel-Lens 1)	%	90.50
Retarding Lens	(Einzel-Lens 2)	%	17.40

Table A2.2 Method parameters for the MAT253.

Parameter	Unit	Value
Gas configuration	-	CO_2
Integration time	s	26
Peak Centre Cup	-	1
Peak Centre Predelay	s	120
Peak Centre Postdelay	s	120

Table A2.3 Peripheral Parameters.

Parameter	Unit	Value
Number of Cycles	-	12
FV Threshold	mBar	0.03
HV Pump Time	s	60
FV Pump Time	s	10

Appendix 3: Clumped-isotope calculations

In order to interpret the required values from the mass spectrometer output provided by the MAT 253 and the Isodat 2.8 system, calculations must be made to transform raw sample and reference gas ratios into the required Δ_i values. Δ_{47}, Δ_{48} and Δ_{49} values are the desired output for a given sample in association with $\delta^{13}C$ and $\delta^{18}O$ values.

The Isodat computer system linked with the MAT253 mass spectrometer was adjusted to give the following numerical output: SA44, SA45, SA46, SA47, SA48, SA49, ST44, ST45, ST46, ST47, ST48, ST49 as well as 13C/12C VPDB and 18O/16O VSMOW.

Instrument tuning parameters are listed in Appendix 2. The values presented were used on all standard and sample measurements. The following equations, constants and calculations are presented in one section and are not listed separately in the Table of Contents.

These following equations and constants are used to calculate the Δ_{47} value from raw counting data of the mass spectrometer for each of the relevant masses analysed. This section of the thesis will describe in detail calculation steps of the clumped isotope Δ_{47} measurement. These calculation procedures were modified from MATLAB code scripts from Huntington et al. (2009), Dennis et al. (2011) and Zaarur et al. (2014). The formulas presented here were entered into Microsoft Excel and sample data imported from the MAT253 Isodat software csv. files are modified for the use in our calculation spreadsheets.

Constants

The working reference gas is used as an internal constant as the comparison material of the mass spectrometer. The carbonate gas sample is compared to the working reference gas to calculate the R and δ values for the sample (McCrea, 1965; Epstein et al., 1951).

RefGas $\delta^{13}C_{RG}$ = -3.64 ‰ (VPDB) (Working Reference Gas - WRG $\delta^{13}C$ value) [δ13rg]

RefGas $\delta^{18}O_{RG}$ = -15.74 ‰ (VPDB) (Working Reference Gas - WRG $\delta^{18}O$ value) [δ18rg]

The Oztech reference gas has a known isotopic composition of $\delta^{13}C$ -3.64 ‰ (VPDB) and a $\delta^{18}O$ value of -15.74 ‰ (VPDB), as determined by comparison to NBS-19.

In order to calculate the Δ and δ values for each sample standard stochastic ratios of R13, R18 and R17 as well as the $\delta^{13}C$ and $\delta^{18}O$ values must be known

Table A 3.1 Constant values for ratios used in the clumped isotope method to calculate Δ_{47} and δ^{47}.

Constant	Measurement scale	$^{13}C/^{12}C$ R_{13} [a]	$^{18}O/^{16}O$ R_{18}	$^{17}O/^{16}O$ R_{17}	Source
$R13_{VPDBcalcite}$	VPDB	0.0112372	0.0020790	0.0003800	Craig (1953)
$R18_{VSMOW}$ $R17_{VSMOW}$	VSMOW	-	0.0020052	0.0037990	Gonfiantini et al. (1995)

[a] R_{13} is defined by Craig (1956) from NBS-19

Lambda (λ) is the variation of $\delta^{17}O$/ $\delta^{18}O$ in natural compounds and refers to that in nature the natural variation of $^{17}O/^{16}O$ is approximately half that of $^{18}O/^{16}O$ (λ = 0.5164; Gonfianti et al., 1995). This parameter is also a prerequisite to calculate the Δ_{47} and δ_{47} values, required for the palaeotemperature calculation.

Isodat MS data set

The mass spectrometer (MAT253) produces a list of various data fields from sample and standard gas measurement cycles. The sample gas is measured as SA voltages for mass 44 to 49 inclusively (e.g SA44; equivalent to sample gas measurement for mass 44). The standard gas is measured and displayed as ST voltages from for mass 44 to 49 inclusively (e.g SA49; equivalent to sample gas measurement for mass 494).

The calculated $\delta^{13}C_{VPDB}$ and $\delta^{18}O_{VSMOW}$ values are displayed as R_{13SA} and R_{18SA} values from the Isodat software for the sample gas only. These are used in calculating the stochastic random distribution of the sample.

$R13_{sa}$ = data(range,x:x)

$R18_{sa}$ = data(range,x:x)

If the signal for mass 49 is too small to measure and returns a negative number it must be estimated. This is accomplished by calculating its value from the mass 47 signal for sample and reference gas respectively.

Therefore, the mass 49 signal is represented by the following function:

$$f\_ST49 = ST47/1000$$

$$f\_SA49 = \frac{(f\_ST49 + f\_ST49)}{2} + SA49 - \frac{(ST49+ST49)}{2}$$

Note: this must be performed on an average of the two bracketing reference gas samples for each sample gas mass 49 measurement made. This was rarely performed during the analysis of this study as most SA voltages of mass 49 were positive.

R_i reference gas stochastic distribution*

To calculate the R_i ratio of a particular mass for a sample gas the stochastic distribution of the reference gas must be known to standardise the ratio of the sample to the relevant working reference gas.

To calculate the reference gas ratios, a random stochastic distribution R_i^* must be assumed. To find the stochastic distribution R_{13}, R_{17}, R_{18} ratios for the reference gas (RG) used (also referred to as the working gas in text) must be found (Huntington et al. 2009). This process uses the known $\delta^{13}C_{RG}$ and $\delta^{18}O_{RG}$ values as specified by the Oztech reference gas as well as constant values from Chapter 3.8.1.1, derived from known values of NBS-19.

$$R_{13}^{RG} = \left(\frac{\delta^{13}C_{RG}}{1000}+1\right) * VPDBcalcite_{R13}$$

$$R_{18}^{RG} = \left(\frac{\delta^{18}O_{RG}}{1000}+1\right) * R_{18\ VSMOW}$$

$$R_{17}^{RG} = R_{17\ VSMOW} * \left(\frac{\delta^{18}O_{RG}}{R_{18\ VSMOW}}\right)^{\lambda}$$

or

$$R_{17}^{RG} = K * R_{18RG}^{\lambda}$$

Where:

$$K = \left(\frac{R_{17\ VSMOW}}{R_{18\ VSMOW}^{\lambda}}\right)$$

Next the abundance of isotopes ($C_{RG}i$) must be calculated, using the ratios of the reference gas (where RG is denoted by *), assuming stochastic distribution of isotopes among all possible isotopologues of CO_2.

$C_{RG}12 = 1/(1+R_{13RG})$

or $[12C] = \frac{1}{1+ R13*}$

$C_{RG}13 = R_{13RG}$ x $^{12}C^{*}$

or $[13C] = \frac{R13*}{1+ C12}$

$C_{RG}16 = 1/(1+ R_{17RG} + R_{18RG})$

or $[16O] = \frac{1}{1+ R17*+ R18*}$

$C_{RG}17 = R_{17RG}$ x C16

or $[17O] = \frac{R17*}{1+ R17*+ R18*}$

$C_{RG}18 = R_{18RG}$ x C16

Or $[18O] = \frac{R18*}{1+ R17*+ R18*}$

The calculated ratios of masses 12, 13, 16, 17 and 18 displaying the random stochastic distribution are then used to calculate the abundance of CO_2 in the reference gas for masses 44 to 49 (C_{44RG} to C_{49RG}).

[44]* = [12][16][16]

[45]* = [13][16][16]+2[12][16][17]

[46]* = 2[12][16][18]+[12][17][17]+2[13][16][17]

[47]* = 2[13][16][18]+[13][17][17]+2[12][17][18]

$C_{RG}121616 = C_{RG}12 \times C_{RG}16^2$

$C_{RG}131616 = C_{RG}13 \times C_{RG}16^2$

$C_{RG}121716 = C_{RG}12 \times C_{RG}17 \times C_{RG}16 \times 2$

$C_{RG}131716 = C_{RG}13 \times C_{RG}17 \times C_{RG}16 \times 2$

$C_{RG}121816 = C_{RG}12 \times C_{RG}18 \times C_{RG}16 \times 2$

$C_{RG}121717 = C_{RG}12 \times C_{RG}17^2$

$C_{RG}131816 = C_{RG}13 \times C_{RG}18 \times C_{RG}16 \times 2$

$C_{RG}131717 = C_{RG}13 \times C_{RG}17^2$

$C_{RG}121817 = C_{RG}12 \times C_{RG}18 \times C_{RG}17 \times 2$

$C_{RG}131817 = C_{RG}13 \times C_{RG}18 \times C_{RG}17 \times 2$

$C_{RG}121818 = C_{RG}12 \times C_{RG}18^2$

$C_{RG}131818 = C_{RG}13 \times C_{RG}18^2$

Therefore the calculated ratios of mass 44 to 49 can be expressed as:

C_{44RG} = C121616

C_{45RG} = C131616 + C121716

C_{46RG} = C131716+C121816+ C121717

C_{47RG} = C131816+C121817+ C131717

C_{48RG} = C131817 + C121818

C_{49RG} = C131818

The reference gas ratios are calculated by dividing the stochastic abundance of the relevant mass by C_{44RG} to give the R_{iRG} ratios for the reference gas assuming random stochastic distribution. These are use in the calculation of the $R_{i\,SA\text{-}RG}$ value for the sample gas, see Chapter 3.8.1.4.

$$Rrg_{45}{}^{*} = \frac{C_{45RG}}{C_{44RG}}$$

$$Rrg_{46}{}^{*} = \frac{C_{46RG}}{C_{44RG}}$$

$$Rrg_{47}{}^{*} = \frac{C_{47RG}}{C_{44RG}}$$

$$Rrg_{48}{}^{*} = \frac{C_{48RG}}{C_{44RG}}$$

$$Rrg_{49}{}^{*} = \frac{C_{49RG}}{C_{44RG}}$$

R_i for the sample gas

The R_i values for a particular mass (44,45,46,47,48,49) of sample (SA) and standard (RG) also termed the reference or working gas, are calculated as shown below. This will yield mass ratios R_{45}, R_{46}, R_{47}, R_{48} and R_{49} for sample and standard respectively, using the sample and standard gas voltages measured by the MS.

Following the equation: $R(sa/rg)_i = \frac{(mass\ i)}{(mass\ 44)}$

where i=[44,45,46,47,48,49] of sample (sa) and standard (rg)

$$Rsa_{45} = \frac{SA45}{SA44}$$

$$Rsa_{46} = \frac{SA46}{SA44}$$

$$Rsa_{47} = \frac{SA47}{SA44}$$

$$Rsa_{48} = \frac{SA48}{SA44}$$

$$Rsa_{49} = f\frac{SA49}{SA44}$$

$$Rrg_{45} = \frac{ST45}{ST44}$$

$$Rrg_{46} = \frac{ST46}{ST44}$$

$$Rrg_{47} = \frac{ST47}{ST44}$$

$$Rrg_{48} = \frac{ST48}{ST44}$$

$$Rrg_{49} = f\frac{ST49}{ST44}$$

The R_i values from the sample and standard gas voltages are then used to calculate calibrated $R_{iSA\text{-}RG}$ ratios that are later used to calculate Δ_{47} values.

Calculating $R_{iSA-RG} = \left(\frac{Rsa_i}{Rrg_i}\right) * Rrg^{*}_{i}$, see Chapter 3.8.3.1, where i = [45,46,47,48,49] of sample and standard.

This calculates a R_{iRG} and R_{iSA} value for a hypothetical CO_2 with $\delta^{13}C=0$, $\delta^{18}O=0$, $\Delta_{47}=0$.

$$R_{45SA-RG} = \left(\frac{Rsa_{45}}{Rrg_{45}}\right) * Rrg^{*}_{45}$$

$$R_{46SA-RG} = \left(\frac{Rsa_{46}}{Rrg_{46}}\right) * Rrg^{*}_{46}$$

$$R_{47SA-RG} = \left(\frac{Rsa_{47}}{Rrg_{47}}\right) * Rrg^{*}_{47}$$

$$R_{48SA-RG} = \left(\frac{Rsa_{48}}{Rrg_{48}}\right) * Rrg^{*}_{48}$$

$$R_{49SA-RG} = \left(\frac{Rsa_{49}}{Rrg_{49}}\right) * Rrg^{*}_{49}$$

δ^{47} calculation for the sample gas

. This calculation is performed automatically by the mass spectrometer and the Isodat software. This is known as a raw delta value δ^{45} through δ^{49}, inclusive for all δ^{i} values for the measured sample gas. It is needed for classification of the Δ_{47} anomaly as well as for the calibration of the mass spectrometer using the empirical transfer function (Huntington et al. 2009).

$$\delta 45 = \left(\frac{Rsa_{45}}{\frac{Rrg_{45} + Rrg_{45}}{2}} \right) - 1 * 1000$$

$$\delta 46 = \left(\frac{Rsa_{46}}{\frac{Rrg_{46} + Rrg_{46}}{2}} \right) - 1 * 1000$$

$$\delta 47 = \left(\frac{Rsa_{47}}{\frac{Rrg_{47} + Rrg_{47}}{2}} \right) - 1 * 1000$$

$$\delta 48 = \left(\frac{Rsa_{48}}{\frac{Rrg_{48} + Rrg_{48}}{2}} \right) - 1 * 1000$$

$$\delta 49 = \left(\frac{Rsa_{49}}{\frac{Rrg_{49} + Rrg_{49}}{2}} \right) - 1 * 1000$$

R_i^* Calculation for Sample Gas

Ratios for the sample gas then calculated assuming a random stochastic distribution R_i^*, calibrated against the working reference gas. In order to do this R_{13}^*, R_{17}^*, R_{18}^* ratios of the sample gas assuming the stochastic distribution, are calculated using the sample's measured $\delta^{13}C_{sa}$ and $\delta^{18}O_{sa}$ values from the mass spectrometer output (Huntington, et al., 2009).

$$R_{13*} = \left(\frac{\delta^{13}C_{sa}}{1000} + 1\right) * VPDBcalcite_{R13}$$

$$R_{18*} = \left(\frac{\delta^{18}O_{sa}}{1000} + 1\right) * R_{18\,VSMOW}$$

$$R_{17*} = R_{17\,VSMOW} * \left(\frac{\delta^{18}O_{sa}}{R_{18\,VSMOW}}\right)^{\lambda}$$

These can also be calculated using Zaarur et al. (2013) and Brand et al. (2010) to calculate R_{13}, R_{18} and R_{17}. This uses the $R_{45SA-RG}$ and $R_{46SA-RG}$ ratio to calculate first the ratio of $R_{18SA-RG}$ and then the subsequent ratios in association with constant K (Gonfiantini et al., 1995).

To find $R_{18SA-RG}$solve the equation below:

$$0 = -3K^2(R_{18SA-RG*})^{2\lambda} + 2 * K * R_{45SA-RG} * (R_{18SA-RG})^{\lambda} + 2 * R_{18SA-RG} - R_{45SA-RG}$$

$$R_{17SA-RG*} = K * R_{18SA-RG}{}^{\lambda}$$

$$R_{13SA-RG*} = R_{45SA-RG} - 2 * R_{17SA-RG}$$

The abundance of isotopes (Ci) is calculated using the ratios of the sample gas, assuming stochastic distribution of isotopes among all isotopologues by either the Huntington et al. (2009) or Zaarur et al. (2014) method. Substituting $R_{13SA\text{-}RA}$ (R13), $R_{17SA\text{-}RA}$ (R17) and $R_{18SA\text{-}RA}$ (R18), gives the following ratios.

C12 = $1/(1+R_{13}^{*})$

or $[12C] = \frac{1}{1+ R13*}$

C13 = R_{13}^{*} x $^{12}C^{*}$

or $[13C] = \frac{R13*}{1+ C12}$

C16 = $1/(1+ R_{17}^{*}+ R_{18}^{*})$

or $[16O] = \frac{1}{1+ R17*+ R18*}$

C17 = R_{17}^{*} x C16

or $[17O] = \frac{R17*}{1+ R17*+ R18*}$

C18 = R_{18}^{*} x C16

Or $[18O] = \frac{R18*}{1+ R17*+ R18*}$

The randomly distributed abundance of CO_2 of all isotopologues is then calculated as shown in Table 2.3 for masses 44 to 49 inclusive.

$C121616 = C12 \times C16^2$

$C131616 = C13 \times C16^2$

$C121716 = C12 \times C17 \times C16 \times 2$

$C131716 = C13 \times C17 \times C16 \times 2$

$C121816 = C12 \times C18 \times C16 \times 2$

$C121717 = C12 \times C17^2$

$C131816 = C13 \times C18 \times C16 \times 2$

$C131717 = C13 \times C17^2$

$C121817 = C12 \times C18 \times C17 \times 2$

$C131817 = C13 \times C18 \times C17 \times 2$

$C121818 = C12 \times C18^2$

$C131818 = C13 \times C18^2$

Therefore:

$C44 = C121616$

$C45 = C131616 + C121716$

$C46 = C131716+C121816+ C121717$

$C47 = C131816+C121817+ C131717$

$C48 = C131817 + C121818$

$C49 = C131818$

This can be simplified to:

$[44]^* = [12][16][16]$

$[45]^* = [13][16][16]+2[12][16][17]$

$[46]^* = 2[12][16][18]+[12][17][17]+2[13][16][17]$

$[47]^* = 2[13][16][18]+[13][17][17]+2[12][17][18]$

This allows the calculation of the $R_i^*{}_{ST\text{-}RG}$ ratios by dividing the stochastic abundance of the relevant mass by C44. The $R_i^*{}_{ST\text{-}RG}$ ratio for the sample assumes the random stochastic distribution of the standard gas (ST) calibrated against the working reference gas (RG).

$R_{45}^*{}_{SA\text{-}RG}$ = C45/C44

$R_{46}^*{}_{SA\text{-}RG}$ = C46/C44

$R_{47}^*{}_{SA\text{-}RG}$ = C47/C44

$R_{48}^*{}_{SA\text{-}RG}$ = C48/C44

$R_{49}^*{}_{SA\text{-}RG}$ = C49/C44

$\Delta_{47\text{-}raw}$ (mass 47) anomaly

The final Δ_{47} value compares, the measured sample ratio ($R_{i\ SA\text{-}RG}$ values), calibrated to the reference gas, to the calculated stochastic R_i^* values for CO_2 with hypothetical values for $\delta^{13}C$ = 0 ‰, $\delta^{18}O$ = 0‰, Δ_{47} = 0‰, calibrated against the working reference gas ($R_i^*{}_{ST\text{-}RG}$). This is represented by the following formula for mass *i*.

$$\Delta_i = \left(\frac{R_{iSA-RG}}{R^*_{iSA-RG}}\right) * 1000$$

Δ_i values for the sample

Δ_{45}=($R_{45SA\text{-}RG}$/ $R_{45}^*{}_{SA\text{-}RG}$-1)*1000

Δ_{46}=($R_{46SA\text{-}RG}$ / $R_{46}^*{}_{SA\text{-}RG}$ -1)*1000

Δ_{47}=($R_{47\ SARG}$ / $R_{47}^*{}_{SA\text{-}RG}$ -1)*1000

Δ_{48}=($R_{48\ SARG}$ / $R_{48}^*{}_{SA\text{-}RG}$ -1)*1000

Δ_{49}=($R_{49\ SARG}$ / $R_{49}^*{}_{SA\text{-}RG}$ -1)*1000

This can be re-written as mass 47, 48, 49 anomalies for the sample, showing isotopologue abundance with respect to the stochastic distribution.

$$\Delta_{47} = \left[\left(\frac{R_{47SA-RG}}{R_{47SA-RG^*}} - 1\right) - \left(\frac{R_{46SA-RG}}{R_{46SA-RG^*}} - 1\right) - \left(\frac{R_{45SA-RG}}{R_{45SA-RG^*}} - 1\right)\right] \times 1000$$

$$Full\ \Delta_{47} = \Delta_{47} - \Delta_{46} - \Delta_{45}$$

$$Full\ \Delta_{48} = \Delta_{48} - 2 * \Delta_{46}$$

$$Full\ \Delta_{49} = \Delta_{49} - 2 * \Delta_{46} - \Delta_{45}$$

This produces 'raw' Δ_{47} values calibrated against the working reference gas $\Delta_{47\text{-}[SG\text{-}WG]}$. These need to be further refined by standardising them into the absolute reference frame (Dennis et al., 2011). This is explained in detail in Chapter 3.8.2. Where non linearity effects are calculated by

comparing data to theoretical Δ_{47} values (Wang et al., 2004) and creating a equilibrated gas line correction for the sample data when comparing it to equilibrated gas samples. This is then used to construct an empirical transfer function.

Samples can also be calibrated against the synthetic carbonate equilibration scheme by Ghosh et al. (2006a) as well as a more current calibration compilation by Zaarur et al. (2014). However the new accepted standard for presentation of results of Δ_{47} and subsequent palaeotemperature equations Δ_{47}-*T*, the Δ_{47abs} or $\Delta_{47\ RF}$ should be used to allow direct intercomparrison of results between studies from various laboratories.

Table A4 Clumped-isotope analysis sample log, April 2014 to October 2014.

Analysis Date	Sample ID	Type	Extraction Date	Sample Weight (mg)	Pressure (mm Hg)
9/04/2014	HG1000°C(BOC)	HG	8/01/2014	-	657
10/04/2014	EG10°C(A-1)	EG	11/02/2014	-	448
11/04/2014	EG25°C(A-1)	EG	14/01/2014	-	435
11/04/2014	EG50°C(A-1)	EG	21/02/2014	-	478
11/04/2014	EG10°C(P-1)	EG	11/02/2014	-	435
11/04/2014	EG25°C(P-1)	EG	14/01/2014	-	463
14/04/2014	EG25°C(P-1)	EG	14/01/2014	-	463
15/04/2014	EG50°C(P-1)	EG	21/02/2014	-	479
15/04/2014	HG1000°C(HP-BOC)	HG	8/01/2014	-	573
16/04/2014	EG50°C(C-1)	EG	19/02/2014	-	471
16/04/2014	EG25°C(C-1)	EG	14/01/2014	-	447
16/04/2014	EG10°C(C-1)	EG	17/02/2014	-	438
17/04/2014	EG10°C(A-1)	EG	17/02/2014	-	436
17/04/2014	EG50°C(A-1)	EG	19/02/2014	-	360
17/04/2014	HG1000°C(1874C)	HG	16/04/2014	-	198
18/04/2014	HG1000°C(UHP-BOC)	HG	9/01/2014	-	621
18/04/2014	HG1000°C(1845C)	HG	16/04/2014	-	204
19/04/2014	HG1000°C(UHP-BOC)	HG	9/01/2014	-	583
19/04/2014	HG1000°C(1847C)	HG	16/04/2014	-	192
20/04/2014	HG1000°C(1845C)	HG	16/04/2014	-	207
20/04/2014	HG1000°C(UHP-BOC)	HG	9/01/2014	-	522
21/04/2014	EG25°C(A-1)	EG	21/04/2014	-	435
22/04/2014	EG25°C(A-1)	EG	21/04/2014	-	435
23/04/2014	EG25°C(A-1)	EG	21/04/2014	-	421
23/04/2014	EG25°C(A-1)	EG	21/04/2014	-	421
23/04/2014	EG25°C(C-1)	EG	21/04/2014	-	440
24/04/2014	EG25°C(C-1)	EG	21/04/2014	-	426
24/04/2014	EG50°C(C-1)	EG	7/02/2013	-	525
25/04/2014	HG1000°C(UHP-BOC)	HG	9/01/2014	-	492
26/04/2014	EG25°C(A-1)	EG	24/04/2014	-	408
26/04/2014	EG25°C(C-1)	EG	24/04/2014	-	420
28/04/2014	EG25°C(C-1)	EG	24/04/2014	-	436
28/04/2014	EG50°C(C-1)	EG	7/02/2013	-	515
29/04/2014	EG50°C(P-1)	EG	7/02/2013	-	497
30/04/2014	HG1000°C(1845C)	HG	30/04/2014	-	210
1/05/2014	HG1000°C(1845C)	HG	30/04/2014	-	200
2/05/2014	EG50°C(C-1)	EG	1/05/2014	-	444
3/05/2014	EG50°C(C-1)	EG	1/05/2014	-	452
3/05/2014	HG1000°C(1845C)	HG	3/05/2013	-	unknown
4/05/2014	HG1000°C(UHP-BOC)	HG	3/05/2013	-	unknown
5/05/2014	HG1000°C(1874C)	HG	3/05/2013	-	unknown
6/05/2014	HG1000°C(1874C)	HG	3/05/2013	-	unknown
8/05/2014	FH_2	STD	28/03/2014	11.224	236

9/05/2014	CM-1_2	STD	28/03/2014	10.928	224
10/05/2014	EG50°C(A-1)	EG	10/05/2014	-	444
11/05/2014	EG50°C(A-1)	EG	10/05/2014	-	441
12/05/2014	CM-1_1	STD	28/03/2014	7.115	143
12/05/2014	HG1000°C(1874C)	HG	12/05/2014	-	unknown
13/05/2014	HG1000°C(1874C)	HG	12/05/2014	-	unknown
14/05/2014	HG1000°C(1874C)	HG	12/05/2014	-	unknown
16/05/2014	CM-1_3	STD	10/04/2014	8.236	174
16/05/2014	HG1000°C(UHP-BOC)	HG	12/05/2014	-	unknown
17/05/2014	c.071600	SA-S	19/11/2013	10.284	217
17/05/2014	c.081953	SA-S	19/11/2013	11.396	240
17/05/2014	c.098606A	SA-S	19/11/2013	9.492	194
18/05/2014	c.098606B	SA-S	20/11/2013	9.551	191
18/05/2014	c.074754	SA-S	20/11/2013	11.206	230
18/05/2014	c.114412	SA-S	20/11/2013	11.446	232
19/05/2014	c.405410	SA-S	20/11/2013	10.926	224
19/05/2014	c.159311A	SA-S	21/11/2013	9.82	205
19/05/2014	c.159311B	SA-S	21/11/2013	11.258	236
20/05/2014	c.348717A	SA-S	21/11/2013	9.71	208
20/05/2014	c.348717B	SA-S	21/11/2013	11.396	239
21/05/2014	c.349881	SA-S	22/03/2013	11.324	229
21/05/2014	c.355060	SA-S	22/03/2013	9.576	195
21/05/2014	c.360014	SA-S	22/03/2013	10.469	219
21/05/2014	c.361481	SA-S	22/03/2013	9.474	201
22/05/2014	CM-1_4	STD	10/04/2014	8.959	175
24/05/2014	FH_3	STD	10/04/2014	6.047	130
24/05/2014	AL-1	SA-G	21/06/2013	7.501	142
25/05/2014	AL-1	SA-G	21/06/2013	7.501	142
25/05/2014	GL-1	SA-G	21/06/2013	10.7	210
26/05/2014	TH-1	SA-G	21/06/2013	9.55	188
27/05/2014	BR-1a	SA-G	19/11/2013	10.961	216
27/05/2014	MG-2a(mud)	SA-G	19/11/2013	16.365	137
28/05/2014	MG-2a(glendonite)	SA-G	19/11/2013	11.477	227
28/05/2014	MG-2a(glendonite)	SA-G	19/11/2013	11.477	227
28/05/2014	MG-2a(shell)	SA-G	19/11/2013	9.561	209
28/05/2014	OR-1a	SA-G	14/11/2013	9.747	193
29/05/2014	OR-2a	SA-G	14/11/2013	10.215	206
29/05/2014	WH-2A	SA-G	14/11/2013	9.42	198
30/05/2014	WH-4	SA-G	14/11/2013	10.188	204
30/05/2014	WH-1f	SA-G	5/11/2013	8.603	183
30/05/2014	WH-1f	SA-G	5/11/2013	8.603	183
31/05/2014	WH-5	SA-G	5/11/2013	8.836	188
1/06/2014	c.074754	SA-S	1/06/2015	8.754	173
1/06/2014	c.081953	SA-S	1/06/2015	8.88	173
1/06/2014	c.098606	SA-S	1/06/2015	8.229	173
1/06/2014	c.098606	SA-S	1/06/2015	8.299	173

2/06/2014	WH-5d	SA-G	25/11/2013	9.726	205
2/06/2014	WH-4	SA-G	25/11/2013	fail	fail
3/06/2014	TUN541.7	SA-G	12/11/2013	9.113	166
3/06/2014	TUN637-dk	SA-G	12/11/2013	8.815	182
3/06/2014	H1-B	SA-G	12/11/2013	8.812	189
3/06/2014	H4-A	SA-G	12/11/2013	9.963	205
4/06/2014	KP-7B_1	SA-G	29/06/2012	6.096	92
4/06/2014	KP-7B_2	SA-G	29/06/2012	12.147	162
4/06/2014	WH-2a	SA-G	29/06/2012	unknown	unknown
5/06/2014	c.114412	SA-S	2/06/2014	11.788	239
5/06/2014	c.159311A	SA-S	2/06/2014	11.69	228
5/06/2014	c.159311B	SA-S	2/06/2014	8.4	173
6/06/2014	c.348717A	SA-S	3/06/2014	8.838	174
7/06/2014	c.348717B	SA-S	3/06/2014	9.817	201
7/06/2014	c.349881	SA-S	3/06/2014	13.356	267
7/06/2014	c.355060	SA-S	3/06/2014	11.156	225
7/06/2014	c.3600161	SA-S	4/06/2014	11.479	201
8/06/2014	c.361481	SA-S	4/06/2014	9.192	185
8/06/2014	c.05410	SA-S	4/06/2014	12.855	261
8/06/2014	c.071600	SA-S	4/06/2014	14.891	299
9/06/2014	CM-1_5	STD	5/06/2014	10.813	215
9/06/2014	CM-1_6	STD	5/06/2014	10.49	208
9/06/2014	CM-1_7	STD	5/06/2014	10.336	205
9/06/2014	KP7-B	SA-G	26/06/2012	12.697	96
9/06/2014	AR-1	STD	21/06/2013	4.03	74
10/06/2014	CB2B	SA-B	12/12/2014	103.2	114
10/06/2014	C4A	SA-B	12/12/2014	100.6	457
10/06/2014	C3A	SA-B	1/10/2013	109.5	137
11/06/2014	C2A	SA-B	1/10/2013	107.2	157
11/06/2014	C1A	SA-B	1/10/2013	100.6	150
17/06/2014	HG1000°C(UHP-BOC)	HG	12/05/2014	unknown	unknown
18/06/2014	OR-1	SA-R	19/09/2013	9.338	192
18/06/2014	OR-2	SA-R	19/09/2013	9.692	195
19/06/2014	OR-3	SA-R	19/09/2013	9.553	198
19/06/2014	RT-1	SA-R	20/09/2013	9.1	185
19/06/2014	SG-1	SA-R	20/09/2013	10.314	216
20/06/2014	SG-2	SA-R	20/09/2013	9.863	206
20/06/2014	SG-3	SA-R	20/09/2013	9.863	194
20/06/2014	OS-2(int.)	SA-R	7/11/2013	8.852	184
21/06/2014	BC-2(calcite)	SA-R	7/11/2013	9.474	196
21/06/2014	URG-1	SA-R	7/11/2013	10.011	206
21/06/2014	CS-2	SA-R	26/09/2013	9.404	190
22/06/2014	CS-11	SA-R	26/09/2013	10.608	220
22/06/2014	CA-1	SA-R	6/09/2013	9.881	215
23/06/2014	CA-2	SA-R	6/09/2013	9.624	153
23/06/2014	DS-3	SA-R	6/09/2013	9.094	142

23/06/2014	CL-1	SA-R	25/08/2013	11.678	191
24/06/2014	CL-2	SA-R	25/08/2013	9.095	131
24/06/2014	CL-3	SA-R	25/08/2013	9.642	221
25/06/2014	AR-4	STD	29/11/2013	11.913	251
25/06/2014	AR-3	STD	29/11/2013	fail	fail
25/06/2014	AR-2	STD	29/11/2013	unknown	310
26/06/2014	AR-2	STD	29/11/2013	5.047	101
26/06/2014	CM-1_2	STD	26/06/2014	10.202	181
27/06/2014	c.071600	SA-S	26/06/2014	9.681	196
27/06/2014	c.074754	SA-S	26/06/2014	9.739	181
28/06/2014	c.081953	SA-S	27/06/2014	9.893	201
28/06/2014	c.098606A	SA-S	27/06/2014	10.057	201
29/06/2014	c.098606B	SA-S	27/06/2014	10.865	219
29/06/2014	c.114414	SA-S	27/06/2014	11.09	220
1/07/2014	CM-1_3(1)	STD	26/06/2014	10.442	207
1/07/2014	CM-1_3(2)	STD	"	"	"
2/07/2014	c.159311A	SA-S	28/06/2014	10.023	201
2/07/2014	c.159311B	SA-S	28/06/2014	9.989	202
2/07/2014	c.348717A	SA-S	28/06/2014	9.84	201
3/07/2014	c.348717B	SA-S	28/06/2014	9.929	200
3/07/2014	c.349881	SA-S	1/07/2014	10.195	193
3/07/2014	c.355060	SA-S	1/07/2014	9.685	199
3/07/2014	c.3600161	SA-S	1/07/2014	9.608	195
4/07/2014	c.361481	SA-S	1/07/2014	9.878	201
4/07/2014	Oztech1996C	STD	4/07/2014	-	-
4/07/2014	CM-1_4	STD	2/07/2014	10.699	2017
4/07/2014	CM-1_5	STD	"	"	"
5/07/2014	AR_5	STD	2/07/2014	9.638	194
5/07/2014	C.405410	SA-S	2/07/2014	9.856	213
6/07/2014	FH-1	SA-B	10/04/2014	11.839	249
6/07/2014	FH-2	SA-B	10/04/2014	6.047	130
7/07/2014	IN-5	SA-R	9/11/2012	5.016	102
7/07/2014	DS-3	SA-R	9/11/2012	5.143	70
8/07/2014	IN-5	SA-R	25/08/2013	10.968	188
8/07/2014	IN-1	SA-R	13/08/2013	9.846	203
8/07/2014	IN-2	SA-R	13/08/2013	9.75	197
9/07/2014	IN-3	SA-R	13/08/2013	11.684	237
9/07/2014	WH-1f	SA-R	23/08/2013	9.971	208
9/07/2014	WH-2A	SA-R	23/08/2013	9.358	184
10/07/2014	WH-4	SA-R	23/08/2013	9.463	197
10/07/2014	WH-5	SA-R	23/08/2013	9.638	200
10/07/2014	NG-1A	SA-R	26/06/2013	9.829	202
11/07/2014	NG-1C	SA-R	26/06/2013	10.081	211
11/07/2014	NG-3	SA-R	26/06/2013	9.94	209
11/07/2014	NG-5	SA-R	26/06/2013	10.588	205
12/07/2014	BC-5	SA-R	27/06/2013	10.23	205

12/07/2014	BC-10	SA-R	27/06/2013	10.363	217
12/07/2014	BC-14A	SA-R	27/06/2013	10.529	217
13/07/2014	BC-14B	SA-R	27/06/2013	8.88	179
15/07/2014	AL90-1A	SA-R	8/08/2013	4.074	80
15/07/2014	AL-90-1B	SA-R	8/08/2013	5.419	115
15/07/2014	AL90-2	SA-R	8/08/2013	4.623	71
16/07/2014	AL90-3A	SA-R	8/08/2013	4.271	15
16/07/2014	AL90-3C	SA-R	9/08/2013	10.654	206
18/07/2014	Bone-F2	SA-B	16/07/2017	15.29	15
18/07/2014	Bone-F3	SA-B	16/07/2017	15.29	12
18/07/2014	Bone-M	SA-B	16/07/2017	6	6
19/07/2014	CM-1_6(1)	STD	19/08/2017	10.559	176
19/07/2014	CM-1_6(2)	STD	19/08/2017	"	"
20/07/2014	CM-1_7(1)	STD	19/08/2017	10.184	178
20/07/2014	CM-1_7(2)	STD	19/08/2017	"	"
22/07/2014	c.071606	SA-S	2/07/2014	10.516	226
22/07/2014	c.074754	SA-S	2/07/2014	9.88	203
24/07/2014	ML-1	SA-G	4/07/2014	10.135	207
24/07/2014	AL-1	SA-G	4/07/2014	10.784	221
24/07/2014	BR-1A	SA-G	4/07/2014	9.572	195
24/07/2014	OR-1A	SA-G	4/07/2014	9.140	186
25/07/2014	OR-2A	SA-G	5/07/2014	10.090	206
25/07/2014	MG-2A(mollusc)	SA-G	5/07/2014	9.967	204
25/07/2014	MG-2A(shell)	SA-G	5/07/2014	9.444	192
1/09/2014	c.081953	SA-S	2/07/2014	10.588	217
27/07/2014	GL-1	SA-G	9/07/2014	9.467	193
27/07/2014	WH-1	SA-G	9/07/2014	9.534	194
27/07/2014	WH-2A	SA-G	9/07/2014	10.206	209
27/07/2014	WH-2B	SA-G	9/07/2014	10.092	206
28/07/2014	WH-4	SA-G	10/07/2014	9.198	187
28/07/2014	WH-5	SA-G	10/07/2014	9.830	201
28/07/2014	WH-5d	SA-G	10/07/2014	10.622	218
29/07/2014	H1-B	SA-G	10/07/2014	10.575	217
29/07/2014	H4-A	SA-G	11/07/2014	10.828	222
29/07/2014	KP-7B	SA-G	11/07/2014	9.076	184
30/07/2014	KP-7B-lt	SA-G	12/07/2014	9.205	187
30/07/2014	TUN541.7	SA-G	12/07/2014	10.901	224
30/07/2014	TUN637-dk	SA-G	12/07/2014	10.481	215
16/09/2014	Oztech1952C	STD	15/07/2014	28.3 mbar	10000mV
16/09/2014	HG1000°C(1996C)	HG	15/07/2014	28.3 mbar	9000mV
17/09/2014	HG1000°C(1996C)	HG	15/07/2014	28.3 mbar	9000mV
17/09/2014	HG1000°C(1996C)	HG	15/07/2014	28.3 mbar	9000mV
18/09/2014	HG1000°C(1952C)	HG	15/07/2014	18.0 mbar	9000mV
19/09/2014	HG1000°C(1952C)	HG	15/07/2014	18.0 mbar	9000mV
19/09/2014	CM-1_8(1)	STD	13/09/2014	10.19	207
19/09/2014	CM-1_8(2)	STD	13/09/2014	"	"

20/09/2014	CM-1_8(3)	STD	13/09/2014	"	"
22/09/2014	ETH-1_1	STD	13/09/2014	10.3	207
23/09/2014	ETH-1_2	STD	13/09/2014	"	"
23/09/2014	ETH-2_1	STD	13/09/2014	9.053	191
24/09/2014	c.098606A	SA-S	17/09/2014	10.949	223
24/09/2014	c.098606B	SA-S	17/09/2014	9.461	193
25/09/2014	c.114414	SA-S	17/09/2014	9.583	198
25/09/2014	c.159311A	SA-S	17/09/2014	10.446	210
26/09/2014	c.159311B	SA-S	17/09/2014	9.404	194
26/09/2014	c.348717A	SA-S	17/09/2014	9.392	194
27/09/2014	c.348717B	SA-S	17/09/2014	9.892	210
27/09/2014	c.349881	SA-S	18/09/2014	10.527	217
28/09/2014	c.355060	SA-S	18/09/2014	9.565	199
29/09/2014	OR-1a	SA-R	18/09/2014	9.623	181
2/10/2014	RT-1	SA-R	22/09/2014	10.510	215
2/10/2014	OS-1	SA-R	22/09/2014	9.943	203
2/10/2014	OS-3	SA-R	22/09/2014	10.635	218
3/10/2014	WH-1	SA-R	22/09/2014	9.661	197
3/10/2014	WH-2	SA-R	23/09/2014	10.229	209
3/10/2014	WH-4	SA-R	23/09/2014	9.559	195
4/10/2014	WH-5	SA-R	23/09/2014	10.259	210
4/10/2014	CA-1	SA-R	23/09/2014	10.332	211
4/10/2014	CA-2	SA-R	24/09/2014	9.440	192
5/10/2014	BC-14B	SA-R	24/09/2014	9.224	188
5/10/2014	BC-14A	SA-R	24/09/2014	10.188	208
6/10/2014	BC-10	SA-R	24/09/2014	9.873	202
6/10/2014	BC-5	SA-R	25/09/2014	10.251	210
7/10/2014	BC-2(calcite)	SA-R	25/09/2014	10.668	219
7/10/2014	SG-3	SA-R	25/09/2014	10.825	222
7/10/2014	SG-2	SA-R	25/09/2014	9.946	203
8/10/2014	SG-1	SA-R	26/09/2014	9.657	197
8/10/2014	CS-10	SA-R	26/09/2014	9.419	192
8/10/2014	CS-2	SA-R	26/09/2014	9.814	200
8/10/2014	IN5	SA-R	26/09/2014	9.463	193
9/10/2014	IN-3	SA-R	30/09/2014	9.242	188
9/10/2014	IN-2	SA-R	30/09/2014	10.326	211
9/10/2014	NG-3	SA-R	30/09/2014	9.951	203
10/10/2014	NG-1C	SA-R	1/10/2014	9.960	203
10/10/2014	NG-1A	SA-R	1/10/2014	9.223	188

CHAPTER 2

Clumped Isotope Geochemistry

ALLAN R. CHIVAS* AND FLORIAN W. DUX

GeoQuEST Research Centre, School of Earth & Environmental Sciences, University of Wollongong, NSW 2522, Australia
*Email: toschi@uow.edu.au

2.1 Introduction

The understanding of recent past climates and environments is reliant on secure estimates of past temperatures and rainfall. Although sediments from the ocean basins now provide a fair indication of global changes from millennial through to million-year timescales, difficulties remain in understanding the effect of changing ocean–atmosphere dynamics upon regional terrestrial climates. Palaeoclimate archives from ice-free continents include lake sediments, speleothems, and ancient soils; however, such archives typically offer indirect, non-linear, or ambiguous evidence for past climate change. There remain few, if any, truly robust means of estimating past air temperature on land, backed with the support of both theoretical and empirical evidence. Nevertheless, it is self-evident that the refinement of terrestrial temperature proxies is of critical importance, given that the bulk of human activities and occupation occur on land, and that climate impact on soil and water resources, agriculture, and habitability may change in the future. Reconstruction of past climate from sedimentary archives is the only means through which our understanding of the global climate system over timescales greater than about 100 years can be challenged, and through which the models used to predict future change can be tested. Developing techniques that provide robust estimates of past temperature and hydrological change is therefore a challenge of great importance.

RSC Detection Science Series No. 4
Principles and Practice of Analytical Techniques in Geosciences
Edited by Kliti Grice

Published by the Royal Society of Chemistry, www.rsc.org

The study[1–3] of multiply substituted isotopologues, commonly called clumped isotopologues, or clumped isotopes of CO_2 liberated from carbonate minerals provides a new palaeothermometer that will greatly assist in the investigation of various geochemical palaeoclimatic problems.

2.2 Background

The development of oxygen isotope geochemistry fundamentally altered the discipline of palaeoclimatology. Sixty years after the pioneering work[4–6] of the Chicago group following Harold Urey, who established the modern theory and application of stable isotope fractionation to geochemistry, oxygen isotope ratios are now measured routinely in a wide range of materials by a variety of mass spectrometric techniques. Arguably the most valuable and unquestionably the most measured archives of oxygen isotope ratios are carbonate and carbonate-bearing minerals, which form in a wide range of environments by both biological and abiotic processes. The oxygen isotope composition (expressed as $\delta^{18}O$; a measure of $^{18}O/^{16}O$) of carbonate minerals is a function of the $\delta^{18}O$ value of the fluid from which they formed and the temperature at which precipitation occurred. Oxygen isotope ratios are thus commonly applied either as a palaeothermometer for waters from which carbonate minerals precipitated or as a tracer for the source or modification (*e.g.* through evaporation) of that water. Whereas the application of oxygen isotope geochemistry has and continues to be a fundamental tool in palaeoenvironmental studies, its utility for establishing unambiguous absolute palaeotemperatures is forever hindered by the requirement to measure independently, or more commonly, to assume, the $\delta^{18}O$ value of the original fluid from which carbonates formed. For marine calcites deposited in the past few million years, confident assumptions of initial $\delta^{18}O_{fluid}$ values may be attempted, but robust approximations for older marine sediments and terrestrial carbonates are virtually impossible to make.

The definition of the $\delta^{18}O$ value (expressed in per mil, or ‰) for palaeotemperature work is by comparison to the now exhausted PDB carbonate standard (a sample of the belemnite *Belemnitella americana* from the Cretaceous Pee Dee formation of South Carolina).

$$\delta^{18}O_{VPDB}(\text{in}\,‰) = \left[\frac{^{18}O/^{16}O_{sample} - ^{18}O/^{16}O_{VPDB}}{^{18}O/^{16}O_{VPDB}}\right] \times 1000 \qquad (2.1)$$

If we allow the ratio $^{18}O/^{16}O$ to be R, equation (2.1) can also be expressed as

$$\delta^{18}O_{VPDB}(\text{in}\,‰) = \left[\frac{R_{sample}}{R_{standard}} - 1\right] \times 1000 \qquad (2.2)$$

In practice, the currently available material[7–9] for interlaboratory comparison is NBS-19, which has a $\delta^{18}O$ VPDB value of -2.2 ‰.

To ensure highly precise data, it is necessary to use two standards, as the measured delta span between two samples commonly varies slightly (up to a few per cent) depending on the mass spectrometer used. Accordingly both NBS-19 and NBS-18 ($\delta^{18}O = -23.0$ ‰ VPDB) are needed. The standard form of mass spectrometry[10] is by electron bombardment (commonly called electron impact (EI), or gas-source mass spectrometry) and uses a dual inlet to permit measurement cycling between the sample CO_2 and a standard CO_2 of known isotopic composition. The CO_2 is generated by reaction[4] of the carbonate mineral with phosphoric acid, originally at 25 °C although more recently commonly at higher temperatures.

A typical $\delta^{18}O$ palaeotemperature equation[5,11] is of the form

$$T(^{\circ}C) = 16.9 - 4.2(\delta^{18}O_c - \delta^{18}O_w) + 0.13(\delta^{18}O_c - \delta^{18}O_w)^2 \qquad (2.3)$$

and refers to calcitic molluscs. There is a family of virtually parallel curves for, among others, aragonitic molluscs,[12] foraminifers,[13] and ostracods.[14,15] Wanamaker *et al.* report updated data[16] for the calcitic portion of the blue mussel *Mytilus edulis*.

In equation (2.3), $\delta^{18}O_c$ refers to the $\delta^{18}O$ value of the carbonate, and can be measured; $\delta^{18}O_w$ refers to the isotopic composition of the water. Except in modern monitored aquatic environments, or laboratory growth or culturing experiments, $\delta^{18}O_w$ may need to be estimated. The offsets on $\delta^{18}O_c$ for different organisms and compared to inorganic carbonate precipitation are commonly referred to as 'vital effects'.

A promising new technique to avoid the prerequisite of knowing the oxygen isotope composition of source fluids to determine palaeotemperature from carbonates of virtually any origin has recently been developed[17,18] by John Eiler and colleagues at the California Institute of Technology. Known as the clumped isotope method, this technique is founded on theoretical estimates based on lattice dynamics of the relative abundance of the isotopologues of carbonate ($^{60-67}CO_3$), not just the most abundant which are typically measured on the CO_2 ($^{44-46}CO_2$) produced by reaction of carbonate minerals in phosphoric acid (for both 'conventional' carbon and oxygen isotope analyses). Clumped isotope measurements are typically expressed in per mil variation of the relative abundance of a specific isotopologue (chiefly $^{47}CO_2$) from the theoretically predicted relative abundance based on a random distribution.[19,20] The clumped isotope palaeothermometer has now been calibrated for inorganic calcite, biogenic aragonite,[17] fish otoliths,[21] foraminifers, and coccoliths,[22,23] molluscs and brachiopods,[24–26] deep-sea corals,[27] and inorganic siderite[28] ($FeCO_3$) and should be applicable to many carbonate minerals that were formed in the 0–150 °C temperature range. Moreover, simultaneous determinations of $^{47}CO_2$ and $\delta^{18}O$ for carbonates will constrain the $\delta^{18}O$ of the water from which they precipitated, which is a sensitive tracer of atmospheric and surface hydrological change. Accordingly, clumped isotope thermometry is rapidly becoming established as a tool through which accurate estimates of

past temperature can be derived,[1,2,29] providing an unique and powerful tool that can address key questions on global climate history.

2.3 How to Measure 'Clumped' Isotopes

Carbonate 'clumped' isotope geochemistry ''is concerned with the state of order of rare isotopes within natural materials. That is, it examines[1] the extent to which heavy isotopes (^{13}C, ^{18}O) bond with or near each other rather than with the sea of light isotopes in which they swim''. The proportion of ^{13}C–^{18}O bonds in carbonate minerals (mass 47 in CO_2, *i.e.* ^{13}C–^{18}O–^{16}O), extracted from $CaCO_3$, is sensitive to their growth temperatures, largely independent of bulk isotopic composition. The reaction temperature[30] between H_3PO_4 and $CaCO_3$ which liberates CO_2 is required to be controlled and constant for a given series of samples and standards.

The various isotopologues[1] of all six masses of CO_2, and their relative abundances are given in Table 2.1.

The temperature signal is derived from the deviation of the ratio of $^{47}CO_2$ in a sample from its stochastic or random isotopologue distribution. This is termed Δ_{47} and $\Delta_{47} = 0‰$ for the stochastic distribution and is readily produced in the laboratory (and used as a standard) by heating any sample of natural CO_2 to 1000 °C for 2 hours. Thus, where R_{47} is the sample and R_{47*} is the stochastic CO_2,

$$\Delta_{47} = \left[\left(\frac{R_{47}}{R_{47^*}} - 1\right) - \left(\frac{R_{46}}{R_{46^*}} - 1\right) - \left(\frac{R_{45}}{R_{45^*}} - 1\right)\right] \times 1000 \qquad (2.4)$$

The theoretical basis for this temperature-dependent isotopologue fractionation has been well discussed[19,20,31–33] and reviewed.[3,34] Additional, albeit small, factors that affect Δ_{47} include the speciation of the dissolved inorganic carbon species (*i.e.* $H_2CO_3/HCO_3^-/CO_3^{2-}$), which is pH dependent,

Table 2.1 Stochastic abundances of the isotopologues of carbon dioxide.[a]

Mass	Isotopologue	Relative abundance[b]
44	$^{12}C^{16}O_2$	98.40%
45	$^{13}C^{16}O_2$	1.11%
	$^{12}C^{17}O^{16}O$	748 ppm
46	$^{12}C^{18}O^{16}O$	0.40%
	$^{13}C^{17}O^{16}O$	8.4 ppm
	$^{12}C^{17}O_2$	0.142 ppm
47	$^{13}C^{18}O^{16}O$	44.4 ppm
	$^{12}C^{17}O^{18}O$	1.5 ppm
	$^{13}C^{17}O_2$	1.6 ppb
48	$^{12}C^{18}O_2$	3.96 ppm
	$^{13}C^{17}O^{18}O$	16.8 ppb
49	$^{13}C^{18}O_2$	44.5 ppb

[a]Source: Eiler.[1]
[b]Assuming $^{17}O/^{16}O$ and $^{18}O/^{16}O$ ratios equal to the VSMOW standard and $^{13}C/^{12}C$ ratio equal to the VPDB standard.

and salinity during carbonate precipitation,[33] and have yet to be addressed and incorporated in empirical temperature calculations.

Ultra-high-sensitivity gas-source mass spectrometry is required, measuring the equivalent $\delta^{18}O$ (*i.e.* CO_2 of mass 46/mass 44) and Δ_{47} to $\pm$ 0.01‰. Hydrocarbon and chlorine contaminants (*e.g.* $^{12}C^{35}Cl$), even at the parts per billion level, are fatal to the analysis. Accordingly, CO_2 masses 48 and 49 are also measured simultaneously (requiring a six-collector array for *m/e* of 44, 45, 46, 47, 48, 49), and CO_2 purification by gas chromatography is mandatory.[35] Several commercially available dual-inlet machines have been used[1,17,35–38] and several instrumental corrections[35,38–40] need to be carefully applied. Long analysis times (2 h) are required to gain the necessary precision to declare a carbonate growth temperature of ± 1.5 °C. Standardisation is by calibrated standard gases, and constant repeat analyses with overlapping unknowns. It is further recommended that Δ_{47} be reported in an absolute reference frame[41] ($\Delta_{47\text{-RF}}$) by the use of a second reference standard, by equilibration of CO_2 with H_2O at 25 °C.

The full range of Δ_{47} values in nature varies from 0‰ to 0.8‰, with an even smaller range from 0.8‰ to 0.5‰ for carbonate precipitated in the Earth-surface temperature range of 0–60 °C. Accordingly, a clumped isotope (palaeo)temperature equation (see below) will only be of use if Δ_{47} can be measured to about $\pm$ 0.01‰.

There have been several attempts at such calibration, for inorganic calcite precipitation[17] with the most recent[42] (equation 2.5) over a larger temperature range, producing a curve (Figure 2.1) that is in better agreement with many biogenic carbonates.

$$\Delta_{47} = 0.053 \times 10^6/T^2 + 0.052 \quad (2.5)$$

Figure 2.1 indicates that a variety of carbonate-secreting organisms grown at controlled temperature, or harvested from environments where the water temperature was monitored, display a Δ_{47}–T relationship similar to that of inorganic calcite. However, Δ_{47} data for shallow-water fast-growing corals,[43] not plotted, lie above the carbonate line, and speleothem calcite Δ_{47} values commonly lie below the line. In each case, kinetic isotope effects related to rapid CO_2 degassing or rapid hydration of CO_2, respectively, are suspected.[3] Notwithstanding such difficulties with these two media, the majority of carbonates appear amenable to palaeotemperature investigation and with the advantage that mineralogical variability (calcite, aragonite, or siderite) and vital effects among most $CaCO_3$-secreting organisms are minimal. The following section provides some examples of successful and plausible applications.

2.4 Geological Applications

A number of studies in the area of palaeoceanography have been chosen to successfully highlight key changes in Earth climates even in the older parts

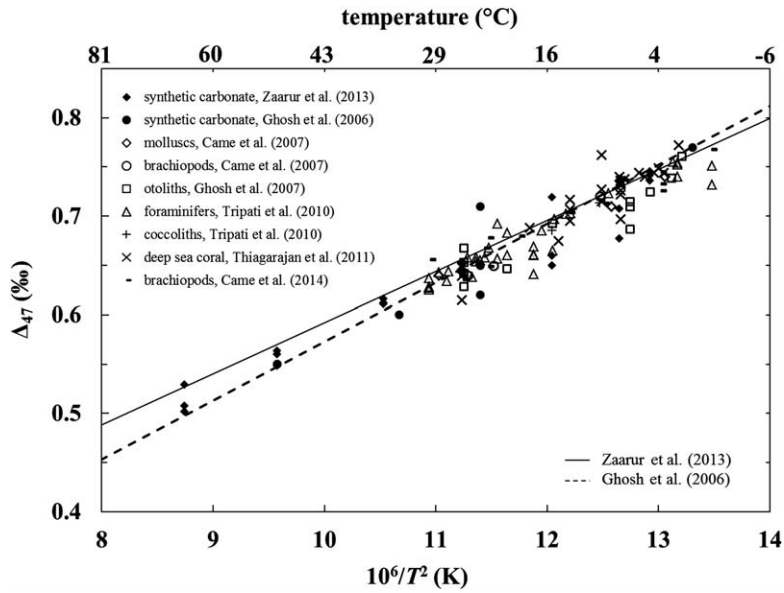

Figure 2.1 Δ_{47}–T calibration line for combined synthetic[17,42] and biogenic carbonates.[21,22,26,27,45] The compilation is from Zaarur *et al.*,[42] and all data are plotted into the Gosh *et al.*[17] reference frame.

of the geological record. Using clumped isotopes, applied to a variety of biota including corals and brachiopods, a short interval of cooling by 5 °C (from 32 to 37 °C) is demonstrated[44] for tropical oceans at the time of the Late Ordovician glaciation, approximately 445 million years ago. Warmer-than-present ocean temperatures are demonstrated[45] in the Early Silurian (~430 Ma), and exceedingly warm tropical sea-surface temperatures (to 39 °C) are proposed[46] for the end-Permian extinction. Other studies have investigated the North American Cretaceous interior seaway,[47] environmental changes at the Cretaceous–Paleogene (66 Ma) boundary,[48] the warm conditions[49–51] of the Late Cretaceous (~140 Ma) and Eocene (~50 Ma), and sea-surface cooling[52] during the last glacial maximum.

In the freshwater domain, clumped isotope data on molluscs[53] from the Canadian Arctic show temperatures during the Pliocene up to 15 °C warmer than today. Aragonitic land snails indicate calcification temperatures at higher than ambient conditions, reflecting snail body temperature[54] at the time of calcification. The carbonate phase of bioapatite is amendable to clumped isotope palaeothermometry, thereby placing vertebrate palaeontology within the realm of investigation. One of the more spectacular results indicates that some dinosaurs were warm-blooded[55,56] and therefore not reptiles.

Speleothems commonly display Δ_{47} disequilibrium and are not yet readily usable in isolation,[57–62] and may need supplementation by an additional independent analytical technique to realise their potential. By contrast, soil carbonates have proven fruitful, with a number of studies[63–69] spanning the

Cenozoic rock record. Several investigations have used carbonate from palaeosols to infer uplift histories[18,70–73] for the Andes and the Colorado Plateau.

Whereas the foregoing studies have attempted to elucidate past Earth-surface temperatures there is scope to look at somewhat deeper geological processes where temperatures up to 100–200 °C are attained. This is the domain of shallow hydrothermal vein formation, mineralised fault planes, diagenesis, low-temperature metamorphism, and ore deposition.[74–81] It also provides an opportunity to examine how higher-temperature carbonates retain or adjust their Δ_{47} values at progressively shallower depths during erosion.[82] The initial studies of rates of cooling and kinetics[83] in such systems show promise and complexity, and further advances can be anticipated. The reliable upper temperature limit for carbonate clumped isotopes will depend on the rate of heating and/or cooling of each rock system. Initial experiments[84] indicate that calcite maintained at around 100 °C for 10^6 to 10^8 years should retain its initial clumped isotope signature.

The original applications[3,85,86] of Δ_{47} were to modern atmospheric CO_2. As a tracer, $\Delta^{47}/\delta^{18}0_{CO_2}$ plots readily distinguish among CO_2 sources from car-exhaust pollution, respiration, and the troposphere. Other atmospheric 'clumped' systems are in development. The minor isotopologues of atmospheric O_2 ($^{18}O^{18}O$ and $^{17}O^{18}O$) are being developed[87] to study its global budget and the technique may be expanded to the study of trapped atmospheric samples in ice cores. The advent of high-resolution gas-source mass spectrometry[88,89] has permitted investigation of the isotopologues of methane and the establishment[90] of a thermometer for methane formation applicable to atmospheric, biological, and geological fields.

References

1. J. M. Eiler, 'Clumped-isotope' geochemistry—The study of naturally-occurring, multiply substituted isotopologues, *Earth Planet. Sci. Lett.*, 2007, **262**, 309–327.
2. J. M. Eiler, Paleoclimate reconstruction using carbonate clumped isotope thermometry, *Quat. Sci. Revs.*, 2011, **30**, 3575–3588.
3. J. M. Eiler, The isotopic anatomies of molecules and minerals, *Annu. Rev. Earth Planet. Sci.*, 2013, **41**, 411–414.
4. J. M. McCrea, On the isotopic chemistry of carbonates and a paleotemperature scale, *J. Chem. Phys.*, 1950, **18**, 849–857.
5. S. Epstein, R. Buchsbaum, H. Lowenstam and H. C. Urey, Revised carbonate-water isotopic temperature scale, *Bull. Geol. Soc. Am.*, 1953, **64**, 1315–1326.
6. H. Urey, The thermodynamic properties of isotopic substances, *J. Chem. Soc.*, 1947, 562–581.
7. R. Gonfiantini, Standards for stable isotope measurements in natural compounds, *Nature*, 1978, **271**, 534–536.

8. T. B. Coplen, C. Kendall and J. Hopple, Comparison of stable isotope reference samples, *Nature*, 1983, **302**, 236–238.
9. T. B. Coplen, P. De Bièvre, H. R. Krouse, R. D. Vocke Jr., M. Gröning and K. Rozanski, Ratios for light-element isotopes standardized for better interlaboratory comparison, *Eos, Trans. Am. Geophys. Union*, 1996, **77**, 255.
10. C. R. McKinney, J. M. McCrea, S. Epstein, H. A. Allen and H. C. Urey, Improvements in mass spectrometers for the measurement of small differences in isotope abundance ratios, *Rev. Sci. Instrum.*, 1950, **21**, 724–730.
11. H. Craig, The measurement of oxygen isotope paleotemperatures, in *Stable Isotopes in Oceanographic Studies and Paleotemperatures*, ed. E. Tongiorgi, CNR-Laboratorio di Geologica Nucleare, Pisa, 1965, pp. 161–182.
12. Y. Horibe and T. Oba, Temperature scales of aragonite-water and calcite-water systems, *Fossils*, 1972, **23/24**, 69–79.
13. J. Erez and B. Luz, Experimental paleotemperature equation for planktonic foraminifera, *Geochim. Cosmochim. Acta*, 1983, **47**, 1025–1031.
14. J. Xia, E. Ito and D. R. Engstrom, Geochemistry of ostracode calcite: part 1. An experimental determination of oxygen isotope fractionation, *Geochim. Cosmochim. Acta*, 1997, **61**, 377–382.
15. A. R. Chivas, P. De Deckker, S. X. Wang and J. A. Cali, Oxygen-isotope systematics of the nektic ostracod *Australocypris robusta,* in *The Ostracoda—Applications in Quaternary Research*, ed. J. A. Holmes and A. R. Chivas, Geophysical Monograph 131, American Geophysical Union, Washington DC, 2002, 301–313.
16. A. D. Wanamaker Jr., K. J. Kreutz, H. W. Borns Jr., D. S. Introne, S. Feindel, S. Funder, P. D. Rawson and B. J. Barber, Experimental determination of salinity, temperature, growth and metabolic effects on shell isotope chemistry of *Mytilus edulis* collected from Maine and Greenland, *Paleoceanography*, 2007, **22**, PA2217.
17. P. Ghosh, J. Adkins, H. P. Affek, B. Balta, W. Guo, E. A. Schauble, D. Schrag and J. M. Eiler, ^{13}C-^{18}O bonds in carbonate materials: A new kind of paleothermometer, *Geochim. Cosmochim. Acta*, 2006, **70**, 1439–1456.
18. P. Ghosh, C. Garzione and J. M. Eiler, Rapid uplift of the Altiplano revealed through ^{13}C-^{18}O bonds in paleosol carbonates, *Science*, 2006, **311**, 511–515.
19. Z. Wang, E. A. Schauble and J. M. Eiler, Equilibrium thermodynamics of multiply substituted isotopologues of molecular gases, *Geochim. Cosmochim. Acta*, 2004, **68**, 4779–4797.
20. E. A. Schauble, P. Ghosh and J. M. Eiler, Preferential formation of ^{13}C-^{18}O bonds in carbonate minerals, estimated using first-principles lattice dynamics, *Geochim. Cosmochim. Acta*, 2006, **70**, 2510–2529.

21. P. Ghosh, J. M. Eiler, S. E. Campana and R. F. Feeney, Calibration of the carbonate 'clumped isotope' paleothermometer for otoliths, *Geochim. Cosmochim. Acta*, 2007, **71**, 2736–2744.
22. A. K. Tripati, R. A. Eagle, N. Thiagarajan, A. C. Gagnon, H. Bauch, P. R. Halloran and J. M. Eiler, ^{13}C–^{18}O isotope signatures and 'clumped isotope' thermometry in foraminifera and coccoliths, *Geochim. Cosmochim. Acta*, 2010, **74**, 5697–5717.
23. A-L. Grauel, T. W. Schmid, B. Hu, C. Bergami, L. Capotondi, L. Zhou and S. M. Bernasconi, Calibration and application of the 'clumped isotope' thermometer to foraminifera for high-resolution climate reconstructions, *Geochim. Cosmochim. Acta*, 2013, **108**, 125–140.
24. R. A. Eagle, J. M. Eiler, A. K. Tripati, J. B. Ries, P. S. Freitas, C. Heibenthal, A. D. Wanamaker Jr., M. Taviani, M. Elliot, S. Marenssi, K. Nakamura, P. Ramirez and K. Roy, The influence of temperature and seawater carbonate saturation state on ^{13}C-^{18}O bond ordering in bivalve mollusks, *Biogeosci. Discuss.*, 2013, **10**, 157–194.
25. G. A. Henkes, B. H. Passey, A. D. Wanamaker Jr., E. L. Grossman, W. G. Ambrose Jr and M. L. Carroll, Carbonate clumped isotope compositions of modern marine mollusk and brachiopod shells, *Geochim. Cosmochim. Acta*, 2012, **106**, 307–325.
26. R. E. Came, U. Brand and H. P. Affek, Clumped isotope signatures in modern brachiopod carbonate, *Chem. Geol.*, 2014, **377**, 20–30.
27. N. Thiagarajan, J. Adkins and J. M. Eiler, Carbonate clumped isotope thermometry of deep-sea corals and implications for vital effects, *Geochim. Cosmochim. Acta*, 2011, **75**, 4416–4425.
28. A. Fernandez, J. Tang and B. Rosenheim, Siderite 'clumped' isotope thermometry: A new paleoclimate proxy for humid continental environments, *Geochim. Cosmochim. Acta*, 2014, **126**, 411–421.
29. H. P. Affek, Clumped isotope paleothermometry: principles, applications, and challenges, *The Paleontological Society Papers*, 2012, **18**, 101–114.
30. U. Wacker, J. Fiebig and B. R. Schoene, Clumped isotope analysis of carbonates: comparison of two different acid digestion techniques, *Rapid Commun. Mass Spectrom.*, 2013, **27**, 1631–1642.
31. W. Guo, J. L. Mosenfelder, W. A. Goddard III and J. M. Eiler, Isotopic fractionations associated with phosphoric acid digestion of carbonate minerals: Insights from first-principles theoretical modeling and clumped isotope measurements, *Geochim. Cosmochim. Acta*, 2009, **73**, 7203–7225.
32. X. Cao and Y. Liu, Theoretical estimation of the equilibrium distribution of clumped isotopes in nature, *Geochim. Cosmochim. Acta*, 2012, **77**, 292–303.
33. P. S. Hill, A. K. Tripati and E. A. Schauble, Theoretical constraints on the effects of pH, salinity, and temperature on clumped isotope signatures of dissolved inorganic carbon species and precipitating carbonate minerals, *Geochim. Cosmochim. Acta*, 2014, **125**, 610–652.

34. M. A. Webb and T. F. Miller III, Position-specific and clumped stable isotope studies: comparison of the Urey and Path-Integral approaches for carbon dioxide, nitrous oxide, methane, and propane, *J. Phys. Chem.*, 2014, **118**, 467–474.
35. K. W. Huntington, J. M. Eiler, H. P. Affek, W. Guo, M. Bonifacie, L. Y. Yeung, N. Thiagarajan, B. Passey, A. Tripati, M. Daëron and R. Came, Methods and limitations of 'clumped' CO_2 isotope (Δ_{47}) analysis by gas-source isotope ratio mass spectrometry, *J. Mass Spectrom.*, 2009, **44**, 1318–1329.
36. T. W. Schmid and S. M. Bernasconi, An automated method for 'clumped-isotope' measurements on small carbonate samples, *Rapid Commun. Mass Spectrom.*, 2010, **24**, 1955–1963.
37. N. Yoshida, M. Vasilev, P. Ghosh, O. Abe, K. Yamada and M. Morimoto, Precision and long-term stability of clumped-isotope analysis of CO_2 using a small-sector isotope ratio mass spectrometer, *Rapid Commun. Mass Spectrom.*, 2013, **27**, 207–215.
38. B. E. Rosenheim, J. Tang and A. Fernandez, Measurement of multiply substituted isotopologues ('clumped isotopes') of CO_2 using a 5 kV compact isotope ratio mass spectrometer: Performance, reference frame, and carbonate paleothermometry, *Rapid Commun. Mass Spectrom.*, 2013, **27**, 1847–1857.
39. B. He, G. A. Olack and A. S. Colman, Pressure baseline corrections and high-precision CO_2 clumped-isotope (Δ_{47}) measurements in bellows and micro-volume modes, *Rapid Commun. Mass Spectrom.*, 2012, **26**, 2837–2853.
40. S. M. Bernasconi, B. Hu, U. Wacker, J. Fiebig, S. F. M. Breitenbach and T. Rutz, Background effects on Faraday collectors in gas-source mass spectrometry and implications for clumped isotope measurements, *Rapid Commun. Mass Spectrom.*, 2013, **27**, 603–612.
41. K. J. Dennis, H. P. Affek, B. H. Passey, D. P. Schrag and J. M. Eiler, Defining an absolute reference frame for 'clumped' isotope studies of CO_2, *Geochim. Cosmochim. Acta*, 2011, **75**, 7117–7131.
42. S. Zaarur, H. P. Affek and M. T. Brandon, A revised calibration of the clumped isotope thermometer, *Earth Planet. Sci. Lett.*, 2013, **382**, 47–57.
43. C. Saenger, H. P. Affek, T. Felis, N. Thiagarajan, J. M. Lough and M. Holcomb, Carbonate clumped isotope variability in shallow water corals: Temperature dependence and growth-related vital effects, *Geochim. Cosmochim. Acta*, 2012, **99**, 224–242.
44. S. Finnegan, K. Bergman, J. M. Eiler, D. S. Jones, D. A. Fike, I. Eisenman, N. C. Hughes, A. K. Tripati and W. W. Fischer, The magnitude and duration of Late Odovician-Early Silurian glaciation, *Science*, 2011, **331**, 903–906.
45. R. E. Came, J. M. Eiler, J. Veizer, K. Azmy, U. Brand and C. R Weidman, Coupling of surface temperatures and atmospheric CO_2 concentrations during the Palaeozoic era, *Nature*, 2007, **449**, 198–201.

46. U. Brand, R. Posenato, R. Came, H. Affek, L. Angiolini, K. Azmy and E. Farabegoli, The end-Permain mass extinction: A rapid volcanic CO_2 and CH_4-climatic catastrophe, *Chem. Geol.*, 2012, **322–323**, 121–144.
47. K. J. Dennis, J. K. Cochran, N. H. Landman and D. P. Schrag, The climate of the Late Cretaceous: New insights from the application of the carbonate clumped isotope thermometer to Western Interior Seaway macrofossil, *Earth Planet. Sci. Lett.*, 2013, **362**, 51–65.
48. T. S. Tobin, G. P. Wilson, J. M. Eiler and J. H. Hartman, Environmental change across a terrestrial Cretaceous-Paleogene boundary section in eastern Montana, USA, constrained by carbonate clumped isotope paleothermometry., *Geology*, 2014, **42**, 351–354.
49. G. D. Price and B. H. Passey, Dynamic polar climates in a greenhouse world: Evidence from clumped isotope thermometry of Early Cretaceous belemnites, *Geology*, 2013, **41**, 923–926.
50. C. R. Keating-Bitonti, L. C. Ivany, H. P. Affek, P. Douglas and S. Samson, Warm, not super-hot, temperatures in the early Eocene subtropics, *Geology*, 2011, **39**, 771–774.
51. C. M. Frantz, V. A. Petryshyn, P. J. Marenco, A. Tripati, W. M. Berelson and F. A. Corsetti, Dramatic local environmental change during the Early Eocene Climatic Optimum detected using high resolution chemical analyses of Green River Formation stromatolites, *Palaeogeogr. Palaeoclimatol. Palaeoecol.*, 2014, **405**, 1–15.
52. A. K. Tripati, S. Sahany, D. Pittman, R. A. Eagle, J. D. Neelin, J. L. Mitchell and L. Beaufort, Modern and glacial tropical snowlines controlled by sea surface temperature and atmospheric mixing., *Nat. Geosci.*, 2014, **7**, 205–209.
53. A. Z. Csank, A. K. Tripati, W. P. Patterson, R. A. Eagle, N. Rybczynski, A. P. Ballantyne and J. M. Eiler, Estimates of Arctic land surface temperatures during the early Pliocene from two novel proxies, *Earth Planet. Sci. Lett.*, 2011, **304**, 291–299.
54. S. Zaarur, G. Olack and H. P. Affek, Paleo-environmental implication of clumped isotopes in land snail shells, *Geochim. Cosmochim. Acta*, 2011, **75**, 6859–6869.
55. R. A. Eagle, E. A. Schauble, A. K. Tripati, T. Tütken, R. C. Hulbert and J. M. Eiler, Body temperatures of modern and extinct vertebrates from ^{13}C-^{18}O bond abundances in bioapatite, *Proc. Natl. Acad. Sci. U. S. A.*, 2010, **107**, 10377–10382.
56. R. A. Eagle, T. Tütken, T. S. Martin, A. K. Tripati, H. C. Fricke, M. Connely, R. L. Cifelli and J. M. Eiler, Dinosaur body temperatures determined from isotopic (^{13}C-^{18}O) ordering in fossil biomaterials, *Science*, 2011, **333**, 443–445.
57. M. Daëron, W. Guo, J. Eiler, D. Genty, D. Blamart, R. Boch, R. Drysdale, R. Maire, K. Wainer and G. Zanchetta, $^{13}C^{18}O$ clumping in speleothems: Observations from natural caves and precipitation experiments, *Geochim. Cosmochim. Acta*, 2011, **75**, 3303–3317.

58. H. P. Affeck, M. Bar-Matthews, A. Ayalon, A. Matthews and J. M. Eiler, Glacial/interglacial temperature variations in Soreq cave speleothems as recorded by 'clumped isotope' thermometry, *Geochim. Cosmochim. Acta*, 2008, **72**, 5351–5360.
59. H. P. Affek, Clumped isotopic equilibrium and the rate of isotope exchange between CO_2 and water, *Am. J. Sci.*, 2013, **313**, 309–325.
60. K. Wainer, D. Genty, D. Blamart, M. Daëron, M. Bar-Matthews, H. Vonhof, Y. Dublyansky, E. Pons-Branchu, L. Thomas, P. van Calsteren, Y. Quinif and N. Caillon, Speleothem record of the last 180 ka in Villars cave (SW France): Investigation of a large ^{18}O shift between MIS6 and MIS5, *Quat. Sci. Revs.*, 2011, **30**, 130–146.
61. T. Kluge and H. P. Affek, Quantifying kinetic fractionation in Bunker Cave speleothems using Δ_{47}, *Quat. Sci. Revs.*, 2012, **49**, 82–94.
62. T. Kluge, H. P. Affek, Y. G. Zhang, Y. Dublyansky, C. Spötl, A. Immenhouser and D. K. Richter, Clumped isotope thermometry of cryogenic cave carbonates, *Geochim. Cosmochim. Acta*, 2013, **61**, 3461–3475.
63. J. Quade, C. Garzione and J. M. Eiler, Paleoelevation reconstruction using pedogenic carbonates, *Rev. Mineral. Geochem.*, 2007, **66**, 53–87.
64. J. Quade, J. M. Eiler, M. Daëron and H. Achyuthan, The clumped isotope geothermometer in soil and paleosol carbonate, *Geochim. Cosmochim. Acta*, 2013, **105**, 92–107.
65. B. H. Passey, N. E. Levin, T. E. Cerling, F. H. Brown and J. M. Eiler, High-temperature environments of human evolution in East Africa based on bond ordering in paleosol carbonates, *Proc. Natl. Acad. Sci. U. S. A.*, 2010, **107**, 11245–11249.
66. K. E. Snell, B. L. Thrasher, J. M. Eiler, P. L. Koch, L. C. Sloan and N. J. Tabor, Hot summers in the Bighorn Basin during the early Paleogene, *Geology*, 2013, **41**, 55–58.
67. N. A. Peters, K. W. Huntington and G. D. Hoke, Hot or not? Impact of seasonally variable soil carbonate formation paleotemperature and O-isotope records from clumped isotope thermometry, *Earth Planet. Sci. Lett.*, 2012, **361**, 208–218.
68. J. H. VanDeVelde, G. J. Bowen, B. H. Passey and B. B. Bowen, Climatic diagenetic signals in the stable isotope geochemistry of dolomitic paleosols spanning the Paleocene-Eocene boundary. *Geochim. Cosmochim. Acta*, 2013, **109**, 254–267.
69. B. G. Hough, M. Fan and B. H. Passey, Calibration of the clumped isotope geothermometer in soil carbonate in Wyoming and Nebraska, USA: Implications for paleoelevation and paleoclimate reconstruction., *Earth Planet. Sci. Lett.*, 2014, **391**, 110–120.
70. K. W. Huntington, B. P. Wernicke and J. M. Eiler, Influence of climate change and uplift on Colorado Plateau paleotemperatures from carbonate clumped isotope thermometry, *Tectonics*, 2010, **29**(TC3005), 1–19.
71. J. Quade, D. O. Breecker, M. Daëron and J. Eiler, The paleoaltimetry of Tibet: an isotopic perspective. *Am. J. Sci.*, 2011, **311**, 77–115.

72. A. Leier, N. McQuarrie, C. Garzione and J. Eiler, Stable isotope evidence for multiple pulses of rapid surface uplift in the Central Andes, Bolivia, *Earth Planet. Sci. Lett.*, 2013, **371–372**, 49–58.
73. C. N. Garzione, D. J. Auerbach, J. J.-S. Smith, J. J. Rosario, B. H. Passey, T. E. Jordan and J. M. Eiler, Clumped isotope evidence for diachronous surface cooling of the Altiplano and pulsed surface uplift of the Central Andes, *Earth Planet. Sci. Lett.*, 2014, **393**, 173–181.
74. J. M. Ferry, B. H. Passey, C. Vasconcelos and J. M. Eiler, Formation of dolomite at 40–80°C in the Latemar carbonate buildup, Dolomites, Italy, from clumped isotope thermometry, *Geology*, 2011, **39**, 571–574.
75. T. F. Bristow, M. Bonifacie, A. Derkowski, J. M. Eiler and J. P. Grotzinger, A hydrothermal origin for isotopically anomalous cap dolostone cements from south China, *Nature*, 2011, **474**, 68–71.
76. K. W. Huntington, D. A. Budd, B. P. Wernicke and J. M. Eiler, Use of clumped-isotope thermometry to constrain the crystallization temperature of diagenetic calcite, *J. Sediment. Res.*, 2011, **81**, 656–669.
77. E. M. Swanson, B. P. Wernicke, J. M. Eiler and S. Losh, Temperatures and fluids on faults based on carbonate clumped-isotope thermometry, *Am. J. Sci.*, 2012, **312**, 1–21.
78. S. J. Loyd, F. A. Corsetti, J. M. Eiler and A. K. Tripati, Determining the diagenetic conditions of concretion formation: assessing temperatures and pore waters using clumped isotopes, *J. Sediment. Res.*, 2012, **82**, 1006–1016.
79. D. A. Budd, E. L. Frost III, K. W. Huntington and P. F. Allwardt, Syndepositional deformation features in high-relief carbonate platforms: long-lived conduits for diagenetic fluids, *J. Sediment. Res.*, 2013, **82**, 12–36.
80. A. Dale, C. M. John, P. S. Mozley, P. C. Smalley and A. H. Muggeridge, Time-capsule concretions: Unlocking burial diagenetic processes in the Mancos Shale using carbonate clumped isotopes, *Earth Planet. Sci. Lett.*, 2014, **394**, 30–37.
81. S. C. Bergman, K. W. Huntington and J. G. Crider, Tracing paleofluid sources using clumped isotope thermometry of diagenetic cements along the Moab Fault, Utah, *Am. J. Sci.*, 2013, **313**, 490–515.
82. K. J. Dennis and D. P. Schrag, Clumped isotope thermometry of carbonatites as an indicator of diagenetic alteration, *Geochim. Cosmochim. Acta*, 2010, **74**, 4110–4122.
83. B. H. Passey and G. A. Henkes, Carbonate clumped isotope bond reordering and geospeedometry, *Earth Planet. Sci. Lett.*, 2012, **351–352**, 223–236.
84. G. A. Henkes, B. H. Passey, E. L. Grossman, B. J. Shenton, A. Pérez-Huerta and T. E. Yancey, Temperature limits for the preservation of primary calcite clumped isotope paleotemperatures, *Geochim. Cosmochim. Acta*, 2014, doi: http://dx.doi.org/10.1016/j.gca.2014.04.040.
85. J. M. Eiler and E. A. Schauble, $^{18}O^{13}C^{16}O$ in Earth's atmosphere, *Geochim. Cosmochim. Acta*, 2004, **68**, 4767–4777.

86. H. P. Affek and J. M. Eiler, Abundance of mass 47 CO_2 in urban air, car exhausts, and human breath, *Geochim. Cosmochim. Acta*, 2006, **70**, 1–12.
87. L. Y. Yeung, E. D. Young and E. A. Schauble, Measurements of $^{18}O^{18}O$ and $^{17}O^{18}O$ in the atmosphere and the role of isotope-exchange reactions, *J. Geophys. Res.*, 2012, **117**, D18306.
88. J. M. Eiler, M. Clog, P. Magyar, A. Piasecki, A. Sessions, D. Stolper, M. Deerberg, H.-J. Schueter and J. Schwieters, A high-resolution gas-source isotope ratio mass spectrometer, *Int. J. Mass Spectrom.*, 2013, **335**, 45–56.
89. J. M. Eiler, B. Bergquist, I. Bourg, P. Cartigny, J. Farquhar, A. Gagnon, W. Guo, I. Halevy, A. Hofmann, T. E. Larson, N. Levin, E. A. Schauble and D. Stolper, Frontiers of stable isotope geoscience. *Chem. Geol.*, 2014, **372**, 119–143.
90. D. A. Stolper, A. L. Sessions, A. A. Ferreira, E. V. Santos Neto, A. Schimmelmann, S. S. Shusta, D. L. Valentine and J. M. Eiler, Combined ^{13}C-D and D-D clumping in methane: Methods and preliminary results, *Geochim. Cosmochim. Acta*, 2014, **126**, 169–191.